University of Basel

Swiss Nanoscience Institute

SNI
SWISS NANOSCIENCE INSTITUTE
EINE INITIATIVE DER UNIVERSITÄT BASEL UND DES KANTONS AARGAU

Annual Report 2015 Supplement

Swiss Nanoscience Institute University of Basel

The Swiss Nanoscience Institute (SNI) is a research initiative of the Canton of Aargau and the University of Basel.

This report summarizes work conducted at the Swiss Nanoscience Institute (SNI) in 2015.

Swiss Nanoscience Institute
Klingelbergstrasse 82
4056 Basel
Switzerland
www.nanoscience.ch

March 2016

Cover illustration: Combination experiment with diatom and celite: hematite (inside the diatom) is used as photoanode material for solar cells (Dr. Roché Walliser)

Contents

Microfluidic sample preparation methods for electron microscopy, electron diffraction and X-ray analysis

Project P1201 Microfluidics to study nano-crystallization of proteins
Project Leader: T. Braun and H. Stahlberg
Collaborators: S. Arnold (SNI PhD Student), T. Maier (Biozentrum, University of Basel), C. Padeste (PSI), A. Bieri (C-Cina, Biozentrum, University of Basel), S. Albiez (C-Cina, Biozentrum, University of Basel), N.L. Opara (PSI) and M. Leist (University of Konstanz)

Introduction

Structural biology currently experiences an accelerated technological development: First, X-ray free electron lasers (XFEL) and, second, transmission electron microscopy (TEM) using direct electron detection (DED) cameras emerged during recent years. DED cameras now allow the structure determination of large biomolecules to atomic resolution by a single particle approach without crystallization [1]. Furthermore, micro electron diffraction (microED) using electrons are becoming an alternative to x-ray diffraction of nano-sized 3D crystals.

However, sample preparation remained largely unchanged in the last twenty years. Standard methods used to prepare samples for electron microscopy (EM) suffer from various drawbacks: First, a large sample volume containing the biological species at high concentration is required. Second, massive blotting steps that remove more than 99% of the sample are employed.

In the course of this project we developed advanced sample preparation methods for EM, microED and potentially for XFEL analysis. The methods developed only consume nanoliters of sample in total, allowing also the preparation of the contents of individual cells for subsequent analysis by EM.

Sample preparation for cryo-electron microscopy (cryo-EM) [2]

Cryo-EM allows to study samples at cryogenic temperatures below -150°C at physiological conditions [3]. In order to prepare cryo-EM samples, two steps must be accomplished: First, a thin water film (few tens of nanometers) must be spanned in the hole of a perforated carbon film covering an EM-grid. Second, the grid must be rapidly cooled to cryogenic temperatures. This ensures that the thin water film is "frozen" before the water molecules can rearrange to form ice crystals. The result is an amorphous or vitreous ice, which is stable in the ultra-high vacuum of the electron microscope and conserves the structure of biomolecules in a physiological state.

In the classical preparation method, two to five microliters of sample are deposited on the holy carbon film. Subsequent, most of the liquid is removed by an extensive blotting step before shooting the grid into liquid ethane to "vitrify" the thin liquid layer.

We developed a method, a device and a system allowing a lossless cryo-EM preparation that only consumes minute amounts of sample (few nanoliter) and does not involve any blotting steps. A typical result of such a vitrification experiment is shown in Fig. 1 [2]. In the future, the cryo preparation method can also be used for 3D- nanocrystals as alternative to trehalose embedding (see the end of this report).

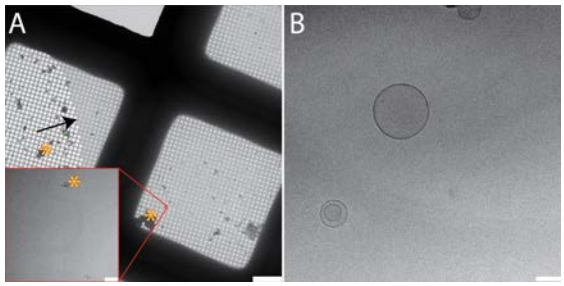

Fig. 1: Result of the vitrification process only consuming few nl of sample. ***A)*** *Overview cryo-EM image showing a 5 nl droplet dispensed on a holy carbon film. Note the homogeneous amorphous water layer. The black arrow indicates the periphery of the dispensed buffer. Scale bar: 20 µm. Inset: Higher magnification view of amorphous buffer (PBS) in a hole. The black spots denoted by '*' likely originate from the aluminum surface supporting the EM grid during glow-discharge treatment prior to sample deposition, and will be avoided by using a different support. Scale bar of inset: 80 nm.* ***B)*** *Higher magnification cryo-EM image of PDMS-based vesicles embedded in amorphous buffer. Scale bar: 100 nm. The ice layer is homogeneous and mostly free of contamination. [2]*

Sample preparation for negative stain EM [4]

Negative stain preparations embed the biological material, e.g., proteins, in amorphous heavy metal salt. Negative stain EM (NS-EM) exhibits an improved signal-to-noise ratio (SNR) allowing the analysis of complex samples, e.g. dynamic protein assemblies. However, the resolution is limited to approximately 16 Å. In this sense, NS-EM complements cryo-EM.

In the classical preparation procedure, the sample is adsorbed on a thin carbon layer and blotted with a filter paper before the negative stain solution is applied. Finally, the negative stain solution is blotted again and the grid is air-dried.

We developed a NS-EM grid preparation method to (i) add NS to the sample, (ii) remove endogenous salts, and, (iii) to dispense the sample onto the carbon film of an EM-grid. For sample conditioning and EM grid preparation, a microcapillary with sample loaded in its tip, is immersed into a reservoir of conditioning solution, e.g., NS; the conditioning is driven by diffusion (Fig. 2). This new conditioning module improves on the previously developed method using microfluidic based dialysis [5], since significantly less biomaterial gets lost by unspecific binding at the the walls of the microfluidic system and an significant smaller sample volumes can be handled.

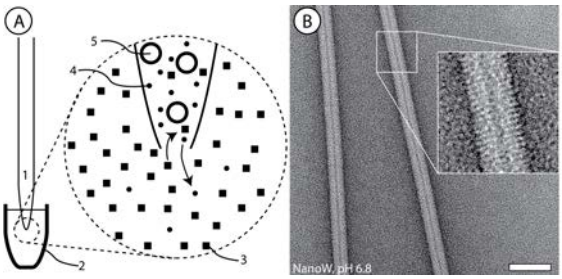

Fig. 2: Sample conditioning of nanoliter sample volumes for EM. A) Principle of diffusion controlled sample conditioning [4]. Note that the proteins exhibit significant lower diffusion constants than salt molecules and are retained in the capillary. 1: Microcapillary for cell lysis, sample uptake and dispensing, filled with system liquid (H2O). 2: Reservoir containing conditioning solution, e.g., heavy metal salts or trehalose (3). 4: Sample salt molecule; 5: sample protein. B) Tobacco mosaic virus prepared with the sample conditioning method. 2% of NanoW solution at pH 6.8 was used. Scale-bar: 50 nm. Inset: Three times enlarged region [4].

Single cell visual proteomics

The diffusion controlled sample conditioning allows the automated preparation of extremely small samples such as the content of an individual biological cell. To test this, the single cell lysis instrument [4] (see Argovia SCeNA Project, A9) was combined with the diffusion controlled sample conditioning method (Fig. 3). Fig. 4 shows the typical outcome of the lysis of an individual HEK 293 cell. This preparation method, with subsequent systematic imaging in the EM, allows to study large protein complexes of individual cells based on their visual appearance in the image ("single cell visual proteomics"). We performed heat-shock experiments using the visual proteomics method and have seen significant differences of the heat-shock protein expression levels between positive and negative control (data not shown).

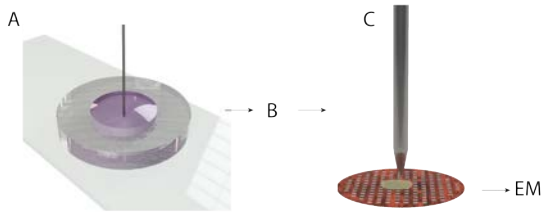

Fig. 3: Combination of single cell lysis set-up and diffusion controlled sample conditioning. A) Adherent eukaryotic cells are grown in miniaturized petri-dishes. Lysis of the cell is performed by electroporation and simultaneous aspiration of approx. 5 nl volume. B) sample conditioning as described in Fig. 2. C) Dispensing on EM grid. The visual appearance of the "proteome" is subsequently analysed by EM.

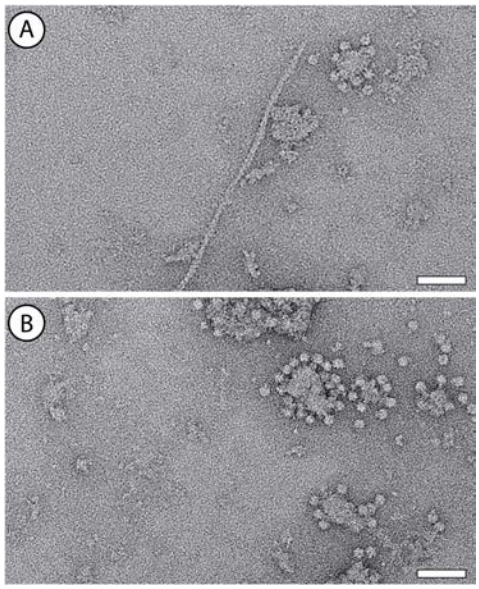

Fig. 4: TEM image of negatively stained single-cell lysate from a HEK 293 cell. A) Filamentous structure that is probably F-actin. B) Membranes decorated with distinctive heads, similar to mitochondrial membranes with ATP-synthases. Negative stain: 2% NanoW, scale bars: 20 nm. [4]

Preparation of 3D nanocrystals by trehalose embedding

The diffusion controlled sample conditioning (Fig. 2) also allows the preparation of 3D nanocrystals. This preparations can be used for analysis by x-ray diffraction, e.g., XFEL, or by microED. For an example see Fig. 4 of the project report P1305.

References for Project P1201

[1] W. Kuhlbrandt. Biochemistry. The resolution revolution. *Science* **343**, 1443–1444 (2014).

[2] S. Arnold, H. Stahlberg and T. Braun. Patent application: PCT/EP2015/065398 "*Lossless cryo-grid preparation stage for high-resolution electron microscopy*", 6.7.2015.

[3] J. Dubochet, M. Adrian, J.J. Chang, J.C. Homo, J. Lepault, A.W. McDowall and P. Schulz. „Cryo-electron microscopy of vitrified specimens", Quarterly Rev Biophys., **21**(02):129–228 (1988).

[4] S. Arnold, S. Albiez, N. Opara, M. Chami, C. Schmidli, A. Bieri, H. Stahlberg, C. Padeste and T. Braun, "*Total sample conditioning and preparation of nanoliter volumes for electron microscopy*". To be submitted.

[5] S. Kemmerling, J. Ziegler, G. Schweighauser, S. Arnold, D. Giss, S.A. Mueller, R. Ringler, K.N. Goeldie, N. Goedecke, A. Hierlemann, H. Stahlberg and T. Braun, *"Connecting mu-fluidics to electron microscopy"*. J Struct Biol., **177**(1):128–34 (2012).

Nanofluidic trapping devices for detecting critical reaction concentrations of reactants

Project P1202 Electrostatic nanotrapping for single-macromolecule analysis
Project Leader: Y. Ekinci and T. Pfohl
Collaborators: M. Gerspach (SNI PhD Student) and N. Mojarad

Introduction

The ultimate limit to analytical sensitivity at the nanoscale is the reliable detection and trapping of single nano-objects, which provides information on local dynamics and reactions. Extensive developments in active trapping methods such as optical and magnetic tweezers have been successfully demonstrated stable confining of single objects. However, they often need demanding setups and externally applied forces. One method of passively trapping and detecting objects smaller than 100 nm is geometry induced electrostatic (GIE) trapping [1].

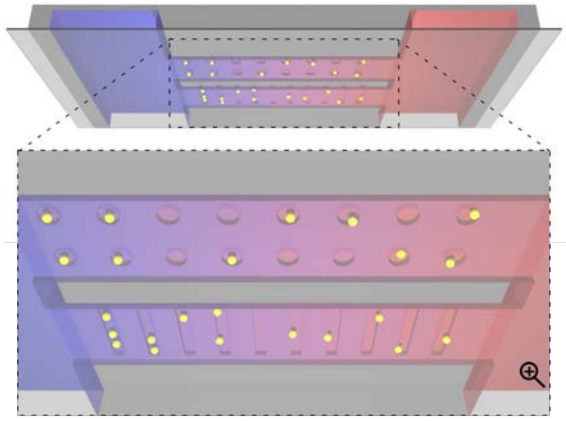

Fig. 1: Schematic of a geometry-induced electrostatic trapping device integrated into a microfluidic system. Nano-objects are trapped within the pockets and grooves of the nano-channels (middle) by electrostatic repulsion. Large supporting micro-channels provide the GIE trapping area with reactant or buffer solution (left and right).

Current GIE trapping devices with enhanced signal-to-noise ratio detection of nano-objects are fabricated from glass substrates using top-down nanofabrication [2]. Single charged nano-objects in the GIE trapping area (zoom of Fig. 1) are passively confined in nanometer sized pockets and grooves by electrostatic repulsion between the charged walls and the nano-objects. Various trapping geometries (pockets, channels or grids) can be realized using e-beam lithography. The trap stiffness can be controlled by altering the trap dimensions, charge density of the object and the device surface, and by the salt concentration of the buffer solution. Depending on this, single nano-objects can be reliably trapped from milliseconds to several minutes.

Integrating GIE trapping into microfluidic systems provides many advantages, including very small sample and reagent quantities, precise control of reactant concentrations as well as short analysis time. Furthermore, using the tools of microfluidics, a precise controlled steady concentration gradient e.g. of reactant or salt can be formed. This setup allows for the analysis of trapped nano-objects in different conditions using only a single device.

GIE trapping integrated int0 active micro-fluidic systems

A multi-height channel design of a GIE trapping device integrated into a microfluidic system is shown in Fig. 2. Two inlets and outlets are connected by two separated micrometer-deep supporting channels (dark red). These supporting micro-channels are connected by several nanometer-height GIE trapping channels (light red), consisting of finer nanostructures, i.e. the actual nanotraps. The final device is thermally bond to a cover glass to seal the fluidic channels and provide optical access. The in- and outlets are connected with microfluidic tubes for sample, reactant and buffer delivery.

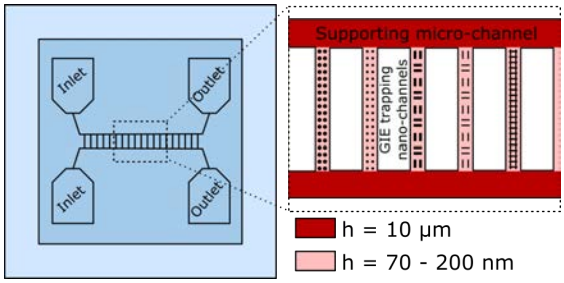

Fig. 2: Design of a GIE trapping device integrated into a microfluidic system. The device consists of two inlets and two outlets connected by two micro-channels of 10 µm height (dark red) that support the nano-channels with sample- and flushing solution. Single nano-objects are getting passively trapped in the confinements of the nano-channels (light red) by electrostatic repulsion.

The device is loaded by injecting the sample volume through the upper supporting micro-channel. The GIE trapping nano-channel region is easily filled with sample solution by capillary forces. After the desired sample is trapped in the GIE trapping area, the upper and lower supporting channels are flushed with buffer and reactant solution. Since the two supporting channels are only connected through the nano-channels, a linear gradient is formed in the GIE trapping area by simple diffusion following Fick's first law of diffusion (see Fig. 3):

$$J_x = -D\,\frac{\partial C}{\partial x} = -D\,\frac{C_2 - C_1}{d}$$

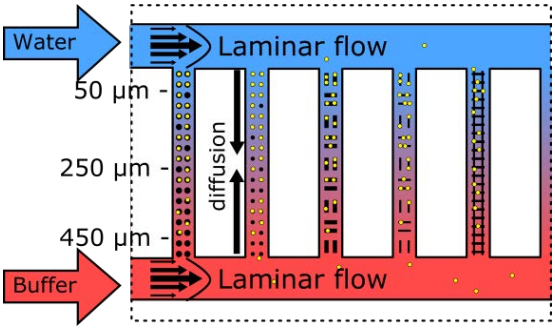

Fig. 3: A steady linear gradient in the trapping region (nano-channels) is created by flowing two different solutions through the upper and lower supporting micro-channels, respectively. The gradient is formed in the nano-channels by simple diffusion. Thus analysis of single nano-objects at different concentrations is achieved within a single device.

Salt gradient influences trap stiffness

As described in the SNI Annual Report 2014 [3], the stiffness of traps reduce when increasing the salt concentration of the solution due to the screening of the surface charges by free counter ions. To demonstrate, a salt gradient in the nano-channels were formed and the trap stiffness along one nano-channel were measured using gold nanoparticles. After loading the GIE trapping area with 60 nm gold particles, a 0.05 mM NaCl solution is flushed through the upper supporting channel whereas a solution of 1.0 mM NaCl is flushed through the lower channel. Since the buffer solutions are refreshed continuously, a linear salt gradient is formed in the 500 µm long nano-channel of concentration

$$C_{\mathrm{NaCl}}(\mathrm{x}) = 0.0019\ {}^{\mathrm{mM}}/_{\mu m} \cdot \mathrm{x} + 0.05\ \mathrm{mM}$$

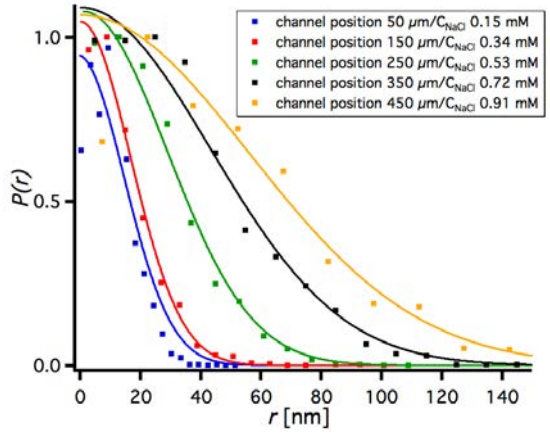

Fig. 4: Histogram of the lateral localization of 60 nm gold particles trapped at different positions/concentrations in one nano-channel. Increased NaCl concentration reduces the confinement of the particles.

The trapped gold particles were recorded at the position x = 50 µm, 150 µm, 250 µm, 350 µm and 450 µm in the nano-channel (compare Fig.3). At these positions, a NaCl concentration of 0.15 mM, 0.34 mM, 0.53 mM, 0.72 mM and 0.91 mM was calculated, respectively. In Fig. 4 the histograms of the lateral positions of the particles are plotted for each position in the nano-channel. For this device configurations, the radial histograms have Gaussian distributions. The closer the particles are trapped to the end of the nano-channel and thus the higher the concentration of NaCl, the histogram plots and the corresponding Gaussian distributions are widen. From the fitted distribution width σ_r, the traps can be modeled as a harmonic potential with a radial stiffness k_r [4]:

$$\sigma_r = \sqrt{\frac{k_b T}{k_r}}$$

In Fig. 5, the trap stiffness is plotted against the position and concentration in the nano-channel. As the salt concentration along the nano-channel is increased, the stiffness of the traps is reduced from 0.08 pN/nm at 0.15 mM NaCl solution to 0.006 pN/nm at 0.91 mM NaCl solution.

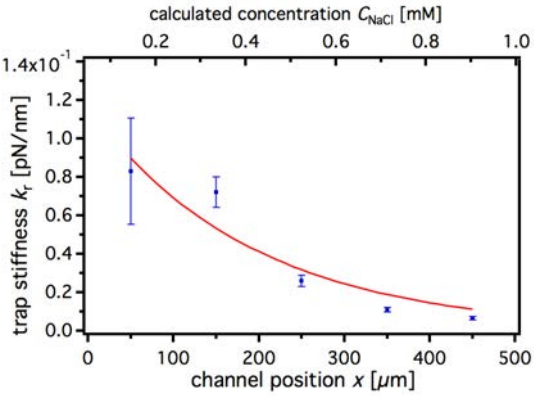

Fig. 5: Trap stiffness of 60 nm gold particles at different positions and concentration in one nano-channel.

GIE trapping devices integrated into a gradient forming microfluidic system can be used to determine critical reaction concentrations of reactants on single trapped nano-objects within a single nano-channel and device. Furthermore, buffer solutions can be easily exchanged during the experiment by flushing through the supporting micro-channel, simplifying our further studies.

References for Project P1202

[1] M. Krishnan, N. Mojarad, P. Kukura and V. Sandoghdar *"Geometry-induced electrostatic trapping of nanometric objects in a fluid"*, Nature **467**, 692 (2010).

[2] M. A. Gerspach, N. Mojarad, Y. Ekinci and T. Pfohl, "*Glass-based geometry-induced electrostatic trapping devices for improved scattering contrast imaging of nano-objects*", Microelectronic Engineering **145**, 43-48 (2015).

[3] M. A. Gerspach, N. Mojarad, Y. Ekinci and T. Pfohl, SNI Annual Report 2014.

[4] Hansen, P.M., et al., "*Expanding the optical trapping range of gold nanoparticles*", Nano Letters, **5**(10), 1937-1942 (2005).

Functionalizing 4,2':6',4''-terpyridines for step-wise assembly into porous on-surface architectures with different binding strength

Project P1203 On surface covalent assembly of coordination polymers with integrated read and write functions
Project Leader: C.E. Housecroft and E.C. Constable
Collaborators: T. Nijs (SNI PhD Student), T.A. Jung, F.J. Malzner, S. Fatayer, A. Wäckerlin, S. Nowakowska, Y.M. Klein, A. Ahsan and S.F. Mousavi

Introduction

For the control of chemical reactions in general, and for catalysis in particular, tunable scaffold architectures such as 'metal organic frameworks' (MOFs) and the 2D 'surface metal organic networks' (SurfMONs) provide a versatile toolkit. The size of the scaffold pockets and the arrangement of functional groups (e.g. metals coordinated inside the ligand frameworks) can be used to control the selectivity of reactions by shape and/or by arrangement of reactive functionalities. Thus, there is an expectation that light harvesting or site/shape selective chemical reactions [1,2] known from complex biomolecular assemblies can be implemented in the simpler 2D surface arrays that we define as SurfMONs.

In this project, we investigate the structure and the assembly mechanisms of surface-supported assemblies of different dimensionalities using 4,2':6',4''-terpyridine derivatives comprising different linker groups which can be activated in stages by exposure to different metal atoms [3]. In the second year, we have commenced the investigation of the pyrimidine functionalized **1** and the methylpyrimidine functionalized **2** (see Fig. 1) [4] on single crystal metallic substrates. In contrast to the chelating 2,2':6',2''-terpyridines, these 4,2':6',4''-terpyridines possess inherent design features to facilitate the formation of extended arrays via coordination through the **N** atoms.

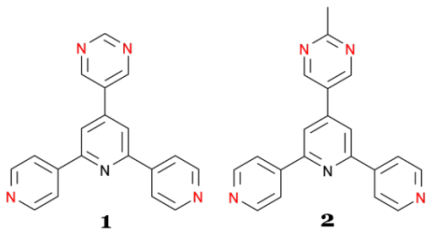

*Figure 1: Pyrimidine **1** and methylpyrimidine **2** functionalized 4,2':6',4''-terpyridines.*

Molecule tuning

As previously reported (SNI annual report 2014), deposition of **1** on Au(111) substrates results exclusively in the formation of extended close-packed assemblies. Due to the geometric similarity of pyrimidine to pyridine, the molecular orientation of **1** on the surface could not be identified (see Figure 2a for the possible orientations). Therefore, we have investigated its close sibling **2**, where the pyrimidine functionalization was modified by adding a methyl group which facilitates 'imaging'. In the observed close-packed assemblies on Au(111), the methyl group is clearly identified by high resolution STM micrographs (Figure 2b). The colinear arrangement of the molecules allows for each molecule to participate in six C–H...N interactions and may be considered as weakly bonded by non-classical H-bonds.

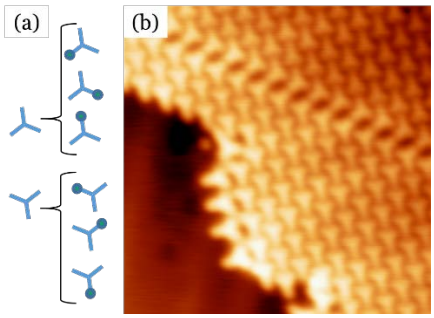

*Figure 2: (a) Schematic visualization of the non-distinguishable molecular orientations in the case of **1** where the functional groups provide insufficient differential contrast for STM imaging. (b) STM micrograph of **2**/Au(111) taken at 5K with clearly distinguishable methyl 'corner' (15x15 nm^2) allowing for the unambiguous identification of the 2D pattern as well as defects contained therein.*

By dosing Cu-adatoms from a thermal evaporation source to the molecule/Au(111) samples, coordination occurs at the **N** atoms (see XPS data in Table 1) resulting in the formation of ladder-like structures.

XPS	-N= [eV]
H-bonded	398.8
Cu-coord.	399.6

*Table 1: N1s XPS data of **1** on Au(111) show also a clear increase of the binding energy upon metal coordination.*

Our observation of ladder-like 1D structures provides evidence that the methyl group does not affect the metal coordination (Figure 3). This agrees

well with our structural model for the ladders of **1** with the pyrimidine functionalization pointing to the outside of the ladder.

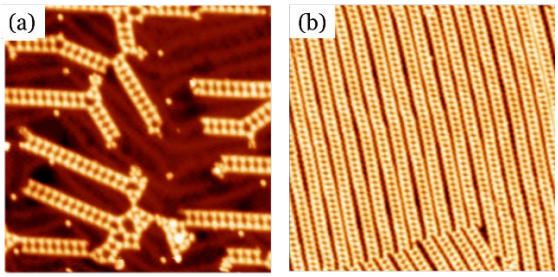

*Figure 3: Similar morphology of the Cu-coordination polymers of (a) **1** and (b) **2** on Au(111) forming 1D ladder-like structures (40x40 and 60x60 nm^2, respectively).*

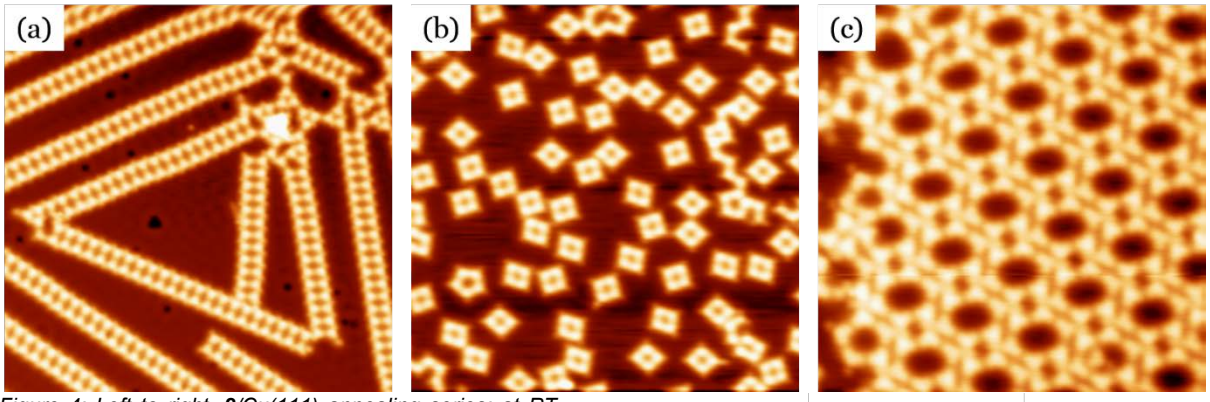

*Figure 4: Left to right, **2**/Cu(111) annealing series: at RT forming ladders, which separate into small, mostly tetragonal clusters during annealing and eventually, at further increased annealing temperatures form hexagonal networks (40x40 nm^2, 40x40 nm^2, 20x20 nm^2 respectively).*

Tuning the Cu coordination polymer

The same ladder structures are also obtained when molecules of **2** are deposited on a Cu(111) substrate (Figure 4a). This suggests that during the sample preparation, sufficient amounts of adatoms can be acquired from the surface held at room temperature. This process depends on the temperature (kT) dependent presence of adatoms, but also on the reaction energetics and kinetics of the molecule with atoms also at other surface sites. The assembly of **2** on Cu(111) can be tuned by controlled annealing. Initially, the ladders disintegrate into discrete squares (Figure 4b), possibly by forming a [4+4] macrocyclic unit involving 4 Cu atoms and 4 molecules of **2**. In a second step however, the assembly reaches a minimum energy arrangement which is identified by the absence of further changes in progressive annealing cycles. The latter arrangement is quite loosely packed compared to the H-bonded structures and combines rectangular and hexagonal shapes in a quasi-hexagonal pattern (Figure 4c). This behavior is consistent with previous findings on the imidazole-functionalized terpyridine molecule, which also forms hexagonal structures if non-hindered [3] (see SNI annual report 2013).

Outlook

Regarding 2D on-surface assemblies, we are able to specifically switch the intermolecular binding motif from hydrogen-bonded to metal-coordinated. This is due to the special designed ligands. Figure 5 shows different ligands which will be synthesized to investigate the influence of the molecular building blocks and the functional groups onto the specific architecture of on surface assemblies and coordination polymers.

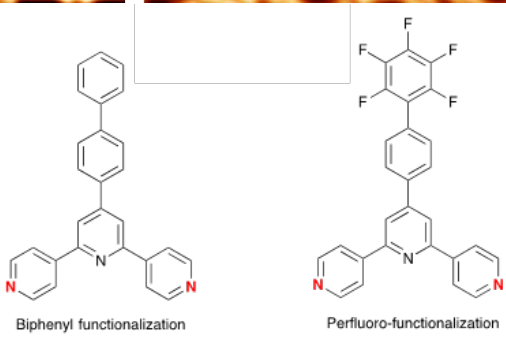

Figure 5: Based on the 4,2':6',4''-terpyridine core, different functionalizations will be investigated in the near future.

Ultimately we aim to understand the design rules for controlling the arrangement of molecular building blocks and their use in the controlled assembly of supramolecular scaffolds with well-defined and functional architectures for applications in e.g. catalysis. In the progress of this work, therefore we shall also investigate the catalytic properties of different SurfMONs

References for Project P1203

[1] A. Shchyrba, *et al.* J. Am. Chem. Soc. **135**, 15270-15273 (2013).
[2] A. Shchyrba, *et al.* J. Am. Chem. Soc. **136**, 9355-9363 (2014).
[3] T. Nijs, et al. Chem. Commun. **51**, 12297-13000 (2015).
[4] Y. M. Klein, *et al.* Polyhedron **81**, 98 (2014).

Long-range magnetic order in a two-dimensional supramolecular chessboard assembly

Project P1204 Site-specific magnetic studies and control of large selfassembled spin systems
Project Leader: T.A. Jung and A. Kleibert
Collaborators: J. Nowakowski (SNI PhD Student), J. Girovsky and M. Baljozovic

Magnetism in low-dimensional systems

Spin-bearing molecules on metallic substrates allow for studying the interplay of magnetic interactions in discrete, well characterized architectures. Such studies are important on fundamental grounds, as magnetism is a cooperative phenomenon which only emerges from the interaction of a certain number of spins in their specific arrangement, but also relate to nanomagnetism i.e. provide insight into the ultimate limits of magnetic data storage and to spintronics. Moreover, it is possible to selectively and reversibly tune the magnetic properties of spin-bearing adsorbates [1, 2]. So far however, due to their paramagnetic character, such molecules were studied mainly on ferromagnetic films [3] or on diamagnetic films at a very low temperature (i.e. several K) in high magnetic field (several T) [4]. Only recently, Scanning Tunneling Microscopy and Spectroscopy (STM/STS) have been used to study the Kondo effect of sub-monolayer amounts of Fe-phthalocyanine (FePc) molecules deposited on a Au(111) substrate [5]. The Kondo effect modifies the interaction of a spin bearing adsorbate or impurity in presence of conduction electrons and has first been observed in gold with magnetic impurities. It can also be investigated using STS, since it evidences itself as a feature at zero bias voltage. A broadening of the Kondo signature below a certain critical temperature has been observed and in absence of direct evidence has been attributed to an antiferromagnetic (AFM) coupling of the nearest-neighbor FePc molecular building blocks [5]. This is a very interesting observation, since classical theory of magnetism (i.e. the Heisenberg model) predicts that there should be no long-range magnetic order in low dimensional systems even at T=0 K [6].

Two-dimensional chessboard structure

The proposed antiferromagnetic coupling of a single component adlayer cannot be investigated by X-ray Magnetic Circular Dichroism (XMCD) and other space-averaging methods because antiferromagnets have no net magnetization. In order to circumvent this limitation we have prepared a molecular monolayer on Au(111) of alternating Fe- and Mn-phthalocyanine molecules by self-assembly. A two component checkerboard pattern can be formed by C-H ... F-C hydrogen bond-like interactions between perfluorinated (all hydrogen atoms replaced by fluorine) and unmodified molecules, as described in Ref. [2] for a passivated ferromagnetic substrate. As shown in the STM micrographs in the Fig. 1., we successfully prepared the chessboard-like structure also on the diamagnetic Au(111) substrate by co-depositing MnPc and FeFPc. The characteristic zig-zag pattern visible in Fig. 1a is due to the so-called herring-bone reconstruction of Au(111). The fact that it withstands in presence of the adlayer suggests that the molecules do not interact strongly with the substrate.

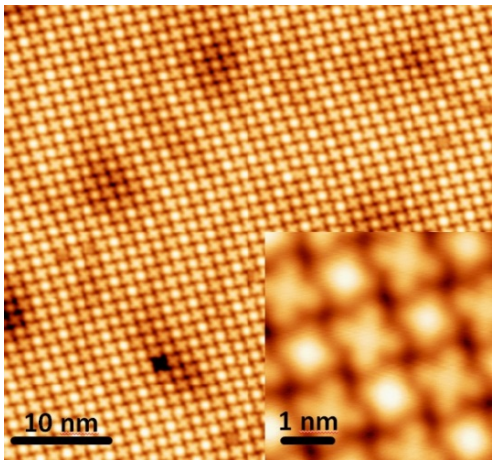

Fig. 1: Large- and small-scale STM micrographs showing the chessboard structure built from alternating MnPc and FeFPc molecules. The brighter molecules are MnPc and the darker ones are FeFPc.

The Kondo resonance visualized by STS

After confirming that we are able to prepare high-quality samples with extended 2D islands of the chessboard-like molecular assembly as shown in Fig. 1, we performed Scanning Tunneling Spectroscopy (STS) measurements above the metal centers of FeFPc and MnPc molecules (Fig. 2 top and bottom, respectively). All the STS spectra taken at different temperatures were acquired on the very same molecule, as the intensity of the resonance feature was changing from molecule to molecule – an effect which we attribute to the complex registry on the large $23x\sqrt{3}$ reconstruction of the Au(111) substrate. Our analysis of the temperature-dependent STS spectra confirmed that the zero-bias feature is due to the Kondo resonance. Also we determined the Kondo temperatures of T_K=12 K for MnPc and T_K=10 K for FeFPc. Those values are in between the values obtained for only MnPc (T_K=36 K, ref. [8]) and for only FePc (T_K=2.6 K, ref. [5]) indicating an interaction between the two molecular sub-lattices.

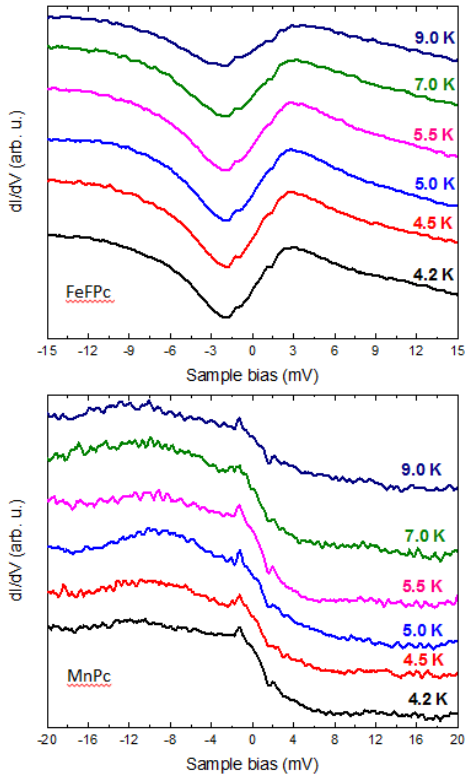

Fig. 2: Scanning Tunneling Spectroscopy data taken above the metal center of the FeFPc (top) and MnPc (bottom) molecule. The Kondo signature is a dip for FeFPc molecule and a step for MnPc, in accordance with the literature.

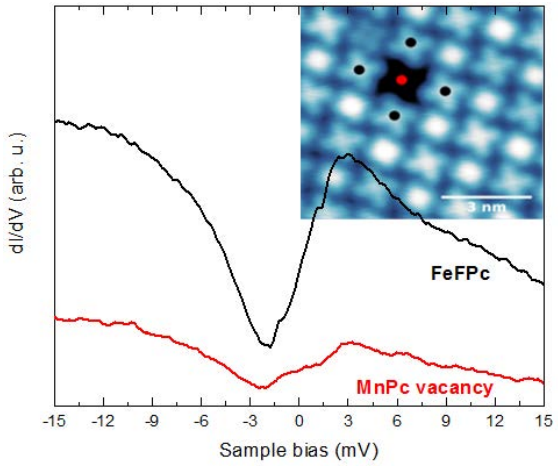

Fig. 3: Comparison of STS spectra taken above the metal center of the FeFPc and in the middle of a MnPc vacancy, as shown in the inset with black and red dots, respectively.

To understand the origin of this interaction, we performed STS measurements on a MnPc vacancy and we compared the results to the other measurments performed on an FeFPc molecule (Fig. 3). The obtained spectra differ in intensity, but the shape of the zero-bias feature is exactly the same for both cases, proving that there is a quantum mirage of the neighboring molecules in the vacancy, similarly to the situation of a magnetic impurity placed in a quantum corral [9]. Such a projection is formed via the electron density waves of the electronic surface state. These waves can also mediate magnetic coupling, i.e. the so-called Ruderman – Kittel – Kasuya - Yosida (RKKY) interaction; this is the interaction that causes this system to become a 2D ferrimagnet at low temperature.

Summary

On the basis of a 2D chessboard-like molecular assembly consisting of two sub-lattices with different metal atoms, the complex interaction of a binary 2D spin array with the Au substrate and in particular with the conduction electrons below has been investigated. STM/STS experiments performed on vacancy defects elucidate the origin of the interaction between the two sub-lattices, i.e. the RKKY coupling. Such prepared and analyzed samples have also been probed using the space-averaging technique of XMCD, where the ferrimagnetic character of the system was further confirmed. Thereby, a 2D spin architecture has been demonstrated as the first 2D ferrimagnet and provided insight into the detailed balance of exchange interactions between the two spin systems mediated by the conduction electrons.

References for Project P1204

[1] C. Wäckerlin, D. Chylarecka, A. Kleibert, K. Müller, C. Iacovita, F. Nolting, T.A. Jung, N. Ballav, Nature Communications, **1** (5), 1–7 (2010).

[2] C. Wäckerlin, J. Nowakowski, S.-X. Liu, M. Jaggi, D. Siewert, J. Girovsky, A. Shchyrba, T. Hählen, A. Kleibert, P.M. Oppeneer, F. Nolting, S. Decurtins, T.A. Jung, N. Ballav, Advanced Materials, **25** (17), 2404–2408 (2013).

[3] A. Scheybal, T. Ramsvik, R. Bertschinger, M. Putero, F. Nolting, T.A. Jung, Chemical Physics Letters, **411** (1-3), 214–220 (2005).

[4] S. Stepanow, P.S. Miedema, A. Mugarza, G. Ceballos, P. Moras, J.C. Cezar, C. Carbone, F.M.F. de Groot, P. Gambardella, Physical Review B, **83** (22), (2011).

[5] N. Tsukahara, S. Shiraki, S. Itou, N. Ohta, N. Takagi, M. Kawai, Physical Review Letters, **106** (18), (2011).

[6] N.D. Mermin, H. Wagner, Physical Review Letters, **17** (22), 1133–1136 (1966).

[7] J. Girovsky, J. Nowakowski, *et al.*, manuscript in preparation.

[8] L. Liu, K. Yang, Y. Jiang, B. Song, W. Xiao, S. Song, S. Du, M. Ouyang, W.A. Hofer, A.H. Castro Neto, H.-J. Gao, Physical Review Letters, **114** (12), (2015).

[9] H.C. Manoharan, C.P. Lutz, D.M. Eigler, Nature, **403** (6769), 512–515, (2000).

Peering into the nuclear pore complex using a high-speed atomic force microscope

Project P1205 Watching the nanomachinery of the nuclear pore complex at work by high speed-AFM
Project Leader: R. Lim and C. Gerber
Collaborators: Y. Sakiyama (SNI PhD Student)

Watching nuclear pore complexes at work

Nuclear pore complexes (NPCs) form the sole passageways between the nucleus and cytoplasm in eukaryotic cells (1). The functional role of each ~100 nm-diameter NPC is to ensure that only specific molecules (i.e., cargo) gain access to the nucleus. To do so, the NPC *a priori* inhibits macromolecules above 40 kDa from traversing its channel. Exclusive access is given to specific cargoes that are accompanied by nuclear transport receptor proteins (i.e., karyopherins or Kaps) that interact with the NPC nanomachinery. These consist of ~200 intrinsically disordered proteins known as phenylalanine-glycine (FG)-repeat nucleoporins or FG Nups) that generate a permeability barrier within the NPC (2).

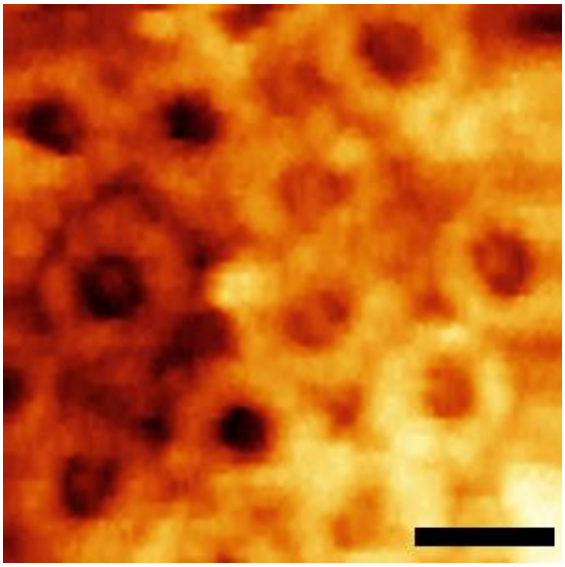

Fig. 1: Watching native NPCs by HS-AFM. Image was obtained at 550 ms per frame. Scale bar = 100 nm.

Still, after more than two decades of research, our understanding of the NPC barrier mechanism continues to be dominated by *in vitro*-derived models that remain disputed (3). For the most part, this problem stems from the fact that the FG Nups - being intrinsically disordered - have defied direct visualization within NPCs even though the overall NPC structure itself has been resolved to 20 Å by cryo-electron tomography (cryo-ET) (4). Therefore, FG Nup behaviour in the NPC remains a "holy grail" in the field. To further complicate matters, NPC transport *in vivo* proceeds in a matter of milliseconds (5). Therefore, the NPC barrier mechanism is governed by the *dynamic* spatiotemporal behaviour of the FG Nups rather than their *static* properties (i.e., time-independent).

Spatiotemporal dynamics of FG Nups

This motivates our current work where we have uncovered the collective spatiotemporal behavior of FG Nups in native NPCs at unprecedented resolution in space and time (Fig. 1). Using high-speed atomic force microscopy (HS-AFM) (6-7), we have obtained the first experimental molecular dynamics movies ever recorded inside the NPC (8). By peering into the pore, we have gained unprecedented access to the NPC barrier, and show that this consists of rapidly fluctuating FG Nups that elongate and retract in a stochastic manner (Fig. 2).

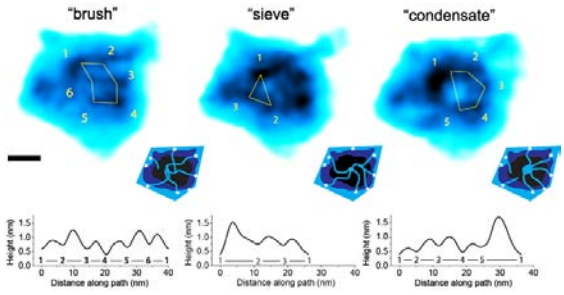

Fig. 2: Metastable "barrier states" in the NPC. Three main features are FG Nup "brushes", "sieves" and "condensates" which recall static NPC barrier models but are in fact short-lived. The accompanying illustrations and legend emphasize the key features in each frame corresponding to the FG Nups including eight tethering points that remain unchanged from frame-to-frame. The time elapsed between frames is 180 ms. The height profiles correspond to the cross-sectional features encountered along the path demarcated by a polygon (yellow). Each number corresponds to the corner of a polygon. Scale bar = 10 nm.

Moreover, the FG Nups that coincide and meet in the central channel can momentarily interlink and detach thereby forming a short-lived sieve-like state. Outstretched FG Nups oftentimes even coalesce with their free ends at the pore center to produce a striking radial arrangement of polypeptide chains that radiate inwardly from their tether points, even appearing to straighten under tension.

In doing so, our findings bring clarity and consensus to NPC models that mainly disagree on static interpretations of how the FG Nups are spatially arranged in the pore. In fact, it is this dynamic behavior that underpins the metastable formation of "meshwork-like" and "transporter-like" barrier states (3), and explains why static measurements cannot appropriately describe the FG Nup barrier (9) (Fig. 3).

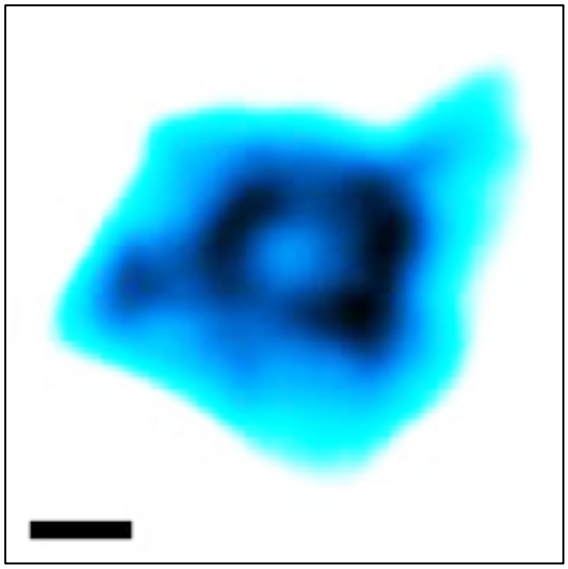

Fig. 3: Average projection of ten successive frames obtained at 180 ms apart simulates the time-independent outcome of an ensemble-averaged measurement (i.e., 1800 ms). Effectively all dynamic FG Nup structure is lost and replaced by a central condensate-like structure. Scale bar = 10 nm.

Summary

The Lim Laboratory has pioneered the use of biomimetic nanostructures and nanotechnological methods to resolve the nanobiophysics of NPCs (10-14). Importantly, we now have the possibility to validate our hypotheses by studying living NPCs via HS-AFM. Indeed, the rapid scanning rates coupled to the ability to work at a low pN force regime minimizes any transfer momentum (i.e., impulse) to the sample. Our next goal will be to watch FG Nup dynamics during the transport of individual NTR-cargoes within single NPCs. Moreover, we are buildling up our collaborations to exploit the HS-AFM to study other biological nanomachines.

References for Project P1205

[1] M. Beck, F. Forster, M. Ecke, J.M. Plitzko, F. Melchior, G. Gerisch, W. Baumeister and O. Medalia. *Nuclear pore complex structure and dynamics revealed by cryoelectron tomography*. Science **306**, 1387 (2004).

[2] D. Grunwald, R.H. Singer and M. Rout, *Nuclear export dynamics of RNA-protein complexes*. Nature **475**, 333 (2011).

[3] M. Fuxreiter, Á. Tóth-Petróczy, D.A. Kraut, A. Matouschek, R.Y.H Lim, B. Xue, L. Kurgan L, V.N. Uversky. *Disordered proteinaceous machines*. Chem Rev. **114** 6806 (2014).

[4] Eibauer, M., Pellanda, M., Turgay, Y., Dubrovsky, A., Wild, A. & Medalia, O. *Structure and gating of the nuclear pore complex*. Nat. Comm. **6,** 7532 (2015).

[5] Dange, T., Grunwald, D., Grunwald, A., Peters, R. & Kubitscheck, U. *Autonomy and robustness of translocation through the nuclear pore complex: A single-molecule study*. J. Cell Biol. **183**, 77-86 (2008).

[6] N. Kodera, D. Yamamoto, R. Ishiikawa and T. Ando. *Video imaging of walking myosin V by high-speed atomic force microscopy*. Nature **468**, 72 (2010).

[7] T. Uchihashi, R. Iino, T. Ando and H. Noji. *High-Speed Atomic Force Microscopy Reveals Rotary Catalysis of Rotorless F-1-ATPase*. Science **333**, 755 (2011).

[8] Y. Sakiyama, A. Mazur and R.Y.H. Lim, *FG Nucleoporin Barrier Dynamics Resolved By High-Speed Atomic Force Microscopy Inside Native Nuclear Pore Complexes*, submitted.

[9] C.W. Akey, *Visualization of Transport-Related Configurations of the Nuclear-Pore Transporter*. Biophys. J. **58**, 341 (1990).

[10] R.L. Schoch, L.E. Kapinos, and R.Y.H. Lim, *Nuclear transport receptor binding avidity triggers a self-healing collapse transition in FG-nucleoporin molecular brushes*, Proc. Natl. Acad. Sci. USA **109**, 16911 (2012).

[11] R.L. Schoch and R.Y.H. Lim, *Non-interacting molecules as innate structural probes in surface plasmon resonance*, Langmuir **29**, 4068 (2013).

[12] L.E. Kapinos, R.L. Schoch, R.S. Wagner, K.D. Schleicher and R.Y.H. Lim. *Karyopherin-centric control of nuclear pores based on molecular occupancy and kinetic analysis of multivalent binding with FG-Nucleoporins*. Biophys. J. **106**, 1751 (2014).

[13] R.S. Wagner, L.E. Kapinos, N.J. Marshall, M. Stewart and R.Y.H. Lim, *Promiscuous binding of Karyopherinβ1 modulates FG Nucleoporin barrier function and expedites NTF2 transport kinetics*, Biophys. J. **108**, 918 (2015).

[14] K.D. Schleicher, S.L. Dettmer, L.E. Kapinos, S. Pagliara, U.F. Keyser, S. Jeney and R.Y.H. Lim. *Selective transport control on molecular velcro made from intrinsically disordered proteins*. Nature Nanotechnol. **9**, 525 (2014).

A nanomechanial oscillator for coherent mechanical driving of a single electron spin

Project P1206 Nanomechanical oscillators for diamond spinoptomechanics
Project Leader: P. Maletinsky and R. Warburton
Collaborators: A. Barfuss (SNI PhD Student), J. Teissier, E. Neu and P. Appel

Introduction and motivation

An individual electronic spin coupled to a nanomechanical oscillator constitutes a prototypical "hybrid quantum system". Such systems form highly valuable quantum resources for fundamental investigations of quantum mechanics and for potential high-performance nanoscale sensors. Specifically, these systems are highly attractive candidates for studying the crossover from quantum to classical physics and they have the potential to yield novel types of high-performance sensing devices for diverse quantities such as mass, acceleration or pressure. Furthermore, such hybrid systems could be exploited for efficient, coherent manipulation of a quantum system by purely mechanical means – an approach which could be highly advantageous over established methods due to its compactness and potential efficiency.

In this project, we have established and now exploit a particular, novel hybrid spin-mechanical system consisting of a single, electronic "Nitrogen-Vacancy" (NV) spin, embedded in a diamond mechanical oscillator (Fig. 1a). The individual sub-systems in our devices - the spin and the oscillator - are highly attractive for the experiments we envisage: Diamond nanomechanical resonators, have been shown to exhibit very high quality-factors up to $Q \sim 10^6$ [1], and therefore form a well-isolated , high-quality nanomechanical system. NV center electronic spins are advantageous for multiple reasons. They form a spin-1, three level system, which is highly cquantum coherent, even at room temperature, with quantum coherence times approaching one second. The NV spin can be conveniently read out and initialized using optical means and coherently manipulated using microwave magnetic fields. Our NV-based hybrid spin-mechanical system is therefore ideally suited to study the subtle effects a single spin could have on the mechanical oscillator and vice versa.

In the starting phase of this project, we have successfully fabricated diamond nanomechanical resonators using dedicated nanofabrication technologies developed in our labs in Basel [2][3]. Using these structures, we explored the strain-induced spin-oscillator coupling and achieved a first quantitative measurement of the corresponding spin-strain coupling constants, which were previously unknown [1]. An important conclusion of these initial studies was that our system allows us to reach the "strong coupling regime", where the coupling of spin and oscillator exceeds the dephasing rates of the individual sub-systems.

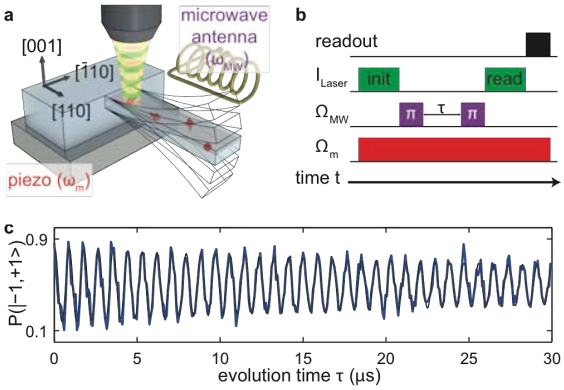

Fig. 1: Strain-induced coherent driving of a single spin. (a) Experimental setting. Indivdual "Nitrogen-Vacancy" (NV) electronic spins (red) are coupled to a cantilever which is resonantly driven at frequency $\omega_m/2\pi$ by a piezo-element. (b) The NV spin is read out and initialised in a pulsed way by green laser light and manipulated by microwave magnetic fields generated by a nearby antenna. (c) Strain-driven coherent Rabi oscillations. Data (blue) and a fit (black) to damped Rabi oscillations.

Key experimental results

The focus of our activities this year lay on exploring the coherent quantum dynamics that our nanomechanical diamond oscillators impose on the embedded electronic NV spin [4]. To that end, we employed time-varying ("AC") mechanical strain generated in the cantilever upon resonant piezo actuation. Under apropriate conditions, this strain can act analougously to an effective, transverse magnetic field on the NV spin. If the spin-splitting between two NV spin states is tuned in resonance with this time-varying field, such AC strain can therefore drive coherent spin rotations. Using an apropriate sequence of optical and microwave pulses (Fig. 1b), we were able to demonstrate such coherent mechanical spin manipulation by observing coherent Rabi oscillations (Fig. 1c). The slow decay time (>30 μs) we observed for these oscillations thereby compared very favourably to alternative methods for coherent manipulation (such as microwave driving) and is further evidence for the high potential of our quantum nano-device for quantum-sensing and computing.

Next to coherent manipulation, our nano-mechanical, coherent drive can also be employed to protect the NV's spin coherence, i.e. prolong its inhomogeneous dephasing time, T_2^*. This coherence protection by continuous driving [5] here is a result of the particular NV spin structure, together with the unique possibility of driving the NV spin through AC strain. We demonstrated this coherence protection by comparing the decay of Ramsey

interference fringes with and without mnechanical driving (Fig. 2a and b, repsectively), which showed a 4.5-fold enhancement of NV spin coherence under mechanical driving. We were able to show that the enhancement initially scales linearly with mechanical driving strength (i.e. cantilever amplitude), as expected, but then saturates to the value shown in Fig. 2. We assigned this unexpected saturation to unwanted noise in the mechanical driving field, which was caused by the driving electronics and the still moderate mechanical Q-factors of our oscillators. Future improvements in quality factors and drive sources should overcome this limitation and lead to significant further improments of NV coherence times.

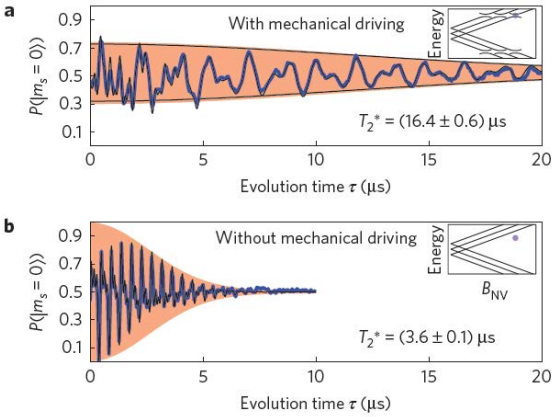

Fig. 2: Protection of NV spin coherence by coherent, mechanical driving. (a) Decay of NV Spin coherence over time, in the presence of a mechanical driving field for coherence protection. (b) Same as in a, but in the absence of mechanical driving. In both a and b, spin coherence was measured as the remaining popolation in one of the NV spin states (here, $|m_s=0\rangle$) after a „Ramsey interference" sequence. The data shows a 4.5-fold enhancement of spin coherence owing to the coherent mechanical drive.

Outlook

The strain-based coherent mechanical driving of NV spins we demonstrated lays the groundwork for several future experiments we will pursue in the next year. On one hand, the combination of our strain drive with coherent microwave spin manipulation, allows us to realize an inverted three-level „Δ-system" with our strain-driven NV spin. In this Δ-system, all three possible spin transitions can be coherently addressed. This setting is known to lead to unconventional spin dynamics, which we plan to investigate for the firts time with our single, highly coherent spin. The resulting spin dynamics will depend sensitively on the phases of the driving fields and can thus be exploited for quantum sensing of e.g. the phase-noise of the nanomechanical oscillator – a quantity which is otherwise hard to assess. In a second line of experiments, we will promote our nanomechanical oscillators to vacuum and cryogenic temperatures, where the quality factors of our diamond nanomechanical resonators will be significantly enhanced. Furthermore, at low temperatures, we will be able to exploit the coherent optical transitions [6] of NV centers for hybrid coupling. Ultimately, this setting should allow us to observe the back-action of embedded spins onto our nanomechanical system and to employ this coupling for cooling [7] of the mechanical oscillator's Eigenmode or to generate spin-squeesing of an NV ensemble embedded in the oscillator [8]. We will additionally further refine nanofabrication of our diamond cantilevers and address both, crystalline orientations [9] and intrinsic dissipation in these devices.

References for Project P1206

[1] P. Ovartchaiyapong, L.M.A. Pascal, B.A. Myers, P. Lauria, and A.C. Bleszynski Jayich, *"High quality factor single-crystal diamond mechanical resonators"*, Appl. Phys. Lett. **101,** 163505 (2012).

[2] J. Teissier, A. Barfuss, P. Appel, E. Neu, and P. Maletinsky. *"Strain Coupling of a Nitrogen-Vacancy Center Spin to a Diamond Mechanical Oscillator"*, Phys. Rev. Lett. **113**, 020503 (2014).

[3] P. Maletinsky, S. Hong, M. S. Grinolds, B. Hausmann, M. D. Lukin, R. L. Walsworth, M. Loncar, A. Yacoby, *"A robust, scanning quantum system for nanoscale sensing and imaging"*, Nature Nano. **7**, 320 (2012).

[4] A. Barfuss, J. Teissier, E. Neu, A. Nunnenkamp, and P. Maletinsky. *„Strong mechanical driving of a single electron spin"*, Nature Physics **11**, 820 (2015).

[5] J.M. Cai, B. Naydenov, R. Pfeiffer, L. McGuinness, K. Jahnke, F. Jelezko, M. Plenio, A. Retzker. *"Robust dynamical decoupling with concatenated continuous driving"* New J. Phys. 11, 113023 (2012).

[6] Y. Chu, N. P. de Leon, B. J. Shields, B. Hausmann, R. Evans, E. Togan, M. J. Burek, M. Markham, A. Stacey, A. S. Zibrov, A. Yacoby, D. J. Twitchen, M. Loncar, H. Park, P. Maletinsky, and M. D. Lukin. *"Coherent Optical Transitions in Implanted Nitrogen Vacancy Centers"*, Nano letters **14,** 1982 (2014).

[7] I. Wilson-Rae, P. Zoller, and A. Imamoglu, *"Laser Cooling of a Nanomechanical Resonator Mode to its Quantum Ground State"*, PRL **92**, 075507 (2004).

[8] S. D. Bennett, N.Y. Yao, J. Otterbach, P. Zoller P. Rabl, and M. D. Lukin, *"Phonon-Induced Spin-Spin Interactions in Diamond Nanostructures: Application to Spin Squeezing"*, PRL **101**, 156402 (2012).

[9] E. Neu, P. Appel, M. Ganzhorn, J. Miguel-Sánchez, M. Lesik, V. Mille, V. Jacques, A. Tallaire, J. Achard, and P. Maletinsky. *"Photonic nano-structures on (111)-oriented diamond"*, Appl. Phys. Lett. **104**, 153108, (2014).

Using proteorhodopsin to drive a molecular hoover

Project P1207 Design of a polymer membrane-based molecular “hoover”
Project Leader: W. Meier and D.J. Müller
Collaborators: R. Goers (SNI PhD Student), J. Thoma, N. Ritzmann

Introduction

The creation of nanocells which resemble a light-driven molecular hoover requires the functional assembly of synthetic membranes and certain membrane proteins, which provide the functionality. The reconstitution process of membrane proteins is still a challenge and requires separate optimization for every membrane protein.[1, 2] Furthermore, after the reconstitution of the membrane protein, it is necessary to evaluate its functionality and to characterize the structure it is localized in (***Fig. 1, a, b***). However, in order to localize the proteins, they must be labeled for detection. Even though the presence of markers like cysteins or His-tags should allow specific targeting of the membrane protein, unspecific interaction with the membrane is very likely.

Materials & Methods

In order to bypass the need for additional labeling, a fusion protein (PR-GFP) of the transmembrane proton pump proteorhodopsin (PR) and the water soluble green fluorescent protein (GFP) was created, connected via PR’s C-terminus (***Fig. 1, c***). Furthermore, the hydrophilic nature of GFP should influence the orientation of PR during reconstitution. The inner hydrophobic domain of the membrane should prevent GFP from passing through and thus, PR’s C-terminus should always be facing outwards of the vesicle. This should lead to proton transport into the interior of the vesicle.

The statistical modeling technique design of experiments (DoE) has gained considerable attention in industry and academic science, especially in engineering topics like process optimization.[3] It allows an efficient screening of relevant factors and their interactions and is thus an ideal candidate for the optimization of membrane protein reconstitutions (***Fig. 1, d***).[3] A definitive screening design was employed to analyze the influence of the detergent n-octyl-β-D-glucoside (OG), the pH value and to find proper ratios of PR to the lipid 1,2-Dioleoyl-sn-glycero-3-phosphocholine (DOPC) or to the $PMOXA_{17}$-$PDMS_{65}$-$PMOXA_{17}$ (ABA) block copolymer, which were also used as parameters. The resulting structures were characterized via dynamic light scattering (DLS), transmission electron microscopy (TEM) and fluorescence correlation spectroscopy (FCS) and hence the PdI, the number average obtained by DLS and the size determined by FCS defined as responses. The results from FCS were of particular interest because only structures containing PR-GFP

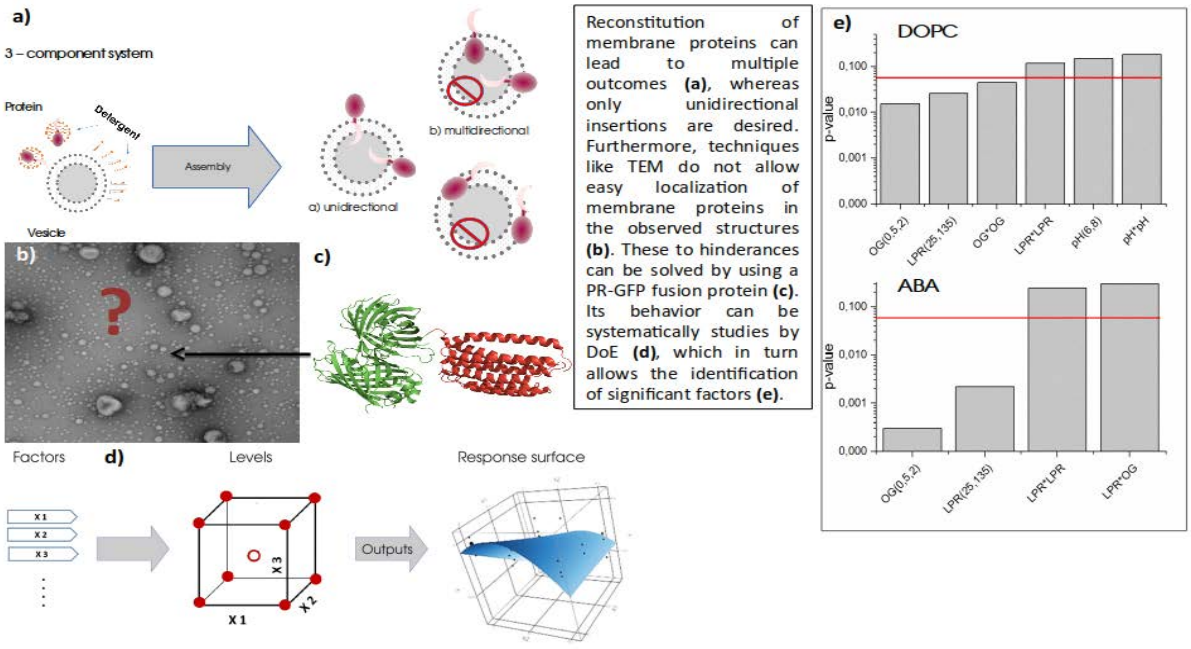

*Fig. 1: Graphical overview of the issues of membrane reconstitution (**a, b**) and the possible approach to solve them (**c, d**). The protein’s behavior during reconstitution and the characterization of the resulting structures can be efficiently studied by applying design of experiments in order to detect significant parameters (**e**). The red line indicates the p-value = 0.05 threshold.*

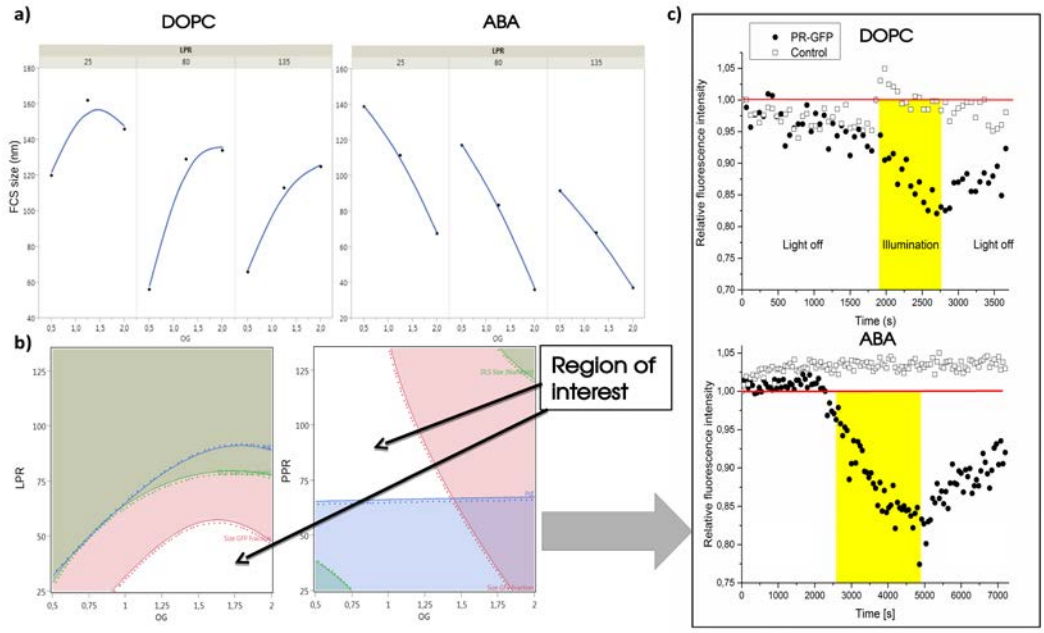

*Fig. 2: (**a**) The sizes data obtained from FCS show very different behavior of PR-GFP insertion. Formation of proteoliposomes appears to require a minimum amount of OG to obtain sizes in the range of 100 nm, whereas proteopolymersomes require low amounts to assemble in a similar size range. Using minimum requirements in terms of size and PdI, a region of interest can be identified (**b**). This parameter space was sampled and obtained proteovesicles revealed proton pumping activity (**c**). The performance in ABA polymersomes is comparable to reports found in liposomes literature.[4]*

Figure2P12 are detectable. The results were used to construct a response surface (RS) which was then used to analyze the influence of these parameters and predict possible optimal conditions. Samples were further analyzed for proton pumping activity by encapsulating the pH sensitive fluorescent dye pyranine and recording its intensity over time during illumination at 525 nm.

Results & Discussion

Analyzing the significant parameters for the reconstitution revealed that they differ between the two membrane types (***Fig. 1, e***). In case of DOPC, the OG concentration and the LPR are below the significance threshold, whereas the pH has no significant effect. Similar results are obtained for the polymer membranes, both the OG concentration and the PPR are strongly significant. In comparison, the behavior of the DOPC and the ABA membranes appear to be opposite. In case of DOPC a certain amount of OG needs to be used to obtain structures which are larger than micelles (> 30 nm) (***Fig 2, a***) which is in good agreement with literature.[3, 4] In contrast, high amounts of detergent have a negative effect on the formation of polymersomes, leading to structures smaller than 50 nm. From these results a response contour was constructed and further analyzed for regions of interest. The minimum requirements were subsequently defined as follows: PdI of the vesicles < 0.2, observable size in DLS and FCS larger than 80 nm both cases (***Fig 2, b)***. Again, the region of interest is different for liposomes and polymersomes. The structures within this parameter range were predicted to meet the requirements and expected to be responsive to illumination. Experimental sampling of this region revealed that indeed the predictions were accurate and proton translocation could be observed (***Fig. 2, c***). The proton pumping process takes approximately twice as long in case of the polymer membranes to build up a similar pH gradient.

Conclusion

In conclusion, this work demonstrates that *i.* DoE is a powerful tool to gain control over the assembly process and offers valueable insight, *ii.* a PR-GFP fusion protein allows simple localization in membrane structures and furthermore *iii.* the predicitons made by the model are acurate and the resulting proteoliposomes and –polymersomes were active in terms of proton transport.

References for Project P1207

[1] C. G. Palivan, R. Goers, A. Najer, X. Zhang, A. Car and W. Meier, Chemical Society Reviews, (2016), DOI: 10.1039/C5CS00569H.

[2] J.-L. Rigaud and D. Lévy, in Methods in Enzymology, Academic Press, **372**, 65-86 (2003).

[3] S. A. Weissman and N. G. Anderson, Organic Process Research & Development, **19**, 1605-1633 (2015).

[4] R. Tunuguntla, M. Bangar, K. Kim, P. Stroeve, Caroline M. Ajo-Franklin and A. Noy, Biophysical Journal, **105**, 1388-1396 (2013).

Decoupling of graphene on Cu(111)

Project P1208 Ultra-sensitive force detection and molecular manipulation
Project Leader: E. Meyer and M. Poggio
Collaborators: M. Schulzendorf (SNI PhD Student), S. Kawai, Th. Glatzel, A. Hinaut, R. Pawlak, U. Gysin, Y. Pellmont, J. Zhang and M. Muntwiler

LT beam deflection AFM close to operation

The new low temperature atomic force microscope (LT-AFM) is close to operation. Pressures close to ultra-high vacuum (UHV) have been achieved. Cooling with nitrogen and helium has been tested. Temperatures close to 4.8 K have been achieved and were maintained for 83 hours. Problems with the transfer shutters of the cryostats, that led to a temperature increase of about 50 K, have been fixed.

Recently a new cleaver, designed and built in-house, has been mounted. It will allow for the in-situ cleavage of inorganic crystals like rock salt (NaCl) or potassium bromide (KBr). Last instruments like a Quartz Micro Balance (QMB) and a refined wobble stick for sample transfer to the microscope head have been mounted.

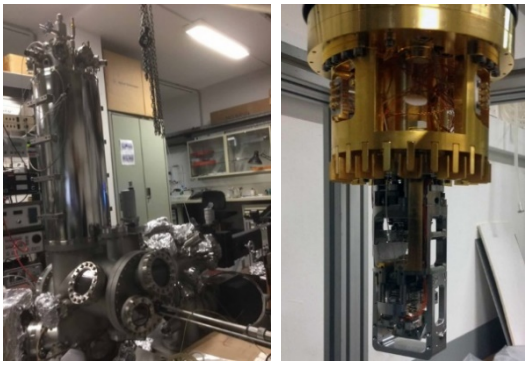

Fig. 1: Overview of the complete set up system (left) and a detailed image of the microscope head (right). At the top wiring and damping system (gold coloured) can be seen. The head itself sitting at the bottom (steel coloured).

First operation and testing is expected for the beginning of the next year.

Graphene and KBr on Cu(111)

Last year we reported on the change of graphene's work function on Cu(111) by the deposition of potassium bromide (KBr), measured by Kelvin Probe Force Microscopy (KPFM). In fig. 2 an overview of the outcome is shown. Graphene was found to be surrounded by KBr. By lack of sub-surface resolution, we were not able to distinguish if the observed change was an effect by intercalation or from interactions at the graphene edges. Our samples have been prepared in-situ and measurements were carried out with a home-built AFM in UHV at room temperature. [1]

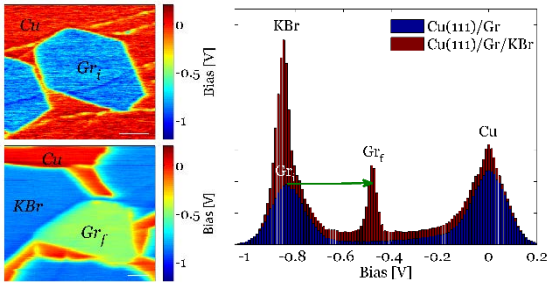

Fig. 2: CPD maps of graphene on Cu(111) (upper left) and after evaporation of KBr (lower left). In the histogram of the CPD maps (right side) the shift in graphene's work function on KBr deposition became clearly visible (indicated by green arrow in the histogram). Data normalized in respect to copper.

Sample preparation and STM at PEARL

Following to the experiments in our lab we began to prepare the samples at the Photo Emission and Atomic Resolution Laboratory (PEARL) beamline within the Swiss Light Source (SLS) to complement our result with scanning tunnelling microscopy (STM) and subsurface sensitive X-Ray Photoelectron Spectroscopy (XPS) measurements.

By STM we were able to judge that the samples were comparable to those prepared in our lab. The round flake shape may came from higher growth temperatures compared to the preparation in our lab. When KBr has been evaporated the standing wave pattern visible on graphene became different, shown in fig. 3. Note that again the KBr was found around the flakes, visible as fringes in the right image of Fig. 3. In addition, free KBr films were still present, visible at the lower left of the image.

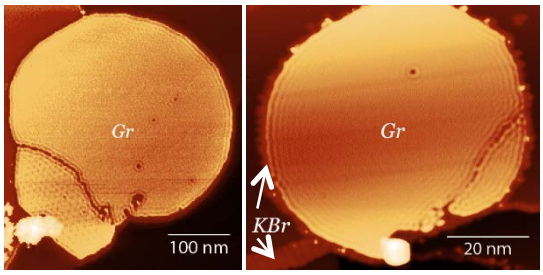

Fig. 3: STM topography of graphene on Cu(111) (left side) and after deposition of KBr (right side). KBr was again found at the edges of graphene. On graphene a standing wave pattern of interface states became visible that was different in presence of KBr (I: 1 pA, U: -200 mV (left) and I: 2 pA, U: - 200 mV (right).

First insights by XPS at PEARL

For graphene flakes on Cu(111), shown in the upper part of Fig. 4, we found a main peak at binding energies of 284.41 eV. As expected by the interaction with the substrate the peak had a lower binding energy than those of graphite with 284.5 eV.[2] In addition, a second peak at lower binding energies could be attributed to a binding of graphene's carbon atoms at the edge to the copper substrate. The contribution was found to be 7.9 %, in agreement with calculations.

After the evaporation of KBr, shown in Fig. 4 lower, adventitious carbon has been added to the sample increasing the C 1s peak area by 10%. The peak for graphene was shifted by 100 meV to a binding energy of 284.51 eV, then comparable to those of graphite. The second peak was shifted by 150 meV to lower binding energies and a decreased contribution of 4.6 %.

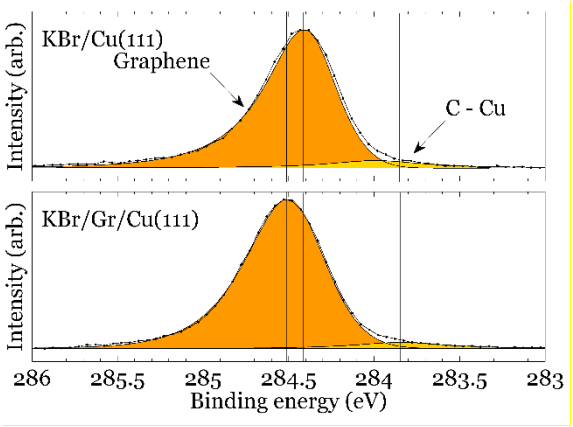

Fig. 4: XPS of C 1s core-level. For Gr/Cu(111) (upper image) the peak of graphene was found at 284.4 eV. A second peak for the interaction of the graphene's edge atoms with the substrate was found at 284 eV. After the deposition of KBr (lower image) the main graphene peak was shifted, matching those of free graphene. The second peak was found at lower binding energies with reduced contribution.

Compared to KBr thin-films on Cu(111) (Fig. 5 upper image) a second species for potassium was found in presence of the graphene islands (Fig. 5 lower image). From the STM images we conclude that one species (A) could be related to free KBr films on the surface. The second species (B) then could be related to the presence of graphene.

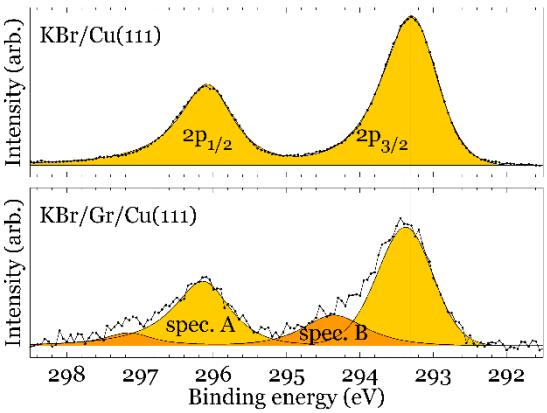

Fig. 5: XPS of K 2p peak for sub-monolayer islands of KBr on Cu(111) (upper) and on Gr/Cu(111) (lower). In presence of graphene islands a second species B at higher binding energies has been found. Species B was attributed to an interaction with the graphene islands.

Summary and outlook

Our STM and XPS measurements at the SLS revealed a clear change in Gr/Cu(111) on KBr evaporation supporting our prior observations made by KPFM. In addition, we observed not only a change in the core level of graphene but also for KBr. Further analysis of angle dependent XPS data should give an insight on the stacking order of sub-monolayer graphene islands and KBr thin-films on Cu(111).

References for Project P1208

[1] L. Howald, *et al.* "*Multifunctional probe microscope for facile operation in ultrahigh vacuum.*" Appl. Phys. Lett. **63**, 117 (1993).

[2] Siokou, a. et al. "*Surface refinement and electronic properties of graphene layers grown on copper substrate: An XPS, UPS and EELS study.*" Appl. Surf. Sci. **257**, 9785–9790 (2011).

Design of polymer nanoreactors with triggered activity

Project P1209 Design of polymer nanoreactors with triggered activity
Project Leader: C.G. Palivan, J. Huwyler
Collaborators: T. Einfalt (SNI PhD Student)

Introduction

The development of advanced stimuli-responsive systems for medicine, catalysis or technology requires compartmentalized reaction spaces with triggered functionality. Normally, synthetic stimuli-responsive compartments are obtained by using copolymers with responsive properties, which favor a change of the compartments upon the presence of the stimulus. Very recently few stimuli-responsive systems preserving the compartment architecture have been reported, but none allows a triggered reaction *in situ* [1]. En elegant nanoscience-based strategy is to engineer such compartments with triggered activity by encapsulation/insertion of active compounds in compartments with stimuli-responsive permeability.

Here, we introduce nanoreactors with pH-triggered activity based on polymersomes with encapsulated enzymes and a membrane equipped with modified channel proteins, acting as "gates" (Fig. 1). By insertion of a chemically modified porin with a pH-sensitive molecular cap we obtained a selective permeability of the membrane. The substrate penetrate inside the cavity and the enzymatic reaction takes place only when the gate is open (by releasing its pH-sensitive cap) [2]. Then the products are released from the nanoreactor.

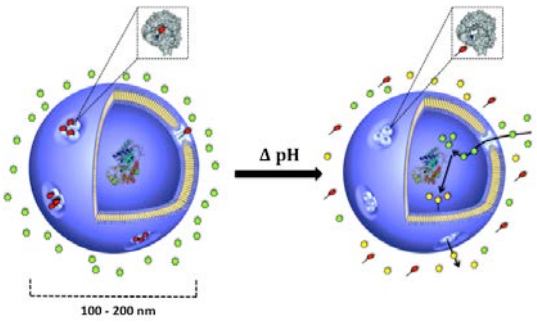

Fig. 1. Concept of a nanoreactor with triggered activity by a chemically engineered protein "gate" inserted in a polymersome membrane. A change in pH induces the release of the sensitive molecular cap (green dots) from the protein "gate" allowing the entrance of substrates (red dots), and the release of the products of the enzymatic reaction (yellow dots).

Polymersomes were prepared by self-assembly of a triblock copolymer poly(2-methyloxazoline)-*block*-poly(dimethylsiloxane)-*block*-poly(2-methyloxazoline) in dilute aqueous solution [3]. Polymersomes were prepared both empty and in the presence of the enzyme horseradish peroxidase (HRP), and chemically modified channel porin, OmpF-CA-Cy_5. OmpF-CA-Cy_5 served to render the membrane permeable when a change of pH in the environment of polymersomes takes place, while HRP serves as an active compound to generate *in situ* a desired pH-sensitive reaction.

OmpF Modification. First, lysine residues were coupled with levulinic acid by a simple sulfo-NHS/EDC reaction (**Scheme 1**), and unreacted levulinic acid was removed by filtration and dialysis. This step introduced reactive carbonyl groups to favor the binding of a pH responsive cap Cyanine5-hydrazide (Cy5-Hydrazide). Cy5-hydrazide was selected as the second part of the pH responsive linker, because its molecular weight matches with the pore size at the constriction region (Figure 2).

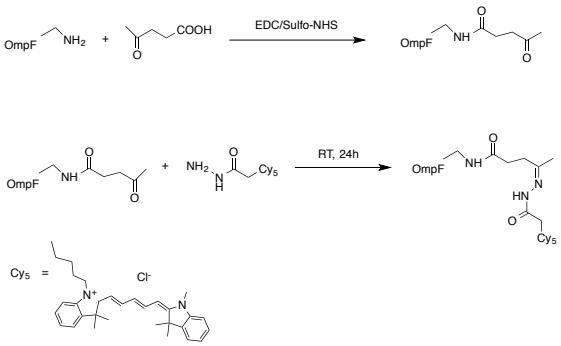

Scheme 1. Chemical modification of Wild Type OmpF with a pH sensitive molecular cap (by coupling levulinic acid and Cy5-Hdrazide)

Design of the nanoreactors. pH-responsive nanoreactors were prepared from $PMOXA_6$-$PDMS_{44}$-$PMOXA_6$ copolymer, and a subset of modified or native OmpFs (OmpF-WT-Cy5, OmpF-WT, OmpF-CA-Cy5, OmpF-CA) and horseradish peroxidase in PBS buffer pH=7.4. We used the film rehydration technique as being suited for enzymes and channel porins (films were rehydrated to a final polymer concentration of 5 mg/ml). All samples were extruded through a 100 nm diameter pore-size polycarbonate membrane in order to obtain size homogeneity. Non-encapsulated enzyme was removed from the nanoreactors by dialysis against PBS.

Characterization of the nanoreactors. A combination of transmission electron microscopy (TEM) and Static and Dynamic Light scattering (SLS, DLS) measurements was applied to determine: (i) the architecture of the 3D assemblies, (ii) the influence of enzyme and porin encapsulation and insertion, and (iii) the stability of the nanoreactors. To ensure that the vesicular structure was stable even at acidic pH, the 3D assemblies were characterized after 7 days in an acidic pH. Both empty vesicles and nanoreactors

preserved their architecture and did not aggregate at low pH. The average hydrodynamic radius of nanoreactors was around **70** nm (Fig 2).

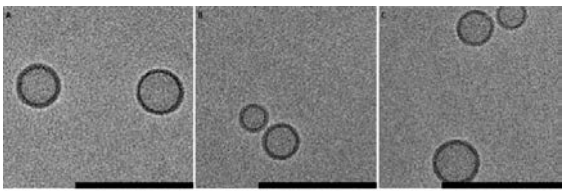

Fig. 2: Cryo-TEM micrographs of: A. nanoreactors without OmpF, B. nanoreactors with reconstituted OmpF-WT, and C. nanoreactors with reconstituted OmpF-CA-Cy5. Scale bar = 200 nm.

Reconstitution of OmpF-CA-Cy5 in polymersomes. In order to determine whether the porin was appropriately modified with a pH-sensitive cap, and inserted into polymersomes, we first investigated the specific binding of the dye to the carbonyl groups of the OmpF-CA. We used fluorescence correlation spectroscopy (FCS) because it measures the mobility of fluorescent molecules and allows establishing their size via Stokes-Einstein equation. FCS autocorrelation curves show a significant difference in τ_d values between freely diffusing Cy5-hydrazide (τ_d = 67 µs), OmpF-CA-Cy5 in 3% OG micelles (τd = 266 µs) and polymersomes with reconstituted OmpF-CA-Cy5 (τ_d = 2914 µs) (Fig 3). Our nanoreactor is pH-sensitive due to the insertion of a chemically modified porin, and not because of an intrinsic property of the polymer 3D assembly [4].

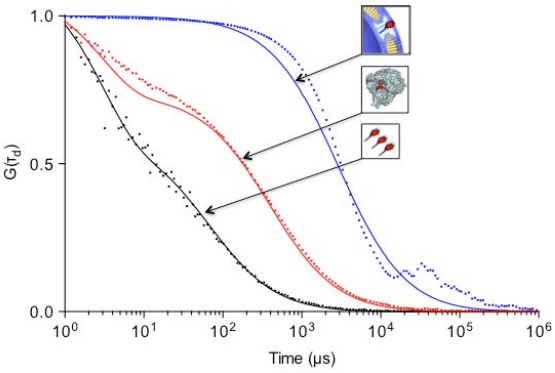

Fig 3: FCS autocorrelation curves 100 nM Cy5-hydrazide in PBS (Black), OmpF-CA-Cy5 in 3% OG (Red) and OmpF-CA-Cy5 in the membrane of polymersomes (Blue). Experimental autocorrelation curves (dotted line), and their fit (full line). Curves normalized to 1 to facilitate comparison.

Enzyme kinetics inside nanoreactors. To assess how the nanoreactor activity was affected by the chemical modification of the porin, we used the Amplex Red enzymatic substrate. The enzymatic turnover of the Amplex Red substrate (predicted polar surface area 72 A2, MW = 257 g mol-1, Log P = 0.89, charge = -0.1 at pH 7.4) was drastically reduced (down to 14%), compared to OmpF-WT nanoreactors acting in similar conditions at pH = 7.4. The blockage of Amplex Red influx through the pore is considered to be due to a combination of effects: (i) closing of the pore by the molecular cap, and (ii) electrostatic interaction of Amplex Red with the molecular cap.

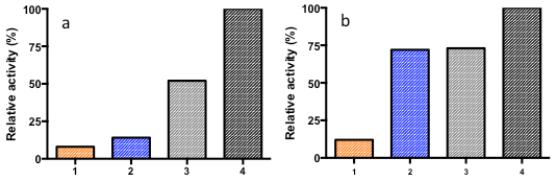

Fig.4: Amplex red conversion kinetics of nanoreactors equipped with different OmpFs: (1) unpermeabilised nanoreactors (orange), (2) OmpF-CA-Cy5 (blue), (3) OmpF-CA (grey), and (4) Ompf-WT (black) at pH 5.5, at time 0 (a) and after 1 hour (b).

Conclusion. We designed a nanoreactor with a pH responsive enzymatic activity, based on a chemically modified channel porin OmpF, which was inserted in the membrane of polymersomes, and acted as a "pH responsive gate". Our system has high potential for biosensing and therapeutical applications that will be further investigated

References for Project P1209

[1] C.G. Palivan, R. Goers, A. Najer, X Zhang, A. Car, W. Meier, *Bioinspired polymer vesicles and membranes for biological and medical applications,* Chem. Soc. Rev. (2015).

[2] T. Einfalt, R. Goers, I.A. Dinu, A. Najer, M. Spulber, O. Onaca-Fischer, C.G. Palivan, *Stimuli-Triggered Activity of Nanoreactors by Biomimetic Engineering Polymer Membranes,* Nano Letters, **15** (11), 7596-7603 (2015).

[3] L.H. Dieu, L.H., D. Wu, C.G. Palivan, V. Balasubramanian, J. Hüwyler, *Polymersomes conjugated to 83-14 monoclonal antibodies: In-vitro targeting of brain capillary endothelial cells,* Eur. J. Pharm. Biopharm. **88**, 316 (2014).

[4] T. Einfalt. R. Goers, I. A. Dinu, A. Najer, M. Spulber, O. Onaca-Fischer, C.G. Palivan, *Design of polymer nanoreactors with triggered activity for medicine and biosensing applications,* Nano DDS Symposium, Seattle (2015).

Nanowires as sensitive scanning sensors

Project P1210 Bottom-up nanowires as ultra-sensitive force transducers
Project Leader: M. Poggio and R.J. Warburton
Collaborators: D. Cadeddu (SNI PhD Student) and A.F.I. Morral

Introduction

This past year we focused on developing two novel applications of nanowries (NWs) as sensitive scanning sensors. In the first, we used as-grown GaAs/AlGaAs NWs as scanning vectorial force sensors. By virtue of slight asymmetries in geometry, a NW's flexural mechanical modes are split into doublets corresponding to two orthogonal directions. By monitoring the frequency shift of both modes as we scan the nanowire above a surface, we construct a vectorial map of the in-plane force gradients in non-contact mode. This capability, combined with the exquisite force sensitivity of nanowire sensors, allows for a type of atomic force microscopy specially suited to directional measurements of weak tip-sample interactions or small friction forces. In the second, we realize a quantum fiber-pigtail. The device consists of a semiconductor quantum-dot embedded into a conical photonic wire that is directly connected to the core of a fiber-pigtail. We demonstrate a photon collection efficiency at the output of the fiber of 5.8% and suggest realistic improvements for the implementation of a useful device in the context of quantum information. We also discuss potential applications in scanning probe microscopy. The approach is generic and transferable to other materials including diamond and silicon. Both of these experimental directions have relied on the unique experimental apparatus and infrastructure built up for this project, i.e. a low-temperature scanning probe microscope customized for use with NW cantilevers and emitters.

Non-contact AFM using a Vectorial NW sensor

Atomic force microscopy (AFM) exists in several forms and is now routinely used to image a wide variety of surfaces, in some cases with atomic or sub-atomic resolution. Due to its versatility, this technique has found application in fields including solid-state physics, materials science, biology, and medicine. Variations on the basic technique, including contact and non-contact modes, allow its application under diverse conditions and with enhanced contrast for specific target signals. Cantilever design can be optimized for operation on samples ranging from biological tissue in liquid to crystalline solids in ultra-high vacuum. Tips functionalized with chemical binding agents or magnetic materials produce either chemical or magnetic contrast. A voltage can be applied to the tip for the measurement of electric forces or work function potentials. The measurement of multiple mechanical harmonics yields information on the non-linearity of the tip-sample interaction, while monitoring higher mechanical modes provides additional types of imaging contrast. Today, these various types of AFM are most often carried out using cantilevers processed by top-down methods from crystalline Si. Fabrication processes start from large wafers and involve optical lithography, chemical etching, and a release step. Typical cantilevers are hundreds of μm long, tens of μm wide, and on the order of one μm thick. Resonant frequencies range from 10 to 100 kHz and spring constants from 0.1 to 10 N/m.

In recent years, however, researchers have developed new types of mechanical transducers, fabricated by bottom-up processes with extremely high mass and force sensitivities. These resonators are built molecule-by-molecule from small to large in processes that are typically driven by self-assembly or directed self-assembly. The most prominent examples include doubly-clamped carbon nanotubes (CNTs), suspended graphene sheets, and nanowire (NW) cantilevers. Unit-by-unit assembly from the bottom up allows for structures with extremely small masses, which are nearly defect free on the atomic scale. Small motional mass allows both for the detection of atomic-scale adsorbates and results in high mechanical resonance frequencies, decoupling the resonators from common sources of noise. The near structural perfection results in low mechanical dissipation, resulting in a high thermally-limited force sensitivity. In particular, CNT mechanical sensors have demonstrated yg mass resolution and a force sensitivity close to 10 zN/(Hz)$^{1/2}$ at cryogenic temperatures.

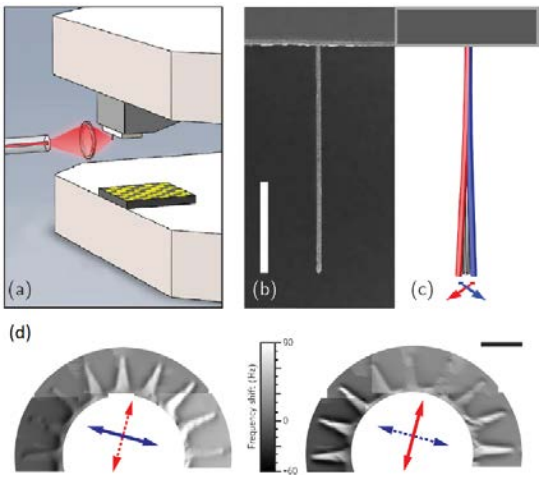

Fig. 1: (a) Schematic diagram of experimental setup. (b) SEM of NW cantilever. (c) Schematic diagram of orthogonal flexural modes used for lateral force microscopy. (d) Example of images of a pattered surface made with each mode showing sensitivity to force gradients in orthogonal directions.

Nevertheless, given their extreme aspect ratios and their ultra-soft spring constants, both CNTs and graphene resonators are difficult – if not impossible – to apply in the cantilever geometries ideal for scanning probe applications. NWs on the other

hand, when arranged in the pendulum geometry, i.e. with their long axis perpendicular to the sample surface, are well suited as sensitive scanning probes. They can be grown in a variety of sizes and from different materials, allowing access to a wide range of resonant frequencies and spring constants, where the pendulum geometry prevents the tip from snapping into contact. Diameters range from tens to hundreds of nm and lengths reach up to tens of μm. Possible materials include Si, GaAs, GaP, InAs, InP, GaN, and AlN as well as alloys and heterostructures thereof. When approached to a surface, NWs experience extremely low dissipation, i.e. non-contact friction, making possible near-surface (< 100 nm) force sensitivies around 1 aN/(Hz)$^{1/2}$. Such properties make them attractive as transducers in ultra-sensitive force microscopies such as Kelvin probe force microscopy, magnetic resonance force microscopy (MRFM), and for the spectroscopy of small friction forces.

Despite these potential advantages, their application as scanning force sensors is complicated by the difficulty of measuring the mechanical displacement of such small structures. In particular, techniques based on optical deflection are not applicable to NWs whose diameters are significantly smaller than the optical diffraction limit. Recently, however, researchers have developed specialized optical techniques to sensitively measure their motion, demonstrating the ability to resolve thermal motion even at cryogenic temperatures. These developments have led to two recent applications of NWs as sensors of nuclear MRFM and of opto-mechanical interactions. As shown in Fig. 1, we have now built an experimental setup to measure and control the motion of NW flexural modes and to scan a NW over a target surface. We demonstrate the use of as-grown NWs as surface-sensitive scanning probes. Individual NWs, due to their orthogonal flexural mode doublets, are used in a type of lateral force microscopy sensitive to the magnitude and direction of the tip-sample forces in the scanning plane. The technique is particularly well-suited to the measurement of extremely small forces, given that the pendulum geometry allows for the use of extremely soft – and therefore sensitive – NW cantilevers. This new type of AFM is made possible by the unique properties of NW cantilevers, in particular their high degree of axial symmetry.

A Quantum Fiber-pigtail

Semiconductor quantum-dots (QDs) are attractive single photon sources. They are robust, compact and provide on-demand single photons at rates in the GHz range. Their potential in the context of quantum optics however relies on the fulfillment of several demanding criteria: high efficiency, high photon purity, and simple operation. Recent progress has nevertheless brought QDs close to such applications. Single-photon operation has been obtained in a compact, table-top Stirling machine, offering a low-cost and user-friendly solution. Thanks to the increasing quality of the epitaxial material, spectrally pure emission has been demonstrated. The last challenge that needs to be addressed is to efficiently couple the emitted light into a single mode fiber. Great progress in this direction has been made with the integration of QDs into micro and nanoscale photonic structures, such as cavities and waveguides, which allow the control of spontaneous emission. In the last few years, important efforts to position the QD in an optimal way and to minimize the diffraction of light at the output of photonic NWs have pushed the collection efficiencies to values > 75% while maintaining a Gaussian spatial profile. These impressive results require, however, the use of objective lenses with large numerical apertures. In parallel, different strategies to couple the emitted light directly into a single mode fiber have emerged.

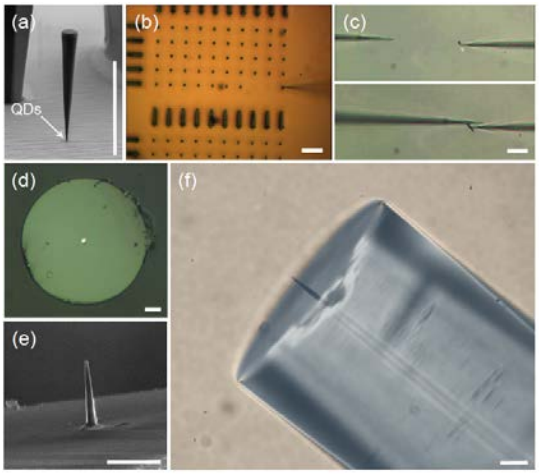

Fig. 2: (a) SEM of photonic trumpet. (b) Removing PW from substrate. (c) Orientation of PW. (d) Top view of bare fiber with glue droplet. (e) and (f) SEM and optical micrograph of fiber-pigtail. Scale bar represents 10 μm.

In Fig. 2, we show the direct coupling of QD single photons to an optical fiber [1]. Our device, the quantum fiber-pigtail, consists of a QD embedded in a tapered photonic wire (PW) that is directly attached to the cleaved end of a single mode fiber. Thanks to adiabatic expansion of the guided mode confined in the PW, we achieve an external collection efficiency of 5.8% at the output of the fiber-pigtail. The result represents a proof-of-principle for an easy-to-operate single photon source, with potential applications in quantum optics or metrology. Furthermore, easily addressable QDs at the end of a nanometer-scale tip have obvious potential as scanning probes. Possible applications include single photon near-field microscopy, deterministic quantum plasmonics, or electric field sensing.

Our collaboration with NW growers such as the Fontcuberta Group at EPFL and the Bakkers Group in Eindhoven has so far been highly productive and efficient.

References for Project P1210

[1] T D. Caddedu *et al.*, Appl. Phys. Lett., in press; *arXiv*:1512.00621.

Electron optics in encapsulated graphene

Project P1211 Electrical properties of ultraclean suspended graphene
Project Leader: C. Schönenberger and D. Zumbühl
Collaborators: C. Handschin (SNI PhD Student), P. Rickhaus, M. Weiss, B. Fülöp and P. Makk

Motivation

The rise of graphene during the last decade can be attributed to several unique features. To name only a few of them: the linear dispersion relation of the charge carriers, which makes electrons to behave as photons, the vanishing density of states at the Dirac point where conduction and valence bands touch, or the high mobility and ballistic electron transport with mean-free paths that can reach or even exceed several micrometers.

Research has shown, that in order to access the interesting physics of "clean" ideal graphene, the environmental influences (potential fluctuations from the substrate, unintentional chemical doping ect.) have to be reduced to a minimum. Currently the two most prominent techniques to obtain "clean" graphene are to either freely suspend the graphene or encapsulate it in between hexagonal boron-nitride (hBN), which like graphene is a layered material but a non-conducting one. Even though suspended graphene yields the highest graphene quality, the device geometries which can be realized are rather limited [1]. This can be circumvented by encapsulating graphene in hBN. In addition, encapsulation yields a stable form as the graphene conductor is no longer in direct contact with the environment. While the resulting device quality of encapsulated graphene is slightly lower than suspended graphene, it has nearly no limitation concerning the device geometry. Furthermore encapsulated graphene holds the potential to create a sharp pn-junctions (using electrostatic gates) which is desirable for the realization of several experiments, such as the Veselago lens [2,3] or a Michelson-Morley interferometer (see below).

Point Contacts in encapsulated graphene

So far, in encapsulated hBN-graphene-hBN heterostructures the graphene could only be accessed via top-contacts or 1-dimensional side-contacts [4] from the side/edge of the graphene sheet. However, for the realization of several theoretical proposals it is essential to be able to place point contacts (contacts with a small geometrical dimension) at an arbitrary position in the middle of the graphene sheet [5,6]. In the realization of an inner point contact to graphene an isolation layer is mandatory. So far this has only been done using evaporated, sputtered or atomic layer deposited dielectrics (isolator), which significantly lowers the graphene quality. We have developed a method that establishes point contacts to graphene encapsulated in hBN, maintaining the high quality of graphene.

Our idea is based on pre-patterning the top hBN layer with a focused ion beam (Ga-FIB), shown in Fig. 1a, before the hBN-G-hBN hetero-structure is assembled (shown in Fig. 1b). This pre-patterning avoids contamination of the graphene with gallium-ions and is therefore compatible with the clean graphene fabrication. Here we drilled 4 holes at equidistant spacing into the hBN, each having a diameter of 100 nm. Note that the Ga-FIB holds the potential to drill holes as small as 20 nm. After drilling the holes, the stack of hBN-graphene-hBN is realized with the top-most hBN layer having the holes. Electrical contact was established evaporating 100 nm of palladium over the drilled holes using standard E-beam technology (shown in Fig. 1c and d).

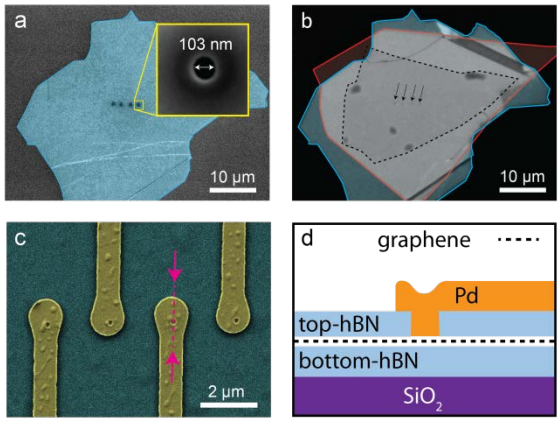

Fig. 1: ***Fabrication of hBN-graphene-hBN heterostructures with top-PCs. a,*** *False color SEM image of the top-hBN on SiO2 substrate after drilling the holes with the Ga-FIB. Inset: Close-up of a single hole.* ***b,*** *Optical image of a final stack. The different layers are indicated in red (bottom hBN), black (graphene) and blue (top hBN). The holes are indicated with arrows.* ***c,*** *False color SEM image of the final stack (blue) with Pd contacts (yellow) overlapping the drilled holes.* ***d,*** *Schematic of the cross-section as indicated in (**c**) by pink arrows and the dashed line.*

Transport-measurements of different 2- and 4-terminal configurations were performed and are in quantitative agreement with an electrostatic model established for this system. These results were published in C. Handschin et *al*, Appl. Phys. Lett. **107** 183105 (2015) [7].

Side-contacts and top-gates

Besides following the point-contact project, considerable effort has been undertaken to improve the quality of regular graphene heterostructures with side-contacts. This includes the improvement of i) the side-contacts, ii) the graphene quality in the heterostructures and iii) detailed investigation of different methods on how to establish stable top-gates. The latter is of great interest since this is required to create a sharp pn-junction in graphene.

The reproducibility and quality of the side-contacts is very good with contact resistances as low as 40-

100 Ω*µm. It is worth mentioning that this is better than most literature values. The graphene quality is on an acceptable level with mobilities up to 150'000 $cm^2/(V*s)$. However, a further improvement would be desirable in order to obtain ballistic transport over longer distances. Concerning the top-gates, three different types have been investigated, each of them having their advantages and disadvantages. Depending on the device-geometry, the most suitable technique can be chosen.

Michelson-Morley interferometer

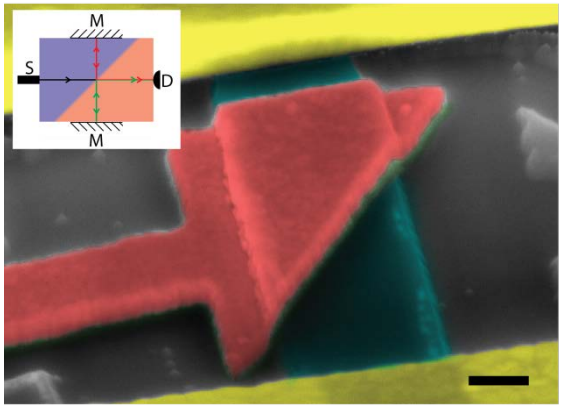

Fig. 2: False color SEM image of the current design used for a pn-junction based Michelson-Morley interferometer in graphene using negative refraction. Source (S) and Drain (D) are shown in yellow, the hBN-graphene-hBN heterostructure is shown in cyan and the local top-gate is shown in red. The edges of the graphene strip act as mirror (M). Scale bar equals 200 nm. Inset: Sketch of the experiment with the pn-junction depicted as blue/red and the graphene edges as mirrors (shaded).

We have previously reported on a Fabry-Perot interferometer in graphene [8]. This is a multi-pass interferometer. In contrast, a two path interferometer is a more fundamental and in principle more simple device. Examples are the Mach-Zehnder and the Michelson-Morley interferometer. Both of them have not yet been realized in graphene. They both need properly working beam-splitters that provide a 50:50 splitting with low loss. Due to the zero-gap in graphene one cannot obtain a tunneling barrier that could be used to split an electron beam. It has been shown theoretically that a sharp pn-junction can provide an effective beam splitter. Based on the concept of a pn-junction beam splitter we came up with a very compact design for a graphene Michelson Morley (MM) interferometer. The device geometry (false color SEM image) and a sketch of the charge-carrier trajectories is shown in Fig. 2. Probably the most striking difference from the classical MM interferometer is the negative refraction of the charge carriers at the pn-junction compared to the normal (positive) refraction of the electro-magnetic wave at the semi-transparent mirror. This leads to a rearrangement of mirrors (M) and detector/drain (D) with respect to each other. In the classical MM interferometer interference is observed by slightly varying the length of one the two paths between beam-splitter and mirror. In the electronic version of the experiment the interference is obtained by tuning the Fermi-wavelength using the global and local back- and top-gates respectively since the path-lengths are fixed.

Even though having measured already several devices with the geometry shown in Fig. 2, the MM interference could not be observed yet. Most likely one (or several) of the following aspects are responsible for the absence of the interference signal. 1) The graphene is not ballistic over the whole device length. Contaminations in the hBN-graphene-hBN heterostructue will lead to scattering of the charge carriers. The latter will smear out the interference signal. 2) Besides scattering in the bulk of the graphene, scattering occurs as well at the edges of the graphene if these are rough (in analogy to a diffusive mirror). 3) If the pn-junction is rough, this has comparable consequences as described in [2]. For the electron wavefunction the graphene edge/pn-junction appears effectively straight if the Fermi wavelength is much larger than the edge/pn-junction roughness. However, this is not entirely satisfied in the current devices due to fabrication limitations using the current approach.

It is worth mentioning, that Ming-Hao Liu and Klaus Richter from the University of Regensburg have supported us with tight-binding simulations for the MM experiment. At this point, we also like to acknowledge contributions from S. Blanter (project student from the TU-Delft), S. Csonka (Budapest) and D. Mathys (ZMB at the Univ. of Basel) to this work. High-quality hBN was provided by K. Watanabe, T. Taniguchi from the National Institute for Material Science at Tsukuba, Japan.

Outlook

Currently we are adjusting several steps in the fabrication procedure which will lead to a reduced edge- and pn-junction roughness. With these improvements we hope to fulfill the requirements needed to see the MM interference.

References for Project P1211

[1] R. Maurand, P. Rickhaus, P. Makk, S. Hess, E. Tovari, C. Handschin, M. Weiss, C. Schönenberger, Carbon **79,** 486 (2014).
[2] V. Veselago, Phys. Usp. **10,** 50 (1968).
[3] G-H. Lee *et al*, Nat. Phys. **11**, 925 (2015).
[4] L. Wang *et al*, Science **342,** 614 (2013).
[5] A. Moghaddam *et al*., Phys. Rev. Lett. **105,** 146803 (2010).
[6] A. Patel *et al*., Phys. Rev. B **86,** 081413 (2012).
[7] C. Handschin, B. Fülöp, P. Makk, S. Blanter, M. Weiss, K. Watanabe, T. Taniguchi, S. Csonka, C. Schönenberger , Appl. Phys. Lett. **107,** 183108 (2015).
[8] P. Rickhaus, P. Makk, Ming-Hao Liu, E. Tóvári, M. Weiss, R. Maurand, K. Richter, C. Schönenberger, Nat Commun **4,** 2342 (2013).

Diamond membranes in a tunable microcavity

Project P1212 Nano-photonics with diamond
Project Leader: R.J. Warburton and P. Maletinsky
Collaborators: D. Riedel (SNI PhD student), D. Najer and S. Starosielec

The nitrogen-vacancy (NV) center in diamond has a coherent spin and this feature is finding numerous applications in quantum sensing. These applications range from probing stray-fields close to the surface of integrated cicruits to the detection of vortices in a high-T_c superconductor at low temperature. In these applications, the NV spin is both initialized and read-out optically. The optical transition is well suited to these two tasks but employing the NV for quantum photonics places more stringent demands on the optical properties. Ideally, the emitted photons should represent a high brightness source of indistinguishable photons. This is far from the case at present. We have already presented a powerful solution to the brightness problem [1] but other serious issues remain. Only a few per cent of the emission goes into the useful zero-phonon-line (ZPL). Also, the frequency of the optical transition fluctuates in time. In fact, the green laser pulses required to reset the NV charge typically cause a shift of the optical frequency, probably by changing the occupation of defect states. Despite these difficulties, quantum optics techniques have been used to entangle two remote NV spins. The entanglement rate is however small and does not obviously represent a route to creating a viable technology. We are aiming at solving these problems. There are two key concepts. The first is the creation of high quality NV centres in single crystal diamond membranes. The starting material is of the highest quality; the nano-fabrication is minimally invasive. Secondly, the membranes are embedded in a miniaturized cavity which should "funnel" the emission into the ZPL once the ZPL is tuned into resonance with the microcavity mode. We present here results on our on-going attempts to put these ideas into practice.

The fabrication of single crystal diamond membranes has become more reliable in the past year. We have developed techniques to bond the membranes to highly-reflective dielectric Bragg mirrors: provided both surfaces are clean the bonding (via the van der Waals interaction) is effective. Furthermore, post bonding, we have demonstrated that the membrane can be etched further allowing us to create membranes just a few hundred nanometres in thickness. These are ideal for the microcavity experiments.

The microcavities have been developed in parallel [2-4], Fig. 1. To build on a secure foundation, we turned initially to experiments on semiconductor quantum dots which have close-to-ideal optical properties at low temperature: a strong optical dipole and a large ZPL ratio [3,4]. To mimic the diamond approach, we employed a lift-off technique by which the active semiconductor layer is released from its host substrate and bonded (again by a van der Waals interaction) to a dielectric Bragg mirror (alternating silica and tantala layers), Fig. 2 [3]. The construction of the microcavity is completed with a curved top mirror, Fig. 1 [2-4]. A number of positive results were demonstrated. First, a finesse of several thousand could be achieved, limited only by the reflectivities of the mirrors. This demonstrates that the semiconductor-dielectric interface does not scatter the light significantly. Secondly, the brightness and linewidth of the quantum dots in the lift-off layer are comparable to those of the quantum dots in the starting material. This demonstrates that the new surface created in the lift-off process is benign regarding charge noise. Finally, a Purcell effect at the microcavity-quantum dot resonance was observed [3]. These results prove an important point of principle: hybrid mirror-emitter structures are useful for cavity QED.

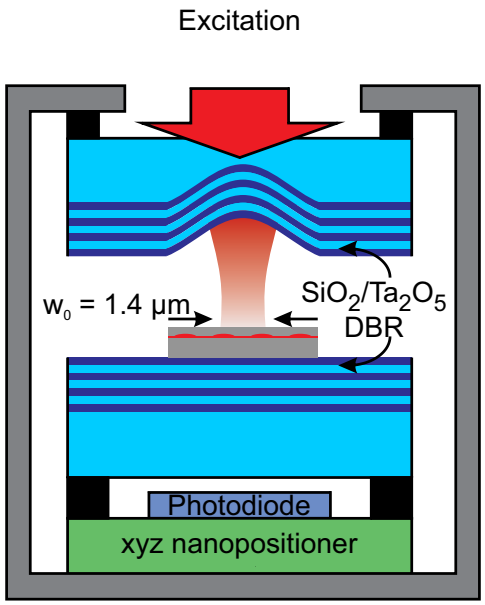

Fig. 1: Schematic of the tunable microcavity.

The Purcell effect of a quantum dot in the microcavity is presently small [3,4]. It can be boosted by reducing the cavity mode volume and by suppressing emission into the lateral "leaky" modes. We have focussed our initial efforts onto the cavity mode volume. The microcavities are of the Fabry-Perot type with typical radii 10-20 microns. The microcavity templates are created by laser ablation of flat silica substrates: it is hard to focus the laser beam more tightly to reduce the radius of curvature. Instead, we have pre-fabricated the silica substrates. This has enabled us to create mirror templates with radii down to a few microns with a depth of a few hundred nanometres, dimensions ideal for cavity

experiments. Microcavity experiments using these ultrasmall mirrors are currently underway.

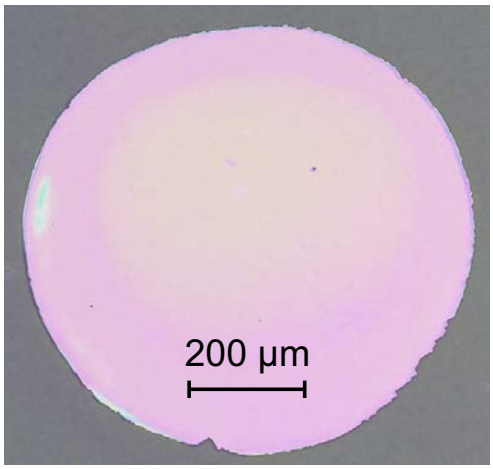

Fig. 2 Semiconductor membrane bonded to a dielectric mirror following the epi-lift-off procedure.

The optical quality of NV centres in the fabricated membranes has been tested by comparing the properties to those in the original substrates. The brightness is roughly the same although there are fluctuations from one NV centre to the next in the membrane. The linewidhts are around 1 GHz for NVs in the membrane, increased above 100 MHz for NVs in the bulk. The reason for this increase is not yet known. However, while these linewidths are not ideal (the transform limit corresponds to ~10 MHz), they are much less than those of NVs in nano-diamond and they are also much less than the present microcavity mode linewidths.

The finesse of a microcavity at 640 nm wavelength (the NV emission wavelength) has been measured with a diamond membrance, Fig. 3. A finesse as high as 5,000 is achieved with the diamond membrane. This demonstrates that the scattering losses at the interfaces and in the diamond material are low. This is a more stringent test than the semiconductor experiment: unlike the semiconductor, the diamond surface is not atomically flat. The experiment demonstrates that the diamond-mirror interface is controlled well enough even in the case of a high-Q cavity in which the light traverses the interface many times before exiting one of the mirrors. We propose to build on these results in the next phase of the project.

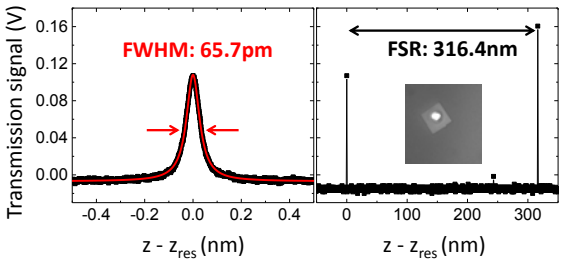

Fig. 3: Microcavity characterization: measurement of microcavity finesse of 5,000 by scanning the mirror separation for a constant laser wavelength (632.8 nm) with a diamond membrane.

References for Project P1212

[1] D. Riedel, D. Rohner, M. Ganzhorn, T. Kaldewey, P. Appel, E. Neu, R. J. Warburton, and P. Maletinsky, *"Low-Loss Broadband Antenna for Efficient Photon Collection from a Coherent Spin in Diamond"*, Phys. Rev. Appl. **2**, 064011 (2014).

[2] L. Greuter, S. Starosielec, D. Najer, A. Ludwig, L. Duempelmann, D. Rohner, and R. J. Warburton, *"A small mode volume tunable microcavity: Development and characterization"*, Appl. Phys. Lett. **105,** 121105 (2014).

[3] L. Greuter, D.l Najer, A. V. Kuhlmann, S. R. Valentin, A. Ludwig, A. D. Wieck, S. Starosielec , and R. J. Warburton, "*Epitaxial lift-off for solid-state cavity quantum electrodynamics*", J. Appl. Phys. **118** , 075705 (2015).

[4] L. Greuter, S. Starosielec, A. V. Kuhlmann, and R. J. Warburton, "*Towards high-cooperativity strong coupling of a quantum dot in a tunable microcavity*", Phys. Rev. B **92**, 045302 (2015).

Hydrogen production based on molecular nanofactories

Project P1213 Artificial metalloenzymes for molecular nanofactories
Project Leader: T.R. Ward and S. Panke
Collaborators: S. Keller (SNI PhD Student), A. Pannwitz and O. Wenger (University of Basel)

Introduction

Hydrogen is an attractive, clean and renewable energy vector. It can be used as an energy carrier and be regarded as a potential transportation fuel. In the presence of dioxygen, dihydrogen donates both its electrons and water is the only waste product formed. Since molecular hydrogen is not present in high quantities on earth, catalysts must be developed that produce dihydrogen efficiently. Ideally, the reaction should proceed in both directions (oxidation and reduction) with high turnover numbers at ambient temperature and pressure relying on solar energy (Figure 1).

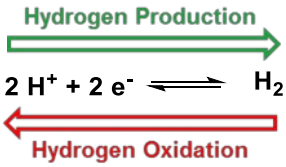

Figure 1 *Hydrogen production and hydrogen oxidation as an environmentally friendly means to store and release energy.*

Hydrogenases are natural enzymes that catalyze these reactions with high turnover numbers. Yet the fragility of these enzymes renders their widespread use challenging. Indeed, these are oxygen-sensitive and are readily denatured at moderate temperature and basic pH. To circumvent these limitations, significant effort has been invested in developing robust artificial hydrogenases. In this context, Ni-based catalyst **1**, developed at the PNNL, is the most promising electrocatalyst for the production of hydrogen from protons and electrons. In particular, it has been shown that its activity can be significantly improved upon fine tuning its second coordination sphere (Figure 2). [1]

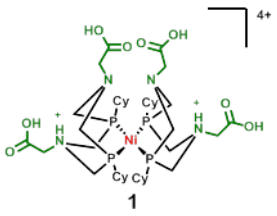

Figure 2 *Nickel-based artificial hydrogenase for hydrogen production. The presence of carboxylic moieties (green) was shown to be critical for its unrivalled activity.*

In the past year, significant effort in the Ward group has been invested in integrating biotinylated Ni-based catalysts within streptavidin (Sav).

Towards an efficient hydrogenase based on the biotin-streptavidin technology

In collaboration with Dr. W. Shaw (PNNL) and Dr O. Rüdiger (MPI for energy conversion), we developed and tested biotinylated Ni-complexes **2-6**. Their catalytic performance was evaluated both in the presence and in the absence of streptavidin (Figure 3). After synthesizing the complexes at UniBas, Mr. Sascha Keller spent two months at the PNNL (Richland, WA, USA) and one month in Mülheim to perform the electrocatalysis experiments. Both hydrogen-oxidation and proton-reduction catalytic transformations were evaluated.

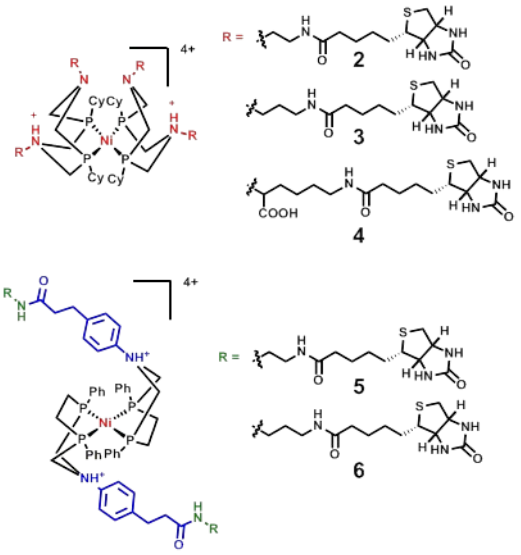

Figure 3 *Biotinylated hydrogen oxidation catalysts **2-4** (top) and hydrogen reduction catalysts **5-6** (bottom) synthesized and tested.*

With the biotinylated catalysts **2-6** at hand, their catalytic profiles were evaluated both with and without streptavidin. For this purpose, cyclic-voltammetry proved most effective. Gratifyingly, catalyst **3** was active as a hydrogen oxidation catalyst both in the presence and in the absence of streptavidin. Unfortunately, no catalytic improvement could be observed upon incorporation within Sav (Figure 4). To gain a more quantitative insight, protein-film voltammetry was required. This method ensures that all artificial hydrogenases are oriented homogeneously on the electrode surface. For this purpose we initiated a collaboration with Dr. Olaf Rüdiger. Despite all our efforts, we were unable to determine any catalytic current for the immobilized artificial hydrogenase. We speculate that, upon immobilization of Sav on the electrode surface, the Ni···electrode distance is too large to

observe efficient electron transfer. Further efforts are ongoing.

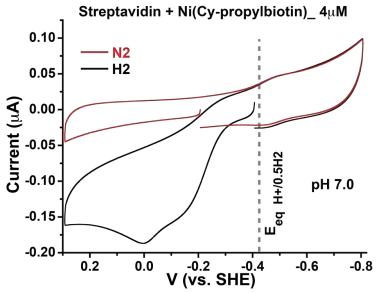

Figure 4 *Cyclovoltammogram of catalyst **3** inside Sav under N_2 (red curve) and under H_2 (black curve). In the presence of dihydrogen, a catalytic current is clearly detectable.*

Photodriven hydrogenase based on the biotin-streptavidin technology

With the aim of exploiting sunlight as energy source to drive the catalytic process (e.g. either hydrogen production or hydrogen oxidation), we set out to engineer a catalytic dyad (or triad) relying on Sav to precisely position a photosensitizer as well as an oxidation- and/or a reduction catalyst. We anticipate that, upon light excitation, the protein-bound photosensitizer $\{Ru(bpy)_2(phen)\}^{2+}$ **7**[2] may abstract (or donate) an electron from a biotinylated catalyst that may lead to the development of a photodriven hydrogenase. With this goal in mind, we tethered the ruthenium photosensitizer **7** to Sav isoforms bearing a single cysteine. Four cysteine mutants were produced recombinantly, purified and characterized by ESI-MS: T66C, R84C, S112C and K121C. Successful covalent anchoring of the photosensitizer **7** was demonstrated by ESI-MS and UV-Vis spectroscopy. Next, the biotinylated triarylamine **8** acting as an electron donor was added to the cysteine-containing mutants (Figure 5).[3] In collaboration with Prof. O. Wenger (UniBas), we characterized the Sav-conjugates by transient absorption spectroscopy. The triad consisting of **8** · Sav S112C–$\{Ru(bpy)_2(phen)\}^{2+}$ **7** with externally added 4,4'-dimethyl-viologen, we could unambiguoulsy detect the oxidized triarylamine **8**.[4]

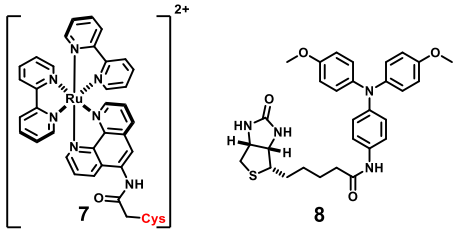

Figure 5 *The $\{Ru(bpy)_2(phen)\}^{2+}$ **7** photosensitizer reacts selectively and irreversibly with a cysteine residue engineered on the surface of Sav. In the presence of viologen, the biotinylated triarylamine **8** acts as a transient electron donor.*

Outlook

Having demonstrated the feasibility of photodriven charge separation using Sav as a protein scaffold, our current efforts are aimed at i) synthesizing a biotinylated cobaloxime hydrogenase[5] as well ii) covalently linking a dialkyl-viologen to the *N*-terminus of Sav.[6]

References for Project P1213

[1] A. Dutta, D.L. DuBois, J.A.S. Roberts and W. Shaw, *"Amino acid modified Ni catalyst exhibits reversible H_2* oxidation/production over a broad pH range at elevated temperatures", PNAS **111**, 16286 (2014).

[2] J. Bos, F. Fusetti, A.J. Driessen and G. Roelfes, *"Enantioselective Artificial Metalloenzymes by Creation of a Novel Active Site at the Protein Dimer Interface",* Angew. Chem. Int. Ed. **51**, 7472 (2012).

[3] M. Kuss-Petermann and O. Wenger, *"Increasing Electron-Transfer Rates with Increasing Donor-Acceptor Distance*", Angew. Chem. Int. Ed. DOI: 10.1002/anie.201509809

[4] S. Keller, A. Pannwitz, O. Wenger and T.R. Ward, manuscript in preparation.

[5] N. Kaeffer, M. Chavarot-Kerlidou and V. Artero, *"Hydrogen Evolution Catalyzed by Cobalt Diimine-Oxime Complexes*", Acc. Chem. Res. **48**, 1286 (2015).

[6] L.S. Witus, T. Moore, B.W. Thuronyi, A.P. Esser-Kahn, R.A. Scheck, A.T. Iavarone and M.B. Francis, *"Identification of Highly Reactive Sequences For PLP-Mediated Bioconjugation Using a Combinatorial Peptide Library*", J. Am. Chem. Soc. **132**, 16812 (2010).

Ultracold atoms and ions on a chip

Project P1214 An ion-atom hybrid trap on a chip: Synthesis and control of nanosystems on the single-molecule level
Project Leader: S. Willitsch and P. Treutlein
Collaborators: I. Rouse (SNI PhD Student), A. Mokhberi and R. Schmied

Introduction

Quantum systems are highly susceptible to the effects of noise and so making the precision measurements required to accurately determine physical concepts such as the "shape" of the electron, or to follow the pathway taken by a chemical reaction, is impossible under standard conditions due to thermal fluctuations and their coupling to the surroundings. However, the development of "particle traps" enables holding a small sample of atoms in an ultra high vacuum (UHV), isolated from the outside world for periods of time from a few milliseconds to days. When combined with the technique of cooling atoms through the application of resonant laser light, this allows for an unprecedented ability to observe quantum effects without the interference of the environment.

In recent years, there has been a trend to scale down the particle traps from the bulky apparatus initially used to microscopic chips, capable of performing much more precisely controlled operations to the trapped particles. In particular, two types of chip have been the subject of a great deal of investigation – "atom chips" and "ion chips". Atom chips generate magnetic fields which cause small shifts in the energy of neutral atoms such that they are guided to a minimum in the magnetic field. Ion chips trap charged particles in a radiofrequency electric field, and with the aid of laser-cooling these particles form ordered structures known as Coulomb crystals. Since the ions are localized in these structures they can be easily individually addressed by lasers and hence are a prospect for quantum computing, or the loss of ions can be observed and used to monitor the progress of chemical reactions atom-by-atom. Here we report for the first time the implementation of an ion-atom chip capable of cooling and trapping both species simultaneously above a microstructured surface.

Design of the microscopic hybrid ion-atom system

Three components generate the trapping fields necessary for different species and stages of the experiment. Charged particles are confined through a variation of the macroscopic Paul trap by applying both static and time-dependent voltages to the ion chip, a gold-coated set of stainless steel electrodes designed to keep the ions at a distance of approximately 300 microns above the surface of the chip. These electrodes rest on a printed circuit board (PCB), which provides them with electrical connections and additionally contains a set of carefully designed wire traces to generate magnetic traps to contain pre-cooled neutral atoms. These atoms are initially collected and cooled to an initial temperatures of 100 microKelvin from a background atomic vapour through the use of a mirror-MOT – a modification of the standard magneto-optical trap. This mirror MOT is formed by passing a high current through a U-shaped wire located underneath the atom chip in combination with cooling lasers reflected from the surface of the ion chip. The atoms may then be transferred to the magnetic trap generated through the atom chip and shuttled to a region where they can undergo Bose-Einstein condenstation and interact with the ions.

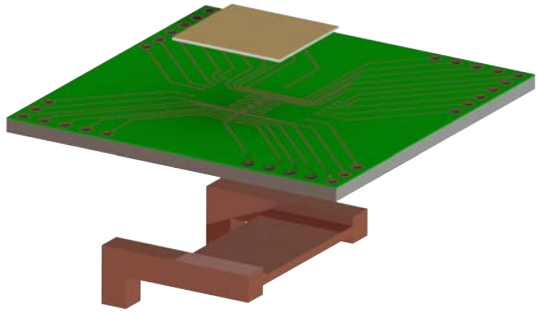

Fig. 1: Exploded view of the three layers of the hybrid chip trap showing the ion chip (top), atom chip (middle) and U-wire MOT (bottom). The long edges of the atom chip are 4cm.

The chip itself forms one wall of a UHV chamber, with the remainder of the chamber consisting of a quartz cell allowing for optimal optical access. A pumping system attached to this cell then generates the vacuum necessary to allow experiments to be performed.

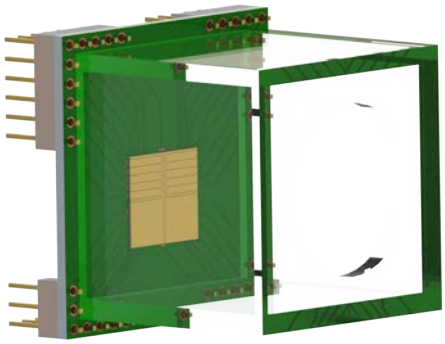

Fig. 2: The hybrid chip attached to a 3cm x 3cm fused silica cell to create a vacuum chamber such that trapped particles are isolated from the environment.

Simulations of trapped particles

Molecular dynamics simulations of the ion chip were performed in order to ensure that the ions could be stably trapped, and in order to predict the temperature of the resulting ion crystal. However, during the validation of the code against experimental results obtained using an existing ion chip, previously hidden properties of the trapped ions emerged [2]. It was found that due to the balance of heating and cooling forces, the behaviour of the ions could not be adequately described by a single temperature. Instead, a more accurate description is given by so-called "superstatistics" - an averaging of thermal functions such as the Maxwell-Boltzmann distribution over a range of temperatures.

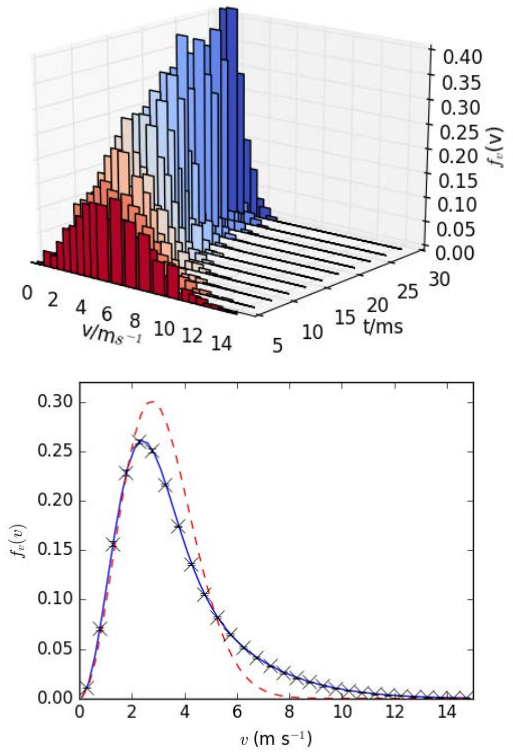

Fig. 3: Time-resolved (top) and time-averaged (bottom) velocity distributions in simulations of an ion trap. The instantaneous distributions are Maxwellian, while the distribution observed during experimental timescales is not. This can be seen in the lower figure comparing the simulated data (crosses) with a Maxwell-Boltzmann fit (red dashed line). A superstatistical treatment (blue solid line) gives a much improved fit.

This behaviour has been shown to have implications for reaction dynamics and precision spectroscopy, and the hybrid chip will allow for a further investigation of these effects.

Manufacturing process

Encouraging early results have shown that the prototype atom chip is compatible with the low pressures and high temperatures necessary for experiments with no loss of performance. A final version of the atom chip has now been designed and is ready for manufacture based on an "insulated metallic substrate" construction method, allowing a more efficient cooling of the chip than possible with traditional PCBs, which enables using higher currents and hence stronger trapping fields. The electrodes of the ion chip trap have been successfully fabricated and are awaiting transfer to the final atom chip. This will require precise alignment to ensure that at the end of the magnetic conveyor series the cloud of ultracold atoms is optimally overlapped with the trapped ion cloud. After this transfer, a fused silica cell will be glued to the chip to form a vapor cell capable of sustaining the low pressures of 10^{-10} mbar required to perform experiments.

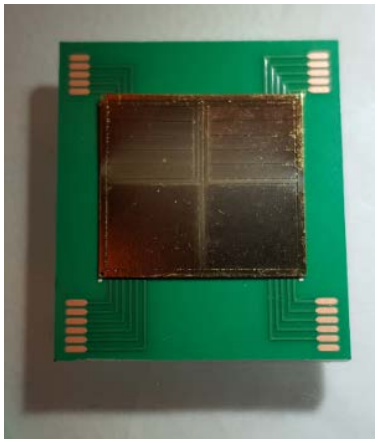

Fig. 4: Top: Gold-plated ion chip on top of a prototype atom chip.

Outlook

The vacuum system is presently being assembled, and, following the construction and attachment of the vapour cell, alignment of the optics system can begin. The initial construction will allow for the generation of ion crystals and an atomic MOT, with a future upgrade after the arrival of precision current sources allowing the atom chip to be used to its full potential to generate a BEC. Initial studies will therefore focus on the reactive dynamics of ultracold ions and atoms, and future work will be able to investigate the behaviour of charged impurities in degenerate quantum systems.

References for Project P1214

[1] S. Willitsch, *"Coulomb-crystallised molecular ions in traps: methods, applications, prospects"*, Int. Rev. Phys. Chem. **31**, 175 (2012).

[2] I. Rouse and S. Willitsch, *"Superstatistical velocity distributions of cold trapped ions in molecular-dynamics simulations"*, Phys Rev. A **92**, 053420 (2015).

Nanoelectronics at ultra-low temperatures on a cryogen-free dilution refrigerator

Project P1215 Nanostructure quantum transport at microkelvin temperatures
Project Leader: D. Zumbühl and D. Loss
Collaborators: M. Palma (SNI PhD Student), D. Maradan, L. Casparis, A. Feshchenko, I. Khaymovich, M. Meschke and J. Pekola

Introduction

Reaching ultralow temperatures on electronic nanodevices would allow to explore new physics such as novel nuclear/electron spin phases [1,2] and fragile fractional quantum Hall states, with applications in topological quantum computing. We have developed an advanced nuclear demagnetization refrigerator, which is equipped with multiple stages of filtering and shielding. The goal is to cool the electrons in nanoelectronic devices around to 1 mK and precisely determine the electronic temperature (T_e), which presents a challenging task below 10 mK.

In collaboration with the Pekola group from Aalto University, we present measurements on a single normal metal - insulator - superconductor (NIS) tunnel junction, which can be used as a thermometer down to 7 mK. Thermal analysis of the device shows that overheating in both normal metal and superconductor is negligible. It means that potentially this thermometer can be operated down to 1 mK [3].

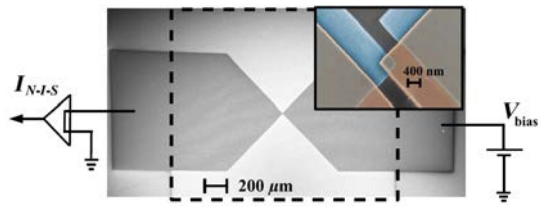

Fig. 1: Scanning electron micrograph of the NIS device and scheme of the measurement setup

NIS thermometer

The NIS is fabricated by electron-beam lithography and two-angle shadow evaporation technique. The junction is formed by the overlap of the Cu pad on top of Al pad in an area of roughly 400x400 nm², the two pads are separated through a tunnel barrier of Al_2O_3, as shown in the inset of Fig.1. The strength of our geometry is the large leads of junction providing a good thermalization of the electrons, see Fig.1. In the NIS thermometer, we use the sharp edge of the superconductor density of states to map the Fermi-Dirac distribution of the electrons of the normal metal (f_N). The tunnel current through the junction can be expressed as:

$$I = \frac{1}{2eR_T}\int_{-\infty}^{+\infty} dE n_S(E)[f_N(e-eV) - f_N(e+eV)] \quad (1)$$

where R_T is the normal state resistance, E is the energy relative to the chemical potential, n_s is the smeared superconductor density of the states, which is described through the Dynes parameter γ [4]. We first perform a least-square fit (full-fit) method (A) described by Eq. 1, where the only free parameter is the temperature T_N^A. The advantage of this method is that T_N^A is γ independent. However, we need to extract the superconducting gap (Δ) at high T and R_T. Furthermore, we present the semi-log method (B), which uses the exponential part of the IV curve to extract T_N^B, where T_N^B is given by the semi-logarithmic slope $T_N^B = dV/d(\ln I)e/k_B$, with electron charge e and Boltzmann constant k_B, see Fig 2.a. The T_N^B extracted is independent of the device parameters (e.g the superconducting gap and the normal state resistance) and it does not need a calibration, i.e. is a primary thermometer. When neglecting the corrections due to the γ parameter. These corrections in the form of higher-order terms will lead to a deviation of T_N^B from the real T_N.

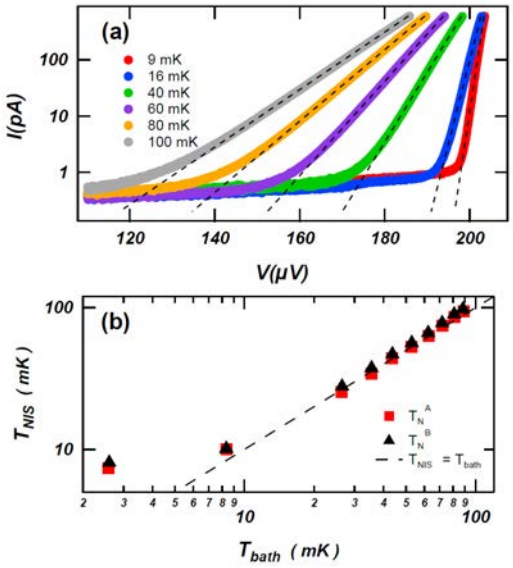

Fig. 2 Panel (a) IV characteristics at different temperatures, the dash line is the semi-log fit. Panel (b) shows the electron temperature of the NIS (T_{NIS}) extracted from both full-fit (red squares) and semi-log fit (black triangles).

However, for γ=2.2e-5 this deviation is 10% or less for temperatures down to 1 mK, if in the semi-log method we measure the differential conductance g(V) instead of the IV curve. The NIS thermometer agrees well with the other fridge thermometers down to 9 mK, as shown in the Fig.2.b. We observe a

saturation of the NIS thermometer around 7 mK when the bath temperature (T_{bath}) is below 2 mK. However, we are able to reach 7 mK only after several weeks, this behavior suggests that the saturation might be due to heat release from the epoxy chip socket. We can reduce the heat release using low release material such as pure metal or sapphire instead of epoxy in important parts e.g socket and chip carrier. In addition, better shielding of the NIS junction can significantly lower T_e.

Sub-gap steps

Owing to an extremely low noise environment, we are able to observe for the first time steps in the sub-gap regime of the I-V characteristic. The steps appear symmetrically around zero bias and are only weakly dependent on the perpendicular B field. The broadening of the step can be described by a Fermi-Dirac distribution, and the Temperatures extracted agree well with other thermometers from 90 mK down to 9 mK. We observe saturation below 9 mK, with a lowest temperature around 4 mK. The steps are present in certain junctions with different normal metal thicknesses (150 nm, 50 nm, 20 nm). In addition, we observed varying step positions upon thermal cycling. The origin of the steps is not fully understood, but the shift of the step position for different cool-downs seems suggest that they may originate from an impurity inside the normal metal [5].

Noise thermometer and BlueFors system

In parallel to the development of new on-chip thermometers, we implemented an advanced network of 16 parallel nuclear refrigerators (NR) operating on a BlueFors cryo-free dilution refrigerator. Furthermore, to measure the electronic temperature in the NR, we implemented a noise thermometer. We measure the thermal fluctuation of electrons inside a high purity silver wire well connected to the Cu stage. For this, we employ a gradiometer made of a couple of pick-up coils counter-wound around the silver wire. To perform an inductive read-out of noise voltage across the gradiometer a DC SQUID is used to amplify the small voltage. In addition, we designed a superconducting double shield to protect the gradiometer against the stray magnetic fields present in our experiment. For calibrating the noise thermometer, a reference point at high temperature (T_{ref}), where all the system parts are perfectly thermalized, is used. To extract the temperature of the noise thermometer T_{noise} we developed the following procedure. First we cut out the excess noise peaks, because they are T independent and they increase the T reading, from the noise spectrum (S_Φ) and then we perform a low pass filter fit, where the fit parameters are the cut-off frequency f_c and the noise plateau (S_o). From the reference curve we extract f_c and S_o (T_{ref}). Then we apply the previous procedure for all the other spectrum with f_c fix to the values extracted for the reference and $S_o(T)$ as only free parameter. The temperature T_{noise} for a given spectrum is $T_{noise}=S_o(T)/S_o(T_{ref})*T_{ref}$. The noise thermometer agrees perfectly with the fridge thermometers over 3 orders of magnitude. The lowest temperature measured is (160±2) μK, which is due to the intrinsic SQUID noise [6].

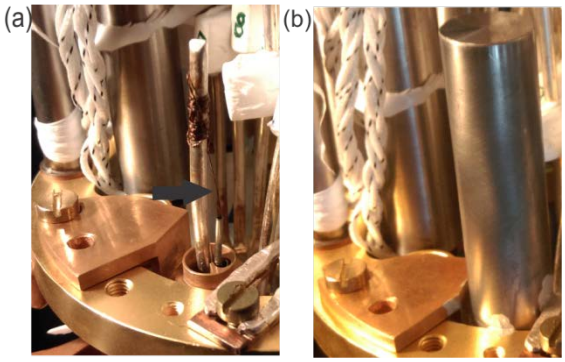

Fig. 3: Panel (a) a picture of the gradiometer and the thermalization piece for the shields, the arrow indicates the pick-up loop. The gradiometer covered by the superconducting double shields (b).

As shown in Fig. 3, the gradiometer now is not in contact with shields to avoid heat transport between them. The shields are thermally anchored to the mixing chamber plate. This change improved the performance of noise thermometer and reduced the heat leak measured into the gradiometer. In addition, the socket made of Ag epoxy has been removed, since we identified it as main source of heat leak. We observed a reduction of the heat leak on all the T sensors from 4-8nW/mol to 1-2 nW/mol (paper in preparation). The remaining heat leak is B field independent that exclude the Eddy current heating, but it suggests a small heat release coming from other parts of the fridge e.g. the Cu pates or Ag wires. For the future, we are planning to install a new chip socket made of sapphire, which is a material with low heat release.

References for Project P1215

[1] P. Simon and D. Loss, Phys. Rev. Lett. **98**, 156401 (2007). P. Simon, B. Braunecker and D. Loss, Phys. Rev. B 77, 045108 (2008).

[2] C.P. Scheller, T.-M. Liu, G. Barak, A. Yacoby, L.N. Pfeiffer, K.W. West and D.M. Zumbühl, Phys. Rev. Lett. **112**, 066801 (2014).

[3] A.V. Feshchenko, L. Casparis, I.M. Khaymovic, D. Maradan, O.-P. Saira, M. Palma, M. Meschke, J.P. Pekola and D.M. Zumbühl, Phys. Rev. Appl. **4,** 034001 (2015).

[4] R.C. Dynes, V. Narayanamurti and J.P. Garno, Phys. Rev. Lett. **41**, 1509 (1978).

[5] R.A. Riedel and P.F. Bagwell, Phys. Rev. B. **48**, 15198 (1993).

Energy dissipation on moiré patterns on graphene/HOPG

Project P1301 Energy dissipation over structural and electronic phase transitions
Project Leader: E. Meyer and M. Poggio
Collaborators: D. Yildiz (SNI PhD Student), M. Kisiel, U. Gysin and Th. Glatzel

Current status of the research

Bodies in relative motion separated by few nanometers gap experiences a tiny friction force [1]. Although the nature of non-contact friction is not fully understood yet, it can be measured by highly sensitive cantilever oscillating like a tiny pendulum over the surface [2, 3]. Recently series of giant dissipation peaks were reported on $NbSe_2$ surface and associated to nonlinear response of the charge density waves (CDW) [4]. In the $NbSe_2$ the observed CDW has a structural character and it is almost only a periodic lattice deformation (PLD). The problem of friction in similar systems still remains unexplored. As a counterexample to $NbSe_2$ sample we have chosen TaS_2, which also posseses CDW, however mostly electronic in nature. Moreover, a phase transition of TaS_2 between Mott insulating (nearly commensurate CDW) and metallic state (commensurate CDW) depending on the temperature has been reported [5]. One of our goal is also to observe energy dissipation changes while working over the phase transition of TaS_2. We also measured energy dissipation on a Highly Oriented Pyrolytic Graphite (HOPG) sample. Both TaS_2 and HOPG are layered crystals with weak interaction between the layers. Yet the origin of dissipation due to tip - sample interaction is dramatically different.

Implementation of the STM line into pendulum AFM microscope

CDWs are observed on TaS2 at high temperatures and transition from metallic state to Mott insulator is observed at low temperature (5.2 K) [5]. Also super periodic electronic structures are known to be formed on HOPG [6]. In order to observe them the system has to be furnished with a Scanning Tunneling Microscopy. Certain effort regarding the STM implementation was taken and in the final state STM measurements are possible with gold coated cantilevers. Figure 1 shows the AFM/STM microscope and STM topography image of TaS2 surface.

Energy dissipation on TaS_2 and HOPG

Force spectroscopy was performed on $NbSe_2$, TaS_2 and HOPG in order to understand the nature of the interaction between tip and sample. Simultaneous energy dissipation was measured as a function of tip sample distance and voltage. Figure 2 (a) and (b) compares energy dissipation between the oscillating AFM tip and $NbSe_2$ (a) and TaS_2 (b) surfaces. Both crystals exhibit CDW however electronic and structural components of charge density waves are different for these materials. In case of $NbSe_2$ CDW has mainly a structural origin, which manifests itself in a series of dissipation peaks, being a result of hysteretic CDW response to the oscillating cantilever. Energy dissipation on electronic CDW in TaS_2 does not show any peaks. Instead it has smooth behaviour versus distance and bias voltage. In particular, dependence on tip - sample voltage is parabolic which is a clear mark for dominance of electronic channel of dissipation.

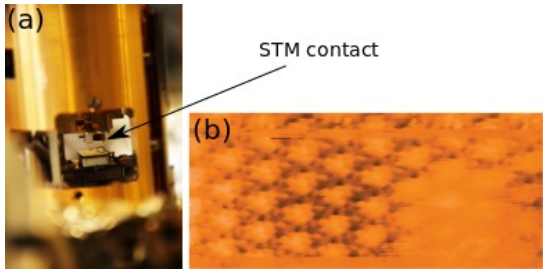

Fig. 1: AFM/STM microscope (a) and STM image of TaS_2 taken at 77K (b). Atomic resolution and CDW's superstructure are visible. The size of the image 5.7 nm x 12.8 nm. Tunneling parameters; I=0.4nA and V=-50mV. Cantilever : ATEC-NC, k=40N/m.

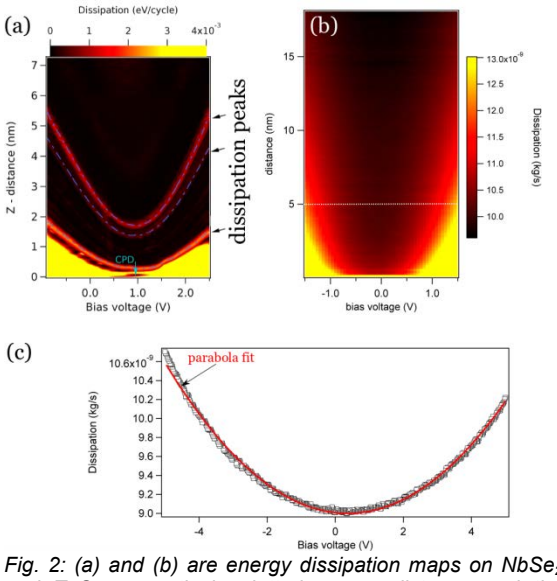

Fig. 2: (a) and (b) are energy dissipation maps on $NbSe_2$ and TaS_2 respectively plotted versus distance and tip-sample voltage. Bright contrast represents high dissipation. Series of dissipation spikes are visible on (a), while for TaS_2 the energy dissipation has a smooth character. Electronic origin of non-contact friction for TaS_2 is shown on (c) where voltage dependent energy dissipation profile Γ (V) for constant tip -sample distance z=5nm is plotted. The measured data obey the relation $\Gamma(V) \sim (V\text{-}V_{CPD})^2$ and the red line is parabola fit to the measured data.

We have shown that there is strong contribution from electrostatic forces acting between the tip and TaS_2 surface to the dissipation. Contrary to TaS_2, almost no electrostatic contribution to friction was observed on clean HOPG surface. Substantial energy dissipation is observed only for close tip – sample distances (<1 nm). Intensity maps of energy dissipation versus tip-sample voltage and distance are shown on Figure 3. They are clearly different from those measured on $NbSe_2$ or TaS_2. While the dissipation signal for TaS_2 strongly depends on the applied bias even for large tip - sample separations, no dissipation signal was observed in the map of HOPG. In particular no real dependence on voltage is observed.

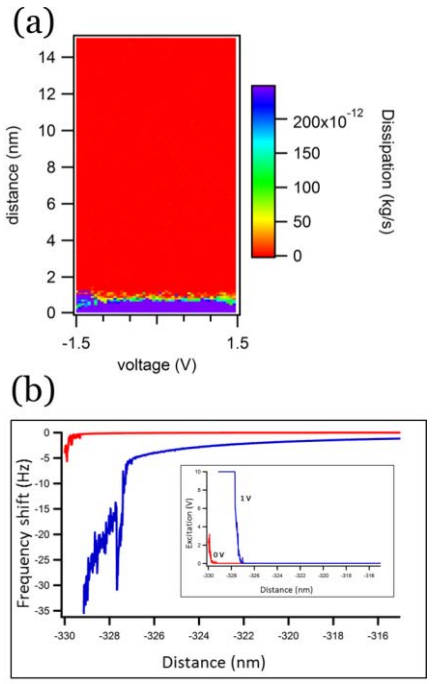

Fig. 3: (a) – energy dissipation map versus tip-sample distance and bias voltage. The map shows lack of dependence of energy dissipation on tip-sample voltage. Therefore, we conclude that the electronic channel of energy dissipation is suppressed. (b) – force versus distance curves for 2 different tip-sample voltages showing that most of tip-sample interaction is due to van der Waals forces.

Our comparitive study of different layered compunds has shown very clear differences in the energy dissipation spectra. The observation might be counterintutitive regarding the fact that all of the materials are thought to be good solid lubricants. Systems with structural CDW cause an enormous rise of energy dissipation due to CDW hysteretic response to the tip perturbation. When CDW changes its character to be electronic-like, we mostly deal with electronic-type of non-contact friction. Finally for HOPG, a material without any CDW, barely any electronic friction can be observed at comparable conditions.

References for Project P1301

[1] A. I. Volokitin, B.N.J. Persson, H. Ueba, *Giant enhancement of noncontact friction between closely spaced bodies by dielectric films and two-dimensional systems,* Journ. Exp. Theor. Phys. **104,** 96-110 (2007).

[2] B. C. Stipe, H. J. Mamin, T. D. Stowe, T. W. Kenny and D. Rugar, *Noncontact Friction and Force Fluctuations between Closely Spaced Bodies,* Phys. Rev. Lett. **87**, 096801 (2001).

[3] S. Kuehn, R. F. Loring and J. A. Marohn, *Dielectric Fluctuations and the Origins of Noncontact Friction,* Phys. Rev. Lett. **96**, 156103 (2006).

[4] M. Langer, M. Kisiel, R. Pawlak, F. Pelligrini, G. E. Santoro, R. Buzio, A. Gerbi, G. Balakrishnan, A. Baratoff, E. Tosatti and E. Meyer, *Giant frictional dissipation peaks and charge-density-wave slips at the NbSe2 surface,* Nature Materials, **13**, 173 (2014).

[5] B. Sipos, A. F. Kusmartseva, A. Akrap, H. Berger, L. Forró and E. Tutis, *From Mott state to superconductivity in 1T-TaS_2 ,* Nat. Mat **7**, 960 (2008).

[6] D. Yildiz, S. Sen, O. Gulseren and O. Gurlu, *Apparent corrugation variations in moiré patterns of dislocated graphene on HOPG and the origin of the van Hove singularities of the moiré system*, (submitted).

Probing the initial steps of bacterial biofilm formation

Project P1302 Dynamic and molecular principles of surface-based cell motility and mechanosensation
Project Leader: T. Pfohl and U. Jenal
Collaborators: N. Sauter (SNI PhD Student) and M. Sangermani

Introduction

We aim to understand the initial steps of bacterial biofilm formation. We study the model organism *Caulobacter crescentus* that has two different stages in its life cycle, it starts as a swarmer cell and develops into a stalked cell after a defined time period or when it comes into contact with a surface. *Caulobacter* swarmer cells adhere to surfaces through their pili followed by an irreversibly binding through the formation of a holdfast [1]. In our studies, we investigate the effect of pili and the beating flagellum to the reversible binding process. For this, we use a custom built set-up for trapping and imaging the cells. To determine which part of the bacteria plays which role in the attaching process, different mutants are used.

Set-up

The experiments are performed using a combined microscope and optical tweezers set-up. It allows for bright field and fluorescence illumination and optical trapping of microobjects. With two steerable IR laser (830 nm), two individual traps are formed. The setup is completed with a camera and a movable stage where microfluidics devices are placed (fig 1). Microfluidics devices allow for a quick and easy handling, exchange of the media and the cells, and experiments can either be performed in chambers in a non-flow environment or under controlled flow conditions in the main channel [2].

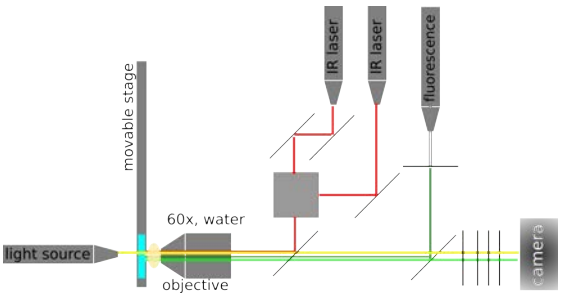

Fig. 1: Set-up, consisting of bright-field and fluorescence illumination, two lasers, generating two independent traps, a movable stage and a camera for imaging.

Optical trap callibration with cells

The stall force of the trap depends on the shape, size and refractive index of the trapped object. The stall force of the tunable laser onto immotile *caulobacter* cells was determined for different currents of the tunable laser via Stokes method. It was found that the stall force that can be exerted onto *caulobacter* cells is up to 2 pN (fig 2). For polystyrene beads, the stall force was found to be up to 20 pN (fig 2, inset).

The size of *caulobacter* cells is comparable to the size of the used beads, the smaller stall force for cells compared to beads might be due to the more rod-like shape and a refractive index closer to the one of water.

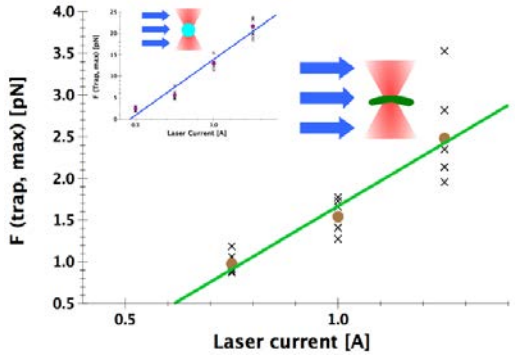

Fig. 2: Stall force for different currents for immotile cells. Inset: Stall force for beads with r = 0.5 µm.

Swarmer cell approaching a surface

With the presented set-up, a wide variety of experiments can be performed. The first experiment is to trap a swarmer cell in one optical trap and approach it to the surface of a colloidal particle (fig. 3). The set-up allows bringing the cells in contact to different surfaces – colloid particles with different surface coatings – in a controlled manner. Our set-up enables the measurement of forces when the bacteria are approached to the surface, of the obstruction of the flagellar motor and in parallel of the exact distances between cell and surface. To trap a swarmer cell, the stall force of the trap needs to be larger than the swimming force of the cell. It was found that the force that is required to manipulate a single swarmer cell is 1.5 pN.

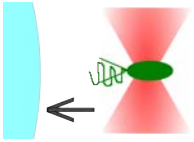

Fig. 3: An optical trap is used to trap a swarmer cell. The trap is then moved towards the surface of the colloid particle. The swarmer cell is allowed to bind to the particle under controlled conditions.

It was found that after a few seconds in the trap, the swimming speed of the swarmer cell is remarkably decreased (fig. 4). Most likely this is caused by phototoxicity, an effect where radicals are formed by photons [3]. We correlate swimming speed with cell viability. If cells swim with the same speed before and after trapping, they are not affected. If their speed is slower after trapping, the cell was affected by radicals. It was found that after 5 s in the trap,

motility of the cell is already decreased. The effect is even stronger when the cell is hold for 10 s in the trap. To investigate the impact of the photons on the cell further, it will be inspected whether the cells regain their initial speed after some recovering time. To prolong the viability of the cell in the trap, we are testing different oxygen scavengers for their effectiveness, for example DMSO, vitamin C and catalase.

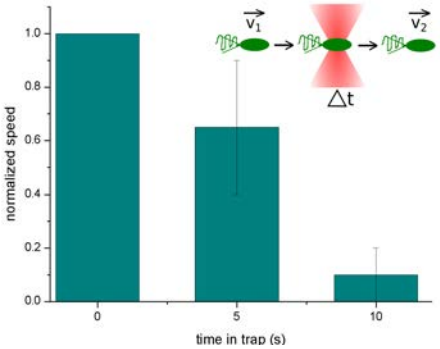

Fig 4: The initial swimming speed of a swarmer cell is measured and compared to the swimming speed after a time Δt in the trap.

Flagellum Forces

To determine the force that is produced by the flagellum, swarmer cells are attaching to beads in solution by themselves. When the daughter cell is produced and its flagellum starts rotating, two different behavior can be observed, depending on whether the bead is hold by a trap or not:

Bead is hold by trap: Due to the beating of the flagellum and because the bead is hold by a trap, the daughter cell is rotating (fig. 5). It was found that the rotation frequency is around 1.5 Hz and is stable for more than a minute.

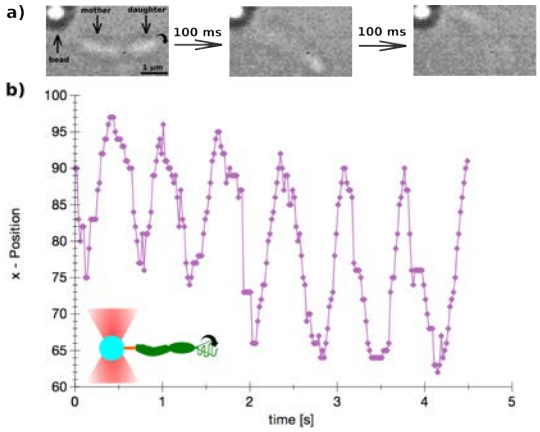

Fig 5 a): Bright field image of a rotating daughter cell. The bead (upper left corner) is hold with a trap. b): Rotation frequency of a mother-bound daughter cell.

Bead is free: When the bead is released from the trap, the daughter cell, the mother cell and the bead are all driven forward by the flagellum (fig. 6). From the speed and the size of the bead, the force generated from the flagellum can be calculated. It was found that the speed of this construct with a bead with a diameter of 1 µm is around 10 µm/s, whereas the speed of a single swarmer cell is up to 60 µm/s.

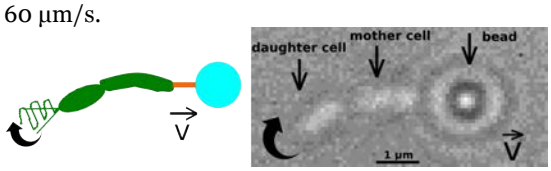

Fig: 6: The rotating flagellum of the daughter cell drives the cells and the bead forward. Speed is around 10 µm/s.

Pili Forces

To investigate the force that can be produced by pili, mutants that only have pili, but no flagellum, are used. The mother cell attaches to the surface of a microfluidics device, then a flow is applied to push the growing daughter cell in a defined direction. A bead is brought into close proximity of the still attached daughter cell with the trap (fig 7). The pili of the daughter cell are reaching out to find a surface where they can attach to and pull towards it. If the pili attach to the bead, the bead is dragged out of the center of the trap. From this, we are able to calculate the force that can be exerted from one or several pili.

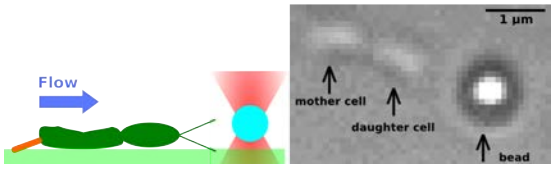

Fig. 7: A mother cell is attached to the surface of a microfluidic device. The daughter cell is challenged with a bead, which is hold in the trap. The pili of the daughter cell are facing towards the bead.

References for Project P1302

[1] D. Bodenmiller, E. Toh and Y. V. Brun, *"Development of surface adhesion in Caulobacter crescentus"*, J. Bacteriol. **186**, 1438 (2004).

[2] E. Stellamanns, S. Uppaluri, A. Hochstetter, N. Heddergott, M. Engstler and T Pfohl, *"Optical trapping reveals propulsion forces, power generation and motility efficiency of the unicellular parasites Trypanosoma brucei brucei"*, Sci. Rep. **4**, 6515 (2014).

[3] M. Koch and A. Rohrbach, *"Object-adapted optical trapping and shape-tracking of energy switching helical bacteria"*, Nature Photon. **6**, 680 (2012).

Molecular muscles: A modular approach

Project P1303 Assembly and investigation of electrochemically triggered molecular muscles
Project Leader: M. Mayor and M. Calame
Collaborators: Y. Aeschi (SNI PhD Student), S. Drayss-Orth and M. Mayor

Mechanically interlocked Molecular Switches

Supramolecular chemistry offers appealing and unique ways to construct highly functionalized, non-covalently linked molecular structures in the nanometer scale by bottom-up approaches. Recognition motifs with high specificity and chemoresponsive features are required to obtain well-defined supramolecular aggregates which could then be integrated into molecular machines. Numerous non-covalent interactions give rise to a large structural diversity of mechanically bonded structures such as rotaxanes and catenanes found in current literature. Several examples of rotaxane and catenane-based molecular switches have been reported in literature, responding to external stimuli such as changes in electrochemical potential, pH or ligand exchange[1,2]. As a subclass of rotaxanes, daisy chains are particularly appealing for the construction of supramolecular systems owing to the self-complementary nature of their monomers[2]. Moreover, the aggregation mode of daisy chains is often concentration-dependent, thus offering the opportunity to obtain either linear or cyclic aggregates by changing concentration[2,3]. Many

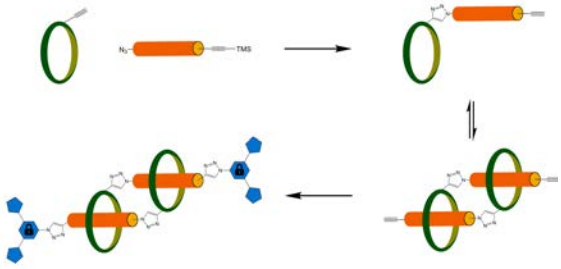

Fig. 1: Stepwise assembly of mechanically interlocked [c2]-daisy chains.

recognition motifs have been applied for the synthesis of daisy chains, the most prominent being crown ether-cation- and cyclodextrin-aryl rod-based systems[2]. The latter system is the most exploited recognition motif for daisy chain assembly in aqueous media. Inspired by *Diederich* et. al. who reported strong complexation of hydrophobic aromatic guests in water by a series of cationic cyclophanes[4,5], our group reported a synthesis towards molecular daisy chains[3], relying on a *Diederich*-type cyclophane as host and a hydrophobic oligophenyleneethynylene (OPE) rod as guest. Our ultimate goal is to introduce functionalities such as redox-active chromophores into the hydrophobic rod component of [c2]-daisy chains in order to integrate them into switchable nanostructures. Current synthetic investigations emphasize the development of a molecular toolbox relying on Cu^{+}-catalyzed *Huisgen* azide-alkyne cycloaddition ("click reaction") to obtain mechanically interlocked daisy chains.

Towards interlocked Daisy Chains

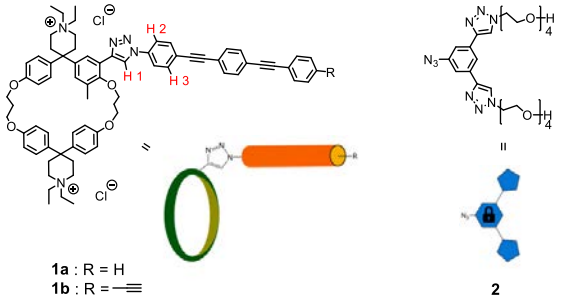

Fig. 2 Structures of daisy chain building blocks and correlation to their schematic representations.

Compound **1a** was synthesized as a model compound to investigate its aggregation behavior in aqueous solution while **1b** should in principle allow to interlock supramolecular aggregates by reaction with bulky stopper **2**. For compound **1a**, ^{1}H-NMR dilution studies were undertaken in D_2O and CD_3CN as co-solvent, which was required as unspecific aggregation in pure water was predominant, resulting in poorly resolved ^{1}H-NMR spectra. Association constants as summarized in **Table 1** were determined by least squares fitting of a dimerization equilibrium to the concentration dependent shifts of aromatic proton resonances.

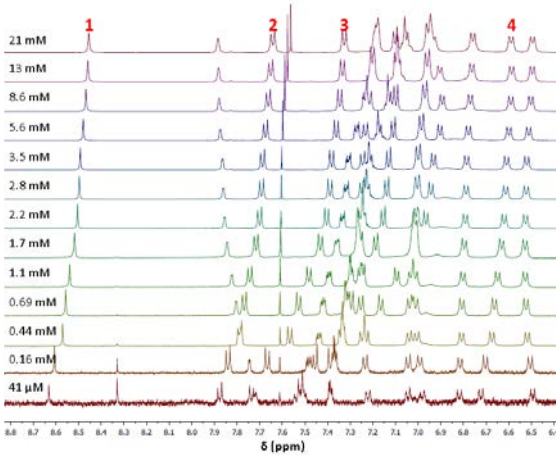

*Fig. 3: Aromatic region of ^{1}H-NMR traces over a dilution series of **1a**. The proton resonances numbered in red were used to determine association constants. Protons 1-3 were assigned as shown in **Fig. 2**, proton 4 is located ortho to one of the arylic ethers.*

Figure 3 shows the peaks in the aromatic region over a typical dilution series in. A strong upfield shift was observed for proton 3, while protons 1,2 and 4 showed weaker upfield shifts. Least squares fitting of the concentration dependent chemical shifts data revealed association constants of 750 M^{-1} up to 1580 M^{-1}, which varied depending on the

proton which was analyzed. Aggregation numbers were determined within a range of 1.91 to 2.01 by the same method we applied in our earlier work[3], indicating that dimeric structures are formed by **1a**.

Proton	K_a M^{-1}	σ M^{-1}
1	750	± 160
2	1220	± 100
3	1580	± 150
4	970	± 60

Table 1: Association constants obtained for aromatic protons 1-4 shown in Fig. 3

For compound **1b** an association constant in an order of magnitude similar to **1a** was assumed, which could be underpinned by a preliminary dilution experiment. Detailed dilution studies were not conducted due to stability concerns with of the free acetylene. For capturing interlocked daisy chains, equimolar amounts of **1b** and stopper **2** in concentrations ranges from 0.5 to 5 mM were examined, using a catalytic amount of $CuSO_4$/sodium ascorbate. The experiments were analyzed by LC-MS and TLC. A reference experiment was conducted in MeOH, in which only negligible aggregation can be expected thus rendering a stoppered monomer. All experiments reactions were indifferent from the reference reaction, which suggests that **1b** undergoes extracavitary association such as *e.g.* stacking of the OPE rods, thus giving non-interlinked dimers in solution and eventually rendering stoppered monomers.

New Design

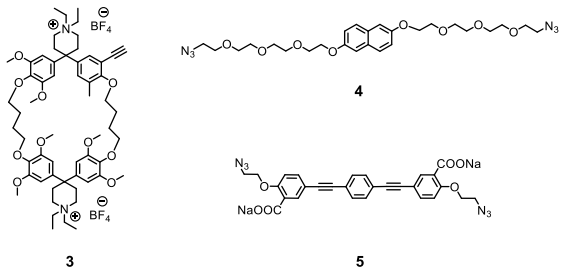

Fig. 4: Structures of the new building blocks

As no interlocked aggregate could be obtained from **1b**, a novel molecular design was elaborated, relying on a cyclophane receptor with higher binding strength and lower tendency of self-aggregation as well as choosing more hydrophilic rod components. A 10-step synthetic route to acetylene-functionalized cyclophane **3** was developed, which is decorated by six methoxy groups. These are known to deepen the hydrophobic cavity and to decrease the self-association of the receptor[5]. **4** and OPE-rod **5** were synthesized as rod components in 3 and 5 reaction steps respectively. Guest **4** comprises a hydrophobic naphthalene core linked to hydrophilic tetraethylene glycol chains, which should prevent homo-aggregation of the hydrophobic part. Guest **5** is designed such that it is water-soluble due to the presence of two ionic carboxylate groups which are remote from the central hydrophobic phenylene unit. Synthesis of the hermaphroditic cyclophane-rod compounds can achieved by reacting **3** with an excess of the rod component.

Balancing hydrophobic and hydrophilic properties is expected to provide the necessary topological features such that that an intracavitary association mode will be predominant. Furthermore, this will eliminate the necessity of a co-solvent such as MeOH or MeCN which drastically lowers association constants.

Investigation on the aggregation behavior of hermaphroditic compounds obtained from **3** with **4** or **5** is currently ongoing.

References for Project P1303

[1] M. C. Jiménez, C. Dietrich-Buchecker and J-P. Sauvage, *"Towards Synthetic Molecular Muscles: Contraction and Stretching of a Linear Rotaxane Dimer"*, Angew. Chem. Int. Ed, **39**, 3284 (2000).

[2] J. Rotzler and M. Mayor, "Molecular daisy chains", Chem. Soc. Rev, **42**, 44 (2013).

[3] J. Rotzler, S. Drayss, D. Häussinger, O.Hampe and M. Mayor, *"Molecular Daisy Chains: Syn-thesis and Aggregation Studies of an Amphi-philic Molecular rod"*, Chem. Eur. J, **19,** 2089 (2013).

[4] F. Diederich, K. Dick and D. Griebel, "Water-soluble tetraoxa[n.1.n.1]-paracyclo-phanes: Synthesis and host-guest interactions in aqueous solution", Chem. Ber, **118**, 3588 (1985).

[5] S.B. Ferguson, E.M. Sanford, and F. Seward, *"Cyclophane-arene inclusion complexation in protic solvents: solvent effects versus electron donor-acceptor interactions",* J .Am. Chem. Soc, **113**, 5410 (1991).

Mechanisms of outer membrane protein folding

Project P1304 Folding mechanisms of beta-barrel outer membrane proteins and their catalysis by natural holdases and foldases
Project Leader: S. Hiller and D.J. Müller
Collaborators: P. Rios Flores (SNI PhD Student), T. Raschle, J. Thoma and B.M. Burmann

β-barrel outer membrane proteins (Omps) are essential functional components of the outer membrane of Gram-negative bacteria, mitochondria and chloroplasts. Their biogenesis poses a complex biophysical challenge to the cell, which is accomplished by several molecular chaperones that pass the unfolded substrates from the ribosome to the destination membrane [1,2]. Because Omps can refold *in vitro* without the help of chaperones into the same three-dimensional β-barrel structures, investigations of the *in vitro* folding pathways yield important biophysical benchmark data. The in-vitro and the in-vivo folding mechanisms of β-barrel Omps from mitochondria or Gram-negative bacteria are so far not understood at atomic resolution.

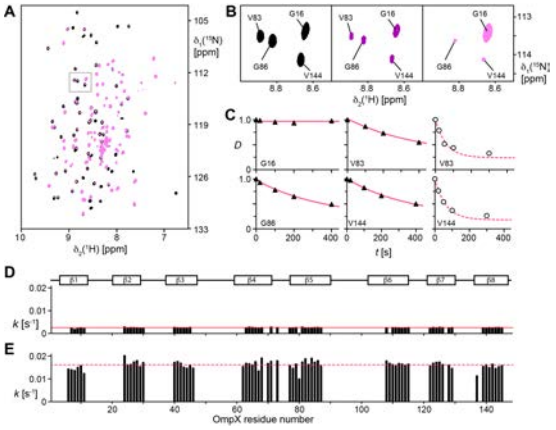

Fig. 1: Residue-specific hydrogen bond formation kinetics of OmpX folding as monitored by high-resolution NMR spectroscopy in combination with H/D-exchange. (A) 2D [^{15}N,^{1}H]-TROSY spectra of OmpX in LDAO micelles. Black: Spectrum after folding in H_2O-based buffer. Magenta: Spectrum after folding in D_2O-based buffer with a folding time T = 400 s. Peak intensities vary due to the differential incorporation of deuterium at the backbone amide position. (B) Enlargement of a spectral region containing four resonances at different folding times. Black: T = 0, purple: T = 100 s, magenta: T = 400 s. (C) Hydrogen bond formation kinetics during folding for the amino acid residues shown in (B). The experimental data (symbols) have been fitted to single exponentials (red lines). Black triangles and solid lines: Folding into DPC detergent; White circles and dashed lines: Folding into LDAO detergent. (D, E) Residue-specific hydrogen bond formation kinetics for OmpX folding into (D) DPC detergent and (E) LDAO detergent. The horizontal lines indicate the average value for the measured rate constants. The secondary structure of folded OmpX with eight β-strands β1– β8 is indicated. Adapted from [4].

Hydrogen-deuterium (H/D)-exchange labeling is a very powerful technique to characterize folding pathways at the atomic level, but it has so far been well established only for soluble proteins [3]. We have developed the technical setup and biochemical protocols to allow application of this methods for the first time to an integral membrane protein, the β-barrel outer membrane protein OmpX [4]. Protein refolding is initiated by rapid dilution of a denatured protein sample with micelle solution. After a variable folding time τ, the buffer is rapidly mixed with a larger volume of D_2O. In the folded state, all amide protons involved in the β-barrel are strongly protected with exchange times of the order of weeks or longer and we can thus quantify the proton occupancy for each residue in the β-barrel using 2D [^{15}N,^{1}H]-TROSY NMR experiments (Figure 1). In addition, the same samples can also be quantified by mass spectrometry, yielding essentially single-molecule quantification of the deuteration degree.

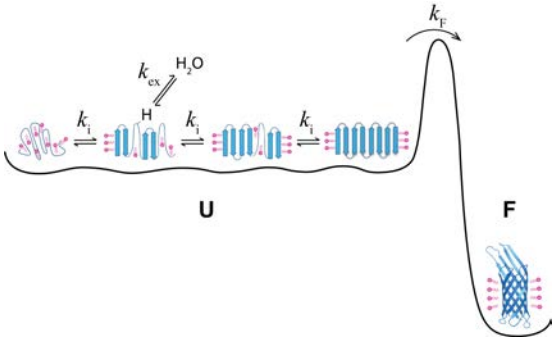

Fig. 2: Free energy diagram for OmpX folding into detergent micelles. Upon rapid dilution from a denatured state, OmpX associates with detergent micelles to a dynamic conformational ensemble state (U). Four arbitrary conformations are shown in cartoon representation, as representatives for the dynamic ensemble. In this state, multiple conformations rapidly interconvert with kinetic rate constants k_i. No long-lived hydrogen bonds are formed, so that all backbone amides are effectively accessible to chemical exchange (k_{ex}) with the solvent. The folded state of OmpX (F) is separated from the conformational ensemble by a rate-limiting folding step with a kinetic rate constant k_F on the minutes time scale. Adapted from [4]

This combination of NMR spectroscopy and mass spectrometry describes the kinetics of hydrogen bond formation during Omp folding and can, at the same time, differentiate between different folding mechanisms. In particular, it can discriminate slow from rare mechanisms. We found that folding of the outer membrane protein X (OmpX) from *E. coli* in detergent micelles propagates via a conformational ensemble state in which backbone amide protons form hydrogen bonds transiently and are thus accessible to rapid exchange with the solvent (Figure 2). OmpX folds from this ensemble by a rate-limiting, irreversible monomolecular reaction, with slow kinetics on the minute scale. Stable formation

of the hydrogen bond network occurs downhill of the rate-limiting transition state and thus appears cooperative on the overall folding timescale. OmpX folding is thus a rare, not a slow event. It is the first time that this folding mechanism could be unambiguously demonstrated for a β-barrel membrane protein.

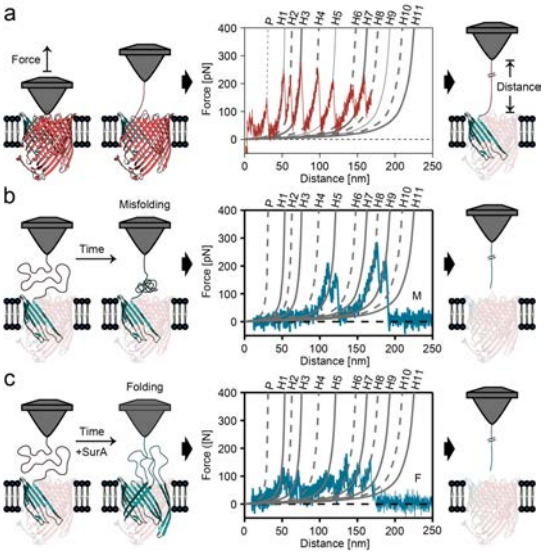

Fig. 3: Application of atomic force spectroscopy to characterize chaperone-modulated refolding of individual FhuA molecules into the E. coli lipid membrane. (a) Partial FhuA unfolding by single-molecule AFM. The AFM tip attaches to the N-terminal plug domain of membrane-embedded FhuA. Subsequent retraction of the tip applies a mechanical pulling force, which induces FhuA unfolding. The force-distance curve records this process with each force peak detecting an unfolding step of FhuA. The part of FhuA unfolded (β-hairpins H1–H8) is colored red and the part remaining embedded in the membrane (β-hairpins H9–H11) is colored blue. (b) and (c) Subsequent to the partial unfolding, the AFM tip is re-approached towards the lipid membrane at a distance of ≈10 nm. The unfolded polypeptide can then relax for a refolding time in the range 0.1–10 s in the absence (b) or presence (c) of chaperones. During this time the polypeptide can possibly reinsert and fold into the lipid bilayer. Subsequently, the tip is retracted to characterize the emerging protein structure by force-distance measurements. In (b), force peaks not coinciding with native FhuA positions, indicate misfolding (M) of the protein. In (c), refolding in the presence of the holdase chaperone SurA results in force peaks showing native FhuA positions, indicating proper folding intermediates (F) of the membrane protein. Adapted from [5].

In a next step, we have used single-molecule force spectroscopy and NMR spectroscopy to observe how the periplasmic holdase chaperones SurA and Skp shape the folding trajectory of the large β-barrel outer-membrane receptor FhuA from *Escherichia coli* (Figure 3, [5]). Either chaperone prevents FhuA from misfolding by stabilizing a dynamic, unfolded state, thus allowing the substrate to search for structural intermediates. During this search, the SurA-chaperoned FhuA polypeptide inserts β-hairpins into the membrane in a stepwise manner until the β-barrel is folded. The membrane acts as a free-energy sink for β-hairpin insertion and physically separates transient folds from chaperones. This stabilization of dynamic unfolded states and the trapping of folding intermediates funnel the FhuA polypeptide toward the native conformation. Overall, the combination of NMR spectroscopy and AFM experiments has provided unique insights into the folding mechanism of β-barrels and has helped us to characterize factors that control and support the insertion and folding of membrane proteins into membranes in general terms.

References for Project P1304

[1] T.J. Knowles, A. Scott-Tucker, M. Overduin and I.R. Henderson, *"Membrane protein architects: the role of the BAM complex in outer membrane protein assembly"*, Nat. Rev. Microbiol. **7**, 206 (2009).

[2] J.G. Sklar, T. Wu, D. Kahne and T.J. Silhavy, *"Defining the roles of the periplasmic chaperones SurA, Skp, and DegP in Escherichia coli"*, Genes Dev. **21**, 2473 (2007).

[3] H. Roder, G.A. Elöve and S.W. Englander, "*Structural characterization of folding intermediates in cytochrome c by H-exchange labelling and proton NMR"*, Nature **335**, 700 (1988).

[4] T. Raschle, P.R. Flores, C. Opitz, D.J. Müller and S. Hiller, *"Hydrogen bond formation in b-barrel membrane protein folding"*, Angew. Chem. Int. Ed., in press (2015).

[5] J. Thoma, B.M. Burmann, S. Hiller and D.J. Müller, "*Impact of holdase chaperones Skp and SurA on the folding of β-barrel outer membrane proteins*", Nat. Struct. Mol. Biol. **22**, 795 (2015).

Ultrathin membranes as packaging of protein crystals for X-ray crystallography at free electron lasers

Project P1305 X-FEL based dynamic studies on 2D and 3D nanocrystals of membrane proteins on solid supports
Project Leader: C. Padeste and H. Stahlberg
Collaborators: N. Opara (SNI PhD Student); T. Braun, S. Arnold, P. Ringler, M. Chami (C-CINA, Biozentrum); X.D. Li, B. Pedrini and I. Martiel (PSI)

To date, synchrotron radiation-based crystallography has been the most efficient approach to determine the structure of proteins, which represent the most important class of macromolecules. This method is, however, limited to well-diffracting 3D crystals, which are in many cases very difficult to obtain in large enough sizes to produce sufficient diffraction intensities. The advent of the novel large-scale facilities such as free electron lasers (XFELs) provides new opportunities for solving protein structures from protein nanocrystals or even from 2D crystals at high-resolution at room temperature or at cryo-conditions. The novel method called "serial femtosecond crystallography" is based on collecting diffraction patterns from large numbers of small crystals using the ultra-bright and femtosecond-short radiation pulses of XFELs.

The solid-support approach to sample delivery for XFEL experiments is especially advantageous when the amount of available crystalline protein material is limited, and when the commonly used liquid jet injector systems lead to too high losses of the precious specimens [1]. Fine grid structures holding membranes, on which the protein sample is deposited, were successfully used for measurements of both, 2D and 3D crystals [2, 3].

This project aims at the optimization of solid supports towards lowest possible X-ray absorption and scattering background, optimization of *in-situ* crystallization methods and sample deposition for minimized sample consumption. Furthermore it includes the development of support systems that maintain an environment of controlled humidity to prevent the water-containing protein crystals from drying out and denaturing before and during the measurement.

Silicon nitride membranes with thicknesses below 100 nm were produced from silicon-nitride coated silicon wafers using standard microfabrication techniques. They provide low background, suitable even for measurements of 2D crystals. Since the material is very brittle, limited in achievable probing area and density as well as relatively expensive when used for high-throughput applications, polymer-based alternatives are of high interest.

While the X-ray absorption can be calculated from the chemical composition, density and the thickness of a membrane, the diffuse scattering due to short- and medium-range order inside the material has to be accessed experimentally (Fig. 1.).

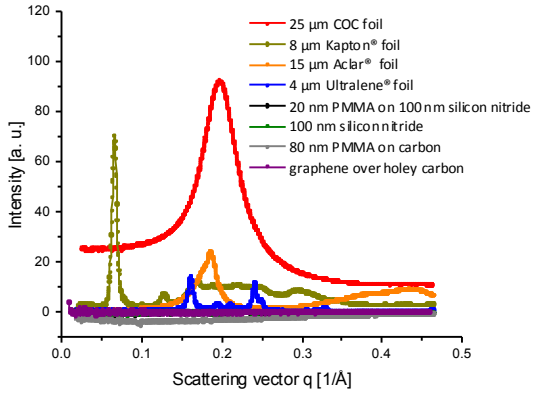

Fig. 1: Intensity of X-ray scattering from ultrathin membranes of various materials at a photon energy of 12.7 keV. Comparison of commercially available thin foil materials (polymers: Kapton, Ultralene, Aclar, COC) and self-fabricated "zero-background" solid supports out of Si_3N_4, carbon and reinforced with PMMA. (Data collected at PX-beamline, SLS).

Foils of different polymers commercially available in thicknesses between 4 and 25 µm all gave substantial background in the scattered intensity, indicated as broad bands at characteristic q-values for each polymer. In contrast, sub 100-nm layers of PMMA and in particular of graphene supported on holey carbon films resulted in basically "zero" background over the whole range of q-values relevant for protein crystallography.

Watertight packing of relatively large protein crystals directly grown on silicon nitride supports was investigated in the frame of a series of time-resolved measurements at the free electron laser facility (LCLS) located at Stanford University. A high density of large lysozyme crystals was achieved by *in-situ* crystallization (Fig. 2.). A lysozyme solution was deposited in the wells of microfabricated silicon nitride membrane chips and crystals were grown via solvent evaporation in a sealed chamber containing a compartment filled with concentrated precipitant solution. To prevent drying-out of the crystals during the measurement, a second chip with slightly bigger windows was placed over the crystal-loaded chips and sealed with a double-sided adhesive tape (Fig. 3). This sandwich-type arrangement kept the crystals humid for at least a few hours. Evaluation of the data collected in these experiments is still going on.

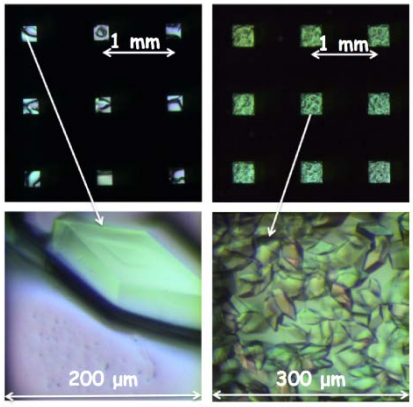

Fig. 2: Large protein crystals directly grown on silicon/silicon nitride chips. The size and density of the crystals have been optimized for a special time-resolved measurement.

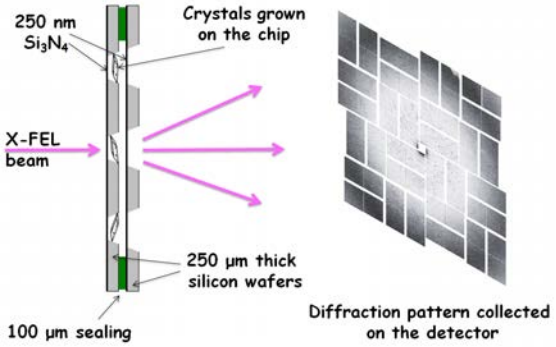

Fig. 3: Sandwich arrangement of protein crystals between two silicon nitride window-chips for X-ray diffraction studies. The sealing with adhesive tape is sufficient to maintain the humidity constant for a few hours before the measurement.

Due to the very high intensity of the X-ray pulses produced at XFELs useful diffraction intensities may be obtained from crystals that are too small for synchrotron-based measurements. Since every crystal can be probed just once, knowledge of the exact positions of the protein crystals on the support can significantly speed up data collection at FELs. Pre-characterization of samples may be achieved with electron microscopy to determine the coordinates of the deposited or grown crystals along with initial testing of their diffraction properties.

The sample shown in Fig. 4 was obtained by deposition of nanoliter volumes of a suspension of lysozyme nanocrystals grown on a standard crystallization plate. Prior to deposition the sample was incubated in a sugar solution aiming at preservation of diffraction properties while desalting the mother liquor surrounding the crystals. Handling of the nanoliter volumes of such material requires a high-humidity environment and cooling to the dew point to lower the evaporation rates.

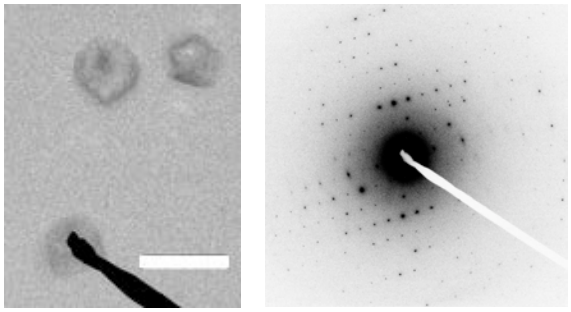

Fig. 4: A) Lysozyme nanocrystals deposited on a TEM grid (scale bar – 1 µm). B) Electron diffraction pattern of as single crystal. Lysozyme was used as a model protein since it is readily forming 3D crystals of different sizes in broad spectrum of chemical conditions.

Depending on the protein and intended measurement strategy, *in-situ* crystallization or deposition of pre-grown crystals may be favored. However, both methods require low-absorption and low scattering background supports [4] and careful control of humidity and temperature during sample preparation processes.

References for Project P1305

[1] I. Schlichting, *"Serial femtosecond crystallography: the first five years"*, IUCrJ. **2**, 246–255 (2015).

[2] S. Boutet *et al.*, *"High-Resolution Protein Structure Determination by Serial Femtosecond Crystallography"*, Science **337**, 362 (2012).

[3] M. Frank *et al.*, *"Femtosecond X-ray Diffraction from Two-Dimensional Protein Crystals"*, IUCrJ **95**, 1 (2014).

[4] G.K. Feld, *Low-Z polymer sample supports for fixed-target serial femtosecond X-ray crystallography*, J. Appl. Cryst. **48**, 1072–1079 (2015).

Nano-pills for mosquitoes to interrupt malaria transmission

Project P1306 Slow-release nano-pills for mosquitoes for interrupting malaria transmission
Project Leader: P. Hunziker and R. Brun
Collaborators: D. Gonçalves (SNI PhD Student), X. Wang, K. Liu, P. Müller and M. Rottmann

Introduction

Malaria remains one of the top tropical and infectious diseases in the world, both in terms of morbidity and mortality, with an estimated more than two hundred million clinical cases every year (WHO report 2014). In recent years, the mosquito stages of the parasite life cycle have received a renewed attention with some progress being made in the so-called Transmission Blocking strategies (TBs). Some attractive targets are the stages in the mosquito midgut where a population choke point occurs, going to as few as 1-5 plasmodia per mosquito [1].

A new radical approach is being studied to use self-assembly polymers to form drug-carrier nanoparticles (NPs) [2], to design a setup to lure mosquitoes into ingestion [3], that would clear, or at least reduce, the parasite density to levels that would render it non-infective and interrupt the disease transmission and propagation. Having a mosquito survival strategy can avoid selective pressure towards the drug-free mosquitoes and by designing nanoparticles to be stage specific and with a slow-release mechanism one will hopefully be able to reduce locally the parasite reservoir in the field, and by exposing the least plasmodium possible to drugs, reducing the likeness of resistance to arise. Finally, this approach avoids the cost and ethical constraints of TBs in humans, and will allow the use of more effective new molecular entities (NMEs) and alternative anti-malarial drugs that for several reasons could not be used in humans.

As proof-of-concept we propose to address a series of goals to validate this strategy:

- design a nanovector, non-toxic for the mosquitoes, that can easily encapsulate a drug of choice and be prepared in situ [4];
- tuning targeting and release system towards specific parasites stages and mosquito tissues;
- screen the best antimalarial candidates taking in to account efficacy, affordability, encapsulation compliance and environmental impact;
- design a highly stable setup, able to endure on the open in tropical settings and maintaining its critical properties;
- predict the impact in Malaria transmission by means of modulation and statistical tools based in laboratory collected data.

Here we report some of the data collected to address the first three milestones.

Results and Discussion

Nanoparticles encapsulation and stability

The stability of NPs was assessed by DLS measurements (size monodispersity) before feeding to mosquitoes. In parallel one NP (self-assembled from functional terminated ABA block-copolymers(table 2) was used as stability model by preparing 0,5 mg/ml in 10 ml of sugar water (same setups used for feeding) that was left at 25ªC and 70% Hr in the environmental chamber during three weeks. One sample per week was taken for polidispersity measurments with DLS with no significant changes in size. The pH sensitivity to midgut and salivary glands environments was also tested in PBS with DLS measurements after two days suggesting no rupture.

Table 2. Library of NPs from blockcopolymers used for Localization and Release studies.

ID	Termination	hydrophilic	hydrophobic
1	T1	A1	B1
2	T1	A3	B1
3	T2	A1	B1
4	T2	A3	B1
5	T3	A3	B1
6	T3	A3	B1
7	T4	A2	B1
8	T4	A4	B1
9	T5	A2	B1
10	T5	A4	B1
11	T6	A2	B1
12	T6	A4	B1
13	T7	A2	B1
14	T7	A3	B1

Non-infected mosquitoes toxicity experiments

By using duplicate cages with random samples of female mosquitoes at same environmental conditions and feeding protocol one was able to compare the impact of nanoparticles in survivability and also their preferential localization by sacrificing random mosquitoes (3 samples every 6 days for all cages including control, 3 days after feeding NPs) along time for fluorescence imaging, first alive with

the stereoscope adapted with a fluorescent kit and then in a confocal microscope. The interval between NPs feedings was designed taking in account previous experiments with NPs with fluorescent dyes (RB and fluorescein) fed at different days and the predominance showing that for the first three days there is strong predominance of fluorescence whit a sharp drop at the 4th day without a reefed and practically non existent in most of the samples after six days. To evaluate the statistical significance of the results a ANOVA covariance analysis was performed using the count of surviving mosquitoes for each day during 4 to 5 weeks to test the null hypothesis of NPs having no impact in mosquito survival.

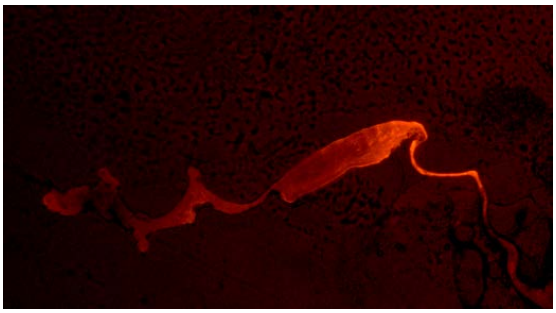

Fig 1: Dissected mosquito fed with fluorescent nanoparticle.

Impact of NPs and drug to infected mosquitoes

To accurately assess the impact of our nanosystem and in particular the efficacy of certain drug in clearing parasites in the mosquito stages and avoid transmission to another host, a complete Malaria life-cycle model was established to follow parasites numbers at different stages and assess transmission rate. *P. berghei* parasites, an exclusive rodent infecting strain genetically modified to express a fluorescence protein (m-cherry) and luciferin when fed with the appropriate substrate was chosen and the mosquito vector Anopheles stephensi were chosen. The goal is to create a scalable model representative of the potential impact and toxicity of different drugs and nanosystems.

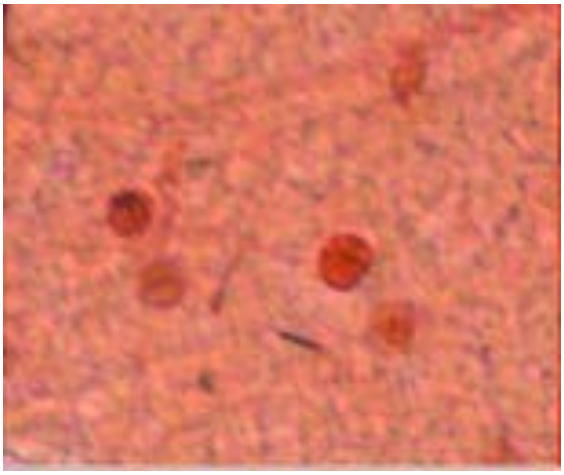

Fig. 2: Oocysts stained with mercurochrome at day 10

Two days after infection, mosquitoes were fed with NPs and methylene blue, on day 10 some of them were sacrificed for oocyst count and compared with same number of mosquitoes non fed in NPs. The remaining were left until day 20 were all of them were sacrificed for sporozoites estimation (counting of purified salivary glands in a 10uL PBS) and also cryostat sectioning and absorbance readouts in a ELISA Reader (no conclusions could be made due to Rhodamine b and . The reason of choosing methylene blue as model drug was the partial solubility in water, known antimalarial activity for mosquito stages and its ability to be seen at naked eye.

Orthogonal Methods

Using alternative and orthogonal analytical methods for NPs quantification might also increase the strength of the data, such as UV absorbance (ELISA reader) of mashed mosquitoes, mass spectrometry and HPLC protocols are being pursued.

Release

NPs with encapsulated Rhodamine-PDMS were prepared with different concentrations for further fluorescence quenching studies to determine the optimal loading for release studies in the mosquito. A protocol for release measurements using UV absorption and dialysis membrane is also being established for atovaquone and methylene blue as model drugs.

Summary and outlook

The project is now in the phase II of the initial proposal. The concept has been tested and an experimental model established. The nanoparticles are being optimized and release systems are currently under study. The next steps is to scale the current model and determine a stochastic model relating the decrease of mosquito infection levels with the transmission of parasites to the rodent host ; developing an automated imaging setup to acquire fluorescence signal from large populations of mosquitoes at once and in situ ; and testing different setups for field applications including attractants and volatiles to attract mosquitoes.

References for Project P1306

[1] Ranford-Cartwright, "*Spreading the seeds of million-murdering death: metamorphoses of malaria in the mosquito"*, TRENDS in Parasitology, 573-580 (2005).

[2] P. Broz, "*Nanotechnologies for targeted delivery of drugs"*, Wiley-VCH, 3731-3732 (2007).

[3] B.G.J. Knols, "*Odour-mediated host-seeking behaviour of the Afro-tropical malaria vector Anopheles gambiae Giles",* Parasitology Today, 159–161 (1996).

[4] K. Liu, "*Microfluidics-based single-step preparation of injection-ready polymeric nanosystems for medical imaging and drug delivery",* Nanoscale, 16983-16993 (2015).

Fabrication of nanojunctions and molecules testing for optoelectronic experiments

Project P1307 Optoelectronic nanojunctions
Project Leader: M. Calame and M. Mayor
Collaborators: J. Overbeck (SNI PhD Student), S. Neumann and O. Wenger

Introduction

In this project, we want to investigate the opto-electronic properties of nanometer-scale junctions consisting of organic molecules within two contacting electrodes. Building on our previous work [1] with mechanically controllable break junctions (MCBJ), optoelectronic phenomena promise to provide new insights into these systems [2]. To this end, a new break junction setup was designed to fit into multiple optical microscope setups. We have investigated modifications to the sample design to incorporate graphene as an electrode material and exploit plasmonic effects that can be tuned through the mechanically controlled electrode separation.

Sample fabrication

Graphene has recently attracted increasing interest as an electrode material for molecular electronics [3,4]. It opens in particular new possibilities in terms of electronic coupling control and mechanical stability. However, incorporating graphene into a suitable geometry for break junction measurements requires its mechanical stabilisation and its protection from adverse influences during fabrication. Towards that end, we follow an approach leading to a self-aligned graphene structure by encapsulating a layer of graphene between a lithographically patterned double-layer gold junction. In this structure, the gold protects the graphene from both sides during reactive ion etching required to suspend the junction (see Fig. 1). The same etching process removes the surplus graphene to shape it into the desired geometry while the gold acts as a support structure and contact electrode.

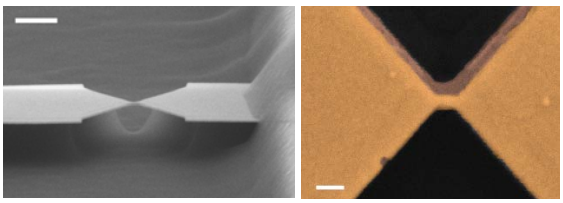

Fig. 1: ***Left****: Scanning electron micrograph of a lithographically defined break junction with underetched junction area. Scale bar 1 µm.* ***Right****: Top-view of a precisely aligned double layer junction. The lower layer junction is the narrower and brighter part of the constriction with an overlay structure roughly twice as wide (reddish colouring). Scale bar 200 nm.*

Currently these sandwich junctions incorporating graphene are being characterized and will next be used to measure molecules that bind selectively to gold or graphene.

Recently, we have started to investigate an alternative approach to fabricate suspended break junctions by using a sacrificial layer of lift-off resist (LOR, cf. Fig. 2 *left*). This technique has been successfully employed to fabricate suspended graphene samples [5]. A major advantage of the protocol is that it does not require the fabrication of a precisely aligned double junction and allows adjusting the suspended area with more flexibility.

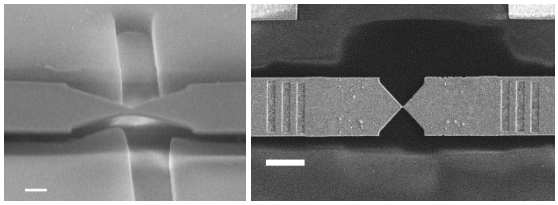

Fig. 2: ***Left****: Scanning electron micrograph of a break junction on LOR with removed resist area defined by e-beam lithography. Scale bar 400 nm.* ***Right****: SEM image of a break junction with optical gratings milled into the leads by focused ion beam. Scale bar 2 µm.*

Another requirement for performing optoelectronic experiments besides precisely defined electrodes is the ability to couple light to and from the sample. As a starting point, we are adapting a design (cf. Fig. 2 *right*) for which transmission of optically excited plasmons through a nano-constriction was reported [6]. This geometry is being optimized to enable the study of light emission from plasmonic excitations propagating along the junction leads. The plasmonic exicitations shall be launched electrically by electrons tunneling through the gap of a broken junction under a given applied bias voltage [7]. Here, we will strive to correlate the characteristics of the radiatively decaying plasmon (intensity, spectral properties) with the electronic signatures of the tunnel junction at which the plasmon is being generated. While recent evidence supports the possibility to modulate quantum plasmonic tunneling between plasmonic resonators separated by a molecular layer [8], our design is expected to provide further mechanical tunability to explore the tunneling regime and additional flexibility to vary the molecular junction.

Setup for optoelectronic measurements

In order to perform optoelectronic break junction measurements, a more compact setup had to be designed that allows coupling of light to the sample and collection of light from it in a microscope. The geometrical constraints and requirements of mechanical stability during optical measurements introduce significant challenges. Currently, a prototype setup is being built and tested. Initial experiments will test the mechanical stability and

optical access without the need for simultaneous driving and stable positioning of the microscopes focal point. These functionalities will be added at a later point. Furthermore, the new design will allow us not only to mechanically break the junction by tensile strain but will also allow inverse bending to produce compressive strain to close an initially existing gap, opening up possibilities for a variety of experiments. The later aspect is in particular important to implement for graphene-modified junctions where a possible shrinking of the junction after opening has to be anticipated.

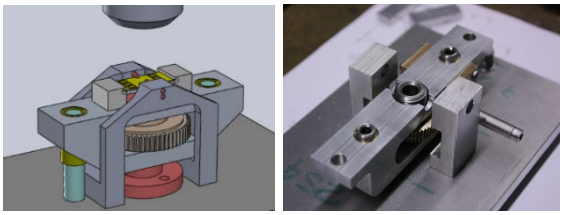

*Fig. 3: **Left**: CAD-design for the new prototype currently being built. **Right**: Picture of the central mechanical assembly with test clamps.*

Charge transfer versus charge transport in molecular systems

In addition to investigating the optoelectronic signatures of molecular junctions with simple (available) compounds, we study the possibility to design optically addressable molecules to be integrated within the junctions. We have established a complementary collaboration with the group of O. Wenger in a project to investigate the dynamics of charge transfer and charge transport in molecules. Here, donor-acceptor systems will be studied to compare photoinduced charge transfer with electrical transport properties. Towards that end, measurements were carried out on the intended molecular backbone (cf. P1406, compound 5) for future Ru-based photoactive molecules and a reference molecule, both with pyridine anchor groups.

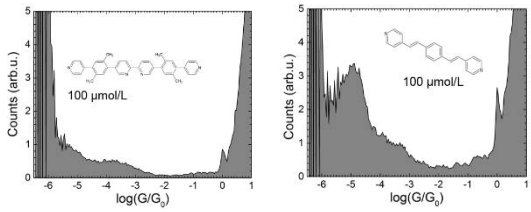

*Fig. 4: Normalized 1D logarithmic conductance histograms for molecules measured in chloroform solvent at 100 µmol/L concentration. **Left**: Histogram for the molecular backbone, 346 traces. **Right**: Histogram of a phenylene vinylene based reference molecule, 275 traces.*

Reference compounds synthesized in the group of M. Mayor where characterized as well for comparison with the new molecular structures being designed.

Outlook

The next steps will consist in testing and validating the optoelectronic setup, in particular for the light collection efficiency and intensifying measurements on the newly available junction geometries.

Acknowledgements

We thank Anton Vladyka for his support with measurements in solvent and data analysis, Kishan Thodkar for help in growing graphene, Axel Fanget for help in optimizing the electron-beam lithography process, Clevin Handschin for help with the focused ion beam milling, Peter Makk for fruitful discussions and Heinz Breitenstein for support with the new setup.

References for Project P1307

[1] See e.g. Z. Li *et al.*, J. Am. Chem. Soc., **136**, 8867 (2014); J.Brunner *et al.*, J. Physics: Cond. Matt., **26**, 474202 (2014); S. Wu, *et al.*, Nature Nanotech. **3**, 569 (2008).
[2] M. Galperin and A. Nitzan, Phys. Chem. Chem. Phys. **14**, 9421 (2012).
[3] F. Prins *et al.*, Nano Lett. **11**, 4607 (2011); C. Nef et al., Nanoscale **6**, 7249 (2014).
[4] C. Jia *et al.*, Acc. Chem. Res. **48** (9), 2565 (2015).
[5] R. Maurand *et al.*, Carbon **79**, 486 (2014).
[6] D. Benner *et al.*, New J. Phys. **15,** 113014 (2013).
[7] P. Bharadwaj *et al.,* Phys. Rev. Lett. **106** (22), 6802 (2011).
[8] S.F. Tan *et al.*, Science **343**, 1496 (2014).

Two-dimensional calixarene-based metal coordination organic networks

Project P1308 Supramolecular charge and spin architectures produced by chemical clipping
Project Leader: P. Shahgaldian and T. Jung
Collaborators: M. Moradi (SNI PhD Student) and L. Tulli

Introduction

Metal-directed self-assembly has emerged as a highly efficient chemical strategy to design supramolecular nanomaterials with applications in a large variety of scientific disciplines ranging from molecular electronics to nanomedicine [1].

Metal-organic frameworks (MOFs) are crystalline materials assembled by attaching metal-containing units with organic linkers to create open crystalline frameworks [2]. MOFs typically exhibit a tremendous porosity, which opens a wealth of potential uses for MOF materials including gas storage and separation, and catalysis. In analogy, two-dimensional metal organic networks (MONs) are produced at liquid or solid surfaces by linking organic building blocks to metal or metal clusters to produce two-dimensional open crystalline networks.

The Langmuir-Blodgett (LB) and Langmuir Schaefer (LS) deposition techniques allow the facile transfer of insoluble monolayers from the air-water interface to solid surfaces, with a control of the number of transferred layers and packing density of molecules within the film. Since the LB films are formed from weak force interactions, they suffer from low homogeneity and stability. Recently, we showed that by introducing supramolecular clips, a stable LB film can be prepared and transferred on solid substrates [2]. Building upon these results, we ambition to use the LB technique for the preparation of 2-dimensional self-assembled architectures on solid surfaces using artificial calixarene-based amphiphiles.

Calixarenes are cyclic oligomers of phenol, produced by the base-catalyzed reaction of *p-t*-butyl phenol and formaldehyde. The use of calixarenes to design artificial amphiphiles is mainly motivated by the possibility given by these molecules to act as organizing entities [3]. The macrocycle allows introducing and orienting hydrophobic and polar moieties in a three-dimensionally controlled fashion in the same molecule. Because of its higher conformational rigidity, the calix[4]arene is generally preferred to the larger analogues to produce amphiphilic calixarenes.

Results

We produced a series of amphiphilic calixarene bearing either cyano or carboxylate functions at the upper rim, and propyl functions at the lower rim (Figure 1).

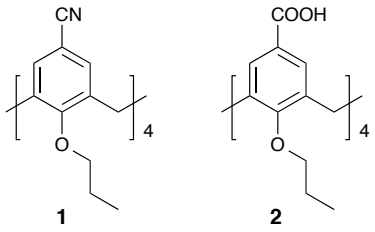

Figure 1: Chemical structures of O*-propyl cyano-* (**1**) *and carboxy-* (**2**) *calixarenes.*

The self-assembly of **1** as monomolecular layers was studied using the Langmuir balance method and Brewster angle microscopy (BAM) on pure water and on a solution of $NiCl_2$ (10 µM).

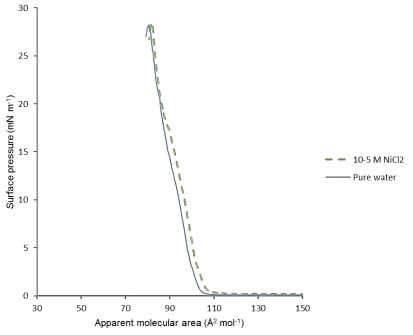

Figure 2: Π/A isotherm of **1** *measured on water (—) and 10^{-5} M $NiCl_2$ (--) subphases.*

On pure water, the compression isotherm of **1** shows a collapse pressure value of 28 mN m^{-1}. This value is high for an amphiphile bearing only short alkyl chains suggesting that the monolayer is additionally stabilized by π-π interactions among neighboring amphiphiles. In the presence of $NiCl_2$, no change is observed for the collapse pressure but a slight shift in the isotherm takeoff (A_o) area suggests an interaction of the divalent ion with the monolayer.

The morphology of the monolayer of **1** on pure water and on a NiCl2 solution (10 µM) were studied by BAM, representative micrographs are given in Figure 3.

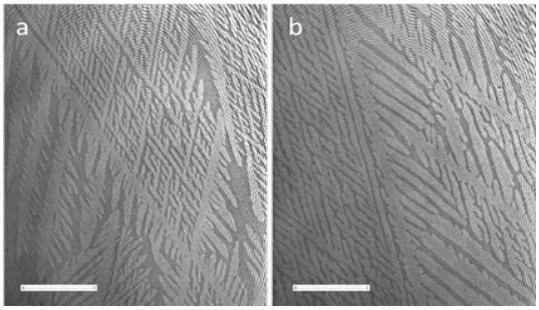

*Figure 3: Brewster angle micrographs of the monolayer **1** on $NiCl_2$ subphase (a) and on pure water (b), scale bar is 100µ.*

The monolayer of **1** at the air-water interface shows macroscopic dendritic and crystalline domains of different contrast suggesting the presence of organized anisotropic domains with distinct molecular organization/directions.

The possibility to transfer by LS transfer Langmuir monolayers of **1** from the air-water interface onto a solid substrate was studied. The transfer of the monolayer turned out to be successful with a transfer ratio of 1 ± 0.1. Surface ellipsometry measurements carried out on the so-produced films confirmed the presence of a monolayer on the substrate surface with a thickness value of 1.1 ± 0.2 nm. This value is consistent with the presence of a monomolecular film of **1** in a densely packed phase with the pseudo C_4 symmetry axis of the calixarene macrocycle oriented orthogonal to the air-solid interface. These layers were further characterized with atomic force microscopy (AFM); the results are presented in Fig. 4. The thickness determined by performing AFM after scratching the layer is 1 ± 0.4 nm. This confirms the presence of a monolayer on the solid surface. Also self-healing was observed in AFM time lapse imaging sequences in that the scratches were progressively removed in subsequent images *cf.* Fig. 5.

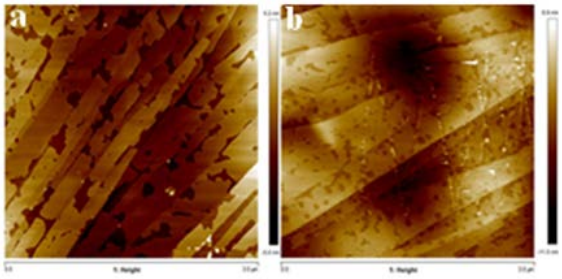

*Figure 4: AFM micrographs of monolayer of **1** (a) and scratched layer (b) transferred onto solid substrates using the LS technique.*

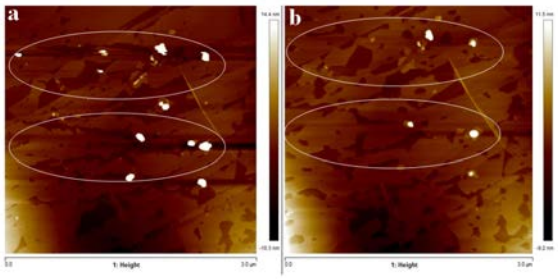

*Figure 5: AFM micrographs of monolayer of **1** after scratching (a) and after ten times scanning (b) transferred onto solid substrates using the LS technique.*

Conclusion

We demonstrated that the careful design of amphiphilic calix[4]arenes plays a crucial role in the development of well-organized calix[4]arene-based Langmuir monolayers at the air-water interface. The metal joints added in the aqueous subphase stabilize the amphiphiles at the interface and favor the transfer of the monomolecular films on hydrophobic substrates with the polar heads of the macrocycles pointing away from the surface. AFM revealed that the monolayers are homogeneous and able to heal themselves by scanning. Work is underway to reveal the structure of such calix[4]arene-based monolayers, deposited on solid substrates, at the molecular level by scanning probe micro

References for Project P1308

[1] K. Ariga, "*Organized Organic Ultrathin Films: Fundamentals and Applications*", Wiley, 2012.

[2] H. Furukawa, *et al.*, "Ultrahigh porosity in metal-organic frameworks Science", **329**, 424 (2010).

[3] L. Venkataraman, J. E. Klare, I. W. Tam, C. Nuckolls, M. S. Hybertsen and M. L. Steigerwald, "*Single-molecule circuits with well-defined molecular conductance*", *Nano Lett.*, **6**, 458 (2006).

[4] L. G. Tulli and P. Shahgaldian, *Calixarenes and Resorcinarenes at interfaces* in *Calixarenes: Functionalization and Applications*, P. Neri, J. L. Sessler and M.-X. Wang, Springer, 2016.

[5] X. Yan, V. Janout, J. T. Hsu and S. L. Regen, "*The Gluing of a Langmuir-Blodgett Bilayer*", J. Am. Chem. Soc. **125**, 8094 (2003).

[6] N. Moridi, C. Wäckerlin, V. Rullaud, R. Schelldorfer, T. A. Jung and P. Shahgaldian, "*Langmir-Blodgett monolayer stabilization using supramolecular clips*", Chem. Commun. **49**, 367 (2013).

Optomechanics with nanostructured silicon nitride membranes

Project P1309 Cooling and control of a nanomechanical membrane with cold atoms
Project Leader: P. Treutlein and P. Maletinsky
Collaborators: T. Karg (SNI PhD Student) and A. Jöckel

Hybrid optomechanics

Light can exert forces on matter through radiation pressure. In optomechanics, these radiation-pressure forces are harnessed to cool and control the vibrations of nanomechanical oscillators, with possible applications in precision force sensing, quantum signal transduction, and fundamental tests of quantum physics [1]. This has many similarities with the field of ultracold atoms, where radiation-pressure forces are routinely used to laser-cool and trap atoms, to prepare them in highly nonclassical states, and to exploit these features for quantum technology.

In this project, we explore the exciting opportunities that arise when nanomechanical oscillators and ultracold atoms are coupled by laser light. In these hybrid mechanical-atomic systems [2], the atoms could be used to ground-state cool the mechanical oscillator in regimes where other techniques fail, to prepare it in highly non-classical states of vibration, and to measure its vibrations with a precision beyond the standard quantum limit. Recently, we reported the first experiment where a nanomechanical membrane oscillator was cooled from room-temperature to millikelvin temperatures through its coupling to laser-cooled atoms [3]. Although impressive cooling factors of about 1000 were observed, the mechanical oscillator was still in the classical regime, mainly because it was placed in a room-temperature environment, resulting in a strong heating rate that competes with the cooling and prevents quantum manipulation. To reach the quantum regime, we are setting up a new optomechanical system with improved parameters that is placed in a cryostat.

Photonic crystal tether membranes

For our new setup, we are currently exploring different mechanical oscillator systems. A particularly promising system are nanopatterned silicon nitride membrane oscillators recently developed in the group of S. Gröblacher at TU Delft [4] (see Fig. 1). These “tether membranes” consist of a small membrane paddle suspended by ultrathin strings under tensile stress. They combine three major improvements over conventional silicon nitride square window thin films: (i) The tether structure results in a very low effective oscillator mass of only 2 ng. (ii) They exhibit ultra-low mechanical dissipation. Ring-down measurements with our samples show quality factors larger than 10 million at oscillation frequencies of 180 kHz. (iii) A hole pattern with sub-wavelength periodicity fabricated at the membrane center locally enhances the optical reflectivity to more than 99%. This photonic crystal allows us to directly use the membrane as an end-mirror in an optomechanical cavity.

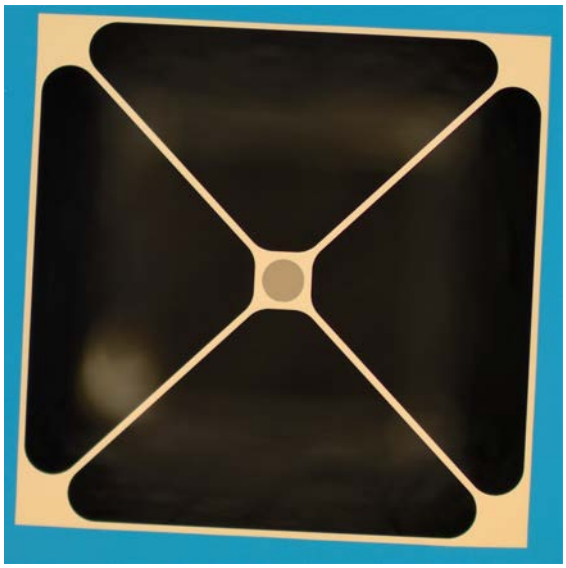

Fig. 1: False-color electron microscope image of a silicon nitride trampoline membrane (yellow). The membrane is suspended on four tethers and is patterned in the center with a photonic crystal structure of 50 µm in diameter. Image courtesy of S. Gröblacher, TU Delft.

All of these properties contribute to an increased optomechanical cooperativity of the membrane coupled to an optical cavity. One challenge here is to spatially match the cavity mode to the size of the photonic crystal which is only 50 µm in diameter. We aim to solve this problem by integrating the membrane into a Fiber Fabry-Pérot cavity [5]. Fiber mirrors laser machined on the end-faces of optical fibres have very small radii of curvature, typically in the range of 0.1 to 1 mm. This makes it possible to build extremely short cavities with mode diameters on the order of 10 µm. An image of a first fibre cavity setup using fibres manufactured in the group of D. Hunger at LMU Munich is depicted in Fig. 2. Using a widely tunable Ti:Sa laser source allows us to measure cavity finesse as a function of the wavelength of light. This is important in order to tune the fabrication process such that the photonic crystal reflectivity is maximal precisely at 780 nm, the wavelength of the D2 transition of our rubidium atoms.

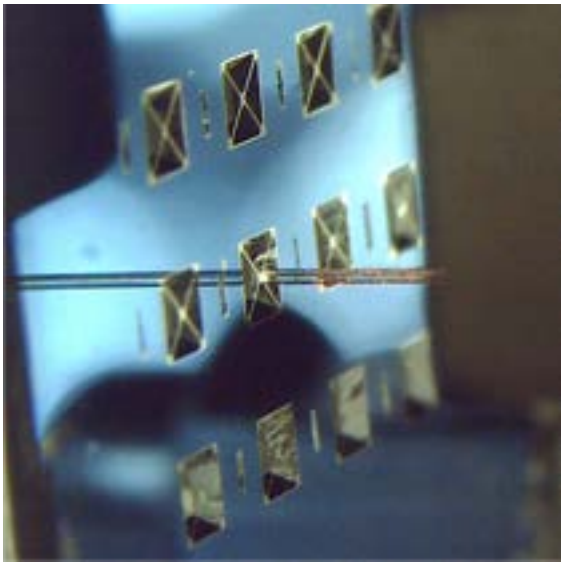

Fig. 2: Fiber cavity setup with a photonic crystal membrane. An optical fibre is approached from the right to a silicon chip hosting an array of photonic crystal membranes. The high-reflectivity coated fibre end-face and the photonic crystal form an optical cavity of about 50 µm in length.

The use of fibre cavities goes along with additional advantages. From the optomechanics point of view, reducing the cavity length is beneficial since it increases the single-photon optomechanical coupling, describing the strength of the radiation pressure interaction of a single phonon of the mechanical oscillator with a single cavity photon. This allows us to operate the cavity at lower photon number such that the laser remains shot-noise limited at the mechanical frequency.

Cryogenic pre-cooling

The final step towards increasing the membrane optomechanical cooperativity is cryogenic pre-cooling inside a liquid helium flow cryostat. Potentially this allows us to reach temperatures as low as 4 K, thereby strongly reducing thermal noise. Our first steps are to measure membrane thermalisation in the cryostat and to investigate heating due to optical absorption. In Fig. 3 images of our first cryogenic membrane mount are shown.

Fig. 3: Top: Membrane chip mounted on a titanium sample holder and bolted to the copper cold finger of a helium flow-cryostat. Bottom: The same membrane inside the copper radiation shield of the cryostat.

In the coming months, we will further characterize the optical and mechanical properties of the tether membranes at low temperatures and finalize the design of the optomechanical system. Once the optomechanical system is fully operational, it will be connected to our ultracold atom experiment in order to perform experiments on atom-membrane coupling.

References for Project P1309

[1] M. Aspelmeyer, P. Meystre and K. Schwab, "Quantum optomechanics", Phys. Today **65**, 29 (July, 2012).

[2] P. Treutlein, C. Genes, K. Hammerer, M. Poggio and P. Rabl, "Hybrid Mechanical Systems", in "Cavity Optomechanics" (eds M. Aspelmeyer, T. Kippenberg, and F. Marquardt) 327–351 (Springer, 2014).

[3] A. Jöckel, A. Faber, T. Kampschulte, M. Korppi, M. T. Rakher and P. Treutlein, *"Sympathetic cooling of a membrane oscillator in a hybrid mechanical–atomic system"*, Nature Nanotechnology, **10,** 55–59 (2015).

[4] R. A. Norte, J. P. Moura and S. Gröblacher, "Mechanical resonators for quantum optomechanics experiments at room temperature", arXiv: 1511.06235 (2015).

[5] D. Hunger, T. Steinmetz, Y. Colombe, C. Deutsch, T.W. Hänsch and J. Reichel, *"A fiber Fabry–Perot cavity with high finesse"*, New Journal of Physics **12**, 065038 (2010).

Nanostructured diffusional guides inspired by the nuclear pore complex

Project P1310 Plasmonic sensing in biomimetic nanopores
Project Leader: Y. Ekinci and R. Lim
Collaborators: D. Sharma (SNI PhD Student)

Nuclear pore complexes (NPCs) are large proteinaceous assemblies in eukaryotic cells that control bi-directional selective nucleocytoplasmic translocation of biological cargoes through biochemical interaction of cargo-carrying nuclear transport receptors (NTRs) and NPC key components known as phenylalanine-glycine nucleoporins (FG Nups). Altogether the FG Nups together with NTRs form a dynamic selective barrier that prevents the translocation of unspecific molecular cargo.

In biological environment selectivity and speed of molecular transport processes are optimized based on "reduction of dimensionality" with diffusion confined to one or two dimensions [1]. This behavior remains highly sought after on polymeric surfaces to expedite diffusional search processes in nanoscale systems [2]. Here, our aim is to exploit such phenomena by engineering biomimetic nanostructures surfaces that replicate the function of biological nuclear pore complexes (NPCs).

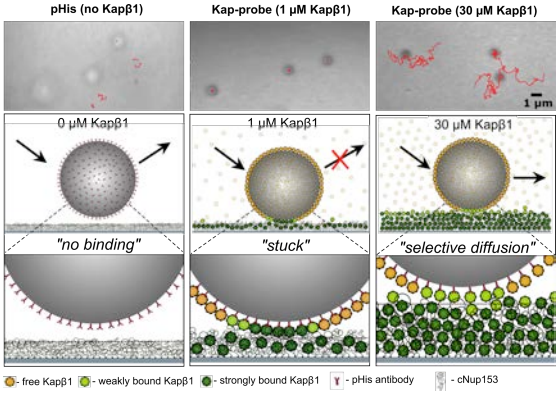

Fig. 1: Trajectory of nuclear transport receptors (Kapβ1)-bearing colloidal particles over FG Nup functionalized surface at different concentration of Kapβ1 inside FG Nup layer [3].

In our previous work, it was demonstrated that a pre-occupancy of binding sites in the FG Nups via NTRs increases the diffusion of NTR-bearing particles over FG Nup coated surfaces [3,4]. Based on that, an NTR-concentration dependent two-dimensional selective diffusion of NTR-bearing colloidal particles has been achieved (see figure 1) [3]. To accomplish one dimensional diffusion on a two-dimensional surface, we have achieved nano pathways of FG Nups on glass substrate using top-down lithography process and surface chemistry for FG Nup immobilization. To understand the impact of the patterned surface on the directionality of diffusion we have studied the diffusivity of NTR-bearing colloidal particle over FG Nup pathways at various background concentration of NTRs in FG Nups.

Diffusion of cargoes over FG Nup-pathways: To achieve FG Nup pathways we have fabricated 500nm wide channels on glass substrate using e-beam lithography and top-down nanofabrication. Patterned surface was etched down to 100nm to obtain 500 width channels on the surface, which is further used to study the impact of reduction of dimensionality on diffusion of cargoes that are 1μm in diameter.

Fabricated samples were further used for APTES-Sulfo SMCC based surface chemistry to immobilized cysteine containing FG Nup153 on surface, and 1μm sized –COOH functionalized polystyrene beads ($\lambda_{Ex} = 540nm, \lambda_{Em} = 600nm$) were coated with nuclear transport receptor Kapβ1 using NHS Ester (N-hydroxysuccinimide ester) surface chemistry to attach $-NH_2$ group containing Kapβ1. To perform diffusion experiments FG Nups were filled with Kapβ1 at different background concentration (see figure 2).

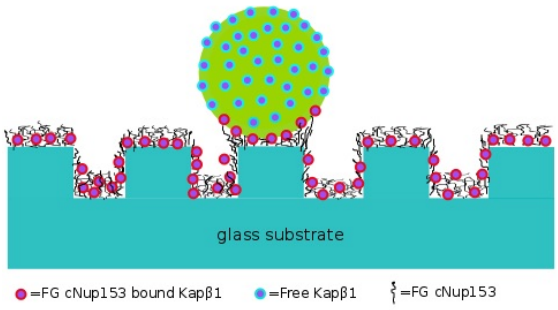

Fig. 2: Patterned glass substrated with immobilized FG Nup153 filled with background NTRs (Kapβ1 or Impβ) and NTR bearing colloidal particles that are used as molelcular cargoes to study the NTR-concentration dependent diffusivity.

Diffusion experiments were conducted using total internal reflection fluorescent (TIRF) microscope with field penetration depth of 200nm. To examine directionality of diffusion, channels were aligned along x-direction during the experiments. Results from patterned sample were compared to the same from un-patterned sample in order to verify the extent of impact of FG Nup nano-pathways on one-directional diffusion of cargoes.

To analyse the directionality of diffusion, diffusion was divided in four modes: (A) stationary mode, (B) simple diffusion mode, (C) direct diffusion mode,

(D) restricted diffusion mode. To analyse the modes, mean-square-displacement (MSD) was calculated at different time intervals (Δt), and $MSD - \Delta t$ curves for x-, y- direction and for two dimensional diffusion were plotted along with the trajectory of cargoes (see figure 3-4). From diffusion equations for simple, and directed diffusion modes, diffusion constant and velocity were calculated respectively and used as one of the parameters to conclude on the directionality and modes of diffusion (see figure 5).

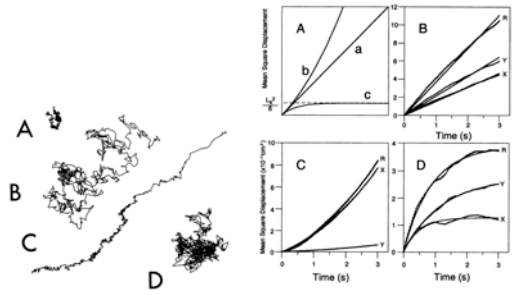

Fig. 3: Particle trajectories at different diffusional modes (Left) and their respective $MSD - \Delta t$ curves: (A) stationary mode, (B) simple diffusion mode, (C) direct diffusion mode, (D) restricted diffusion mode. [5]

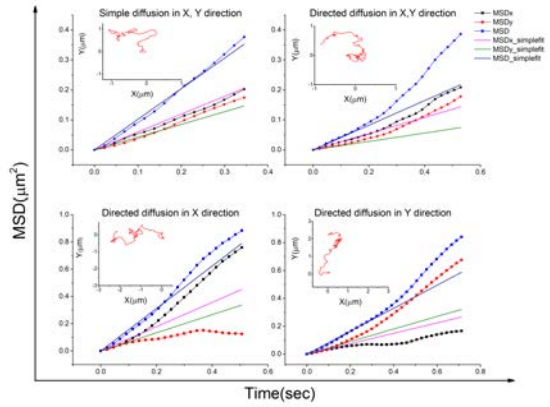

Fig. 4: Different trajectories travelled by cargoes with $MSD - \Delta t$ curve. Top-left and top-right figures show simple diffusion and directed mode respectiiely in both x, and y direction. Whereas bottom-left and bottom-right figures show directed diffusion in x, and y-direction respectively.

Result and Conclusion: Experiments at different background concentration of Kapβ1 showed that number of particles showing higher Diffusion coefficient increases by increasing background concentration of Kapβ1 and in the absence of Kapβ1 particles stick to the surface via kapβ1-FG domain binding. Control experiment was conducted with BSA coated polystyrene beads at physiological Kapβ1 concentration of 30μM, where due to no BSA-FG domain binding, particles showed high diffusivity.

From our current analysis and experiments, we are able to distinguish different diffusional modes and directionality of diffusion via $MSD - \Delta t$ plots, diffusion constant, and velocity of cargoes to a certain extent. However, in case of multi-diffusion mode (see figure 5) it is difficult to conclude on the directionality of diffusion without observing particle trajectory. Besides, at physiological concentration of Kapβ1 we observed 14% higher directional diffusion along x or y-direction on patterned surface comparative to un-patterned surface. To achieve directional diffusion at higher extent further analysis of data and studies are required.

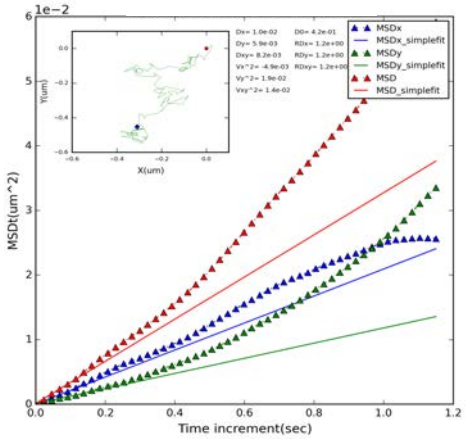

Fig. 5: Trajectory and $MSD - \Delta t$ curve where diffusion mode is the combination of both restricted and directed mode in x-direction.

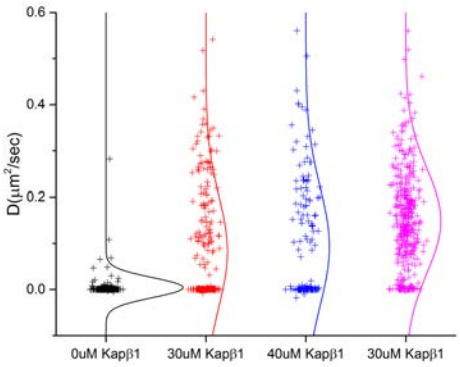

Fig. 6: Scattering plot along with normal distribution of diffusion constant: (black, blue and red) for Kapβ1-bearing cargoes , and (pink) for BSA coated cargoes.

References for Project P1310

[1] O. G. Berg *et al.*, Annu. Rev. Biophys. Biophys. Chem. **14**, 131-160 (1985).
[2] S. Santer et al., Polymer **45**, 8279-8297 (2004).
[3] K. D. Shleicher *et al.*, Nature Nanotechnology **9**, 525 (2014).
[4] L. E. Kapinos *et al.*, Biophysical Journal **106**, 1751-62 (2014).
[5] A. Kusumi *et al.*, Biophysical Journal **65**, 2012-2040 (1993).

Targeted proteomics to study spreading of protein aggregation

Project P1401 Targeted single cell proteomics using magnetic nanoparticles to study prion-like spreading of amyloid nanoparticles
Project Leader: T. Braun and H. Stahlberg
Collaborators: C. Schmidli (SNI PhD Student), A. Bieri and R. Sütterlin (C-CINA, Biozentrum)

Biomedical background

Stereotypic spreading of protein aggregation through the nervous system is a hallmark of many neurodegenerative diseases. This was demonstrated for Alzheimer's disease (AD, amyloid-β & tau protein) and Parkinson's disease (PD, α-synuclein, or α-syn). α-syn is a natively unfolded, presynaptic protein of unknown function and unusual conformational plasticity. Evidence accumulates that progression of synucleinopathies not only involves transmission of simple "*protein misfolding*" but rather specific "*structural information*" from one cell to the next, leading to the progressive proliferation of "*structural α-syn strains*". It is now suspected, that different forms of α-syn inclusions lead to different phenotypes of neurodegeneration, i.e., lead to different synucleinopathy diseases, such as PD, Dementia with Lewy body disease, or Multiple System Atrophy disease. How is such specific structural information transmitted? To date the mechanisms are unknown, but a prion-like transmission via an intrusion of protein nanoparticles imprinting their specific folding onto native host proteins is most likely.

Unfortunately, today's biophysical and biochemical methods can trace the presence of proteins, but do not allow detecting *and* monitoring the structural arrangement of the involved proteins or structural strains. The characteristics of neuronal cells and the stochastic nature of transmission processes make an analysis at the single-cell *and* single-molecule level essential.

Targeted visual proteomics

Recently we developed a fast and quantitative method that enables the fast and specific extraction and recovery of target proteins from minute volumes of cell lysate (total of 40k cells) without the need for genetic engineering to introduce affinity tags (Fig. 1) [1]. A main advantage of this method is that the whole process from cell lysate to EM grid prepration only consumes around 150 min of time. Samples are deposited on transmission electron microscopy (TEM) grids and examined at the single molecule level by quantitative TEM (qTEM), which additionally delivers structural information. Our method also allows potential binding partners to be detected and analyzed. These either co-purify with the primary target protein or can be extracted using it. Immunogold labeling both aids protein identification and localizes specific proteins in the extracted multi-molecular complexes.

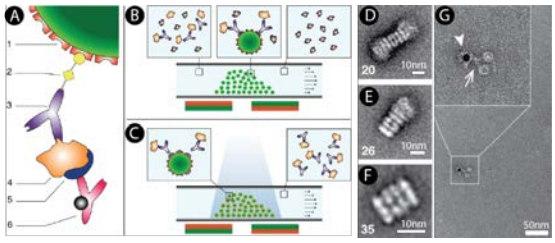

Fig. 1: Principle of the microfluidic affinity isolation method. (A) Antibody (AB)-biotin conjugate bound to a streptavidin-coated magnetic bead. The AB binds to a target protein, a secondary AB with gold label recognizes a binding partner of the target protein. (B) Affinity extraction. (C) Photocleavage and elution. Streptavidin coated magnetic beads (1) are trapped in a microcapillary using external magnets positioned in close proximity below it (B). The capillary is then rinsed with sample solution that was previously incubated with biotinylated ABs (3) against target structures (4); the crosslinker (2) conjugating the ABs to biotin is photocleavable. Biotin and streptavidin form a complex immobilizing the ABs, and thus the target proteins, on the magnetic beads. Optionally, the capillary can next be rinsed with potential binding partners (5) of the target structures and/or with immuno-gold (6) to label immobilized target proteins or their interacting partners. Target structures are recovered by illuminating the beads with UV-light and by eluting the released AB-target protein complexes (C). Downstream applications using quantitative TEM analysis follow. (D-F) Isolation of endogenous 20S proteasome from HEK293 cell lysate (40k cells), representative averages are shown (numbers indicate the number of particles). The 20S proteasome was found with two regulatory 16S subunits (D), one 16S unit (E) or no regulatory unit (F). Identification was performed by the visual appearance of the binding partners. (G) Interaction labeling of binding partners using immunogold (6, arrowhead) after fishing binding partners (5) using a primary target protein (4). Both extraction steps were carried out in cell lysate (Giss et al., 2014).

We now improve this method to bring the technology on single cell level. To this end, we combine superparamagnetic nanoparticles directly with antibodies. Initial experiments to build a magnetic trap strong enough to trap the nanoparticles were successful (Fig. 2, A). This trap can be directly combined with the single cell lysis set-up developed in the framework of another project (see report of the ARGOVIA project "single cell nanoanalytics, A9). Furthermore, we modified super-paramagnetic nanoparticles with antibodies, which specifically bind to target proteins (Fig. 2 B). Note, that the superparamagnetic nanoparticles do not need to be removed from the antibody, in contrast to the method shown in Fig. 1 .

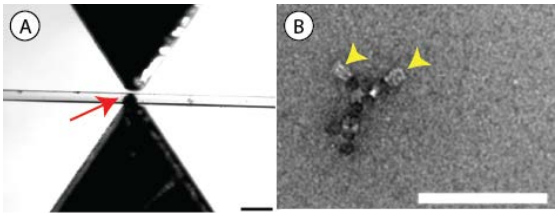

Fig. 2: Microfluidic magnetic trap and super-paramagnetic nanoparticles. A) Magnetic trap immobilizing super-paramagnetic particles as small plug (red arrow) in a micro-capillary. Scale bar: 1 mm. B) Super-paramagnetic particles (dark dots) conjugated to antibodies, with bound proteasome 20S (side views are marked by yellow arrow-head). Scale bar: 100 nm.

Quantitative EM (qTEM)

A semi-automatic, TEM image acquisition and data analysis procedure was developed to quantify protein amounts (Fig. 3). Thereby, images are recorded from defined regions of each TEM grid and the target proteins are detected by their visual appearance and counted, allowing the total amount of protein to be measured. For example, the apparent dissociation constants of ABs to their target can be determined (Fig. 3 F) [1, 2].

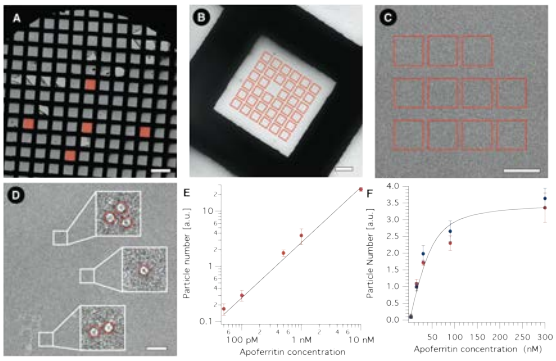

Fig. 3: TEM procedure for image acquisition and data-analysis [1, 2]. (A) Step 1: Manual selection of five squares of a TEM grid. (B) Step 2: The procedure targets 35 sub-squares per grid square. (C) Step 3: 11 images are recorded per sub-square. (D) Step 4: Image processing. Particles of interest are detected by their visual appearance in negative stain on the total of 1925 images per grid, either manually or automatically using a template, and counted. Scale bars, 200 µm (A), 20 µm (B), 2 µm (C) and 200 nm (D). (E) Adsorption function of apoferritin (AF) particles on TEM grids. Note the linear response. (F) Transfer function of the microfluidic affinity isolation method for AF determined by qTEM. A typical binding curve for ABs is measured and an apparent binding constant of 47 nM was determined [1].

Model system to study the prion like spreading

In order to study the prion like cell-intrusion and spreading of protein aggregate related to neurodegenerative diseases, we established a cell line of dopaminergic neurons. Furthermore we developed procedures to produce α-syn protein nanoparticles, which are fluorescence labeled. These nanoparticles are used to seed the differentiated neuronal cells. As shown in Fig. 4, the particles are readily taken up into the cell and are accumulating in the cell somas and axons.

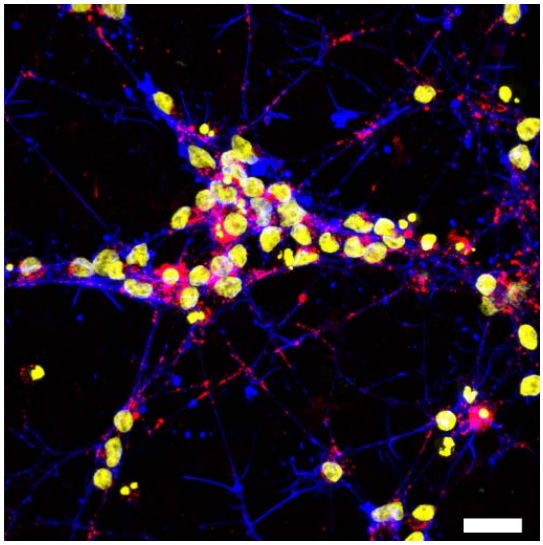

Fig. 4: LUHMES cell lines, differentiated for eight days to dopaminergic cell. Nuclei are stained yellow, aktin filaments are labeled in blue. The α-syn protein nanoparticles, which accumulated in the cells, are shown in red.

We now are analysing the results by classical methods (EM and fluorescence microscopy) and our new visual proteomics approaches. The latter allows the characterization of individual cell and the analysis of the protein aggregation status of the cell on single molecule level.

References for Project P1401

[1] D. Giss, S. Kemmerling, V. Dandey, S. Stahlberg and T. Braun, "*Exploring the interactome: microfluidic isolation of proteins and interacting partners for quantitative analysis by electron microscopy*", Anal. Chem. **86**, 4680–4687 (2014).

[2] C. Schmidli and D. Giss, H. Stahlberg and T. Braun, "*Protein quantification by single particle transmission microscopy*", in preparation.

Pushing the limits of lightweight materials

Project P1402 Lightweight structures based on hierarchical composites
Project Leader: C. Dransfeld and C. Schönenberger
Collaborators: W. Szmyt (SNI PhD Student), S. Vogel, M. Calame and J. Gobrecht

Context

Carbon fibre reinforced polymer (CFRP) composites have gained great importance as lightweight materials. As they are lighter and stronger than any metal, these materials have an increasing impact on industry as they start to replace metals in high volume applications such as commercial aircrafts or automotive industry. Their high strength- and stiffness-to-weight ratio makes them ideal for highly tailored engineering applications, while outperforming conventional metallic solutions. Such CFRPs are supremely effective when exploiting their tensile properties in the unidirectional fibre direction. Nevertheless, the failure of a state of the art CFRP laminate is almost always governed by compressive failure in fibre direction (driven by the comparatively low matrix stiffness, resulting in buckling of single fibres at the microscopic level) or transverse strength (driven by the matrix strength at the fibre to matrix interface). Therefore, there has always been a high interest to enhance the properties of the fibre to matrix interface.

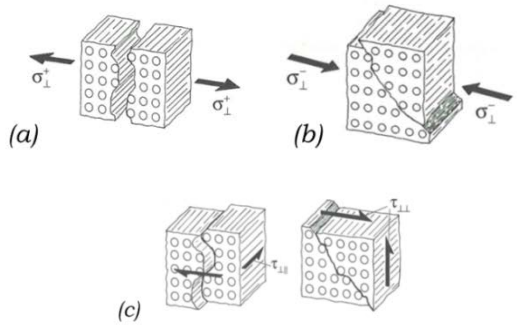

Fig. 1: Interface and matrix dominated failure modes from CFRPs; (a) transverse tensile, (b) transverse compression, (c) shear. These failure modes are an order of magnitude lower than the strength in fibre direction [1].

Objective

A novel and promising approach to the challenge of the fibre-matrix disparity of properties is the development of multi scale, or hierarchical composites. Such materials contain reinforcing fibres at typically two length scales; the nano- and micro-metre [2]. The reinforcing fibres in the nanometre length scale are typically carbon nanotubes (CNT) with their extraordinary intrinsic mechanical properties, and complement the micron sized (ø7 µm) carbon fibres.

Stable growth of CNTs on the carbon fibre substrate was achieved by applying an oxide layer on the fibre by atomic layer deposition, prior to application of a metal catalyst, followed by the CNT growth via chemical vapour deposition (CVD), as demonstrated by Perrin et al.[2]. The Al_2O_3 layer protects the carbon fibre surface and thereby solves the reported fundamental problem, as of generated defects in the carbon fibre and substantial reduction of its tensile strength during CVD processing. However, the interface between the oxide layer and the carbon fibre is stressed by temperature loads during the CVD process and may debond, therefore requiring restrictions of processing temperatures. These mechanisms were identified [3] such that carbon fibre with strength values close to their virgin state and a well-conditioned interface with highly aligned CNT growth could be realized.

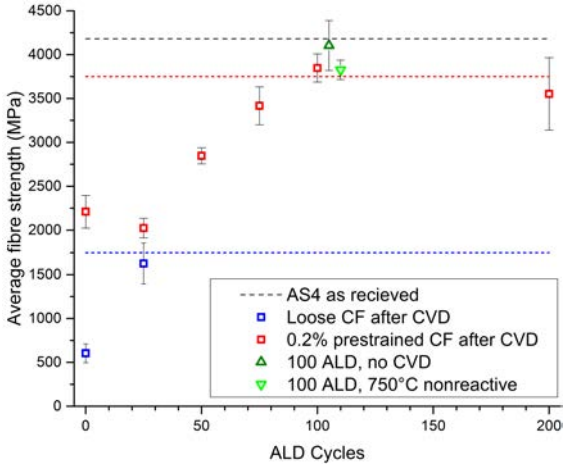

Fig. 2: An optimum thickness of the oxide layer (corresponding to 10.5 nm) reconstitutes the original strength of the reference fibre [3].

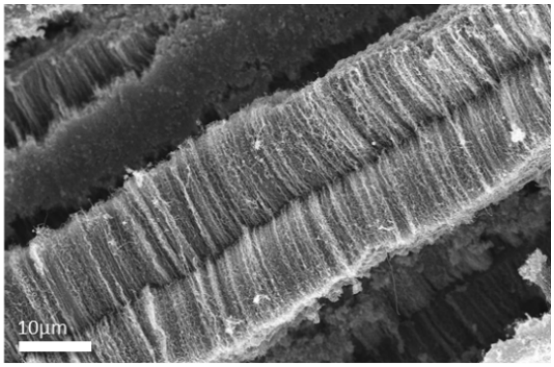

Fig. 3: SEM Image of highly aligned CNT's grown on carbon fibre. The CNT length exceeds the fibre diameter. It becomes apparent the CNTs from neighbouring fibre start interact leading to novel mechanisms of load transfer (Source: S. Vogel - unpublished).

Outlook

The SNI PhD project with W. Szmyt, which started in October 2015, will aim at understanding in depth the mechanism of fibre strength degradation through metal catalyst nanoparticles and to apply novel approaches for CNT growth to mitigate these effects. Furthermore the interaction of these "hairy fibres" as constituents in a diglycidether-bisphenol-A based epoxy polymer matrix will be of particular interest.

References for Project P1402

[1] H. Schürmann, Konstruieren mit Faser-Kunststoff-Verbunden, 2 ed.: Springer, 2007.

[2] M. Perrin, C. Schönenberger, M. Calame and G. M., *"Advanced Carbon Fibers for Next Generation Toughened Composites",* Project Report, p. 66, 2009.

[3] S. Vogel, C. Dransfeld, M. Calame and J. Gobrecht, *"Improved fibre strength of carbon fibres after CNT growth by application of thin alumina layer",* presented at the Composites week@Leuven and Texcomp 11 Conference, Leuven, 2013.

Fluorous tails give peptides wings

Project P1403 Tailor-made proteins and peptides for quantum interference experiments
Project Leader: V. Köhler and M. Mayor
Collaborators: J. Schätti (SNI PhD Student), U. Sezer[#], L. Mairhofer[#], J. Cotter[#], P. Rieser[#] and M. Arndt[#] ([#]Faculty of Physics, University of Vienna)

Thermal transition to the gas phase

Quantum interference experiments at high masses require slow molecular beams while accelerated ionic gas phase species generated e.g. by electro spray are not (yet) suitable.[1] Slow molecular beams can be formed by thermal evaporation or sublimation of especially designed analytes under high vacuum, although relatively high quantities of sample have to be applied (~50 mg per experiment). Peptides and proteins however display i) very low vapor pressure ii) low thermal stability. Sublimation of unmodified peptides seems to be limited to dipeptides.[2] Their low vapor pressure can be traced back to strong intermolecular interactions, namely hydrogen bonding and ionic attraction. After a first design round, a set of tripeptides was analyzed in respect to their thermal evaporability under electron impact mass detection. In this set either internal ionic charges or charges and hydrogen bond donors were removed by amidation and *N*-methylation, respectively (Fig. 1). Only peptide **3** showed signals at higher m/z ratios and even (very low) counts for M^+.

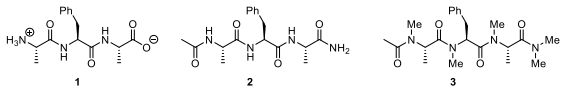

*Fig. 1: Tripeptides for initial evaporation studies with an Ala-Phe-Ala core structure: parent peptide **1**; charges removed by amidation in **2**; additionally hydrogen bond donors were removed in **3** by N-methylation.*

The next set of designs included fluorous tails, i.e. perfluorinated alkyl chains. Fluorinated compounds display significantly higher vapor pressure compared to their hydrogenated analogues (e.g. acetic anhydride, MW 102, bp 140 °C vs. trifluoro acetic anhydride, MW 210, bp 40 °C). Two fluorous tails in charge free peptide **6** turned out to be sufficient to observe promising counts for M^+ at lower fragmentation compared to analogous (charge free and *N*-methylated) peptides **4** and **5** (Fig. 2).

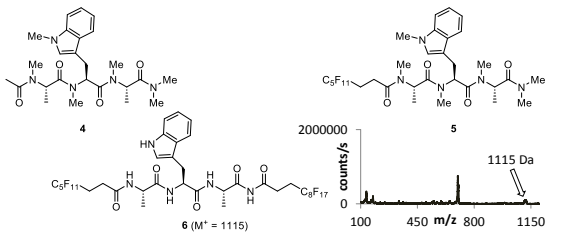

*Fig. 2: Charge free tripeptides with an Ala-Trp-Ala core structure. N-methylated peptide **4**; permethylated peptide **5** with one fluorous tail; volatile peptide **6** with two fluorous tails but remaining hydrogen bond donors (NH groups), EI-MS after thermal evaporation of **6** (~240°C).*

VUV ionization of peptides

Although slow particles are required for diffraction experiments at high masses (and accordingly beams of neutral particles) charge needs to be introduced subsequently for manipulation and detection. Previously highly stable dye molecules such as porphyrine derivatives were employed, which apart from electron impact can also be ionized by VUV (vacuum ultra violet radiation) at 157 nm (7.9 eV).[3] Out of the 20 proteinogenic amino acids tryptophan displays the lowest ionization energy and is susceptible to single photon ionization at 157 nm. Medium sized peptides with a high tryptophan content such as gramicidin A (1884 Da, 15 amino acids including 4 tryptophan residues) and even clusters thereof (up to 7536 Da) have been previously successfully ionized by VUV.[4] The molecular beams for these experiments have been generated by laser desorption (355 nm) into an adibatically expanding noble gas jet. Insulin on the other hand as a large peptide/small protein (5808 Da), which does not contain a single tryptophan, could not be detected under these conditions. As a first step towards high mass photoionizable peptide structures decatrypthophan **7** (1880 Da) was prepared and successfully photoionized, with the desired ion clearly most abundant among the detected species (Fig. 3). An alternating lysine-tryptophane 20 mer has already been prepared - so far without purification. This construct has i) by itself a mass of 3161 Da ii) provides 11 amino groups for derivatization e.g. with fluorous tails.

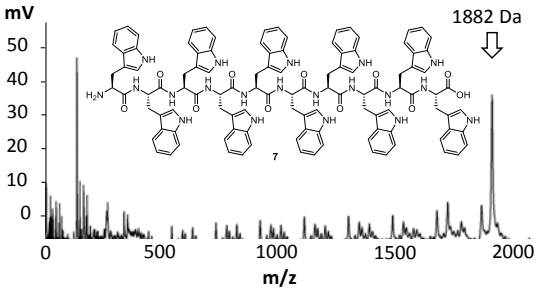

Fig. 3: TOF-MS of decatryptophan after laser desorption into a cold buffer gas and photoionization at 157 nm.

Derivatization of insulin

In an attempt to enable photoionization of insulin its derivatization with chromophores was investigated. A small set of agents for protein amidation with frequently employed reactive groups (NHS-ester, sulfonated NHS ester, tetrafluorosulphonyl ester) was initially considered, prepared and some tested in reactions with amino groups under mild conditions (partly aqueous

solvent, room temperature, moderate pH). Conveniently, the reactions with insulin could be performed with simple NHS esters of 1-napthalene and 1-pyreneacetic acid (IE ~8.1 and 7.4 eV, respectively) in water-THF mixtures.[5] The reactions led to a distribution of acylated products which in the case of 1-naphthalene acylation converged by acid treatment to one major species. (Presumably through hydrolysis of competitively formed modifications of other side chains, such as serine and threonine only amidated products remained.) For either chromophore trisubstituted species were isolated in high purity (25 mg for naphthalene substitution, sum of two runs, 29% yield and 72 mg for naphthalene substitution, 18% yield) which were most likely modified at the two *N*-termini and the side chain of the single lysine residue (tryptic digest is not sufficient to pinpoint the side of modification and MS-MS experiments would have to be performed, Fig. 4). The photoionization experiments however were unsuccessful leading to weak signals and fragmentation.

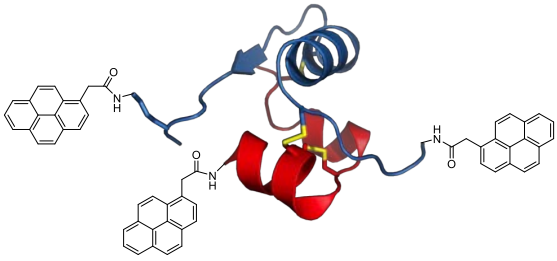

Fig. 4: Cartoon display of pyrene modified insulin. Representation based on PDB ID 4INS. The most likely sites for 1-pyreneacetylation are displayed.

Interference of a peptide

The encouraging results obtained with peptide **6** (successful thermal evaporation, EI ionization with promising counts for M^+) made it possible to perform interference experiments. In a first attempt without velocity selection, very short averaging times and after heavy processing a first interferogram was obtained (Fig. 5). The experiment was performed in a KDTLI (Kapitza-Dirac-Talbot-Lau Interferometer) with a thermal source, electron impact ionization and mass detection.[6] The experiment has been repeated twice in the meantime.

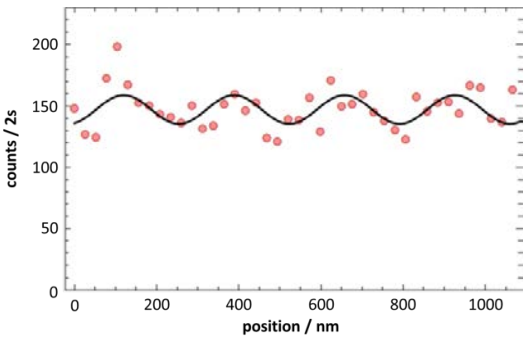

*Fig. 5: First interferogram of a peptide (**6**) recorded on a KDTLI.*

Given higher signal strength and increased signal duration, interferometry should enable the distinction of sequence isomers based on differing polarizabilities of the peptides.[7] To this end >500 mg of each of the fluorinated sequence isomers **9**-**11** depicted in Fig. 6 have been synthesized and isolated.

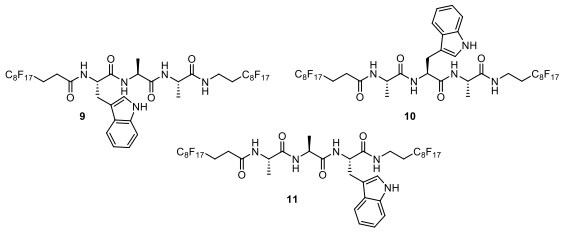

Fig. 6: Sequence isomers of Ala-Trp-Ala with fluorous tails prepared for interferometry.

References for Project P1403

[1] T. Juffmann, H. Ulbricht and M. Arndt, *"Experimental methods of molecular matter-wave optics"*, Rep. Prog. Phys. **76**, 086402 (2013).

[2] D. Gross and G. Grodsky *"On the Sublimation of Amino Acids and Peptides"*, J. Am. Chem. Soc. **77**, 1678 (1955).

[3] P. Schmid, F. Stöhr, M. Arndt, J. Tüxen and M. Mayor *"Single-Photon Ionization of Organic Molecules Beyond 10 kDA"*, J. Am. Soc. Mass. Spectrom. **24**, 602 (2013).

[4] M. Marksteiner, P. Hasslinger, M. Sclafani, H. Ulbricht and M. Arndt *"UV and VUV Ionization of Organic Molecules, Clusters and Complexes"*, J. Phys. Chem. A **113**, 9952 (2009).

[5] L. Malik, J. Nygaard, R. Hoiberg-Nielsen, L. Arleth, T. Hoeg-Jensen and K. J. Jensen *"Perfluoroalkyl Chains Direct Novel Self-Assembly of Insulin"*, Langmuir **28**, 593 (2012).

[6] S. Gerlich, L. Hackermüller, K. Hornberger, A. Stibor, H. Ulbricht, M. Gring, F. Goldfarb, T. Savas, M. Müri, M. Mayor and M. Arndt *"A Kapitza-Dirac-Talbot-Lau interferometer for highly polarizable molecules"*, Nature physics, **3**, 711 (2007).

[7] R. Antoine, I. Compagnon, D. Rayane, M. Broyer, P. Dugourd, N. Sommerer, M. Rossignol, D. Pippen, F. C. Hagemeister and M. F. Jarrolds *"Application of Molecular Beam Deflection Time-of-Flight Mass Spectrometry to Peptide Analysis"*, Anal. Chem. **75**, 5512 (2003).

Engineering polymersomes for nucleocytoplasmic transport

Project P1404 Selective transport of functionalized nanocarriers into biomimetic and natural nuclear pore complexes
Project Leader: R. Lim and C. Palivan
Collaborators: C. Zelmer (SNI PhD Student)

Introduction

Nuclear pore complexes (NPCs) form the sole passageways between the nucleus and cytoplasm in eukaryotic cells [1]. Exclusive access through each ~100 nm-diameter NPC is given to soluble transport receptors that are able to ferry specific cargoes such as transcription factors [2] or even staggeringly large messenger ribonucleoproteins [3]. This process is mediated by a complex interplay between transport receptors, known as karyopherins (kaps) importins or exportins, and the NPC comprising nucleoporins (Nups) and is generally known as nucleocytoplasmic transport [4, 5].

Up to now, it remains challenging to study how large, deformable objects enter into the NPC. In this respect, synthetic-biomimetic approaches using nanometer sized objects are expected to advance the study of NPC transport. In fact, an understanding of how large complexes might enter the NPC could lead to strategies for drug delivery and gene therapy. Indeed, amphiphilic copolymers represent ideal candidates because they self-assemble in different architectures (micelles, polymersomes, and nanotubes), with a large variety of properties (size, stability, flexibility), and the possibility of functionalizing their external surfaces for targeting approaches [6, 7].

Design of polymersomes for nucleocytoplasmic transport

We are applying a step-wise bottom-up strategy that uses synthetic compartments to mimic natural translocation mechanisms. We are engineering polymersomes that allow for the insertion, encapsulation, and attachment of transport receptors in order to support nucleocytoplasmic transport (Fig. 1).

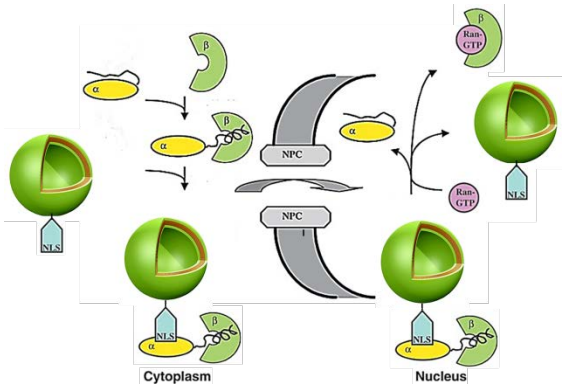

Fig. 1: Applying intrinsic cellular signals for the translocation of artificial nanocarriers into the cell nucleus.

Polymersomes were generated by self-assembly of amphiphilic block copolymers PMOXA-*block*-PDMS-*block*-PMOXA. PMOXA-*block*-PDMS-*block*-PMOXA based polymersomes stand out for their enhanced membrane strength and stability compared to liposomes as well as their prominent biocompatibility [6, 7]. Furthermore, their ease for synthetic surface modification was essential in this study to attach specific transport receptors (Importin α/Importin β transport receptors) favouring transportation across the nuclear envelope through the NPC. Therefore, the first necessary step was to generate polymersomes that expose at their surface binding sites for transport receptor conjugation.

Synthesis of transport receptor linkable polymer

Maleimide linker end-group functionalized PMOXA-*block*-PDMS-*block*-PMOXA was synthesized in a three-step synthesis route (Fig. 2).

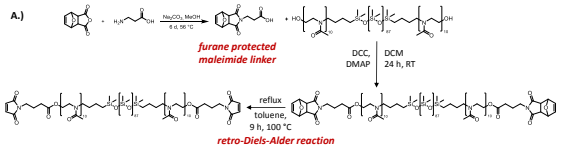

Fig. 2: Three-step synthesis developed to synthesize maleimide end-group functionalized PMOXA-block-PDMS-block-PMOXA.

In the first step, a furane protected maleimide linker was synthesized and was afterwards condensed to the both end sides of PMOXA-*block*-PDMS-*block*-PMOXA.

Thereafter, the thermal labile furane groups were split off to result the maleimide functionalized PMOXA-*block*-PDMS-*block*-PMOXA.

Polymersome preparation

For the polymersome formation, the maleimide functionalised copolymer was mixed with unfunctionalized one (in a ratio of 1/5) and the mixture was self-assembled by film rehydration method. In order to trigger the attachment of transport receptors Importin α and Importin β to polymersome surfaces, the polymersomes had to be tagged with a particular nuclear localization sequence (NLS). To do so, a cysteine containing NLS conjugate was covalently bound to the maleimide linker decorated polymersome surface via thiol-ene coupling. Importin α and Importin β together form a heterodimer complex which recognizes and binds NLS on polymersome surface and hence, resulted in the desired transport receptor surface coded polymersomes (Fig. 3).

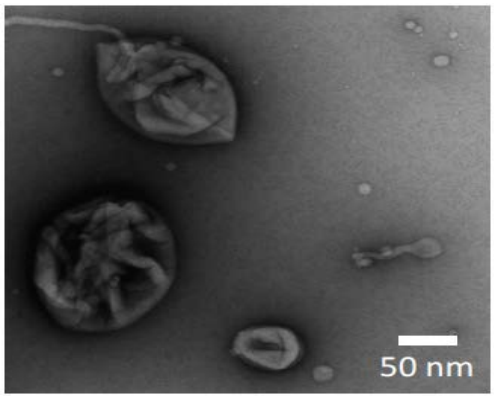

Fig. 3: TEM micrographs of polymersomes for nucleocytoplasmic transport.

Importin-conjugated polymersomes bind to FG Nups

Next, we tested the binding of the importin-conjugated polymerosomes to the intrinsically disordered NPC proteins known as FG nucleoporins (or FG Nups) using surface plasmon resonance (SPR) [5]. From here, we conclude that the polymersomes bound specifically to the FG Nups further verifying that the conjugated importins preserved their functionality on the polymerosome surface.

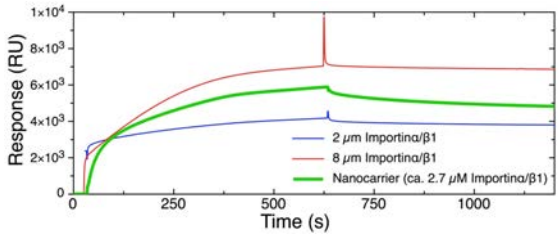

Fig. 4: SPR measurements of importin-conjugated polymerosomes to a surface of FG Nups (i.e., Nup153). This is consistent with the binding of soluble importinβ to Nup153.

Summary

Significant progress has been made in this project since starting in early 2015 being a relatively short time. This underscores the synergy between both the Lim and Palivan labs. Christina is able to reproducibly modify, assemble and conjugate functional importins to the polymerosomes. Our next steps will be to test for the viability of polymerosome transport into the nuclei of living cells. This will be complemented by a thorough analysis of the physico-chemical properties of the polymerosomes.

References for Project P1404

[1] A. Hoelz, E.W. Debler and G. Blobel, Ann Rev Biochem **80**, 613-643 (2011).
[2] Y.M. Chook and K.E. Süel, Biochim. Biophys. Acta **1813**, 1593-1606 (2011).
[3] D. Grünwald, R.H. Singer and M. Rout, Nature **475**, 333-341 (2011).
[4] M. Stewart, Nat Rev Mol Cell Biol **8**, 195-208 (2007).
[5] L.E. Kapinos, R.L.Schoch, R.S. Wagner, K.D. Schleicher and R.Y.H. Lim, Biophys. **106,** 1751-1762 (2014).
[6] S. Egli, M.G. Nussbaumer, V. Balasubramanian, C.G. Palivan and W. Meier, J. Amer. Chem. Soc. **133**, 4476-4483 (2011).
[7] V. Mikhalevich, C. Zelmer, C.G. Palivan and W. Meier, *"Bioinspired Membranes",* RSC, submitted.

Towards highly coherent, near-surface spins for nano-sensing in life-sciences and technology

Project P1405 Surface-functionalization of diamond nano-magnetometers for applications in nano- and lifesciences
Project Leader: U. Pieles and P. Malentinsky
Collaborators: M. Batzer (SNI PhD Student), P. Appel, M. Ganzhorn, L. Thiel and Sina Saxer

Introduction

The Nitrogen Vacancy (NV) center in diamond over the last years has been established as a powerful tool for nanoscale magnetic imaging and sensing [1][2]. The NV center is host to an electronic spin sytsem, which can be conveniently initialized and read out using optics and coherently manipulated with microwaves. Importantly, and essential to NV magnetometry, the NV center exhibits quantum coherence times approaching one second, even under ambient conditions. Quantum qoherence ist he basis for the NVs excellent magnetic field sensitivity, while room temperature operation is essential to many applications. NV magnetometers are therefore amenable to a wide variety of high-sensitivity applications, ranging from the life-sciences, over materials engineering to fundamental questions in solid state physics.

The versatility of such NV magnetometers has been demonstrated in first proof-of-concept studies to yield single electron spin sensitivity [3] and imaging resolutions down to the nanoscale [4]. In order to fully exploit the potential of NV magnetometry in scientifically relevant settings and future application in sensing, stable and highly quantum-coherent NV centers have to be created in close proximity to the diamond surface, where they can positioned within few nanometers from an imaging target [2]. However, such shallow NV centers are highly susceptible to and influenced by the chemistry of the nearby diamond surface. Indeed, recent studies have shown that such "shallow" NV centers exhibit significantly decreased spin coherence times as compared to their bulk counterparts [5], due to fluctuating electronic spins on the diamond surface [6]. As a result, near-surface NVs do not fully exploit their potential in magnetic sensing – a shortcoming we aim to overcome in the future.

The goal of this project is to gain full control over diamonds' surface chemistry, to yield highly spin coherent NV center spins within few nanoemetrs of the diamond surface. To that end, we will explore various approches to surface termination, involving wet-chemistry and plasma treatment, and investigate the effects of the resulting diamond surface chemistry on the NVs' sensing performance. Our primary goal is to employ such functionalization to prolong the NVs spin coherence times. However, full control over the diamond chemistry will prove much more versatile than this. It will form the basis for functionalizing diamond nanostructures with scientifically valuable targets, such as large bio-molecules, induvidual cells or even neurons. The resulting control over the NVs' environment will allow for NV-based nanoscale quantum sensing with unprecedented robustness and performance. Ultimately, our experiments might yield sensors which provide atomically resolved, structural information of large bio-molecules on the single-molecule level. Such sensing would offer deep insights into the structural behaviour of a broad range of molecules and would open up a new route to biosensing applications with ultimate sensitivity.

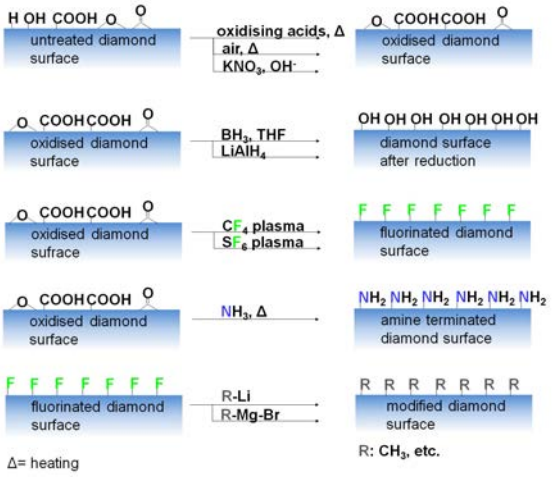

Fig. 1: Potential diamond surface terminations, chosen to protect coherence of shallow NV spins and to allow for future, chemical attachment of bio-molecules for sensing. The present surface termination schemes can be applied using wet-chemistry, while plasma-based processes will be explored as well.

Results achieved thus far

During the first year of this project, we have laid the ground for our wide-range exploration of diamond surface functionalizations. In particular, we have performed in-depth literature research to identify the most promising target surface functionalizations (illustrated in Fig. 1) to be pursued [7][8]. These should on one hand yield long NV spin coherence times and on the other hand allow for later chemical attachment of bio-molecules to our diamond devices. We have taken first steps towards implementing the surface terminations we identified, using the wet-chemistry approaches indicated in Fig. 1. Characterization of the treated surfaces will initially be performed using X-ray

photoemission spectroscopy (XPS) and ultimately using shallow, few nanometer deep, NV centers – the most accurate, local sensors for fluctuating magnetic fields emanating from the diamond surface.

NV based magnetometry is commonly performed using diamond nanostructures for efficient NV photon collection or for scanning probe microscopy. The most viable approach to fabricating such structures consists in electron-beam lithography and subsequent plasma-etching of diamond [4]. While this approach yields diamond nanostructures of great scientific and technological interest, it is also known to deteriorate the spin coherence properties of embedded NV centres. To systematically study this detrimental effect of etching plasmas on NVs, we have fabricated test samples containing a range of diamond nan-structures of various dimensions (Fig. 2). The shallow (~10 nm deep) NV centers in these structures are currently investigated with regard to photo-stability and spin coherence times at room temperature and will form the basis for our subsequent studies.

Fig. 2: Diamond test-structure including shallow nitrogen-vacancy centers electronic spins (red spheres) for assessment of diamond surface-functionalization steps. The sample contains a matrix of diamond nan pillars of varying diameter (100 nm – 1000 nm) and length (200 nm – 1500 nm). It is thereby ideally suited to study the influence of nano-fabrication and plasma etching on NV spin coherence and the effectiveness of the planned diamond surface functionalization recipes.

Outlook

In the next months we will start implementing the various proposed diamond surface termination schemes (Fig. 1) to our diamond samples. We will initially treat single-crystalline, bulk diamond samples of various crystalline orientations (predominantly {100} and {111}) and analyze the outcome of our chemical treatment using XPS. With these procedures established, we will proceed by treating our nano-structured diamond reference sample (Fig. 2) and systematically study the effect of surface termination on NVs in nanopillars of varying length and diameter. Once the most promising surface termination for coherence protection and chemical attachemnet is identified, we will proceed by functionalizting our diamond nano-devices with large bio-molecultes containing spin labels (such as TEMPO) for imaging and sensing. Another exciting avenue to pursue is to employ our diamond surface terminations to firmly attach magnetic nanoparticles to the diamond surface, next to the NV spin. It was recently shown [9] that such an arrangement could be used as a "magnetic field amplifier" that would increase sensitivities in NV magnetometry by several orders of magnitude. The resulting magnetometer would be the best of it's kind and find various, profound applications in the fields mentioned earlier.

References for Project P1405

[1] J. Taylor J. M. Taylor, P. Cappellaro, L. Childress, L. Jiang, D. Budker, P. R. Hemmer, A.Yacoby, R. Walsworth, and M. D. Lukin, *„High-sentivity diamond magnetometer with nanoscale resolution"*, Nature Physics **4**, 482 (2008).

[2] L. Rondin, J.-P. Tetienne, T. Hingant, J.-F. Roch, P. Maletinsky and V. Jacques, *"Magnetometry with nitrogen-vacancy defects in diamond",* Rep. Prog. Phys. **77**, 056503 (2014).

[3] M. S. Grinolds, S. Hong, P. Maletinsky, L. Luan, M. D. Lukin, R. L. Walsworth and A. Yacoby, *"Nanoscale magnetic imaging of a single electron spin under ambient conditions"*, Nature Physics, **9**, 215 (2013).

[4] P. Maletinsky, S. Hong, M. S. Grinolds, B. Hausmann, M. D. Lukin, R. L. Walsworth, M. Loncar and A. Yacoby, *"A robust, scanning quantum system for nanoscale sensing and imaging"* Nature Nanotechnology **7**, 320 (2012).

[5] B.K. Ofori-Okai, S. Pezzagna, K. Chang, M. Loretz, R. Schirhagl, Y. Tao, B.A. Moores, K. Groot-Berning, J. Meijer and C.L. Degen, *"Spin properties of very shallow nitrogen vacancy defects in diamond"*, Physical Review B, **86**, 081406(R).

[6] L. Luan, M.S. Grinolds, S. Hong, P. Maletinsky, R.L. Walsworth and A. Yacoby, *„Decoherence imaging of spin ensembles using a scanning single-electron spin in diamond"*, Scientific Reports **5**, 08119 (2015).

[7] M. Kaviani, P. Deák, B. Aradi, T. Frauenheim, J. Chou and A. Gali, *"Proper Surface Termination for Luminescent Near-Surface NV Centers in Diamond",* Nano Letters **14**, 4772 (2014).

[8] A. Krueger and D. Lang, *"Functionality is Key: Recent Progress in the Surface Modification of Nanodiamond" ,* Advanced Functional Materials **22**, 890 (2012).

[9] L. Trifunovic, F. L. Pedrocchi, S. Hoffman, P. Maletinsky, A. Yacoby and D. Loss, *"High-efficiency resonant amplification of weak magnetic fields for single spin magnetometry at room temperature"*, Nature Nanotechnology **10**, 541-546 (2015).

The 2,2'-bipyridine ligand motif in molecular break junctions

Project P1406 Charge transfer versus charge transport in molecular systems
Project Leader: O. Wenger and M. Calame
Collaborators: S. Neumann (SNI PhD Student) and J. Overbeck (SNI PhD student)

Motivation

With this project, we want to help to clarify the differences and similarities between electron transfer and electron transport in molecular junctions. Therefore, we aim to design donor-acceptor systems which can mediate photoinduced charge transfer in solution and can further be studied in mechanically controllable break junction (MCBJ) experiments.

We identified Ru(2,2'-biypridine)$_3^{2+}$ as a suitable sensitizer for photoinduced electron transfer and have therefore made first attempts to incorporate the 2,2'-bipyridine ligand motif into molecular break junctions. The developed molecular structure consists of a 5,5'-disubstituted-2,2'-bipyridine unit with pyridine moieties at either end for anchoring to the gold electrodes (**5**, Fig. 1).

Synthesis of the 2,2'-bipyridine bridge

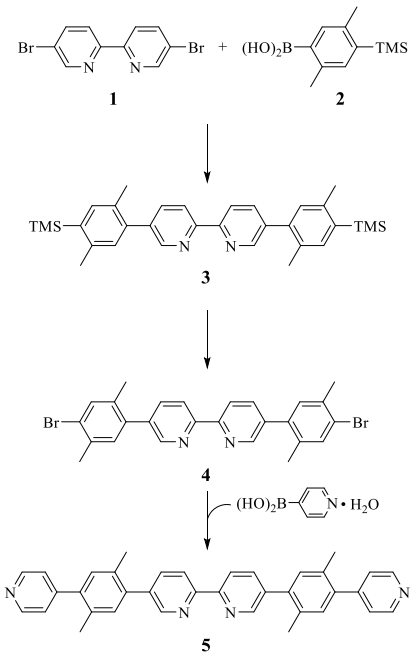

*Fig. 1: Synthesis of the molecular bridge **5**.*

The synthetic route to compound **5** is based on 5,5'-dibromo-2,2'-bipyridine (**1**)[1] and 2,5-dimethyl-4-(trimethylsilyl)phenylboronic acid (**2**)[2] (Fig. 1). The bipyridine **1** was obtained via *Stille* coupling of 5-bromo-2-iodopyridine and the boronic acid **2** was prepared in two steps from 2,5-dibromo-*p*-xylene. Therefore, the *p*-xylene was TMS-protected once and the unprotected site was transformed into the boronic acid **2** afterwards. Symmetric *Suzuki* cross-coupling of **1** with **2** gave compound **3** which was deprotected to compound **4** by the addition of bromine. The desired bridge **5** was obtained via *Suzuki* cross-coupling.

First MCBJ measurements

First MCBJ measurements were carried out at room temperature with a 100 µM solution of the synthesized bridge **5** in chloroform (Fig. 2).

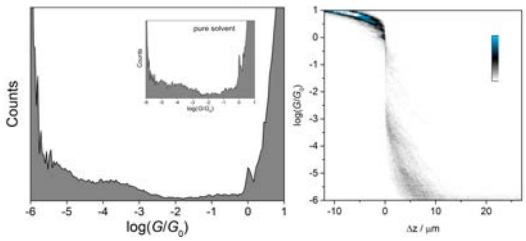

*Fig. 2: **Left**: 1D logarithmic conductance histogram for **5** conducted from 346 individual traces and recorded with a bias voltage of 0.10 V. **Right**: 2D conductance histogram of **5**.*

These preliminary measurements did not provide any direct evidence for the formation of a single molecule junction. The anticipated signal in the range between log(G/G_0) = -4 to -6 which would indicate the formation of a single-molecule conductance were absent.

Test measurements with a *p*-phenylene vinylene based reference molecule (Fig. 3), which also contains pyridine units as anchor groups, indicated the successful formation of a single molecule break junction. Importantly, this reference molecule is somewhat shorter than compound **5** from Figure 1. We suspect that our bipyridine-based system is somewhat too long in order for log(G/G_0) to be significantly above the noise level.

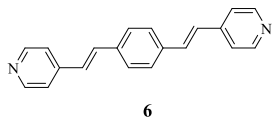

*Fig. 3: Phenylene vinylene based reference molecule **6**.*

Conclusion

Preliminary MCBJ experiments suggest that the developed molecular bridge **5** is too long. The next step will be to replace its pyridine anchor groups by isonitriles. This molecular re-design will shorten the overall length of the bridge significantly, and the isonitrile anchor groups might provide stronger electronic coupling to the electrodes than pyridines.

On the basis of the obtained results, new molecular structures need to be developed so that the desired donor-acceptor systems can be studied photochemically and in break junction experiments.

References for Project P1406

[1] S.-J. Liu, Q. Zhao, R.-F. Chen, Y. Deng, Q.-L. Fan, F.-Y. Li, L.-H. Wang, C.-H. Huang and W. Huang, *"π-Conjugated Chelating Polymers with Charged Iridium Complexes in the Backbones: Synthesis, Characterization, Energy Transfer, and Electrochemical Properties"*, Chem. Eur. J. **12**, 4351 (2006).

[2] J.C. Freys and O.S. Wenger, *"Supramolecular and Intramolecular Energy Transfer with Ruthenium-Anthracene Donor-Acceptor Couples: Salt Bridge versus Covalent Bond"*, Eur. J. Inorg. Chem., 5509 (2010); K. H. So, R. Kim, H. Park, J. Kang, K. Thangaraju, Y. S. Park, J. J. Kim, S.-K. Kwon, Y. H. Kim, *"Synthesis and characterization of a new iridium(III) complex with bulky trimethylsilylxylene and applications for efficient yellow-green emitting phosphorescent organic light emitting diodes"*, Dyes Pigm. **92**, 603 (2011).

Coupling an ultracold ion to a metallic nanowire

Project P1407 Coupling a single ion to a nanomechanical oscillator
Project Leader: S. Willitsch and M. Poggio
Collaborators: P. Fountas (SNI PhD Student)

Introduction

Over the past years, theoretical and experimental developments in physics have led to an unprecedented level of control over the quantum properties of atoms, ions and nanoscale systems. One of the most striking examples includes the manipulation of the internal and external degrees of freedom of single quantum systems such as laser cooled trapped ions [1]. The asset of using such a system lies in its isolation from the environment achieved by trapping via a radiofrequency electric field in ultra-high vacuum. By laser cooling the ion to its motional ground state in the trap, its motion can be manipulated on the quantum level with little interference from the environment. These intriguing properties have rendered cold trapped ions one of the most advanced systems in the domain of quantum information processing.

Similarly, recent experiments have demonstrated an impressive level of control over nanomechanical oscillators, e.g., cooling to their quantum-mechanical motional ground state as well as the control of single phonons. Currently, a great challenge is to couple mechanical to other quantum systems while maintaining good coherence properties. Here, we report for the first time the implementation of an ultracold ion-metallic nanowire (hybrid) system in a layer ion trap with the aim to study the resonant coupling between these two systems mediated by electric fields.

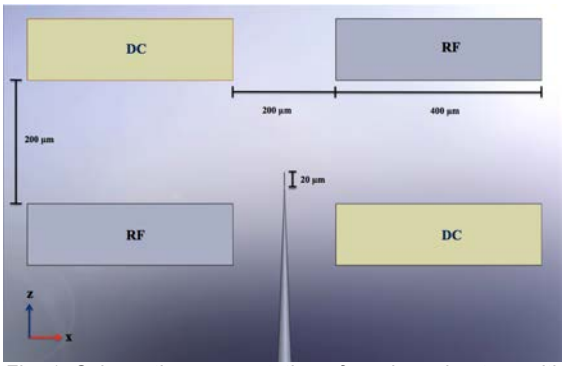

Fig. 1: Schematic representation of our layer ion trap with 200 µm distance between the layers and 200 µm tip-to-tip distance between RF and DC electrodes. A cylindrical metallic nanowire of 20 µm length and 200 nm diameter glued on the tip of a tungsten holder is inserted close to the ion in the center of the assembly (not shown).

Numerical Simulations of the Layer Chip Trap

In a first step of the project, we characterized the ion-nanowire hybrid system numerically through simulations. The ions are confined in a layer trap, i.e., a trap consisting of four segmented wafers forming the trap electrodes, using static (DC) and time-dependent (RF) electric fields, see Figure 1. Specifically, the trap consists of two RF electrodes and fourteen segmented DC electrodes. The electrode wafers have a thick-ness of 100 µm and the tip-to-tip distance is 200 µm with a 200 µm separation of the electrode layers.

The choice of trap is based on its open geometry which allows to insert and align a metallic nanowire in a suitable position to enable the resonant coupling between the nanowire and a laser-cooled ion in the center of the trap. Furthermore, the current setup gives flexibility in moving the nanowire and it also creates a deeper and more harmonic trapping potential for the ions as compared to, e.g., surface-electrode chip traps [2]. It also leads to stronger confinement of the ion and less distortion of the trapping potential when the charged nanowire is inserted. Numerical calculations were performed in order to obtain an accurate description of the electric potential trapping the ion and its distortion by the charged nanowire. Fig. 2 shows 2D-cuts of numerical results of the total unperturbed (left panel) and distorted potential including the nanowire (right panel) of the layer chip trap for a single $^{40}Ca^{+}$ ion. It can be seen that even with the distortion by the nanowire, a sufficiently deep, locally harmonic potential is obtained enabling an efficient trapping of an ion.

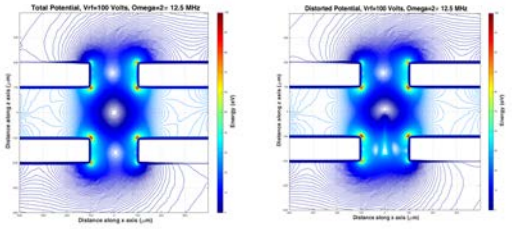

Fig. 2: Results from numerical simulations of the electric potentials for a $^{40}Ca^{+}$ ion generated by the RF and the DC electrodes. Left figure: Total trapping potential for a single $^{40}Ca^{+}$ ion. Right figure: Distorted potential including the effect of charged nanowire and holder.

MD simulations of the ion-cantilever system

To confirm that the ion is indeed trapped and responds to the nanowire's motion, molecular dynamics calculations have already been performed. Newton's equations of motion for a single trapped $^{40}Ca^{+}$ ion under the action of a vibrating cantilever were solved numerically. The forces included were those due to the interaction of the ion with the electric field produced by the electrodes, the radiation force acting as a friction force that causes

laser cooling, a stochastic force representing the collisions with the background gas and the electric force due to the coupling between the ion and the nanowire. We neglected the back action of the ion on the nanowire, because its mass is many orders of magnitude larger than the one of the ion. Consequently, the force field of the cantilver was approximated as that of a spherical oscillating particle located at a distance from the ion. The trapping parameters were based on realistic values taken from previous experiments [3]. Fig. 3 shows the shift of the equilibrium position as well as the change of amplitude of oscillation for a single $^{40}Ca^{+}$ ion for different ion-nanowire distances.

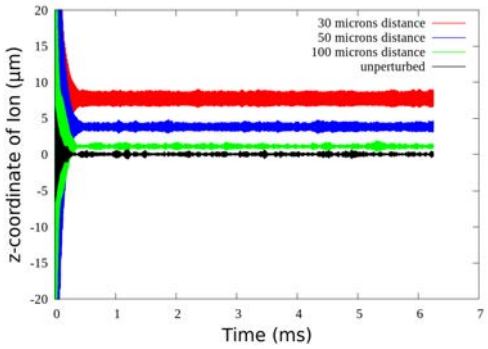

Fig. 3: Position of a single $^{40}Ca^{+}$ ion computed by MD simulations for different relative distances between the ion and the nanowire within a simulation interval of around 6 ms. The black line corresponds to a trapped and cooled ion without nanowire. The closer the cantilever is palced to the ion, the larger its displacement from its unperturbed equilibrium position and its vibrational amplitude.

We also characterized the response of the ion to the nanowire to resonant excitation by performing calculations with different nanowire driving frequencies, see Fig. 4. Resonant mechanical excitation of the ion is observed when the drive frequency of the cantilever matches the motional frequency of the ion in the trap.

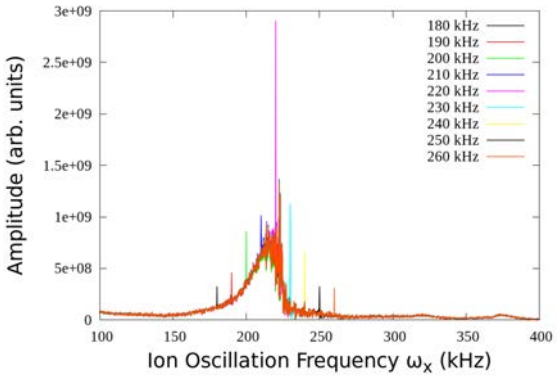

Fig. 4: Fourier transform of the motion of a single $^{40}Ca^{+}$ ion obtained through MD simulations for different driving frequencies of the nanowire. Resonant excitation is observed at 220 kHz which corresponds to the motional eigenfrequency of the ion (magenta line).

Outlook

Based on optimal geometric and electrical parameters that have already been obtained from our numerical simulations, an experimental setup is currently designed. After the assempling of the chip and the metallic nanowire in a vacuum chamber, we will study experimentally the strength of the perturbation that the ion will receive from the nanowire and the motional excitation caused by a resonant mechanical drive. Subsequently, the ion's motion will be cooled to its quantum-mechanical ground state and the effects of the cantilever on the ion's quantum dynamics will be explored. This experiment will form the basis of an entirely new research direction towards ion-solid state interfaces, with a range of potential applications in, e.g., quantum technology and mass spectrometry. It will also establish a new approach to precisely shape trapping potentials for ions using nanowires which will be of considerable interest for all types of ion experiments.

References for Project P1407

[1] S. Willitsch, "Coulomb-crystallised molecular ions in traps: methods, applications, prospects", Int. Rev. Chem. **31**, 175 (2012).

[2] A. Mokhberi and S. Willitsch, *"Structural and energetic properties of molecular Coulomb crystals in a surface-electrode ion trap"*, New J. Phys. **17**, 045008 (2015).

[3] M. Germann, X. Tong and S. Willitsch, *"Observation of electric-dipole-forbidden infrared transitions in cold molecular ions"*, Nat. Phys. **10**, 820 (2014).

Clean graphene nanoribbons with crystallographic edges

Project P1408 Clean zigzag and armchair graphene nanoribbons
Project Leader: D. Zumbühl and D. Loss
Collaborators: M. Rehmann (SN PhD Student), Y.B. Kalyoncu, T. Camenzind and C.P. Scheller

Introduction

Graphene has attracted a lot of interest as an extraordinary material for fundamental research and applications. Graphene nanoribbons (GNRs) are of particular interest as a playground for novel quantum states: in ribbons with crystallographic zigzag (zz) edge termination, ferromagnetic order of electron spins localized on the edge has been predicted [1], with spins at opposite ribbon edges pointing potentially in opposite directions due to inter-edge exchange. In armchair (ac) GNRs, on the other hand, theory has predicted that a giant spin-orbit coupling can be artificially induced with an adjacent array of nanomagnets [2], opening the door for helical states and topological phases sustaining Majorana fermions.

Zigzag Edges in Graphene and Graphite Defined with a Remote Hydrogen Plasma

Fabricating clean GNRs with high quality crystallographic edges is very challenging. We use a technique employing a cold remote hydrogen plasma [3] which exhibits highly anisotropic etching yielding hexagonal shaped etch pits with zz edges. Here, we present an experimental characterization of the remote plasma process on graphite flakes, and we show how the process can be made to work also on single layer (SL) graphene [4]. Further, in combination with ebeam lithography, we define clean zigzag graphene nanoribbons on a hexagonal boron nitride (hBN) crystal (see Fig. 1 b and Fig. 2), which are characterized with atomic force microscopy, micro-Raman spectroscopy and by performing electronic transport spectroscopy at temperatures down to 1.5 K.

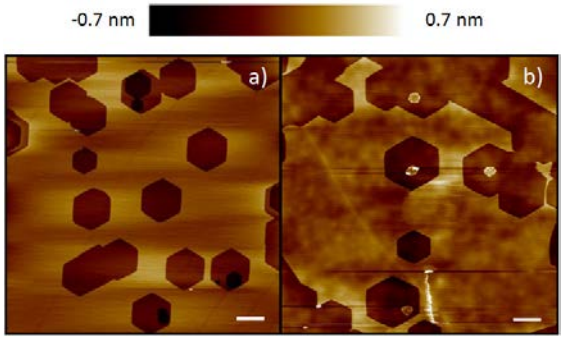

Fig. 1: Anisotropic hydrogen plasma etching of a) graphite and b) single layer graphene on hBN. Scale bar equals 1 µm in a) and 70 nm in b).

Electronic Transport in zzGNRs

The goal is to fabricate clean GNRs with low disorder which are reaching the ballistic limit. Ballistic GNRs are expected to exhibit subband formation and the resulting conductance quantization. The subband spacing in Graphene is given by $\Delta E = \pi\hbar v_F/W \sim 21\text{meV}$ which is rather large for a given width W = 100 nm compared to other materials (e.g. GaAs) due to the large Fermi velocity $v_F = 10^6$ m/s in graphene. Such a large subband spacing facilitates the observation of conductance quantization since the resulting large energy scale can more easily exceed the disorder broadening.

Figure 2 shows a SL zzGNR defined between two hexagonal shaped etch pits with zz edge termination on a hBN substrate. First two terminal conductance measurements show signatures of conductance quantization, reflecting the high quality of the GNR.

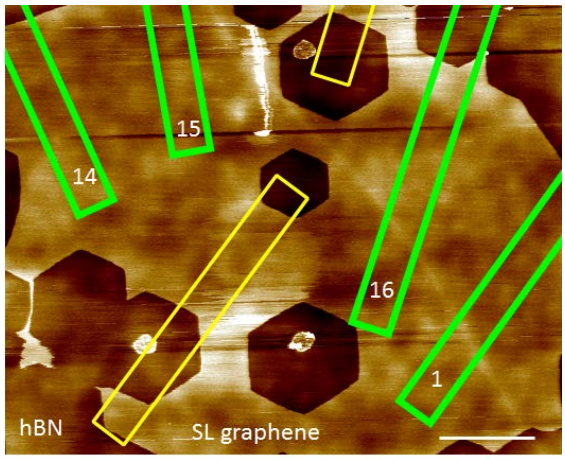

Fig. 2: SL zzGNR on hBN defined between two hexagonal shaped etch pits. Electric contacts are shown in green and areas where the graphene was cut by means of RIE in yellow. Scale bar equals 500 nm.

acGNRs Defined with Reactive Ion Etching (RIE)

Since acGNRs have been proposed to be suitable for the realization of helical modes, we started investigating the electronic transport of acGNRs on hBN. To determine the crystallographic orientation of the graphene flake, we employed anisotropic etching in a H-plasma.

Figure 3 a) shows a SL graphene sample on hBN where we cut the graphene by means of an Ar/O_2-plasma to define ribbons along the armchair direction. The graphene edges defined by RIE are known to show a relatively high degree of disorder.

However, Klinovaja et al. have calculated that the predicted physical phenomena are robust against a certain degree of edge roughness [2]. The ribbons were fabricated with an aspect ratio of one to prevent localization of the charge carriers due to edge defects. Unfortunately the evaporated Cr/Au contacts did not work and there were problems arising with gate leaks to the back gate. Therefore this sample could not be electrically characterized in transport measurements. However, the problems with both the contacts and the gate leaks have been solved in the meanwhile and new acGNR samples are fabricated.

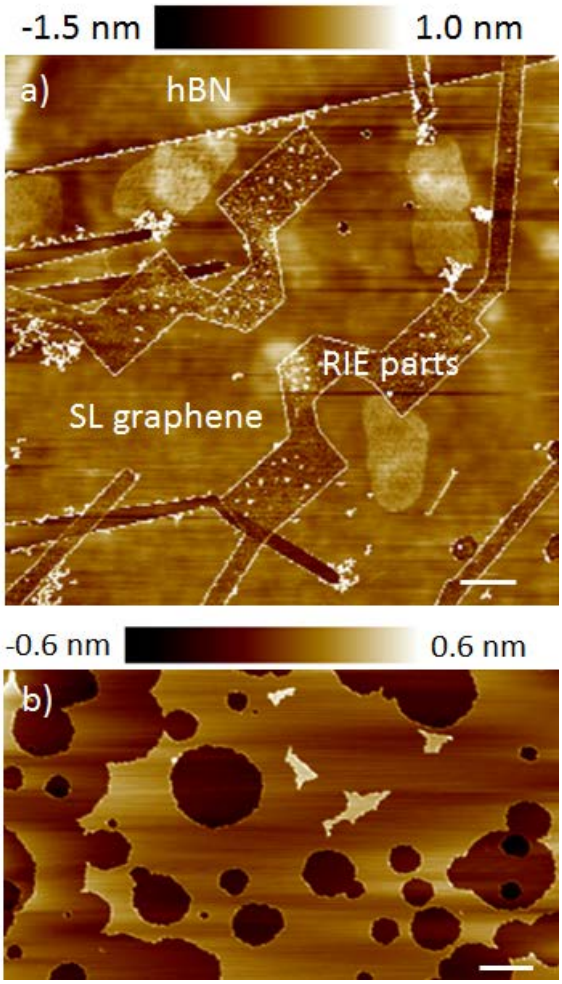

Fig. 3: a) acGNR defined with RIE by means of an Ar/O_2-plasma. The crystallographic orientation of the graphene flake was determined by anisotropic H-plasma etching prior to cutting the flake with RIE. Scale bar equals 500 nm. b) Graphite surface after exposure to a remote Nitrogen plasma at a pressure p = 1.7 mbar and temperature T = 700 °C. Scale bar equals 1 µm.

Development of an Anisotropic Etching Technique along the Armchair Direction

Besides defining the acGNRs by means of RIE, it is known that exposing graphite surfaces to a remote Nitrogen (N) plasma is expected to anisotropically etch along the ac-direction [5], which could therefore be used to define the ribbons. To establish this N-plasma etching technique in our lab, we started to investigate the etching of graphite surfaces when exposed to the N-plasma at different temperature and pressure values.

Figure 3 b) shows an AFM image of a graphite surface after exposure to a remote N-plasma at a pressure p = 1.7 mbar and temperature T = 700 °C. Some of the etch pits indicate a tendency towards an anisotropic character of the etching. However, further work needs to be done to improve the process. In particular, we will try to also tune the plasma power and develop a method to filter out ionic species which are expected to negatively influence the anisotropy of the etching.

Outlook

Future experiments will focus on the investigation of the electronic transport behavior of charge carriers in zzGNRs and acGNRs. For the zz case we plan to acquire data on further ribbons to reproduce the signatures of conductance quantization observed in two samples so far. Since these two samples were measured in a two terminal configuration, it cannot be excluded, that doping of the contacts plays an important role and influences the features observed in the transport data. Therefore we try to measure further zzGNRs in a four terminal configuration. Moreover we will study conductance quantization in magnetic fields, as a function of bias, temperature and width of the ribbon.

Further we will fabricate and characterize acGNRs in transport experiments. In particular, we plan to optimize them, making them long enough to pattern nanomagnets along the sides. This is expected to lead to rather unique transport properties which we will investigate in low temperature quantum transport experiments.

References for Project P1408

[1] Y.-W. Son *et al., "Half-metallic Graphene Nanoribbons"*, Nature **444**, 347 (2006).

[2] J. Klinovaja and D. Loss, *"Giant Spin-Orbit Interaction Due to Rotating Magnetic Fields in Graphene Nanoribbons"*, Phys. Rev. X **3**, 011008 (2013).

[3] R. Yang *et al.*, *"An Anisotropic Etching Effect in the Graphene Basal Plane"*, Adv. Mat. **22**, 4014 (2010).

[4] D. Hug, S. Zihlmann, M. Rehmann, L. Marot and D. Zumbühl, „Defining zigzag edges in Single Layer Graphene with a Hydrogen Plasma", in preparation.

[5] L. Zhang *et al., "Surface modification of highly oriented pyrolytic graphite by reaction with atomic nitrogen at high temperatures",* Appl. Surface Science **257**, 5647 (2011).

Bio-DURABLE self-cleaning paint: development of dirt repellency coatings for large surfaces

Project A8.1 Bio-DURACLEAN (FHNW, University of Basel, Walter Mäder AG Killwangen)
Project Leader: O. Glaied
Collaborators: U. Pieles, W. Meier and J. Reiter

Creating a stable and robust synthetic surface that repels dirt and various liquids has broad technological implications for areas ranging from nanotechnologies and surfaces to polymers. However, the development of these surfaces has proved to be extremely challenging.

Bio-DURACLEAN is a project aiming to develop a durable dirt-repellent large surface. The project innovation is based on the combination of three ideas: A new approach to mimic the lotus effect (Fig. 1) with a surface roughness given by the nano-/microparticles, water-repellent polymer that gives a dirt repellency effect and, for the first time, the use of cellulose nanoparticles.

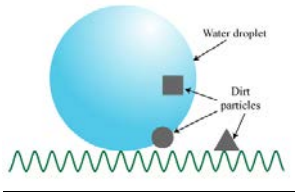

Fig. 1: Self-cleaning effect on the surface of a leaf.

To address these challenges, we here present the study to create a self-cleaning painted surface. The surface has a special, characteristic roughness: Systematically arranged painted surface, nano- and microparticles, and water-repellent polymer covering the whole surface. For the nano particles, two kinds of nanoparticles were studied. The first are silica nanoparticles and the second are cellulose nanoparticles. Combined with the micro- and nanoparticles, the water-repellent surface makes the painted surface super-hydrophobic, i. e. non-wettable, giving it the self-cleaning properties.

To reach a high durability, the Mader technology is used to well disperse the formulation and to covalently link the nanoparticles, the microparticles, the hydrophobic macromonomer and the painting layer to the polymer matrix.

I. Development of the lotus-like organization

The plant's ability to repel water and dirt results from a combination of a superhydrophobic surface of micron-scale hills, valleys and nanometer-scale waxy bumps that create rough surfaces don't giving water or dirt the chance to adhere. To address several unique applications, we attempted here to duplicate the lotus surface using a variety of materials, including paint, a combination of nano- and microsilica, and nanocellulose crystals.

Based on these project objectives, Bio-Duraclean is divided on two studies which are conducted in parallel; the first concerns the development of a dirt-repellent surface with the combination of the nano- and the microparticles of silica, and the second a bio-approach by using the cellulose nanoparticles with the silica microparticles on the surface.

I.1. First approach: Paint formulations based on lotus-like organization obtained with silica nano- and microparticles.

The first part of the paint surface development based on lotus-like organization obtained with the combination of nano- and microparticles of silica concerns the synthesis of silica particles with different sizes and the study of their organization on the paint surface.

To prepare monodisperse and uniform-size nanoparticles, silica particles were synthesized following the Stöber method using sol-gel process. For the nanometric particles, various-sized particles in the range 20-460 nm were synthesized. For the micrometric silica size, a one-pot method has been studied to prepare monodisperse silica particles in which TEOS was continuously supplied to an ethanolic solution of water and ammonia in the presence of electrolytes. Various-sized particles in the range 1.8-3.6 µm were synthesized.

The silica particles have a negative zeta potential due to Si-OH on the particle surface, which causes a hydrophilic effect. In order to organize the silica nanoparticles around the micro ones, the idea was to graft a cationic charge onto the silica microparticles' surfaces and to adsorb the silica nanoparticles on the surface of the micro ones based on an electrostatic link. The studied reaction is presented in Fig. 2.

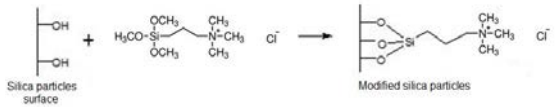

Fig. 2: Silica microparticle cationisation.

The modified cationic microparticles were incorporated in a coating formulation. A flat surface of the paint formulation was obtained with a spin coating method and UV cross linking under inert atmo-

sphere. The coating layer was analyzed with contact angle and SEM microscopy (Fig.3 and 4).

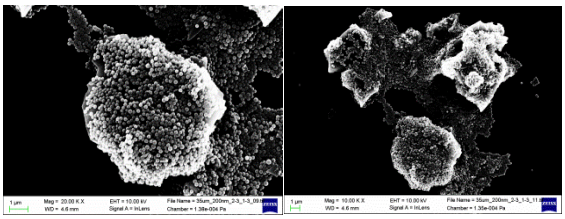

Fig.3.1: SEM pictures of a mix of cationic nano- (200 nm) and microparticles (35 mm) in a ratio 1:2

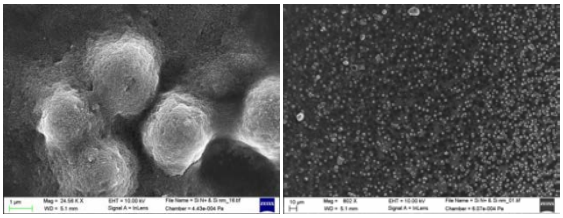

Fig. 3.2: SEM pictures of the coated surface. Encapsulation of the silica cationic microparticles (25% w) with the silica nanoparticles (75% w).

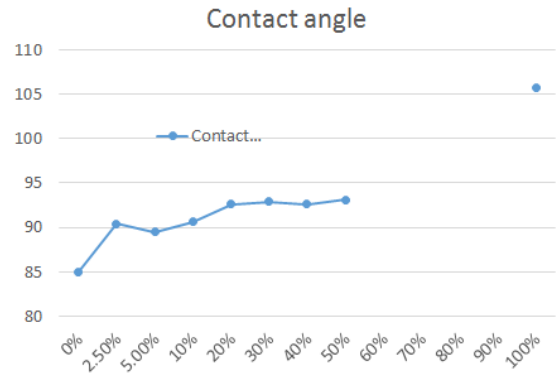

Fig 4: measurement of the contact angle for different ratios of PDMS (polydimethyl siloxane) and linking substance (10%) applied to mix of Fig 3.1.

The quantity of added PDMS was evaluated as a factor increasing the contact angle of the final formulation.

For further improvement of the contact angle values, it was planned to prepare different formulations including a higher ratio of microparticles. In addition, a good covering of the micro particles (4-50 μm) with the nanoparticles (200 nm) should result in a zeta potential higher than +35 mV.

I.2. Bio-approach: Coating formulations based on lotus-like organization obtained with cellulose nanofibers and silica microparticles

The second part of the project was dedicated to the study of nanocellulose fibers' effect in the paint formulation in order to obtain the lotus-like organization. Under controlled conditions of acid hydrolysis treatment and exposure to microwave radiation, rod-shaped cellulose from 70-200 nm in length was obtained, leading to the formation of high-purity single crystals (Fig. 5).

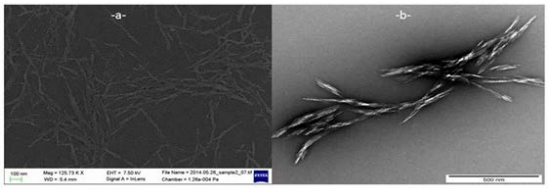

Fig. 5: -a- SEM pictures/-b- TEM pictures of nanocellulose crystals

The nanocellulose crystals were used to encapsulate the cationic silica microparticles as detailed in fig. 6. The obtained organization is followed by UV cross linking of the paint on the surface.

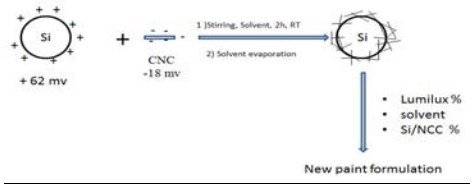

Fig. 6: Development of the self-cleaning surface based on the lotus surface organization

The study of the wetting behavior shows significant increase in the contact angle of the new formulation paint layer compared with unmodified lumilux surface. The SEM pictures (Fig. 7) show the roughness of the surface. The silica microparticles were completely surrounded by nanofibers and the paint is covering the whole system. The new formulation resulted with 35% increase of SCA and therefore an improvement of the surface hydrophobicity.

The use of nanocellulose instead of the silica nanoparticles resulted in improved properties for water repelling.

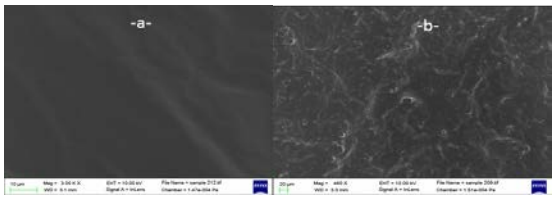

Fig. 7: SEM pictures: -a- unmodified paint surface, -b- paint formulation based on paint, silica microparticles and nanocellulose fibers.

References for Project A8.1

[1] Y. Shimazaki, Y. Miyazaki, Y. Takezawa, M. Nogi, K. Abe, S. Ifuku, H. Yano, "*Excellent Thermal Conductivity of Transparent Cellulose Nanofiber/Epoxy Resin Nanocomposites*", Biomacromolecules **8**, 2976 (2007).

Synthesis and mobility properties of new nanoparticles for colored e-readers

Project A8.3 EL-ENA (FHNW, CSEM Muttenz, BASF Research Center Basel)
Project Leader: U. Pieles
Collaborators: Ch. Jablonski, S. Stebler, G. Grundler, U. Pieles[a], R. Oehrlein[b] and Z. Szamel [c]

a) FHNW, University of Applied Sciences, ICB, Muttenz
b) BASF Research Center Basel
c) CSEM Muttenz

Abstract

A new approach based on non-pigmented, stable colored nanoparticles able upon the application of a current to migrate in the electrical field has been developed for the improvement of the color brightness of e-displays.

The scientific challenges comprise first efficient syntheses of tri- and difunctional dendrimers including branching points for further extension, the covalent attachment of these scaffolds to silica nanoparticles via hydrosilylation and final decoration with the dyes (Fig. 1 yellow, magenta, cyan).

Introduction

New display technologies such as e-paper and e-ink have recently gained significance. However, mostly grey scale electrophoretic displays are available on the market (Amazon Kindle or SONY PRS for example) and the few color displays available on the market lack in picture brightness.

The project aims at the synthesis and characterisation of new nanoparticles attached to a dendrimer of first generation and decorated with a dye (yellow, magenta, cyan). It was established that commercially available silica particles are preferable to gain enhanced brightness of the colors. Three branched and two branched functionalized dendrimers were prepared and evaluated.

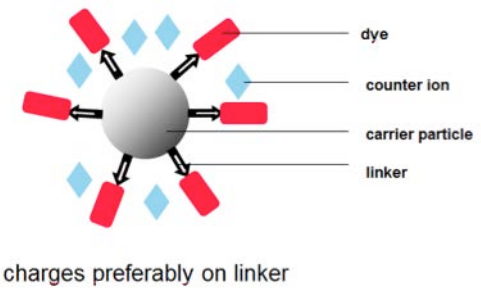

Fig 1: final assembly charged comprising the dye, dendrimer and silica nanoparticles.

Different dendrimer structures were designed individually depending on the functionality present on the dye.

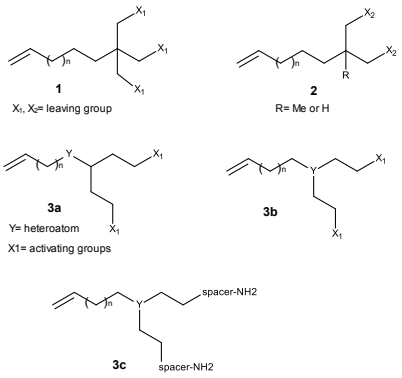

*Fig. 2: structures of the three and two branched dendrimers developed, respectively **1** was too hindered, **2** was used for the yellow dye, **3a** for the magenta dye, **3c** for the blue dye as dendrons for final assemblies.*

In a last stage, in-situ charging enabled the movement of the nanomaterial in an electrical field which was screened in a small customized device at CSEM.

Results

Yellow dye nanomaterials: dendrimer **2** (R=H) reacted readily with a short spacer which formed a sulfonamide with the yellow dye in moderate yield. Subsequent catalytic hydrosilylation conducted to non charged nanoparticles.

Suitable reaction conditions for the activation of the chloride of the yellow dye could not yet be established for the final functionalization of the structure (introduction of a hydrophobic chain and in-situ charging).

Magenta dye nanomaterials: dendrimer **3a** after extension with a short protected spacer was attached to the silica nanoparticles quantitatively. After deprotection of the spacer, the magenta dye was coupled to the particle-dendrimer assembly in good yield.

Final functionalization to increase the solubility and in-situ charging was achieved on 50% of the linkers on small scale. In the six step sequence developed from **3a**, only one purification by chromatography was necessary. The finals constructs were analyzed by ^{1}H and ^{13}C NMR.

Functionalized blue dyes: the originally planned structure was synthesized in five steps which were optimized in good to high yields, The purifications by chromatography were reduced to two steps. However, this blue dye remained completely unreactive in all coupling attempts. Dendron **3c** was finally built for the coupling to a precursor of the blue dye (red color- two step synthesis) which afforded the expected blue dye-dendron construct in limited yield (15%). The latter was attached by hydrosilylation to silica nanoparticles quantitatively and then partly positively charged (50%) by reaction with a compatibilizer.

Tests for the mobility: the final charged assemblies prepared with the magenta and blue dyes were tested applying a voltage of 10-60V of different polarization. The expected results were obtained: the particles were mobile when submitted to the electric field. Unfortunately, the dendrimer-dyes-silica nanoparticles showed agglomerates in all the tests performed. More material should be synthesized to study in more detail the electrophoretic properties.

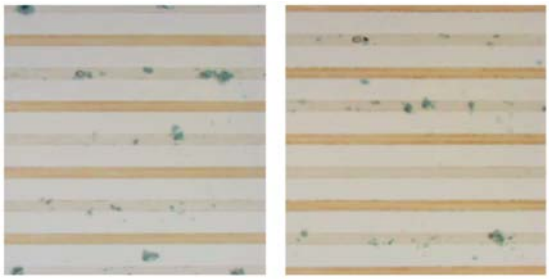

Fig. 3: mobility of blue dye- dendrimer-nanoparticles shown when a voltage of -50V(left) and +50V (right) is applied.

The principle of electrophoretic mobility of the nanoparticles in the electric field is explained on Fig 5a. Films could be recorded showing the movement, the velocity of the particles was influenced by the intensity of the voltage.

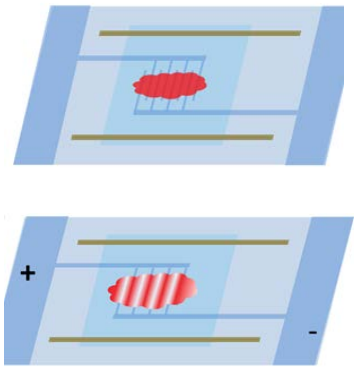

Fig. 4a: charged nanoparticles in an electric field of 10-60V of variable polarisation

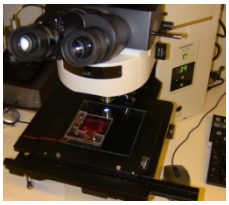

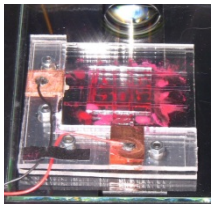

Fig. 4b: device elaborated at CSEM for the test of mobility of charged nanoparticles: ITO electrode thickness 150 μτm, foil thickness used for all the tested particles in the project

Conclusion and further steps

Silica nanoparticles covalently linked to a UV-stable yellow dye via a two branched dendrimer were prepared in nine steps in a good overall yield and limited efforts for purification. However, the introduction of a second linker on the construct enabling particles mobility by electrophoresis is not yet established.

The attachment of the magenta dye to nanoparticles linked to a two branched dendrimer could be optimized and led to a fully functionalized and charged assembly. The mobility of the charged particles was proved at CSEM.

A two branched dendrimer **3c** was prepared for the linkage to a red dye precursor of the blue dye. The coupling was successful in a low yield and would require an optimization by a thorough screening of the reaction conditions (palladium catalyzed Buchwald-Hartwig reaction). The properties of the final assemblies prepared with the magenta and blue dyes showed the expected mobility in an electric field of 10-60V although agglomerates were formed. Further tests would require the preparation of the final assemblies in gram scale..

References for Project A8.3

[1] R. Öhrlein et al. Chimia **63**(6), 351 (2009).
[2] N. Sabourault et al. Organic Lett. **4**(13), 2117 (2002).
[3] A. Marra et al. Eur. J. Org. Chem. 1144, (2013).

Silver-based catalyst development

Project A8.7 NANOX (FHNW, University of Basel, SKAN AG Allschwil)
Project Leader: U. Pieles
Collaborators: O. Scheuber, C. Redard-Jacot and J.-B. Sauvet

Introduction

The aim of the NANOX project is the development of a new efficient catalyst made of metal or metal oxides immobilized on a stable inorganic to allow an easy conversion of methanol into formaldehyde. Following previous studies, silver has been chosen among other catalysts because of its stability. The silver deposition was carried under liquid phase by reducing silver ions to its metal form on a surface.

The most popular method for silver deposition, known as the Tollens reaction, consists in a redox reaction between a silver complex and an aldehyde in alkaline conditions.

The reaction pathway can be described as follows:

$$2\ [Ag(NH_3)_2]^+ + RCHO \rightarrow 2\ Ag^0$$

With $[Ag(NH_3)_2]^+$, the silver diamine complex, obtained by reaction between $AgNO_3$ and NH_3.

During the reaction, an aldehyde, RCHO, is oxidized to its corresponding carboxylic acid while the complex is reduced. In this work, glucose was used as it is a commonly employed aldehyde in Tollens reaction.

In this study, the use of ceramic beads (Fig. 1) was preferred as inorganic carrier. The advantages are the possibility to change the shape of the filter frame and an easier coating in solution.

Fig. 1: Ceramic beads used (~ 5mm in diameter)

Thus, this work takes into account different aspects such as the production method, the optimization of this coating or the use of the catalyst.

Herein, we describe the production of a silver containing catalyst but also a pre study of this catalyst efficiency using Finite Element Method (FEM) based model applied to Computational Fluid Dynamics (CFD) coupled to kinetics and Ergun equation for pressure drop estimations (See below).

$$\Delta P = \frac{150\mu}{Dp^2}\frac{(1-\varepsilon)^2}{\varepsilon^3}L\left(\frac{\Phi}{S}\right) + \frac{1.75\rho}{Dp}\frac{(1-\varepsilon)}{\varepsilon^3}L\left(\frac{\Phi}{S}\right)^2$$

Using this model, the goal of this FEM study is to predict the catalytic activity of a model filter (Fig. 2) to allow a better understanding of the catalytically induced degradation as well as the optimization of the final filter design.

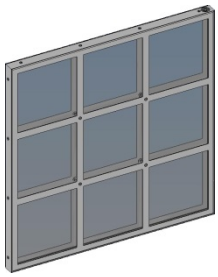

Fig. 2: Model filter for in-silico FEM study of the catalyst (480 mm x 480 mm x 20 mm).

Procedure

Concerning the deposition method, since the requirements are a good reproducibility and a liquid phase process, a direct impregnation of the beads with the Tollens reagent solution appeared as a good alternative. Therefore a procedure for the deposition of silver on highly porous ceramic in solution is proposed.

Before beginning the coating process, the ceramic beads were impregnated with water. This wet substrate was then immersed in a freshly prepared Tollens reagent solution for coating and the glucose solution added to initiate the deposition. The reaction was continued for a total of about two hours. The resulting material was then washed three times using water and finally dried at 80°C.

Morphological characterizations were performed by scanning electron microscopy (SEM) (Supra 40 VP, Carl Zeiss AG, Germany). The predictive FEM calculations for the formaldehyde conversion were obtained using COMSOL software (COMSOL Multiphysics version 5.1) and data from literature and from real conversion process.

Results

During the reaction, the initially white beads slowly turn black. The silver deposition occurs at the surface and is easily visible (Fig. 3) since a slight covering appears on the beads after 20 minutes. However, it is clearly visible that after 2 hours, the coating can be considered as optimal. Indeed, not increase of the deposition was observed. The remaining solution remains limpid.

Fig. 3: Coating procedure on ceramic beads by direct impregnation (left, after 20 min ; right, after 2 hrs).

As it appears on the SEM pictures, the beads topography before (Fig. 4, left) and after silver coating (Fig. 4, right) remains unchanged. This proves the absence of silver clusters formation and confirms the deposition of a silver film as expected to keep the high specific surface of the ceramic material.

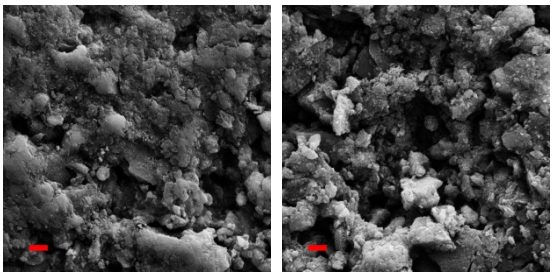

Fig. 4: SEM picture of ceramic beads surface. Non-coated (left) and coated material (right) (scale bar 1 µm).

The study of the methanol conversion by FEM reveals that a filter as described in Fig. 2 is able to degrade a species (Fig.5). This model will then be extrapolated to define or optimize the shape of the filter. Indeed, it appeared that by changing only the design of this one, but using the same volume of catalyst, the degradation efficiency change drastically.

The analysis of fluid velocity (Fig. 5) reveals that the maximum pressure drop is coming from the reduced size of the filter. Indeed, a high flow is expected in the filter macro pores to reach a better conversion. This confirms the importance of the filter design on the catalytic efficiency.

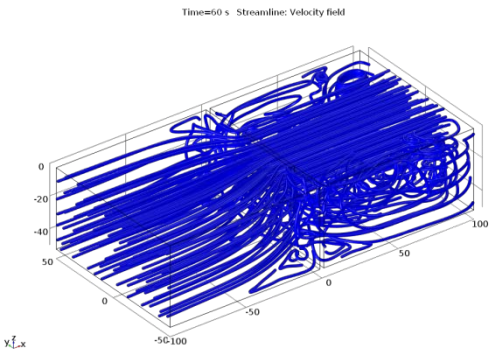

Fig. 5: Velocity predictions for a square type model filter.

Finally, the FEM model also allow to estimate the conversion evolution either by the increase of the fluid flow in the degradation chamber, or by an increase of the catalytic filter thickness (Fig. 6 an Fig. 7).

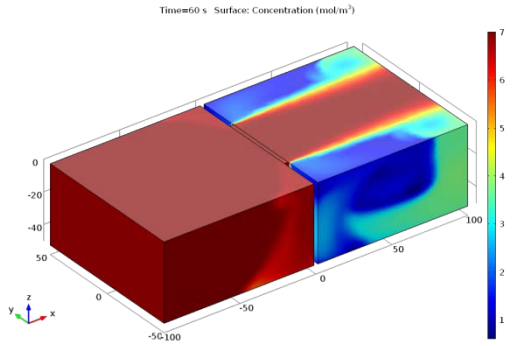

Fig. 6: Formaldehyde concentration estimations

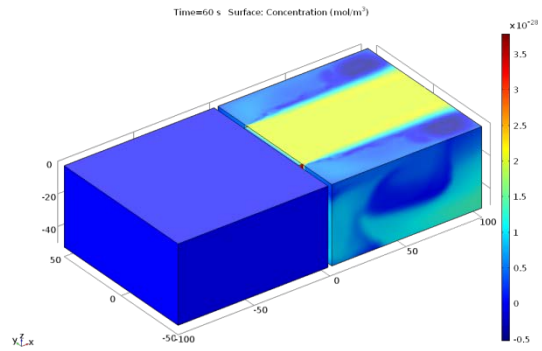

Fig. 7: Methanol concentration estimations

Conclusion

A straightforward procedure is described for the obtaining of a homogeneous silver deposition on a ceramic support. The choice of a liquid phase procedure appears as a good alternative and presents the advantage to avoid the release of harmful aerosols during the production. Considering the easy procedure and the isotropic nature of electroless silver deposition, the obtained product was studied in different ranges of applications. Furthermore the possibility to adapt the filter thickness to the needs should allow tunable oxidation reactions. Further experiments will enable to improve the FEM model and will lead to the obtaining of a well optimized filter.

References for Project A8.7

[1] B.G. Dehkordi and H.H, Jafari, *Numerical simulation of flow through tube bundles in in-line square and general staggered arrangements*. International Journal of Numerical Methods for Heat & Fluid Flow, **19,** 1038-1062 (2009).

[2] S.H. Zhang, *et al.*, *Synthesis of silver nanotubes by electroless deposition in porous anodic aluminium oxide templates*. Chem. Commun., The Royal Society of Chemistry, 1106-1107 (2004).

Polymer emulsion-segmented electroconductive nanofibers for antistatic textile finishing

Project A9.2 em-SELECT (FHNW, PSI, HeiQ Materials AG Bad Zurzach)
Project Leader: U. Pieles
Collaborators: M. Bader, V. Vaché, A. Leisibach (FHNW-ICB), J. Gobrecht (PSI), M. Kristiansen (FHNW-INKA), M. Height and W. Bender (HeiQ Materials AG)

From nanotechnology to new textiles

Introduction

Electrostatic discharges of work-wear's textile as in medical garments, for oilfield's workers or in the electronic industry, may cause hazards, fire incidents, severe damages to the electronic equipment and discomfort for the wearer. State of the art is the incorporation of metal fibers into the textile or use of graphite to obtain durable antistatic properties. These methods exhibit significant disadvantages by limiting the colors and the wear comfort. The target is the integration of wash resistant antistatic properties in the industrial standard finishing process, the last wet process of the textile production chain, which does not affect the other physical properties of the fabric (such as appearance, durability and hand-feel).

The aim of the em-Select project is to produce conductive micro- and nanofibers using a new approach. The conductive fibers have to be applied by the standard padding process in the textile finishing bath, providing antistatic properties to the produced fabric.

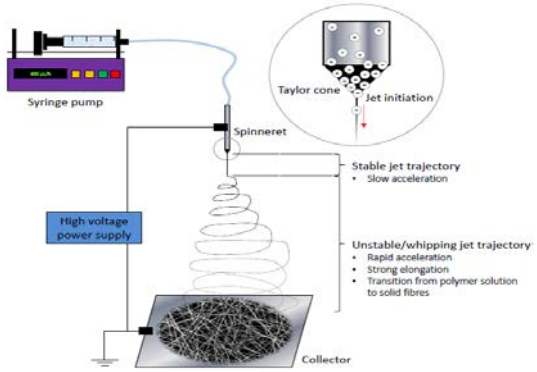

Fig. 1: Schematic representation of electrospinning setup.

These conductive fibers have to be a minor component of the textile and therefore need to be extremely thin and small. The electrospinning technology, presented in Fig. 1, is the most suitable technique for producing such fibers.

Concept

The concept, presented in Fig. 2, is based on fibers made from two different polymers: a conductive polymer that is not soluble in water and a non-conductive polymer, soluble in water, referred to as an auxiliary polymer. For the electrospinning process, an emulsion of the conductive polymer in an organic solvent and the auxiliary polymer in water has to be done. Experiments showed that the vice-versa case is also possible depending on the type of conductive polymer you choose.

The reason of this process is to generate a web of continuous polymeric nanofibers mostly consisting of interconnected conductive with some non-conductive polymer segments. The auxiliary polymer parts will be removed when the fibers are added in a water bath. The network of the remaining conductive fibers of a nano-scale diameter can then be segmented in fibrils by using an Ultra-Turrax mixer, at a high speed and during repeated short time periods. The cutting was tested on auxiliary polymer fibers and the result, in Fig. 3, shows fibrils homogeneous in length.

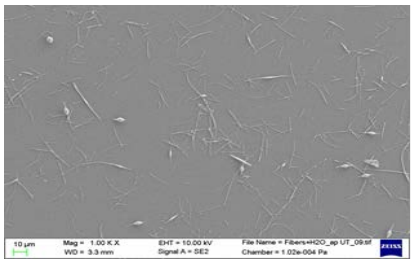

Fig. 3: Auxiliary Polymer Fibers after cutting with Ultra-Turrax.

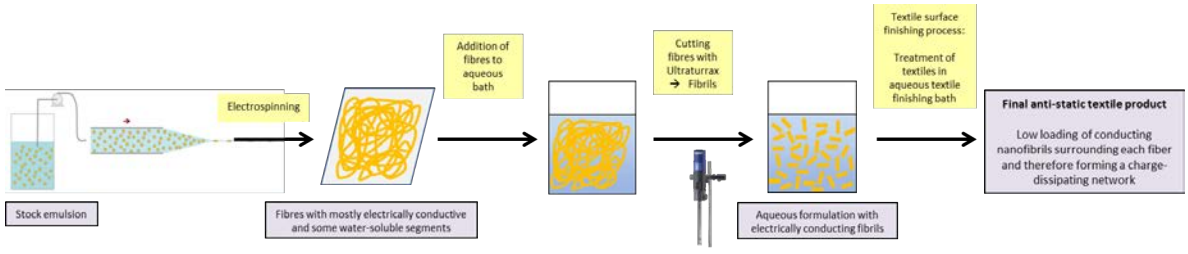

Fig. 2: Stock emulsion electrospinning approach.

Materials

There is little literature about making fibers from conductive polymers. Regarding what is used to make solar panels and simple electrospun fibers, different combinations of conductive and auxiliary polymers were tested. Conductive polymers such as polyaniline (PAni), Poly(3-hexylthiophene-2,5-diyl) (P3HT) and poly(3,4-ethylenedioxythiophene) combined with Polystyrene sulfonate (PEDOT:PSS) were investigated. Some of them are unconductive as such and have to be doped. PAni was doped with camphorsulfonic acid (CSA).

Auxiliary (non-conductive) polymer such as poly(methyl-methacrylate) (PMMA) and polyethylene oxide (PEO), of different molecular masses, were mixed with the conductive ones to get the nanofibers' web. Solvents such as dimethyl-acetamide (DMAc) or chloroform ($CHCl_3$) were used to solubilize the polymers.

Results

From the auxiliary polymer alone, fibers with an average diameter of 110 nm could be produced from the electrospinning process. Combinations of conductive and non-conductive polymers were tested. The main hurdles of this project are the low solubility of the conductive polymers in organic solvents, preparation of stable dispersion and formation of bead-less fibers from the spinning process.

Some conductive polymers can be spun alone in organic solvents, such as P3HT in $CHCl_3$, but the fibers are more likely to be electrospray than electrospun, resulting in a collector full of droplets. Experiments showed that better results are achieved when the polymers are electrospun coupled with an auxiliary polymer. The fibers are also improved, in some cases, when adding surfactants (such as SLS or Triton X-100) [1]. Others variations, such as the molecular masses of the auxiliary polymers and optimization of the electrospinning parameters lead to fibers that were more in the diameter range we were looking for.

Two couples of polymers were mostly investigated since they showed good results: P3HT coupled with PEO in $CHCl_3$ and PEDOT:PSS coupled with PEO in water. One of the good point of P3HT is it's well solubility in organic solvent, due to the fact that it is inactive as such and has to be doped, which leads to high concentration of it in the fibers. The spinning process is also quite easy and gives lots of fibers with a diameter under 1 µm, like shown in Fig. 4.

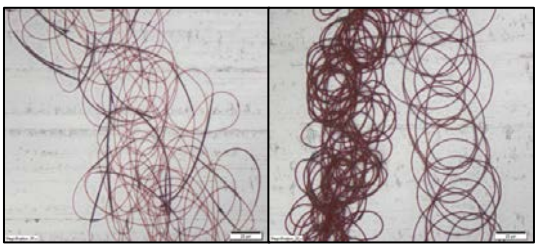

Fig. 4: LM (relfection) of electrospun P3HT/PEO Fibers on aluminium collector. Scale bar 20 µm.

Unfortunately, the doping of those fibers is not stable in time and it is difficult to isolate one fiber to control its conductivity.

More experiments were done with the PEDOT:PSS couple since the first results were promising. The dispersion of the polymer is also easy but to have an enough concentrated solutions, we had to use less auxialiary polymer. Good results could be achieved, with fibers having a diameter around the µm, as shown on Fig. 5. The main problems with those solutions were the low amount of fibers produced and the low reproducibility of the spinning process.

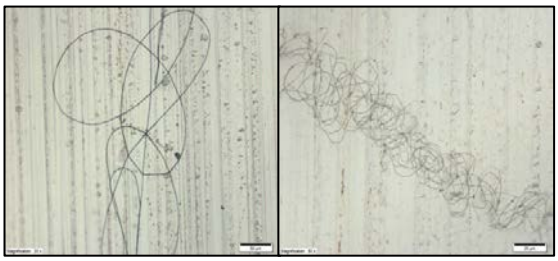

Fig. 5: LM (relfection) of electrospun PEDOT:PSS Fibers on aluminium collector. Scale bar left 50 µm, right 20 µm.

Conclusion

It is possible to produce uniform and bead-less fibers of different combinations of electrically conducting polymer with an auxiliary polymer around. It is possible to achieve good diameter under 1 µm and have a lot of them.

The main problem remained throughout the trials in the lab: the dispersion of the conductive polymer being most of the time quite difficult, it was finally not possible to measure properly the conductivity on a single fiber.

The reasons for that are: the amount of conductive polymer in the final product was apparently too low or badly dispersed throughout the fibers and it is difficult to isolate single fibers when hundreds are spun.

Despite that, some conductivity measurements were conducted on the fibers web produced and a good conductivity was achieved.

Polymer-blend-solution's homogeneity and electrospinning process parameters were improved and more controlled but those improvements only allowed us to approach the goal. Due to confidentiality agreements and the end of this project, latest and more advanced results cannot be shown here.

References for Project A9.2

[1] B. Fan, Significant conductivity enhancement of conductive PEDOT:PSS films by adding anionic surfactants into polymer solution, Macromolecules **41** 5971-5973 (2008).

Functionalized nanofiber-enhanced filter media for capturing elemental mercury in gases: optimization of synthesis and testing results

Project A9.6 NANOFIL (PSI, FHNW, Alstom AG Birr)
Project Leader: C. Ludwig
Collaborators: M. Tarik, M. Paraskevopoulos, F. Pilger, A. Testino, M. Waser, U. Pieles, D. Winkler, G. Timothy, I. Thanou and M. Bialkowski

Introduction

In order to improve the performance of the current fabric filter systems, e.g. more efficient fine particle removal and higher specificity for heavy metals, either in the ionic or in the elemental state, an entirely new approach was planned. The strategy was to develop materials with high specific surface area, thermal and mechanical stability, and functionalized with sulfur (S) groups, which have high specificity for heavy metals.

During the first year, the "NANOFIL" project was devoted to the development of new organic, inorganic, and composite nanofibers. The organic nanofibers are produced by electrospinning, the inorganic material is based on hydrothermally prepared cerium dioxide (CeO_2) nanoparticles. In the second year of the project, the synthesized fibers were tested by using an in-house constructed setup, to evaluate the Hg sorption properties, and thermal stability.

Synthesis of nanofibers

For the selection of the base filter material, the flue gas temperature, continuous and peak, is the most important criterion for filter media selection. Fibers can survive short term exposure to temperatures above their continuous operating temperature limit, but the high heat will degrade them. Additionally, chemical attack, such as contacts with acids and alkalis, can have similar effects. For the manufacturing of the project's filter media, two materials have been selected: polyphenylene sulfide (PPS) and P84 (Polyimide). The latter has outstanding properties such as high temperature stability, good chemical resistance, high mechanical strength and minimal abrasion. Since the nanofibers will be applied in the same environment as the base material, P84 was also chosen as the material for the electrospinning. P84 was electrospun as a solution in DMF to produce nanofibers that can be tailored from diameters of approx. 60 nm up to 1 µm.

In this project nanofiber materials able to capture S were developed, which can then be used to remove specific heavy metals such as Hg from flue gases. One way to achieve that was to modify the P84 material to bear thiol groups which can sorb mercury. Therefore the electrospun P84 nanofibres were reacted with cysteamine (See figure 1 in the SNI report 2014).

Alternatively CeO_2 nanoparticles were synthesized and their capability to capture sulfur was investigated. The activated nanoparticles can be directly deposited on the base filters (Figure 1) or electrospun as composite along with P84 (See figure 2b in the SNI report 2014).

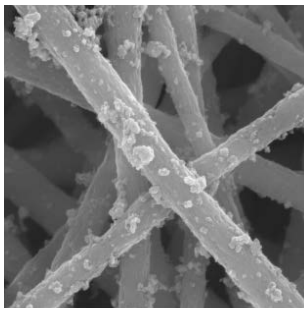

Figure 1: Example of CeO_2 modified fibres: SEM of CeO_2 deposited on fibres.

Functionality tests on the developed filters

The testing setup has been designed and constructed and is able to provide a specific mercury concentration in a flow of argon by use of a permeation tube (Figure 2). The volume flow of argon is kept at 1 L/min. The Hg permeation tube consists of a plastic container filled with a two phase equilibrium (liquid and gaseous) of mercury. The permeation tube is placed inside a glass tube, which itself is surrounded by a temperature-controlled water bath. Depending on the temperature and the dilution flow a defined rate of mercury is generated. The resulting Hg permeation rate is approximately 100 ng/min at 70 °C. The mercury-laden gas is led through heated PTFE pipes (also at 70 °C to avoid recondensation of Hg) into an oven at 180 °C. Two filter holders inside the oven are equipped with different nanofiber-enhanced filters (Figure 3). After passing the filters the remaining Hg is removed by 2 impinger bottles containing $KMnO_4$ in a 10 %-H_2SO_4 solution [1].

Once the set-up is properly heated the operating regime is defined by loading the filter with Hg for 30 minutes and another 30 minutes of Hg-free gas flow

through the filter afterwards. This is accomplished by a three way valve, which allows the bypassing of the permeation tube. The filters are removed from the oven (at room temperature) and were preserved in glass bottles.

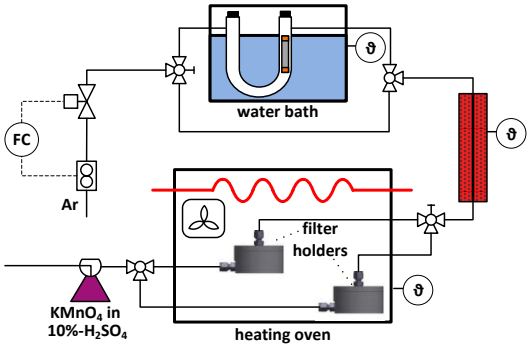

Figure 2: Schematic test setup for the removal of Hg from an Argon carrier gas with nanofiber filters.

Figure 3: Drawing (left) and picture (right) of the filter holder.

Analysis of Hg-treated filters

Inductive Coupled Plasma Mass Spectrometry (ICP-MS), which is a well-known powerful technique for elemental analysis, was used for the analysis of the tested filters. However, Hg has a relatively high first ionization potential (10.44 eV) and is easily lost in water-based solutions [2,3]. Therefore, two reported methods in the literature for the ICPMS analysis of Hg using diluted aqua regia (HCl 3% and HNO_3 1%) alone or along with 100 ppb Au solution (as $AuCl_3$) were tested. Transient ICP signals (intensity versus time) were recorded and Hg calibration was carried out using concentrations ranging from 0.02 to 100 ng/ml (Figure 4). In both cases the response time was below 2 s and the ICP-MS signal of 1.14 ppb Hg solution, for example, showed a RSD of 2.4% over 5 min measuring duration. Hg sensitivity of more than 1.6 10^4 cps/(ng/ml), and LOD (limit of detection) of 10.2 pg/ml were calculated. Based on these results diluted aqua regia without Au was used for the analysis of Hg.

The three tested filters (conventional, reference and modified filters) were cut and digested in a high-pressure microwave digestion using concentrated HCl (9.75 ml), HNO3 (1.5 ml) and H2O2 (0.5 ml). The digested solutions were then diluted with MilliQ water. The calibration and sample solutions had a final HCl and HNO3 concentration of 3% and 1%, respectively. Four Hg isotopes and two S isotopes with an integration time of 0.2 s were measured using helium as collision gas. Two measurements at different dates (one 1 week and another one month after the Hg loading test) were carried out, and their results are summarized in table 1.

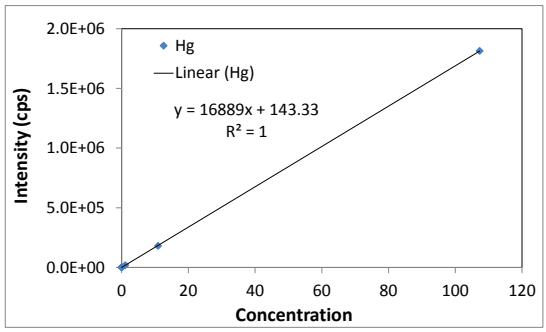

Figure 4: Calibration curve of mercury using diluted aqua regia (HCl 3%, HNO3 1%).

Table 1: ICP-MS results of the Hg analysis for three tested filters.

	Filter	Filter weight (mg)	Average Hg conc. (ng/g)	Hg amount/filter weight (ng)
Hg	Conventional Filter	1428.2	58.4	82.7
	Reference Filter	301.1	102.1	30.4
	Modified Filter	435.1	575.3	247.7

An average enhancement factor in Hg concentration in the filter modified with thiol of more than 5.6 and 9.8 were found compared to the conventional and reference filters, respectively. A decrease of Hg content in the second measurement for the 3 filters were observed, which might be due to the Hg distribution on the filters, samples preparation or physical desorption. In the modified filter higher content of S were measured (~ 27 mg/g) as expected, which maybe caused by the presence of unbound S on the electrospun fibers.

Conclusions and outlook

In the second year of the NANOFIL project, the synthesis of the nanofiber materials, were further optimized. The capability of Hg capturing was demonstrated by loading elemental Hg on the electrospun filters bearing S groups and subsequent ICP-MS analysis. Hg concentration on the modified filter were about 575 ng/g and was more than 5 times higher than that of the reference filter. After the proof of concept, other filter geometries need to be tested, in order to study its effect on the Hg capturing capacity. For a complete quantification of their Hg capturing capacity, online Hg measurement should be carried out, in order to determine the Hg capturing breakthrough curve.

References for Project A9.6

[1] Determination of particulate and gaseous mercury emissions from sewage sludge incinerators, Method 101A, US EPA.

[2] Agilent ICP-MS Journal, February 2011 – Issue 45, Successful Low Level Mercury Analysis by ICP-MS, Ed McCurdy.

[3] Mercury preservation techniques, US EPA environmental protection agency.

Numerical design and manufacturing development of trenched nanoscale MOS-controlled FETs

Project A9.7 NanoSiCTrenchFet (CSEM, PSI, University of Basel, ABB Baden-Dättwil)
Project Leader: M. Schnieper
Collaborators: H.R. Rossmann, F. Zanella, N. Marjanović, M. Schnieper, T.A. Jung, E. Meyer, J. Gobrecht, R.A. Minamisawa and H. Bartolf

Introduction

One of the main obstacles in state-of-the-art planar SiC metal–oxide–semiconductor field-effect transistor (MOSFET) technology is the comparably low carrier mobility inside the thin conducting channel that forms if a sufficiently high gate voltage is applied. This effect has been attributed to defect states at the SiC/oxide interface which cannot be as easily passivated as in the case of Si by hydrogen annealing. An alternative to physically complex passivation processes, whose underlying mechanism is still not clearly understood, is offered by aligning the channel along different crystal facets which have demonstrated higher mobilities. Furthermore, the U-shaped trench geometry benefits by a higher cell density and by the abandonment of the junction gate field-effect transistor (JFET) region.

Process Workflow

A simplified scheme on the main processing steps of the SiC trench MOSFET is illustrated in Fig. 1a-f. With the exception of the dopant implantation (Fig. 1a) and the polycrystalline Silicon (poly-Si) filling (Fig. 1d) all fabrication steps are carried out at the LMN clean room facilities at PSI.

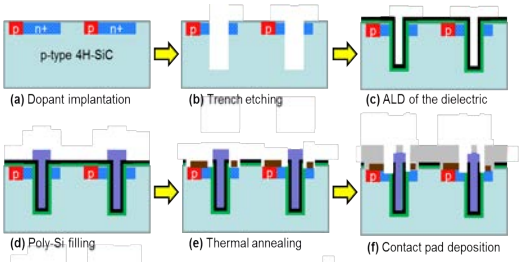

Figure 1a-f: Simplified cross-sectional view on the main fabrication steps of the SiC trench MOSFET process flow.

During the first year an inductively coupled plasma (ICP) based dry etching process (Fig. 1b) has been established and optimized to avoid undesired trenching effects/sharp edges that would cause high electric field strengths and a premature breakdown of the device at reverse bias conditions [1]. Thereafter the focus of the project work has been put to the 4H-SiC/oxide interface since it is well known that a high density of interface states D_{it} significantly degrades the output characteristics of the final MOSFET device [2]. For testing the gate oxide quality the capacitance versus voltage (*C-V*) characteristics of a thermally grown SiO_2 layer have been compared to an ALD (Atomic Layer Deposition) deposited Al_2O_3 dielectric for planar and trench geometries in terms of their interface state densities. Further, the transition from a Schottky to an ohmic contact behavior has been studied at the interface between the highly doped wafer substrate and Ni. It has been demonstrated that after annealing at 1000 °C for more than 20 s the Ni/SiC contact becomes ohmic. For extracting the Schottky barrier height by the means of *C-V* measurements, 20 Schottky diodes have been fabricated and characterized. The measured barrier height was found to be ϕ_B=1.79 V with a device-to-device variability of 5% which is in reasonable agreement with literature values [3].

MOS Capacitors

In a second step of the project, MOS capacitor devices have been fabricated fully 'in-house'. A cross-sectional electron micrograph of a trench MOS capacitor comprising a deposited oxide below a 500 nm thick Al film is shown in Fig. 2. The thermally grown SiO_2 is of limited thickness of about 10 nm due to the fabrication type of the available oxidation furnace; in contrast, the dielectric layers deposited by ALD can easily reach 50 nm which is state-of-the-art in power devices. In the latter case the experimentally measured values of 40–50 nm match the targeted layer thickness.

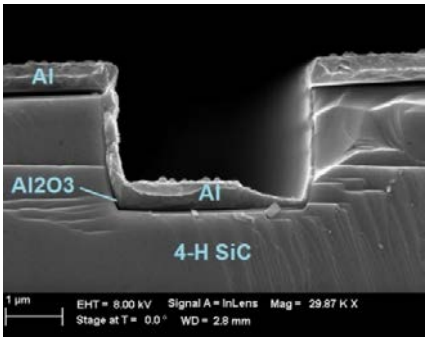

Figure 2: Cross-sectional electrograph of the fabricated trench MOS capacitors within the NanoSiCTrenchFet project. U-shaped trenches have been etched into p-type 4H-SiC epi layers prior to Al_2O_3 dielectric and Al contact deposition.

In order to evaluate the electronic characteristics of these trench MOS capacitors, *C-V* measurements were performed at a frequency of 1 MHz. As shown in Fig. 3 the first sweep caused a charging of

interface trap states and hence the threshold voltage (V_T) of subsequently recorded curves is shifted towards higher values.

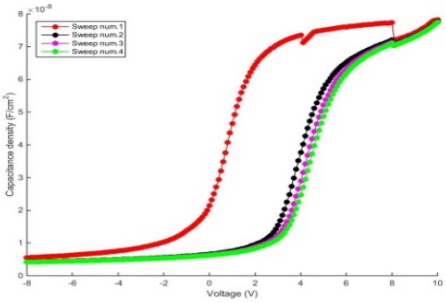

Figure 3: C-V curves recorded for a trench MOS capacitor with ALD deposited Al_2O_3. 4 subsequent bias voltage sweeps are shown.

Device Parameters Extractions and Simulations

In the ideal case the MOS interface between the semiconductor and the insulator is electrically neutral. In real devices however, the insulator is not electrically neutral due to defects or trapped charges at the interface. Electrons or holes can be trapped in these states and they can disturb the device performance e.g. V_T. A figure of merit to characterize the quality of the interface between the insulator and the semiconductor is the interface trap density D_{it}. The D_{it} values can be extracted out of *C-V* measurements following the low and/or high frequency method [4]. CSEM's semi-automatic probe station TP-10 allows measuring, among others, *C-V* and *C-f* characteristics. Then the results are analyzed with CSEM's parameter extraction platform [5] in order to extract, e.g. D_{it} (Fig. 4).

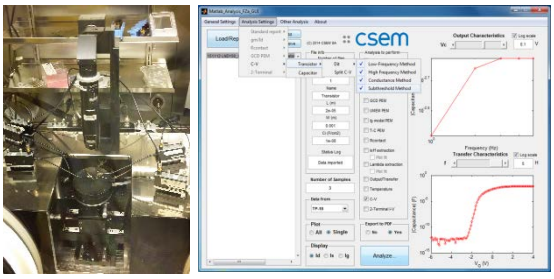

Figure 4: CSEM's TP-10 setup (a) and parameter extraction platform (b).

CSEM measured 130 trench MOS capacitors fabricated at PSI ($C = 20 \pm 7$ nF/cm² at $V = 0$ V and $f = 1$ MHz). Fig. 5 shows the interface trap density, D_{it}, extracted from such a capacitor. The obtained values of the D_{it} in the accumulation regime are in the range of $10^{10} - 10^{12}$ $cm^{-2}eV^{-1}$, which are typical for SiC.

The influence of trap states was investigated by Sentaurus TCAD (Technology Computer Aided Design) simulations at the University of Basel. At concentrations above 10^{11} cm^{-2} the *C-V* curves start to shift towards higher voltages. A comparison with experimental data (cf. Fig. 3) indicates concentrations of $10^{12} - 10^{13}$ cm^{-2}. The static simulations show both branches (accumulation/ inversion), whereas the experimental *C-V* curves do not show inversion due to the absence of minority carriers due to the wide-band gap of ~3 eV of the Silicon Carbide crystal.

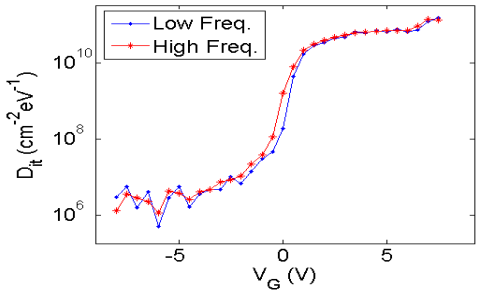

Figure 5. Interface trap density (D_{it}) versus gate voltage for a trench MOS capacitor.

Therefore, the analysis of the *C-V* curves (Fig. 6) can be used to determine the trap concentrations and to probe the influence of these trap states upon the performance of the MOSFET devices.

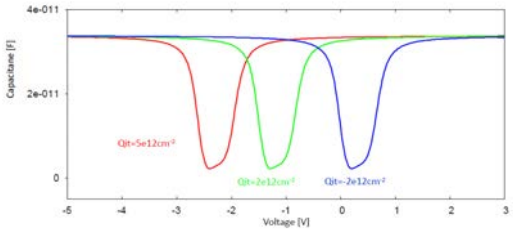

Figure 6: Capacitance vs. applied top voltage as a function of different trap densities.

Conclusion

SiC-based MOS capacitors were fabricated and characterized containing both thermally grown and ALD deposited gate oxide layers. Several D_{it} extraction methods were implemented in order to fully characterize and understand the interfacial trap states. We demonstrated impressively [1] by numerical simulations the superiority of the 4H-SiC trench MOSFET geometry with respect to the planar one.

The development of a manufacturing scheme for MOSFET's to be fully characterized is underway.

References for Project A9.7

[1] H.R. Rossmann et al., Microelectron. Eng. **145**, 166-169 (2015).
[2] J. Rozen et al., IEEE Trans. Electron Devices **58**, 3808-3811 (2011).
[3] A. Itoh and H. Matsunami, phys. stat. sol. (a) **162**, 389-408 (1997).
[4] Dieter K. Schroder, Semiconductor material and device characterization, IEEE press, (2006).
[5] F. Zanella, PhD Dissertation, EPFL (2014).

*NANO*zyme: Nanobiocatalysts based on artificial metalloenzymes

Project A9.9 NANOzyme (FHNW, University of Basel, INOFEA AG Basel)
Project Leader: P. Shahgaldian (FHNW)
Collaborators: P.F.-X. Corvini (FHNW), T.R. Ward (University of Basel), M. Hestericová (PhD Student University of Basel), B. Ricken (PhD Student FHNW), M.R. Correro (FHNW), and Y. Dudal (INOFEA AG)

Introduction

Biotechnology is predominantly based on the ability of enzymes to efficiently catalyze chemical reactions. Indeed, enzymes are potent biocatalysts that operate under mild conditions with high regio- and stereo-selectivity, elevated turnover rates, and often good substrate selectivity. However, the use of enzymes in industrial processes is limited by their significant fragility and fast decay in non-physiological environments. Additionally, the industrial use of enzymes necessitating organic cofactors is strongly hindered by their prohibitive price and instability. The efficient chemical and electrochemical recycling of enzyme cofactors such as nicotinamide adenine dinucleotide (NAD) is of high interest for white biotechnology and pharmaceutical applications and has been intensively investigated as an alternative to enzymatic regeneration. [1]

The group of TW has developed a series of different artificial metalloenzymes.[2] The groups of PFXC and PS have jointly developed a chemical strategy to grow at the surface of silica nanoparticles a layer of organosilica with a nanometer-precision.[3] This approach has been successfully applied to develop stable nanobiocatalysts. The present works aims at combining both approaches to create novel nanobiocatalysts, which allow the in situ regeneration of organic cofactors (*e.g.*, NADH, $FMNH_2$).

Results and discussion

In order to develop an enzymatic system possessing the ability to regenerate NADH *in situ,* an artificial transfer hydrogenase (ATHase)[2] and a NADH-dependent FMN reductase (RED) were produced, co-immobilized on the surface of silica nanoparticles (SNPs) and further embedded in an organosilica layer (Fig. 1).[3]

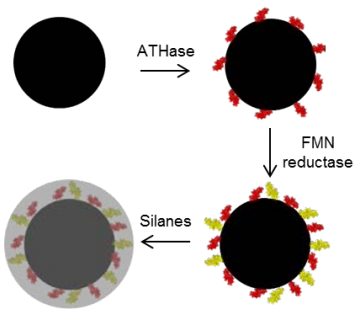

Fig. 1: Schematic representation of the sequential ATHase and RED co-immobilization and protection

Production of ATHase and RED – Artificial transfer hydrogenases (ATHases) are created by the non-covalent incorporation of an organometallic cofactor within streptavidin mutants (Sav), which are genetically optimized by the introduction of point-mutations on the Sav gene. A series of different streptavidin (SAV) isoforms with mutations at positions S112 and K121 were produced and screened for enantioselective transfer hydrogenation of cyclic imines (salsolidine) or the NAD^+ reduction. Among the different SAV mutants, the [Cp*Ir(biot-p-L)Cl] · S112A-K121A (ATHase) revealed the highest catalytic activity toward NAD^+ reduction. Thereafter, it was chosen as artificial enzyme to produce the first intermediate (NADH) of the chain reaction.

The RED was heterologously expressed in E. coli. For the ease of purification and for the increase of soluble RED a His6 followed by a SUMO-tag was cloned to the 5' end of red. After IMAC purification the His6-SUMO tag was cleaved by Ulp1 digestion before immobilization.

Nanobiocatalyst synthesis - In order to efficiently co-immobilize the selected ATHase and RED onto SNPs, a series of important parameters (temperature, pH and buffer composition) were carefully evaluated. Moreover, since the natural RED is a very efficient catalyst compared to the artificial ATHase, the adequate ratio of the two enzymes was assessed and optimized. A sequential co-immobilization of the ATHase and RED was successfully achieved by using glutaraldehyde as a crosslinker. The controlled organosilica layer growth was achieved by incubation of the SNPs in a mixture of organosilanes; the SNPs produced were analyzed by means of scanning electron microscopy (Fig. 2). Optimization of the synthetic conditions allowed producing a protective layer of 10 nm fully shieleding the immobilized enzymes.

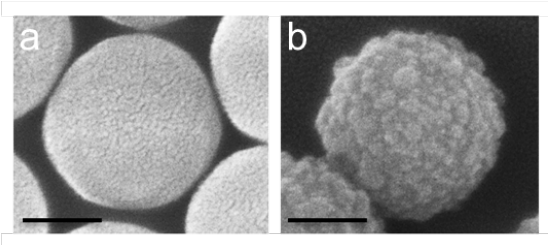

Fig. 2: SEM micrographs of SNPs before (a) and after (b) the layer growth (scale bars represent 100 nm)

Biocatalytic activity testing - The immobilized and protected ATHase displayed an enhanced catalytic

activity with regard to the soluble catalysts. The turnover numbers were calculated based on the iridium content, which was quantified by means of ICP-MS. Dried SNPs contain approx. 0.04 ng Ir / mg SNPs. Importantly, the SNP could be recycled at least twice, with only a slight decrease in conversion rates (Table 1). In order to demonstrate the efficiency of the protected catalysts, further experiments were performed in complexes biological media including cell lysates (CL), cell free extracts (CFE), milk, blood, serum and urine. In all the tested conditions, the protected catalysts successfully performed the salsolidine precursor reduction (Table 2).

Table 1: Asymmetric imine reduction yielding salsolidine. The reactions were performed using silica nanoparticle-immobilized ATHases.

entry	SNP	reaction type	ee (%)	Conv. (%)	TON
1	[Cp*Ir(biot-p-L)Cl]·S112A SAV	1st reaction	52	21	75758
2		1st recycling	51	14	48887
3		2nd recycling	58	14	49541
4	[Cp*Ir(biot-p-L)Cl]·S112K SAV	1st reaction	-56	22	78926
5		1st recycling	-53	12	41814
6		2nd recycling	-58	9	33025
7	[Cp*Ir(biot-p-L)Cl]·K121A SAV	1st reaction	13	59	213003
8		1st recycling	14	33	118067
9		2nd recycling	8	26	92014
10	Cp*Ir(biot-p-L)Cl]·S112A-K121A SAV	1st reaction	36	96	346114
11		1st recycling	29	89	319147
12		2nd recycling	26	78	282731

Table 2: Salsolidine reduction in different biological matrices by immobilized and protected ATHase.

entry	SNP	Cellular debris	ee (%)	Conv. (%)	TON
1	Cp*Ir(biot-p-L)Cl]·S112A-K121A SAV	milk	41	24	85515
2		yeast extract	37	1	4112
3		urine pH 6	25	11	39239
4		blood pH 7	35	1	5349
5		blood serum	27	6	20060
6		empty vector CFE	89	3	11222
7		empty vector CL	33	1	5262

Cascade reaction screening - In order to evaluate the NADH regeneration resulting from a cascade reaction, a soluble luciferase was added into the system. The luciferase, in the presence of O_2, oxidizes $FMNH_2$ into FMN and releases H_2O_2. The ATHase–RED cascade was performed in the presence of luciferase and the production of H_2O_2 was monitored spoectrophotometrically over time. As depicted in Fig. 3, the amounts of H_2O_2 produced by the protected catalysts were 7.6, 10.5 and 11.7 μg mL^{-1} after 1, 2 and 3 hours respectively. The soluble enzymes produced only 4.1, 5.8 and 8.8 μg mL^{-1} after 1, 2 and 3 hours and the immobilized non-protected enzymes showed the lowest catalytic activity with 1.7, 3.5 and 7.0 μg mL^{-1} after 1, 2 and 3 hours respectively. This set of results represents a clear proof of the positive effect of the enzyme/substrate confinement in a cascade reaction.

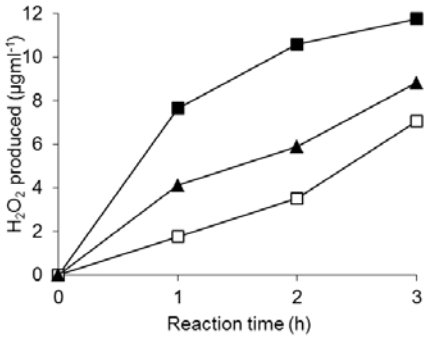

Fig. 3: H_2O_2 quantification as indicator of the cascade reaction for protected (full squares), immobilized only (empty squares) and soluble enzymes (triangles)

Outlook

We have successfully developed a nanobiocatalyst that catalyzes a cascade reaction allowing cofactor regeneration "*in situ*". The cascade reaction is catalyzed by *a)* two different enzymes immobilized on SNPs and protected by an organosilica layer and *b)* a soluble enzyme which uses as cofactor the product of the enzymatic cascade. We have demonstrated that the cascade reaction catalyzed by the protected enzymes is improved compared to the one produced with soluble enzymes or with simply immobilized enzymes. These results suggest that the protective layer not only causes a beneficial substrate confinement, but also enhances the enzymatic activities of the protected catalysts.

Next steps include the development of detection kits for the detection/screening of sulfonamide antibiotics-resistant bacteria. Because of its high potential, the produced nanobiocatalysts, may find applications not only in pharmaceutical/health care industry but also in sustainable processing and production of chemicals and fuels.

References for project A9.9

[1] V. Kohler, Y. M. Wilson, M. Durrenberger, D. Ghislieri, E. Churakova, T. Quinto, L. Knorr, D. Haussinger, F. Hollmann, N. J. Turner, T. R. Ward, *Synthetic cascades are enabled by combining biocatalysts with artificial metalloenzymes*, Nat. Chem. **5**, 93 (2013).

[2] T.R. Ward, *Artificial metalloenzymes based on the biotin-avidin technology: enantio-selective catalysis and beyond,* Acc. Chem. Res. **44**, 47 (2011).

[3] A. Cumbo , B. Lorber, P.F. Corvini, W. Meier, P. Shahgaldian, *A synthetic nanomaterial for virus recognition produced by surface imprinting,* Nat. Commun. **4**, 1503 (2013).

Improving resorbable polymer implants by topographical surface structuring – part II: cellular response

Project A9.10 PATCELL (FHNW, PSI, Synthes GmbH Oberdorf)
Project Leader: P.M. Kristiansen
Collaborators: C. Rytka, S. Neuhaus, M. Grob, U. Bruggisser* (FHNW-INKA), J. Köser (FHNW-ICB), R. Holtz (FHNW-IPPE), V. Guzenko (PSI) and S. Beck (Synthes GmbH)
* former team members (UB now at Roche Diagnostics International AG)

Motivation

Beneath a number of other factors, the surface properties of a biomaterial are responsible for its acceptance in a host tissue. An implant surface tailored to better interact and to attract the favored cellular tissue, e.g. a bony or a soft tissue, will more easily integrate into the host tissue. A better assimilated biomaterial is generally considered to be more successful and allows for an uneventful use according to its application. This is especially true for resorbable polymer implants.

For this purpose, the effect of surface structuring on different length scales on the cell response to such topographically modified polymer implant materials is investigated.

While the first project year was mainly concerned with the production of structured poly(lactide-co-glycolide) (PLGA) samples, the second year focused on the characterization of cellular responses on these samples.

Surface structuring of polymers

Surface structures of two different cell-dimension related classes were analyzed: a) *sub-cellular sized features* (5-20 µm) with a height of 5 µm, and b) *cell-harboring micro-wells* with diameters D = 10, 30, 50 and 100 µm, depths of D/2 and spacings d = 10, 30, 50, 100 µm.

Master structures with subcellular sized features were successfully replicated into 250 µm films of PLGA by *hot embossing* and fully characterized by laser-scanning confocal microscopy (LSCM). Comparison of the topographical characterization of master and replica, respectively, revealed that high fidelity replication was achieved.

PLGA samples with a panel of different cell harboring micro-well structures were produced by injection molding. Micro-well master structures were laser machined into stainless steel and subsequently replicated into poly(phenylene sulfone) (PPSU) by hot embossing to yield inverted tone structures that served as mold insert for *injection molding* of PLGA samples (see Fig. 1).

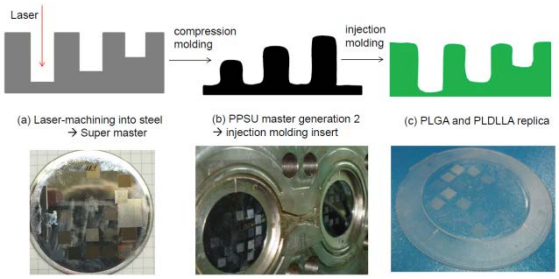

Fig. 1: Scheme of the process chain used for injection molding of PLGA substrates with a panel of different cell-harboring micro-well structures. The depicted PLGA sample (lower right) has a diameter of 6.5 cm.

Cellular morphology and nuclear shape

MC3T3-E1 pre-osteoblastic cells were grown on the micro-structured substrates and their morphology and nuclear shape subsequently analyzed by fluorescent staining of the actin cytoskeleton with rhodamine-phalloidin and the DNA with DAPI. It was observed that on substrates with well structures with a diameter of up to 20 µm (regularly or irregularly shaped) cells preferred to grow on top of the structures whereas on pillar structures the majority of the cell bodies is squeezed in between the elevations as evidenced by the deformed nuclei in between individual pillars (Fig. 2).

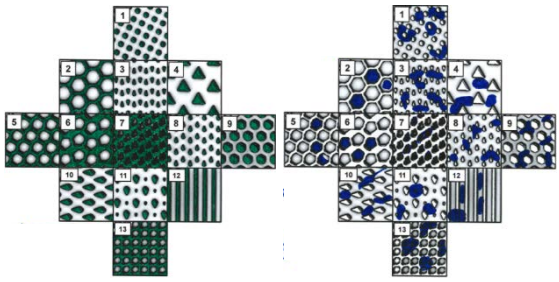

Fig. 2: MC3T3-E1 osteoblast cell and nuclear morphology on micro-patterned PLGA substrates. Experiments were performed on multi-pattern embossed PLGA substrates with a 2x2 cm area each. Left: Scheme of the multi-patterned samples analyzed by LSCM (green indicates the top level of the PLGA substrate), right: schematized nuclear morphology observed on the different microstructures.

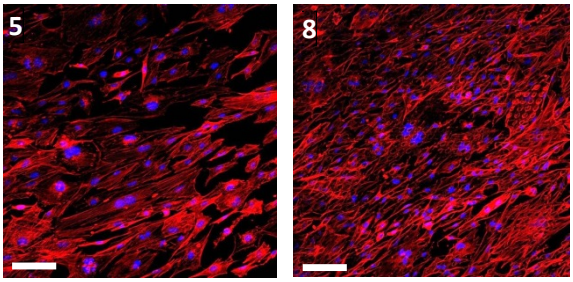

Fig. 3: Micrographs of rhodamine-phalloidin/DAPI double stained MC3T3-E1 cells on patterns No. 5 and 8 (details see Fig. 2). Scale bars 100 µm.

Cell proliferation

To assess influences of certain substrate patterns on the cell proliferation, MC3T3-E1 osteoblast cells were grown on structured PLGA substrates and quantified using the metabolic stain Alamar Blue®. All patterns reduced cell proliferation with the strongest effect being an inhibition of more than 40% (structures marked in red in Fig. 4).

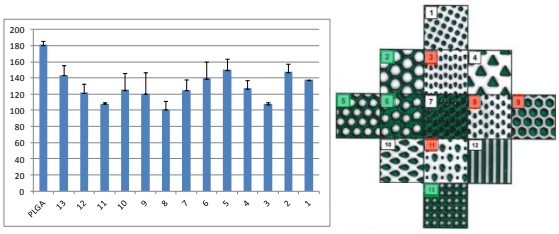

Fig. 4: MC3T3-E1 osteoblast cell proliferation on micro-patterned substrates in comparison with unstructured PLGA. Proliferation was assayed with the metabolic stain Alamar Blue® (left side, arbitrary units). Schematic representation of the patterns allowing best proliferation (marked in green, right side); least proliferation was observed on the red marked structures.

Supracellular organization and mineralization

Within the PATCELL project PLGA substrates harboring micro-wells of varying dimension were produced to identify the optimal microstructures for bone cell proliferation and differentiation.

To analyze the above in detail, MC3T3-E1 cells were seeded on micro-well harboring PLGA substrates and grown under conditions allowing differentiation and mineralization after which they were stained with alizarin red to show mineralized areas.

We observed certain regions with increased staining intensity: mainly areas where the substrate was roughened due to incomplete release of the PLGA sample during the injection molding process (see Fig. 5). However no clear increase was observed for any of the regions patterned with micro-well structures.

Fig. 5: Mineralization and supra-cellular organization of MC3T3-E1 on micro-welled PLGA substrates. MC3T3-E1 pre-osteoblasts were grown on PLGA substrates with different dimensioned micro-well structures (left) under mineralizing conditions for up to 6 weeks and subsequently stained with alizarin red to mark mineralizing regions (right).

When the supra-cellular organization of MC3T3-E1 cells on these substrates was investigated it turned out that, in accordance with observations made on the embossed substrates, the cells easily spanned smaller micro-well structures of 10 µm (Fig. 6, left), whereas the cells seem to avoid larger pits with a diameter of 70 µm and preferably grew on the flat regions in between the wells (Fig. 6, right).

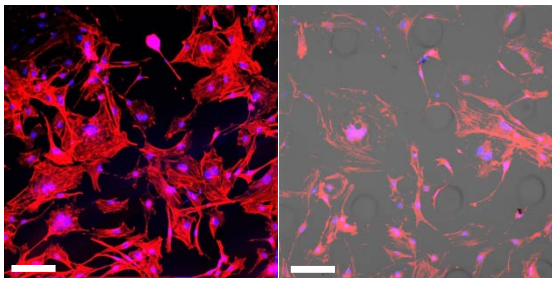

Fig. 6: Micrographs of rhodamine-phalloidin/DAPI stained MC3T3-E1 cells on micro-well structures with a diameter of 10 µm and a spacing of 8 µm (left) and a diameter of 70 µm and a spacing of 130 µm (right, combination of fluorescent and brightfield view to allow for the localization of the well structures). Scale bars 100 µm.

Conclusions and Outlook

A large variety of surface structured PLGA films were successfully prepared throughout the first year of the project while the analysis of the cellular response was the focus of the second year.

While we did not observe increased mineralization in MC3T3-E1 osteoblast cultures on PLGA surfaces with micro-well structures of 10-70 µm, it was observed that certain microstructures reduced cell proliferation by up to more than 40%. Especially single standing, elevated structures without specially defined dimensions proved useful in this respect, which makes them suitable target structures for PLGA implants were reduced osteoblast cell proliferation is desired as e.g. parts which face the connective tissue.

References for Project A9.10

[1] J. Koeser, U. Bruggisser, R. Holtz, C. Rytka, M. Grob, S. Neuhaus, S. Beck, P.M. Kristiansen, *"Cell instructive micropatterns: effects and limitations"*, SNI annual meeting, Lenzerheide, Sept. 2015.

Single-cell nano analytics

Project A9.12 SCeNA (University of Basel, FHNW, F. Hoffmann-La Roche AG Basel)
Project Leader: T. Braun
Collaborators: H.-P. Lang (University of Basel), G. Schlotterbeck, C. Berchtold (FHNW), G. Dernick (F. Hoffmann-La Roche AG), S. Arnold and L. Rima (C-Cina, Biozentrum, University of Basel)

Introduction

The stochastic nature of biological systems inherently leads to heterogeneous cell populations. To date, most bioanalytical methods measure cell assembly averages, obscuring the cell heterogeneity and the biomolecular interaction networks. The investigation of single cells is crucial for future biomedical studies. Single-cell analysis is hindered by three main obstacles: First, the tiny amount of analyte, second, the sample conditioning required for the analysis, and third, the difficulties encountered when trying to connect single cell cultivation and the employed detection instrumentation.

The specific aim of the SCeNA project is to combine a cell culturing and single-cell lysis device with various bioanalysis methods that characterize different aspects of the cell status: (A) label and amplification free transcriptomics using nanomechanical viscosity sensors; (B) protein detection by enhanced reverse phase protein microarrays (RPPA); (C) visual proteomics by visually analyzing the cytosolic proteins using high-speed atomic force microscopy (AFM); (D) metabolomics by liquid chromatography mass spectrometry (LC-MS).

Single-cell lysis and handling platform

A second-generation cell cultivation and single-cell lysis set-up was completed and tested. All processes are now automated by the openBEB macro system [1]. This significantly improved the reproducibility of both the lysis of individual cells and the uptake of the cell contents. Precise liquid handling of 5 nl droplets is routinely performed. Procedures to deposit single-cell lysate on carriers for analysis by reverse-phase protein array (RPPA) techniques (B) or mass spectrometry (MS, D) are optimized. The hand-over system for visual proteomics by atomic force microscopy (AFM) is currently being tested (D).

We used either adherent HEK 293 or LUHMES cell cultures for our experiments and can differentiate the latter cells to dopaminergic neurons. Both cell types are grown on indium tin oxide (ITO) coated microscope slides. A platinum-coated microcapillary electrode (MCE) is used to target and lyse individual cells by electroporation. Following lysis, the ruptured cell is immediately aspirated into the tip of the MCE in a volume of 3 to 5 nl [2, 3]. The first year of the project focused on the development and testing of individual hand-over systems, which are compatible with the corresponding analysis modules (A-D).

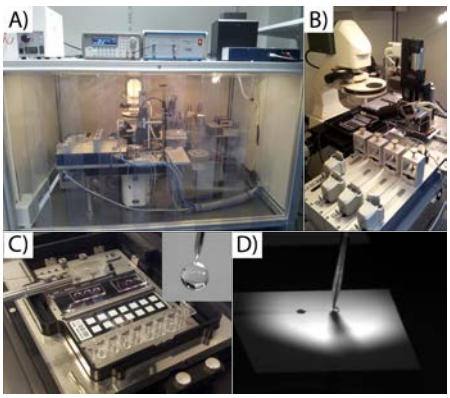

Fig. 1: Second generation single-cell lysis set-up. A) Overview of the whole set-up built around an inverted microscope. B) High precision syringe pumps. C) Microscope cell-incubator stage with custom-made holder for the cell culture slide or the nitrocellulose (NC)-coated glass slide required for RPPA techniques (module B). Inset: Functionalized microcapillary electrode (MCE) with hydrophobic properties to allow controlled sample deposition. D) Deposition of an array of 5 nl spots onto the NC pad of a coated glass slide for RPPA [2,3].

A: Transcriptomics

The microviscometer employed in this module is optimized for high-throughput screening of liquid droplets in a two-phase microfluidics system [4]. We developed a top-down hand-over system that allows cell lysate to be directly fed into a two-phase microfluidics cartridge by a capillary gap handover (Fig. 2). We can load the cartridge with a series of sample droplets (minimal volume tested: 15 nl, larger volumes of several µl are possible) separated by an inert oil. The open pipetting system employed allows cell lysis, aspiration of the lysate, addition of an RNA probe, and introduction of the mixture to the two-phase microfludics cartridge in a single uninterrupted work-flow.

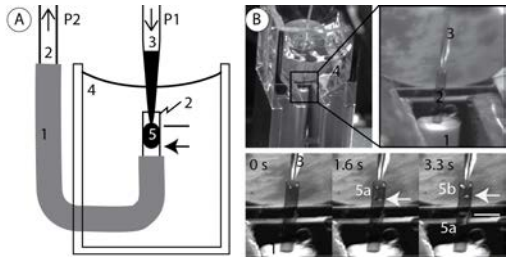

Fig. 2: Capillary gap handover device for the top-down handover of nl to µl volumes from the cell picking MCE (Fig. 1) to a retrieving microcapillary cartridge. The latter can be easily removed from the handover device and directly connected to the microviscometer by press-fittings. (A) Schematic illustration of the hand-over principle. The system is based on two high-precision pumps pushing (P1) and aspirating (P2) with tuned relative speeds, e.q.,

equal speed. 1: Guiding sleeve around the receiving capillary to help position it; 2: Recipient capillary of the hand-over system; 3: Micro-capillary electrode for cell lysis; 4: Cuvette filled with carrier oil. B) Upper row: Embodiment of the hand-over device (left) and enlarged view, numbered the same as B. Lower row: Movie frames showing the hand-over of 15 nl droplets. 5a: First 15 nl droplet generated. 5b: second 15 nl droplet. Arrows: leading buffer/water fronts. Line: the trailing interface.

B: Single-cell RPPA

In RPPA entire sets of complex biological samples, e.g., cell lysates, are immobilized on a surface as spots and then probed by specific antibodies for particular proteins. Only a very small amount of sample is needed and we optimized the deposition by our single cell lysis set-up (Fig. 1) for the analysis. For house-keeping proteins, we observed a roughly linear response to the number of cells lysed and dispensed. Currently, experiments are performed to asses biological experiments on single cell level, such as the probing for heat-shock proteins.

C: Visual proteomics by AFM

We are developing a handover-platform to analyse the cell content of individual cells by AFM. First we develop preparation methods for the AFM analysis in the dry state and, subsequently, we extend the technology for analysis in buffer solution.

We use mica as substrate for 5 nl sample deposition. The mica is pre-structured using a focused ion beam (FIB)-equipped SEM (Fig. 3). This is needed for following reasons: (i) Sample spreading on the highly hydrophilic surface must be controlled, since the AFM has a limited scan range; (ii) the structuring will serve as guide, helping to align the AFM head above the sample.

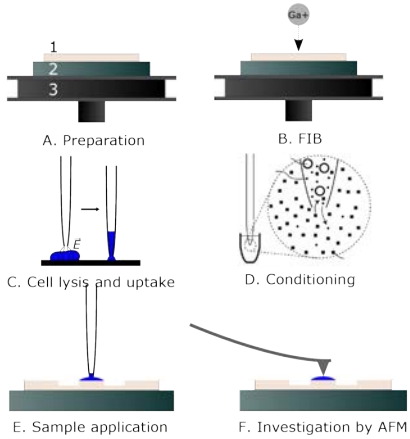

Fig. 3: Process of single cell lysate investigation by AFM (not to scale). 1: A piece of mica (A) is glued to a flat support (B; e.g., iron sheet) and mounted on a SEM pin stub holder (C); 2: The mica is structured by a foced ion-beam; 3: 5 nl of sample or cell lysate form the single cell lysis set-up are apirated (Fig. 1); 4: The sample is conditioned in a volatile buffer (see project P1201, Fig. 2&3); 5: dispensing on the sample on the mica pillar; 6: imaging in the AFM.

In order to remove the salts form the sample, which leads to salt crystals during drying, the sample is conditioned before dispensed on the mica (Fig. 3, D). To this end, a newly developed method called diffusion controlled sample conditioning (see project 1201) is applied. First results show, that this sample preparation method indeed can be used to prepare AFM samples only consuming around 5 nl (Fig. 4).

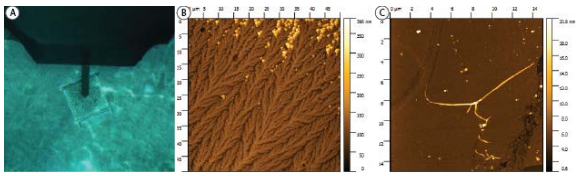

Fig. 4: Total preparation of 5 nl sample for AFM. A) alignment of AFM tip above structured mica; B) Deposition of sample without conditiong, resulting in massive salt structures; C) deposition of sample after condition with a volatile buffer. Filamentous structures typical for proteins involved in neurodegerative diseses are visible.

D: Metabolomics by LC-MS

Two major challenges have to be overcome to enable single cell metabolomics by LC-MS: (i) Sensitivity: Since the total volume of a single cell is very small (pL range) only a very small amount of compound (pg to fg) is available for analysis. (ii) Transfer of the small sample volume into the MS system. Today's systems are optimized for the injection of microliter volumes (2-20 µl).

In order to overcome these complications we developed a novel hand-over system based on droplet deposition, washing out of metabolites and conditioning on a LC-column. Experiments show, that single cell detection of specific metabolites, such as glutamate, is in reach.

References for Project A9.12

[1] C. Ramakrishnan, A. Bieri, N. Sauter, S. Roizard, P. Ringler, S. A. Müller, K. N. Goldie, P. Ringlier, K. Enimanev, H. Stahlberg and T.Braun, *"openBEB: open biological experiment browser for correlative measurements"*, BMC Bioinformatics; **15** (1), 1–14 (2014).

[2] S. Kemmerling, S. A. Arnold, B. A. Bircher, N. Sauter, C. Escobedo, G. Dernick, A. Hierlemann, H. Stahlberg and T. Braun. *"Single-cell lysis for visual analysis by electron microscopy"*, J Struct Biol, **183** (3), 467–73 (2013).

[3] S. Arnold, S. Albiez, N. Opara, M. Chami, C. Schmidli, A. Bieri, H. Stahlberg, C. Padeste and T. Braun, "*Total sample conditioning and preparation of nanoliter volumes for electron microscopy*". To be submitted.

[4] B. A. Bircher, R. Krenger and T. Braun. *"Automated high-throughput viscosity and density sensor using nanomechanical resonators"*, Sensor Actuat B-chem. **223** (C), 784–90, (2016).

SINAPIS – Slurry injection of nano-scale particles into implant surfaces

Project A9.15 SINAPIS (FHNW, University of Basel, WATERjet Robotics AG Oftringen)
Project Leader: R. Schumacher
Collaborators: A.M. Rohner, A. Melzner, M. de Wild, O. Braissant, M. Straubhaar, W. Maurer and M. Schmied

Introduction

Total hip and knee arthroplasties are considered as key treatments in medical technology with more than 200'000 hip replacements in Germany every year. The number of implanted artificial joints is increasing while the age of patients is decreasing. Therefore, it has become necessary to increase the implant's lifetime of currently 15 to 20 years and to further improve anchoring in the bone.

On the one hand, research is focusing on the contact between implant and bone and on attempts to maximize the fixation by applying open porous surface structures for better bone attachment. On the other hand, research is addressing the wear resistance of the articulating surfaces which are made of plastics such as UHMW-PE, ceramics like Al_2O_3 or metals such as CoCrMo in various combinations and with dissimilar success.

Material and Methods

In this 2-year project, we are aiming for the structuring and functionalization of implant surfaces by hydro-mechanical treatment including the incorporation of nanoparticles into the implant material. For these purposes, we are using a novel implant surface-treatment provided and operated by our industry partner WaterJet AG. This process uses a focused suspension of water and particles under high pressure to functionalize implant surfaces (fig. 1).

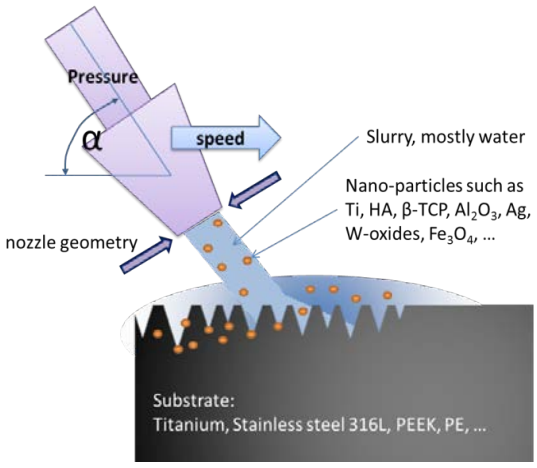

Fig. 1: Scheme of slurry injection process.

In a first step we investigated the ability to structure biomaterials such as PE and titanium by the use of inert zirconia powder [1] by using small substrate specimens of ø14 mm in diameter and 1 mm in thickness, see fig. 2.

In the second project year we have been investigating the introduction of bio-active particles like Silver (Ag, particle size < 45 µm) and Hydroxyapatite (HA, particle size < 45 µm). We introduced them into the liquid suspension for structuring the Ti samples, see fig. 1. These materials, HA and Ag have potentially positive effects on implant surfaces, whereupon HA is expected to improve osseointegration while Ag is supposed to reveal bactericidal effects [2]

The surface-treated and structured samples were analysed towards their morphology and chemical compositions by using SEM/EDX (Hitachi TM-3030plus) with a back-scattered and secondary electron as well as EDX detector (Quantax 70, Bruker).

A customized 1600 W ultrasonic device (KKS Ultraschall AG) was used for cleaning experiments to determine anchorage of the particles injected into the surface.

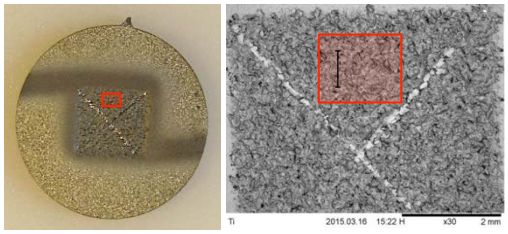

Fig. 2: Left: Specimen disk of ø14 mm in diameter, 1 mm in thickness, with water jet pre-structured surface. The x-shaped location lines serve as reference marks. Area of interest (red) was indicated by marking previous to REM/EDX analysis. Right: Surface morphology after pre-structuring with water jet.

Results

In the first year of the project we demonstrated that this new slurry injection method could be used for the structuring of biomaterials. By adjusting process parameters, various surface morphologies could be reproducibly generated.

In the second project year we proved that this novel method of surface treatment allows injecting bio-active agents into Ti implant surfaces. The formed morphology of the surface, the amount and distribution of the incorporated particles can be adjusted with process parameters like standoff distance, nozzle angle, nozzle speed, slurry pressure, speed and the concentration of particles in the slurry.

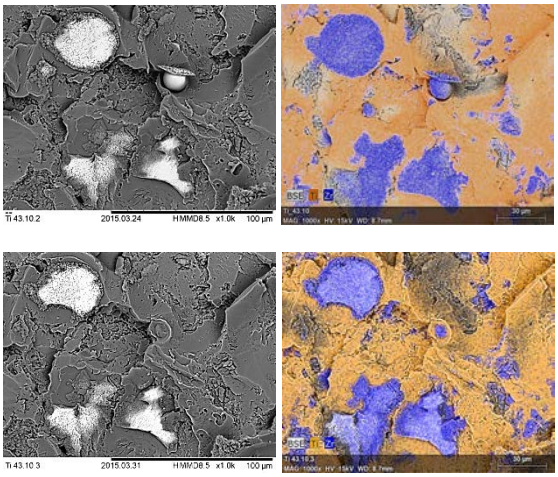

Fig. 3: ZrO_2-slurry-treated Ti samples before (top) and after intensive ultrasonic treatment (bottom): Left: SEM image of structured topography with incorporated ZrO2 particles. Right: EDX mapping to identify residual ZrO_2 particles (purple) on Ti surface (orange).

Fig. 3 shows that the ZrO_2-enriched slurry allows structuring of the titanium surface and deposition of particles. Even after harsh ultrasonic treatment for 15 minutes, the majority of the ZrO_2-decoration remains on the surface, proving a strong anchorage. The concentration of Zr was reduced from 11 wt.% to 9 wt.%.

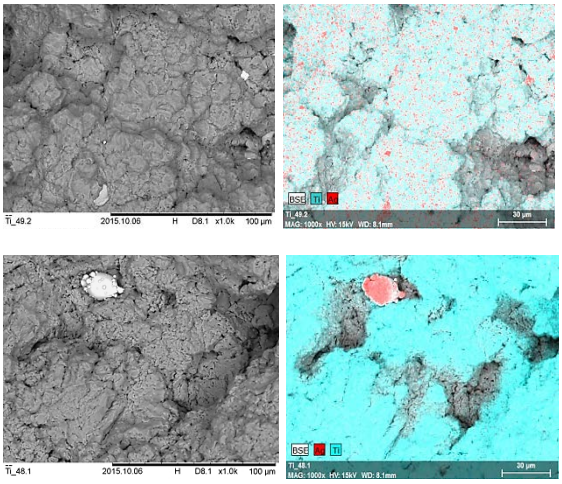

Fig. 4: Ti samples after slurry treatment with fine Ag particles (top) and large Ag particles (bottom). Left: REM image showing Ti surface with incorporated Ag particles (bright). Right: EDX mapping exhibiting homogenously distributed small nano-sized Ag particles and strongly fixed large Ag-particles (red) on the Ti surface (blue).

The Ag-treated Ti samples in Fig. 4 show finer structured surface topology compared to ZrO_2-treated surfaces of Figure 3. While bigger Ag particles seem to be stuck in the structured Ti sample surface (see Fig. 4 bottom), a higher amount of small nano-scale sized Ag particles seem to be homogeneously distributed over the surface.

Further investigations shall address the examination of different particle deposition mechanism by this novel slurry deposition process.

Discussion

Although we used the same slurry injection process parameters for all materials, ZrO_2-, HA- and nano-sized Ag-treated samples resulted in different structuring effects. This might be explained by different densities of the particles and therefore different kinetic impact on substrate surface.

In the next studies, we will further analyse the anchorage of the ZrO_2, HA and Ag particles in the Ti substrates. Additionally, the biological effects of the SINAPIS-treated surfaces will be investigated using micro-calorimetry measurements of cell reaction in contact with these SINAPIS-specimens.

References for Project A9.15

[1] Ralf Schumacher, A.M. Rohner, A. Melzner, M. de Wild, O. Braissant, “SINAPIS - Slurry Injection of Nano-scale Particles into Implant Surfaces” SNI Annual Meeting, Lenzerheide, Switzerland, 2014

[2] Erich Wintermantel and Suk-Woo Ha, Medizintechnik: Life Science Engineering, Springer Verlag, 2009.

Towards biomimetic omniphobic polymer surfaces by combining hierarchical surface patterns and e-beam assisted grafting

Project A10.07 RepAll (FHNW, PSI, Cellpack AG Packaging Villmergen)
Project Leader: S. Neuhaus
Collaborators: P.M. Kristiansen, J. Schmidli (FHNW), R. Kirchner, C. Padeste (PSI) and A. Cousins (Cellpack AG Packaging)

Introduction

Duck feathers, lotus leaves and the Salvinia plant serve as examples from nature for extremely hydrophobic surfaces. Their outstanding properties often arise from the combination of hierarchical surface structuring and optimized surface chemistry. Apart from water, omniphobic surfaces also repell numerous other liquids [1] and are of great interest for industrial applications. In this project we combine the possibilities of greyscale electron beam lithography (EBL), roll-to-roll replication and electron beam assisted grafting reactions to mimic surfaces inspired by nature.

Exploiting possibly de-wetting surface patterns

A variety of surface patterns with feature sizes ranging from submicron to fractions of a millimeter were prepared and transferred into relevant packaging materials (different polyolefins, not disclosed due to confidentiality) by means of hot embossing and roll embossing, respectively. These surfaces were investigated for their wettability by different liquids as well as their roll-off behavior.

It is well known that a reduction of the solid fraction in contact with a liquid leads to an increase in contact angle due to the formation of the so-called Cassie-Baxter state, which is illustrated exemplarily for water on a polyolefin surface in Figure 1.

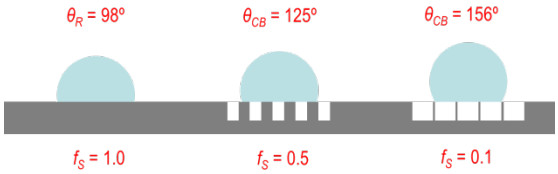

$$\cos\theta_{CB} = f_S(\cos\theta_R + 1) - 1$$

Fig. 1: Effect of reduction of the fraction of solid surface f_S on the contact angle of water on a polyolefin surface. The values for f_S < 1 were calculated based on the measured contact angle θ_R of a smooth reference surface.

Hierarchical topographies by EBL

Greyscale electron beam lithography [2] was used to prepare a variety of surface topographies differing in the fraction of solid f_S in a 2 µm thick PMMA resist and used directly for water contact angle measurements. Figure 2 shows some examples of grid structures (left side) and pillar arrays (right) with corresponding values for f_S and θ_{CB}.

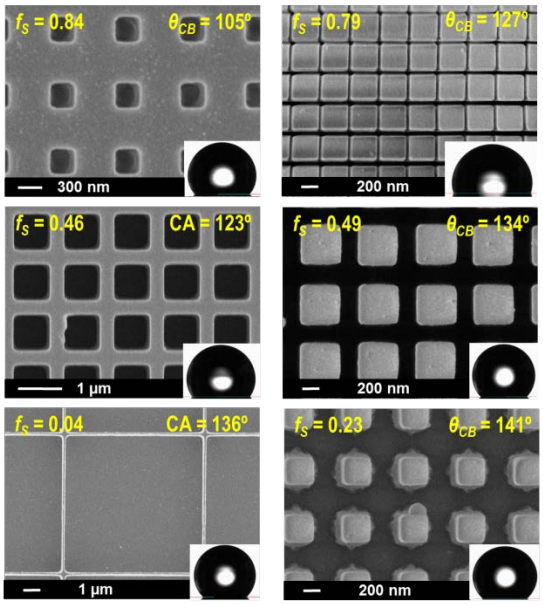

Fig. 2: Scanning electron micrographs of selected surface topographies displaying different fractions of solid surface f_S. Left: grid structures, right: pillar arrays.

As seen from Figure 3, the obtained values for f_S were usually smaller than targeted. Measured contact angles on grid structures correlated quite well with the predicted values for f_S > 0.5 but leveled off at lower f_S values possibly due to pinning effects.

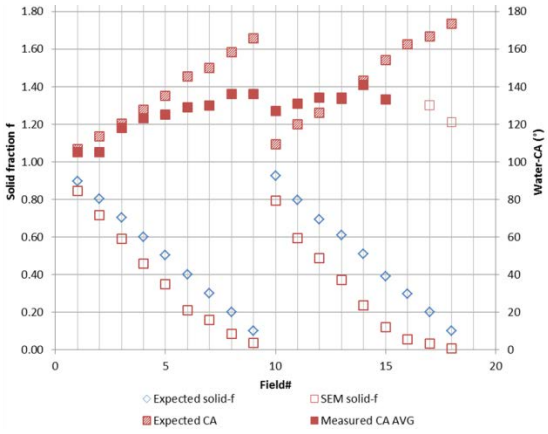

Fig. 3: Theoretical (expected) and measured water contact angles for surface topographies with different fractions of solid surface f_S. Fields 1-9 refer to regular grid structures, fields 10-18 to regular pillar arrays (height was always 2 µm).

Alternative approach: replication of wire meshs

Interestingly, strongly repelling surfaces have also been achieved by hot embossing of LDPE with steel gauzes [3]. We adapted this approach by using special wire mesh grids (used e.g. for melt filtration during extrusion) for structuring of the polyolefin materials relevant for packaging applications. As can be seen in Figure 4, strongly repelling topographies resulted in a macroscopic Cassie-Baxter wetting state with substantially augmented contact angles for various liquids [4].

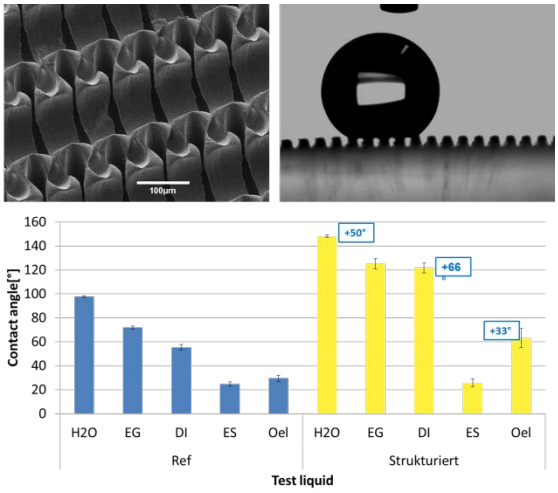

Fig. 4: top left: Scanning electron micrograph of a polyolefin film after hot embossing of a hierarchical structure. Top right: Water contact angle measurement on said polyolefin surface, revealing a true Cassie-Baxter state with entrapped air pockets underneath the water droplet (here ~3 µl). Bottom: Comparison of contact angles of different test liquids (EG=ethylene glycol, DI=diiodomethane, ES=acetic acid, Oel=rapeseed oil) on smooth (blue) and structured (yellow) surfaces.

Adding roughness through plasma treatment

It is known that oxygen plasma treatment can induce nanoscale surface roughness on polymer substrates. Different substrate materials were subjected to oxygen plasma treatment and subsequently analyzed for induced variations in surface topography (see Figure 5).

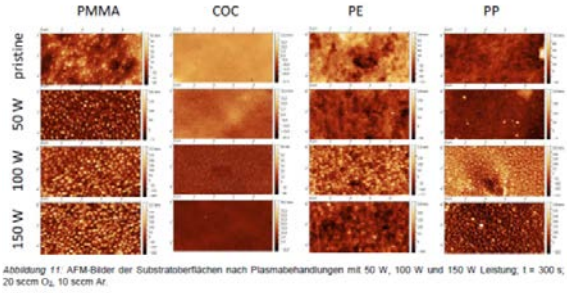

Fig. 5: AFM micrographs of different substrates before (top row) and after plasma treatment under different conditions. Plasma power levels: 50W, 100W and 150W (indicated on the left side), treatment time: 300 s, atmosphere: 20 cm² O_2 / 10 cm² Ar.

Chemical modification by e-grafting

Further improvement of the dewetting characteristic of topographically structured polyolefins proved to be difficult by means of e-grafting modification. In order to achieve a stronger hydrophobicity of the surface, the use of silicones or aliphatic graft molecules would likely be required as fluoro-polymers are not desired particularly for food packaging materials. However, the effects obtained so far did not lead to a significant improvement of the repelling and roll-off characteristics.

Exploitation of other substrate materials

The modification of wetting characteristics is of broad interest not only for packaging materials but also for other applications. Therefore, besides of polyolefins, a series of other polymers were also structured with the most promising surface topographies. In brief, the augmentation of the water contact angle proved to be very similar for a variety of polymers with surface energies ranging from 20 to 40 mN/m, thus, essentially covering the entire range of polymeric materials. This somewhat surprising finding poses some additional fundamental qustions which will be addressed throughout the second year of the project.

Conclusions and outlook

It could be demonstrated that repelling structures can be realized based on topographic structuring on different length scales with at least two different promising approaches for mastering and subsequent continuous replication by thermal roll embossing.

The second year of the project will strongly focus on the scale-up of the most promising surface patterns to larger areas and the continuous replication by means of thermal hot embossing, which could be readily integrated into the existing production process of one of the primary products of interest .

References for Project A10.07

[1] A.K. Kota et al. “Superomniphobic surfaces : Design and Durability“, MRS Bulletin **38**, 383-390 (2013).

[2] A. Schleunitz, V.A. Guzenko, M. Messer-schmidt, H. Atasoy, R. Kirchner, and H. Schift, *“Novel 3D micro- and nanofabrication method using thermally activated selective topography equilibration (TASTE) of polymers”*, Nano Convergence 1:7 (2014).

[3] E. Bormashenko et al. “Robust technique allowing manufacturing superoleophobic surfaces”, Appl. Surf. Sci. **270**, 98-103 (2013).

[4] P.M. Kristiansen, J. Köser, J. Schmidli, C. Rytka, S. Neuhaus, H. Schift, J. Gobrecht, "Enabling technologies for mass manu-facturing of micro- and nanostructured polymer surfaces", *i-net Innovation Landscape Nano Event*, Muttenz, Sept. 9, 2015.

Atomic-scale analysis of the SiC/oxide interface to improve high-power MOSFET devices

Project A10.08 Atolys (University of Basel, PSI, ABB Baden-Dättwil)
Project Leader: S. Goedecker
Collaborators: T. Jung, J. Lehmann and H. Bartolf

Introduction

In Metal Oxide Semiconductor Field Effect Transistors (MOSFETs), the gate electrode is separated by a thin insulating layer (typically silicon- dioxide) from the semiconductor material. If a gate-voltage $V_g > V_{th}$ is applied between the gate and the source electrode, a conduction channel is formed below the insulator to semiconductor interface. The quality of this interface is crucial for the attainable device performance: In order to achieve high carrier mobilities in the inversion channel, the density of interface defect states as well as the interface roughness has to be as low as possible. For Si-based devices this goal has been achieved by passivation of interface states localized at e.g. dangling Si bonds by annealing in hydrogen atmosphere. As compared to the Si/SiO_2 interface, the number of interface defects in the SiC/SiO_2 system is higher by several orders of magnitude. This is plausible due to the more complicated oxidation process which requires removal of carbon atoms from the SiC crystal in the form of e.g. CO or CO_2. The removal is progressively hindered as the gate-oxide thickness increases.

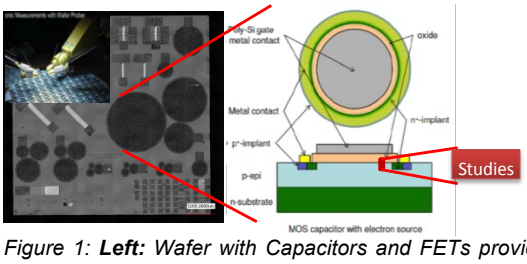

*Figure 1: **Left:** Wafer with Capacitors and FETs provided by ABB. **Right:** Metal Oxide Semiconductor (MOS) Capacitor with n+ source*

Even after decades of intensive R&D, it remains a pestering question, however, what type of defects (dangling bonds, carbon clusters, near-interface traps, etc.) are most abundant and which are most relevant for degrading the SiC device performance. Furthermore, it has been recently concluded that post-oxidation annealing in $POCl_3$, N_2O or NO atmospheres can lead to a substantial passivation of interface defects [1]. Additionally, the pre-implantation of column-V elements [2] shows 5-6 times higher carrier-mobility values as compared to the state-of-the-art N_2O passivation. The microscopic mechanisms which are responsible for the passivation remain unclear and alternative, potentially improved approaches still provide a topic of investigations.

Interface Defect – Simulations

Theoretical studies of the $SiC-SiO_2$ interface containing defects and its structural evolution during the oxidation process were performed using minima hopping simulations. The framework involves a fast method for calculating the energy, force, stress etc. (Density Functional Tight Binding scheme), density functional schemes like modified Becke-Johnson exchange potential in combination with L(S)DA correlation, conformational and transition path sampling methods like Minima Hopping Method (MHM) and Minima hopping Guided Path Search (MHGPS) method. A clear band gap (~3.1eV) for the $4H-SiC/SiO_2$ interface has been found. With a few dangling bonds positioned at the interface, defect states appeared within the band gap, which could be passivated by hydrogen atoms later on. By the inclusion of oxygen traps in the model, the created interface states could be passivated by nitrogen. To simulate the carbon related defects at the SiC/SiO_2 interface, small carbon clusters (up to 10 atoms) were created at the interface. Stable interface structures

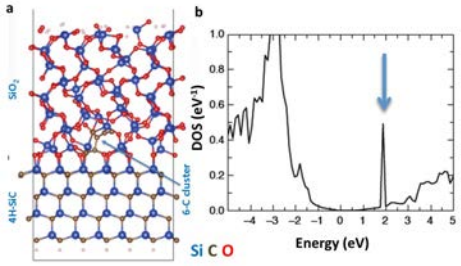

Figure 2: Density of States (DOS) of SiC/SiO_2 interface structures with 6-atom carbon clusters (unit cell with 382 atoms). The arrow shows the interface states near the conduction band.

with carbon clusters of different sizes were found and some states appeared in the band gap (Fig. 2). During our studies of oxidation of the Si-terminated (0001) surface of SiC to understand the origin of those defects, we found that the oxygen atoms seem to bind to the first silicon layer quite easily and form Si-O-Si bridges. Just near the interface, the carbon atoms were found to align in a chain-like configuration or in connected 5- or 6-membered rings (Fig. 3). Carbon clusters are consistently found at the interface and create electronic states near the conduction band as well as near the valence band. Frequently, the outward diffusion of Si and C atoms created a Si-C layer on top of the SiO_2 layers. The

mechanisms of C removal, Si-C layer formation and the corresponding activation barriers are currently investigated. Also reliable passivation strategies for all different carbon related defects have yet to be worked out.

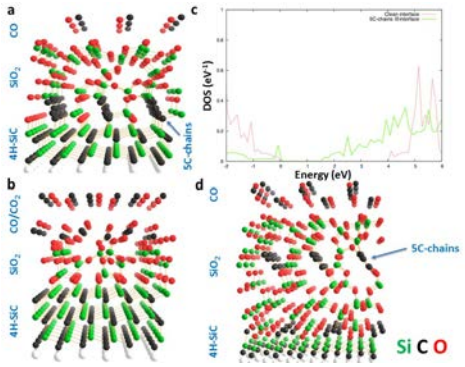

Figure 3: (a) and (b) are low energy intermediate structures during oxidation of SiC,. (c) shows the DOS of (a) and (b) referred as "5C-chain @interface" (green,a) and "Clean interface" (red,b) respectively. (d) shows the lowest energy conformation after a more complete oxidation. (a) and (d) have 5-C chains at or near the interface.

Experimental Study: Microscopic Analysis

SiC/SiO_2 interfaces manufactured by the TGO (N_2O based gate-oxide formation [1]) and DRY (dry O_2 based) oxidation processes have been investigated by Atomic Force Microscopy (AFM) and Scanning Electron Microscopy (SEM). For this purpose, the specimens have been stripped by the oxide layer via an HF etch uncovering the SiC underneath. Both techniques provide conforming insight into the step bunching which evolves during the high temperature treatment in the oxidation of the SiC/SiO_2 interface in the oxidation furnace. Average step heights according to the AFM line profiles are 1.6 nm and 1.1 nm for the DRY and the TGO oxidized respectively. Further investigations are necessary to find the causal link between the observed steps/ roughness and mobility and to understand how to reduce different step corrugations in order to diminish defect-genesis during the gate-formation.

Complementary to these investigations, Local Electrode Atom Probe (LEAP) [3] investigations were successfully done for the first time on SiC-based samples with the help of our colleagues at the ETH Zürich. Here a certain volume of the specimen is disassembled in an atom-by-atom or cluster-by-cluster way to reconstruct 3D maps of the atomic composition. Laser pulses in conjunction with an electric field of 10 MV/m are simultaneously applied to the apex of the pillar shaped specimen in order to "field-evaporate" small units in a controlled way. Thereby, chemical information is obtained by Time of flight (TOF) mass spectrometry which can be de-convoluted to provide a 3D tomograph of the chemical composition of the pillar (Fig. 4). In the high resolution chemical 3D maps, the overall C-concentration is found to decay smoothly towards the SiO_2, while C4 clusters appear frequently near the interface as it is recognized by an iso-chemical composition recognition routine.

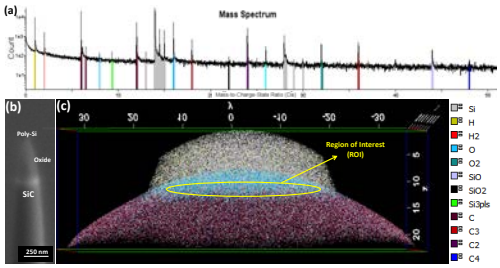

*Figure 4: (a) Mass spectrum showing the atoms and clusters originated from the apex of the pillar during its systematic disintegration in a LEAP experiment. (b) SEM image of the tip showing differing contrasts for each material layer i.e. poly-Si, amorphous oxide and crystalline SiC layers. (c) The reconstructed chemical map of the LEAP pillar (b), which integrates the overall shape from SEM and the chemical information combining non-destructive SEM and destructive LEAP. The Region of Interest (ROI) is the region where few layers of oxide have been grown on SiC (*further zoom in Fig: 5).*

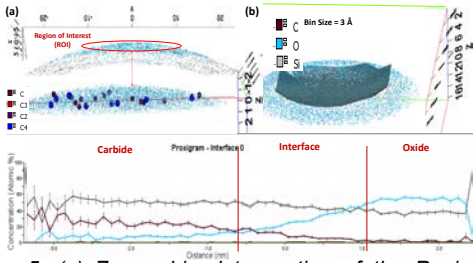

Figure 5: (a) Zoomed-in data section of the Region of Interest (ROI) with the positions of C clusters denoted. The C_4 cluster is quite prominent among the other C clusters (b) Iso-chemical-composition surface for the oxide layer at the interface drawn in the ROI. The interface as identified in this automatic routine extends across 1.5 nm and does not exhibit a sharp boundary. (bottom) The atomic concentration of C, O and Si has been analyzed in function of distance from the isosurface. In this region C_n gradually decreases without showing any sharp peak; hence there is no significant accumulation of average C_n, while there is some evidence that C4 are frequently observed at the interface.

Further LEAP experiments and numerical simulations are needed to reach conclusions on the attributes and impacts of carbon-clustering upon the electronic MOS-interface performance, specially in relation to the degraded carrier mobility near the interfaces as observed in transport measurements [1,2]. In parallel to the successful, unique and novel preparation of first LEAP specimens, other lamellae for Transmission Electron Microscopy (TEM) studies have been prepared. TEM analysis is less destructive than LEAP and thereby can provide insights into the local atomic structure around certain defects as well as about their occurrence. Therefore, TEM provides complementary information to LEAP and to numerical simulations towards improving the structure and the material properties near interface defects, and in particular their influence upon the mobility.

References for Project A10.08

[1] A. I. Mikhaylov et al., Materials Science Forum **821-823**, 508-511 (2015).
[2] A. I Mikhaylov et al., Japanese Journal of Applied Physics, accepted publication (2016).
[3] T. Kelly, Rev. Sci. Inst. **78**, 031101 (2007).

Bactericidal nanostructures mimicking cicada wings for consumer products

Project A10.10 Nano-Cicada-Wing (University of Basel, FHNW, DSM Nutritional Products Ltd. Kaiseraugst)
Project Leader: E. Meyer
Collaborators: M. Kisiel, T. Glatzel, M. Wasser, J. Köser and H. Hug

Project overview

An unique and novel bactericidal mechanism has been recently discovered [1, 2] on cicada (*Psaltoda claripennis*) wing surfaces. The Austalian origin insect provides a completely new and exclusive mechanism of bacterial killing, which is contrary to already applied antibacterial activity based on chemical toxicity. The surface of cicada wings and a few other nanopillared surfaces with varying geometries [3] provide a purely mechanical principle of working, that means the rupture of the bacterial cell membrane upon contact with the nanostructured surfaces. In our project we try to mimic these insect wing surfaces by means of nanostructured and chemically modified polymer surfaces. We combine plasma exposure polymer surface (PEEK, polystyrene (PS), polycarbonate (PC)) structuration, chemical functionalization and antimicrobial activity assays with Fluorescent Microscopy, Scanning Electron Microscopy (SEM) and Atomic Force Microscopy (AFM).

Generation of nanostructured polymer surfaces and chemical modification

Artificial cicada wing polymer surfaces might be successfully produced by means of low energy plasma and the structure, the height of the produced pillars and distance between them strongly depend on plasma power, exposure time and plasma composition. The effect of plasma condition was investigated to obtain optimally structured polymers. These include polymers used for the production of medical devices like PEEK (Fig. 1) as well as for consumer goods like PS or PC. We have found that the increase of the exposure time results in increased length of the pillars, which as the plasma exposure goes on, stick together due to pillars softening and electrostatic attraction between them. In order to control surface charging and surface hydrophobicity that eventually lead to increased bacteria adhesion and killing rate the polymer surfaces were additionally gold coated to allow for the chemical modification by thiol based self-assembling monolayers (SAMs). This procedure also increased the stiffness of the pillars. Since insect wing structures as well as bactericidal reported black silicon structures are of hydrophobic nature we expect this property to play a pivotal role regarding the bacteria adhesion and bactericidal effect. This is still an ongoing work. A summary on the materials and nanopillar-structures which have been investigated by different research groups for their bactericidal effect is given in Table 1.

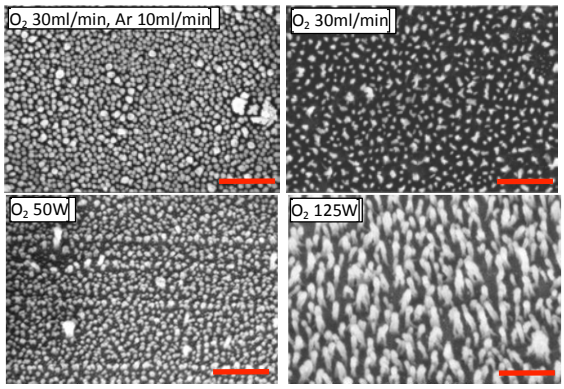

Fig. 1: Tuning of polymer surface nanostructures by adaptation of the plasma treatment conditions. PEEK surface treatment conditions are indicated and samples are visualized by SEM (the lower two samples are 45° tilted). Scalebars 500nm.

structured material	diameter	height	spacing	Contact angle unstructured material (data from literature)	killing rate
Cicada wing	50	200	200	Waxes, >140°	
Dragonfly wing	<30-40	240	>200	waxes	
bSi	40-70	500	200	mainly Si -> 90°	
Brdll cicada	167	83	252	waxes	50%
DD cicada	57-104	183	175	waxes	
DF dragonfly	53	241	123	waxes	
PET	250	1000	50	72°	
PET	250	1000	200	72°	
PET	250	1000	400	72°	
PMMA	70	210	100	70°	> 10%
PMMA	190	300	130	70°	< 10%
PMMA	215	300	380	70°	
PS	< 50	220	< 150	87°	
PEEK	30-40	200	< 100	71°	
PC	< 50	180	< 100	82°	

Table 1: Structural and chemical parameters of nanostructured surfaces which have been investigated by different research groups (as by 2015-10) for their antimicrobial activity in comparison to structures created within the Nano-Cicada Wing project (PS, PEEK, PC, lower three rows). The structures marked in green show close to 100% killing activity, the yellow and orange marked structures approximately 50% and 10% killing efficiency and the red structures not any detectable bactericidal effect. The height given for the plasma structured polymers are typical values. The spacings between neighboring pillars are slightly iregular, the indicated values give the maximum radius around a pillar before encountering the next.

AFM-based biomechanical characterization of *E. coli* bacteria under liquid environment

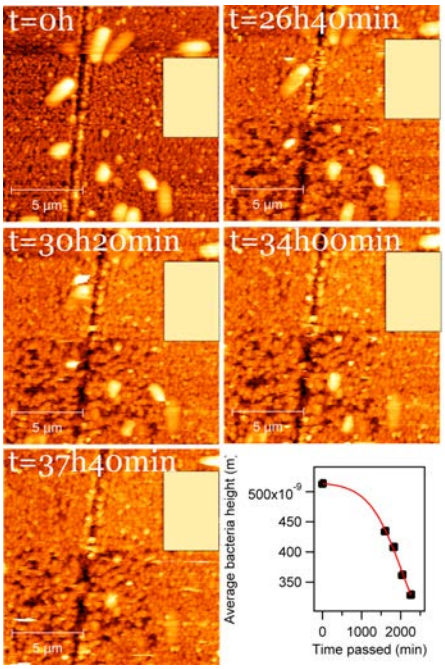

Fig. 2: Time sequenced AFM images of E. coli bacteria situated onto gold coated PEEK surface. Scan area equals 15µm-15µm. The yellow rectangle marks the same position on the sample surface. The apparent bacterial height decreased by a factor of 2 after 2500 minutes of measurement.

While most of the experiments reported in literature (SEM for instance), operate under ex-situ conditions, our goal is to work under in-situ liquid environment, with living bacteria cells during the initial stage of the experiment. We operate the AFM microscope in aqueous environment in order to observe the mechanical rapture of the living cell membrane. The preliminary liquid AFM results showed that only a small fraction (about 5%) of bacteria are killed by a native structured polymer PEEK surface. Our goal is to increase this number by means of surface chemical modification. Figure 2 shows time sequenced AFM images of *E. coli* cells on a 30nm – gold coated nanostructured PEEK surface. The height of the pillars for plasma exposed PEEK is equal to 100nm – 200nm and bacteria cells settled onto the surface were incubated in synthetic medium. It is clearly seen that bacterial membranes are getting destroyed by the structure, however the whole process is relatively long and involves time scales up to two days.

We also deposited living *E. coli* membranes onto gold coated polycarbonate samples (Figure 3) with pillar structures roughly 10 times smaller in height as compared to PEEK. In this case the bacterial membranes stay intact, presumably due to the reduced length of the pillars.

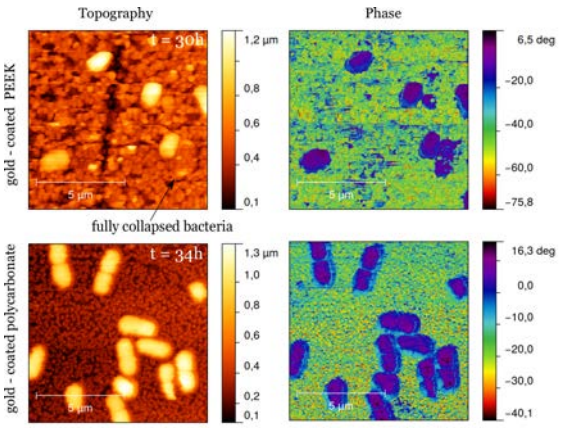

Fig. 3: Comparison of AFM topography and phase (stiffness) images of E. Coli membranes deposited on gold – coated PEEK (upper) and gold – coated polycarbonate (lower) after about 30h of scanning. Scan areas are equal to 10µm-10µm. The bacteria on polycarbonate stay intact as compared to those on PEEK.

SEM analyses were performed to investigate the interaction of bacterial membranes with nanostructured surfaces. The interaction of the pillar structures with E.coli cells are clearly seen, obvious membrane distortions however are only visible if the nanostructured pillars are additionally chemically modified, e.g. with quaternary amine harboring silanes (Fig. 4).

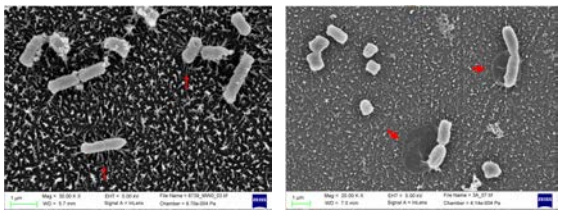

Fig. 4: SEM images of E. coli following ON incubation on nanostructured PEEK (left) versus quaternary amine silane modified nanostructured PEEK (right)..

References for Project A10.10

[1] E.P. Ivanova, J. Hasan, H.K. Webb, V.K. Truong, G.S. Watson, J.A. Watson, V.A. Baulin, S. Pogodin, J.Y. Wang, M.J. Tobin, C. Löbbe, R.J. Crawford, *Natural bactericidal surfaces: mechanical rupture of Pseudomonas aeruginosa cells by cicada wings.* Small **8**, 2489-94 (2012).

[2] S. Pogodin, J. Hasan, V.A. Baulin, H.K. Webb, V.K. Truong, T.H. Phong Nguyen, V. Boshkovikj, C.J. Fluke, G.S. Watson, J.A. Watson, R.J. Crawford, E.P. Ivanova, *Biophysical model of bacterial cell interactions with nanopatterned cicada wing surfaces.* Biophys J **104**, 835-40 (2013).

[3] E.P. Ivanova, J. Hasan, H.K. Webb, G. Gervinskas, S. Juodkazis, V.K. Truong, A.H. Wu, R.N. Lamb, V.A. Baulin, G.S. Watson, J.A. Watson, D.E. Mainwaring, R.J. Crawford, *Bactericidal activity of black silicon.* Nat Commun **4**, 2838 (2013).

Micro-optics with ultra-smooth surfaces

Project A10.13 SurfFlow (PSI, FHNW, Heptagon Advanced Micro Optics Rüschlikon)
Project Leader: H. Schift
Collaborators: S. Neuhaus and M. Altana

Optically smooth surfaces

Optical microlenses are used in various devices, including in smartphones. They have lateral dimensions of a few micrometers up to millimeters, but optically they are often not different from the macroscopic lenses used in cameras. They have to focus or expand a light beam by refraction which means that light with different wavelengths has to be deflected by surface topographies. Since the lenses are so small and require special shapes, they have to be processed using novel 3D lithographic methods that sequentially build the lenses from thin layers. Similarly to this, a pyramidal structure is composed of thin squares starting with a large base and subsequently placing smaller squares on top of each other, the smallest constituting the tip. The envelope of this stepped structure would be a perfect pyramid with defined sidewall angles, a sharp tip and four smooth prism-like surfaces. The thinner the combined levels are, the better the shape resembles the final structure. This is similar to Egyptian pyramids, which are composed of steps which appear smooth from far.

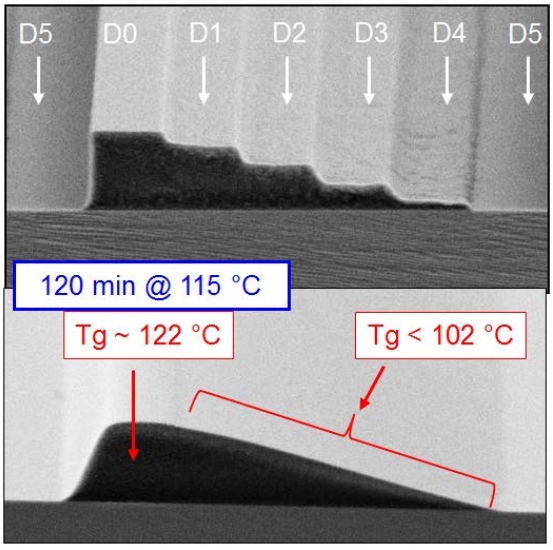

Fig. 1: A stepped structure made by grayscale electron beam lithography can be transformed into an ultra-smooth slope.

Even if many of such levels are used, the incremental steps are still large with respect to the optical wavelengths used. Depending on the location where the light is penetrating the structure in vertical direction, the light undergoes different "optical paths". Small deviations from the optimum paths will lead to to scattering or even interference effects and will result in a large noise background or unwanted color effects. They are particularly detrimental if the step-like deviations from the ideal prism-like structures are regular and not random. Such effects can be excluded if this step-like roughness, here due to the discretization in vertical direction, is below one 10th of its wavelength, i.e. in the case of visible light below 50 nm.

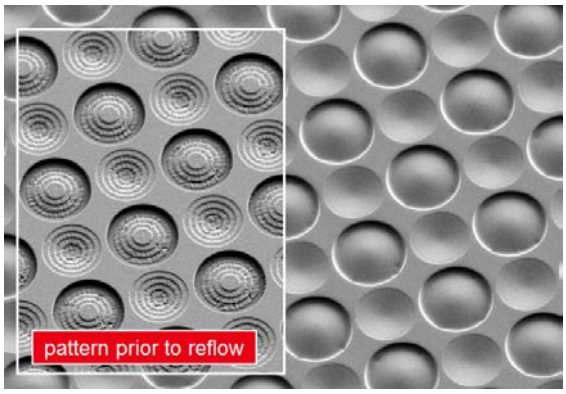

Fig. 2: Array of convex and concave lenses with 5 µm diameter each. The stepped structures can be transformed into structures with ultra-smooth surface by locally selective thermal reflow, called TASTE.

Now, many 3D technologies such grayscale lithography with a focused electron beam (EBL) or by two photon polymerization (2PP) are still not made for high throughput, therefore the number of levels and thus the reduction of the step sizes from layer to layer cannot be considered as a viable route. Instead, the realization of a structure with a few steps which can be "leveled out" by post-processing would be best. A process would be needed, in which the entire surface could be equilibrated in one step in a defined way. This could be done by defined "erosion" or – in case of thermoplastic polymers – by using the ability of the material to flow at elevated temperature, i.e. above its glass transition. At this temperature T_g, which is typically around 100 to 120 °C for polymers used for EBL such as PMMA (known as Plexiglas), the polymer changes from a solid state to a viscous-elastic and finally viscous liquid. Therefore in the past a "reflow" process was applied in a furnace or on a hot plate in which a stepped polymer structure, only defined by its lateral boundaries and height, could be transformed into a lens. This self-optimizing process is governed by surface tension and generates convex spherical shapes with nanometer roughness. It has found applications in sensors and lithography. In contrast to this, concave shapes are not possible by this process, but they can be generated from convex structures by replicating a negative copy. However, most critical are structures where both convex and concave shapes have to be realized or even vertical sidewalls have to be combined with shallow, smooth slopes. Therefore ways have to be found to start with step-like structures and smoothen out surface roughness, but in a locally selective way, in which only the slopes would be affected.

Locally selective thermal equilibration by TASTE

Aim of the SurfFlow project is to set up a nano-scaled, surface-selective and micro-geometry maintaining equilibration process for polymer surfaces towards super-smooth surface roughness as needed in optical applications. This process is similar to thermal reflow of lithographically designed, micro-optical lenses, but uses a localized contrast in the glass transition temperature. It enables reflowing sub-micron surface undulations while the functional macroscopic shape remains intact. The researchers are using a method known as TASTE, which was developed at PSI in the framework of a European FP7 project. It involves selectively changing the material properties of the part of the sample that needs modification and is now applied in a modified way to optical lenses [1].

The local material contrast is created via exposure to surface sensitive methods such as plasma, electrons and UV-light, which have all proven to modify the molecular weight of specific polymers used for lens mastering. In case of EBL, in which a focused electron beam is scanned over a polymer layer (resist), this is by changing the solubility of the resist in wet developers, which is higher for lower polymer molecular weights. This way, defined steps can be written into a resist, which means that depending on the dose (D1 to D5 in Fig. 1) different speeds of dissolution in a specific liquid ("developer") can be achieved. By coincidence, this reduction also leads to a lowering of the glass transition temperature of about 20 °C. This reduction is large enough that at a temperature near the original glass transition of the unexposed material (D_0), the exposed steps are reflowed while the unexposed step stays (almost) intact. The viscous polymer is – due to the moderate reflow temperature – only locally displaced, which is enough to smoothen out the small steps and the surface roughness, but still preserves steep sidewalls. The outcome is the ultra-smooth envelope of the desired shape like prisms used for outcoupling of light in display backlight applications [2]. The achievable roughness is well below 10 nm.

Surface selective smoothing

The TASTE process has also the desired capabilities to manufacture both convex and concave structures in the same substrate by EBL and thermal reflow (Fig. 2). However, the SurfFlow project is aimed towards a solution of the surface corrugation problem involved in new 3D lithography techniques based on 2PP, which is at present prohibitive for micro-optical applications as needed by Heptagon. These structures are often much higher than those made with EBL and the roughness is more pronounced. Therefore apart from electron exposure, other methods were tested. The aim is not only to modify the polymer in the lateral direction but also to confine the reflow process to the upper areas of polymer surfaces, at best in depths in the order of the roughness (Fig. 3). At the same time, ablation due to the induced "damage" should be kept to a minimum to avoid any loss of height of the structure. Methods based on UV-exposure were found most suitable and are particularly advantageous because they can be performed in ambient. PSI was thus producing test structures with challenging designs which were transferred into PMMA. With the help of FHNW, the polymer was characterized before and after modification with different exposure doses. This enables a quantitative approach and a balance between smoothing and preservation of structural details for different lens structures. Scientists hope that this approach will allow them to find ways of making new 3D lithographic methods suitable for use in the production of optical lenses.

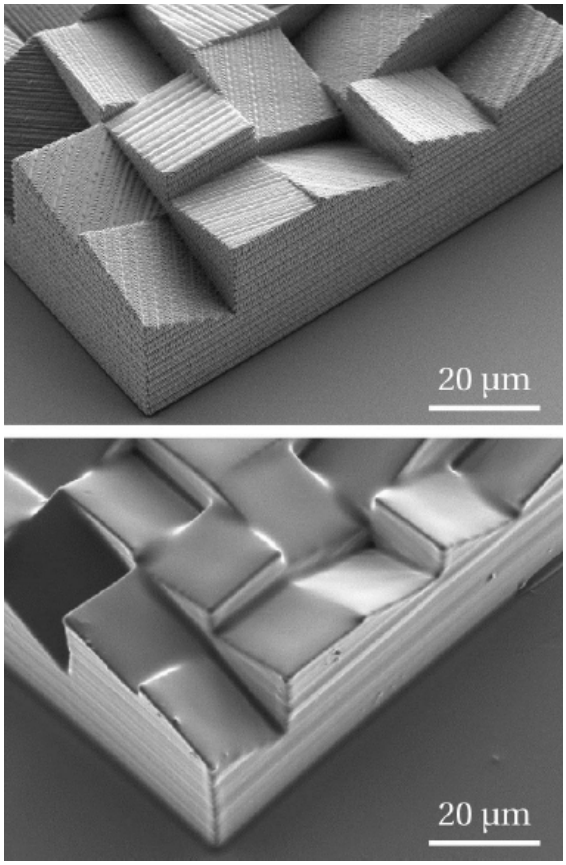

Fig. 3: Test structure made by two photon polymerization with characteristic roughness due to the discretization of the writing data. This roughness can be leveled out by surface selective exposure and thermal reflow.

References for Project A10.13

[1] A. Schleunitz, V.A. Guzenko, M. Messerschmidt, H. Atasoy, R. Kirchner, and H. Schift, *"Novel 3D micro- and nanofabrication method using thermally activated selective topography equilibration (TASTE) of polymers"*, Nano Convergence **1**, 7 (2014).

[2] H. Schift, *"Nanoimprint lithography: 2D or not 2D? A review"*, Applied Physics A **121**(2), 415-435 (2015).

Versatile lithography with multi-level phase masks

Project A10.14 VERSALITH (PSI, Eulitha AG Würenlingen, FHNW)
Project Leader: J. Gobrecht
Collaborators: V. Guzenko, H. Solak, Ch. Dais and P.M. Kristiansen

The goal of our research has been on the development of a stable and efficient process to create multi-level phase masks on quartz blanks that can be used for Displacement Talbot Lithography (DTL) exposures (1). Multi-level phase masks provide a much better control over the printed image with a much higher contrast than achievable with standard phase masks or amplitude masks. The multi-level phase masks were created with greyscale e-beam lithography on a Si wafer and subsequently replicated with Ormostamp material on quartz mask blanks

For the multi-level phase masks a "vortex phase" pattern with a period of 3µm and 1µm with hexagonal symmetry was designed. A schematic of the exposed pattern is shown in Figure 1.

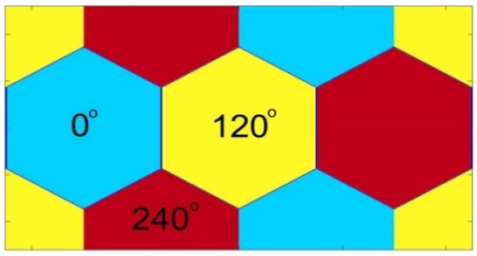

Fig. 1: Schematic of the vortex phase pattern that was used in the grayscale e-beam lithography.

The challenge is to design and optimize the e-beam exposures and photoresist process to create a three level phase mask with the right height steps in order to achieve phase shifts of the light of 0°, 120° and 240°. Since Ormostamp material with a refractive index of 1.5 will be used for DTL exposures, the target height step between honeycomb cells should be Δ=220-230nm. In order to get this accuracy the contrast curves of the chosen PMMA resist was carefully measured (see Figure 2) and the proximity effect simulated in order to get a resist profile with vertical sidewalls.

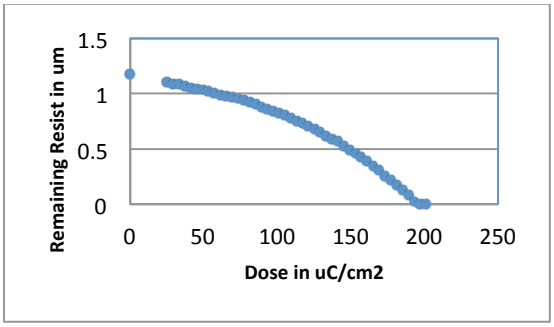

Fig. 2: Contrast curve of PMMA950K, 672.08. Developed in undiluted MIBK at 20°C for 4 minutes.

For the ebeam exposures 4" Si wafers with 1µm thick PMMA 950K-molecular weight resist were prepared. After exposure the wafer was developed with undiluted MIBK which is a low contrast developer and therefore of advantage for the grayscale lithography method. The development was stopped and restarted several times between which the step heights were measured with AFM. This iterative procedure was finally stopped when the required step height of around 230nm was reached. A 3D AFM image of the created pattern with a period of 3µm is shown in Figure 3. Clearly the three height levels are resolved and the structures have a hexagonal shape. The height plot in Figure 3 indicates steep sidewalls between the plateaus. However the height steps are not equidistant and are slightly less deep than the target height step of 230nm. The first step from the top has a depth of 205nm whereas the second step has a height of 220nm. Also the plateau on top is with a diameter of 3.1µm larger than the plateau at the bottom with 2.9µm. These issues will be addressed in further experiments by fine adjusting the e-beam pattern design, exposure dose and the development time.

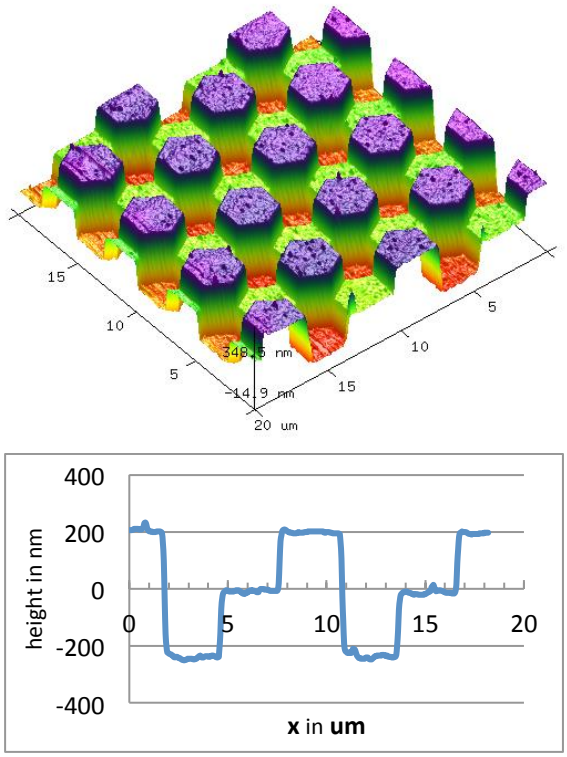

Fig. 3: Top: 3D AFM image of the vortex phase pattern in PMMA on Si. Bottom: Corresponding height plot of the three level PMMA structures.

The next step was to replicate the pattern from the Si substrate to a 5" Quartz mask blank which is the standard substrate for DTL exposures. For replication we used Ormostamp from Micro Resist Technology which is a hybrid polymer that is commonly used to produce transparent imprint stamps. The process starts with spin-coating the Quartz mask with Ormoprime, the recommended primer, for better adhesion. Next, a few drops of Ormostamp are dispensed on top of the structures on the Si wafer followed by carefully putting the Quartz mask over the Si wafer. The Ormostamp spreads now slowly in the gap between mask and wafer. It is important to wait a reasonable time (30min) for filling the structures with the polymer and to push captured air bubbles out of the structured area. Subsequently the Ormostamp is cured with UV light using a mask aligner. The wafer/mask sandwich was then put in acetone for several hours to slowly dissolve the PMMA and separate the mask from the Si wafer. Figure 4 shows on top an AFM image of the replicated Ormostamp structures obtained on the quartz mask blank with a period of 3µm. The hexagonal shape of the structures is clearly visible and the height plot proves the one-to-one transfer of the height steps from PMMA to Ormostamp. The first step from the top has now a depth of 205nm whereas the second step has a height of 220nm.

In the next step we used the same process to create structures with higher resolution. The bottom image of Figure 4 shows the replicated vortex phase pattern in Ormostamp with a period of 1um. The first step from the top has a depth of 215nm whereas the second step has a height of 230nm. In further iterations we will fine adjust the e-beam dose to get equidistant height steps.

In the period after July 2015 this project could be continued with support from the Forschungsfonds Aargau. We will use the created multi-level phase masks in DTL exposures. After the completion of this first test cycle the project will proceed with fabrication of optimized phase shifting masks with the current design and other designs which will include higher resolution versions of the "vortex phase" design.

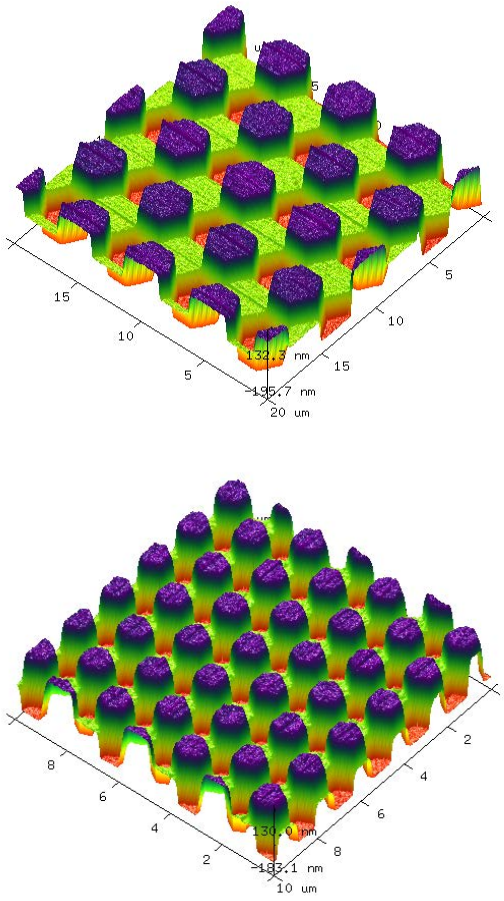

Fig.4: 3D AFM images of the vortex phase pattern after one-to-one replication into Ormostamp. The period of the structures are 3µm (top) and 1µm (bottom).

References for Project A10.14

[1] Harun H. Solak, Christian Dais, Francis Clube, Li Wang, Microelectronic Engineering, **143**, 74–80, (2015).


KANTON AARGAU


SNI
SWISS
NANOSCIENCE
INSTITUTE
EINE INITIATIVE DER UNIVERSITÄT BASEL
UND DES KANTONS AARGAU


Universität
Basel


Fachhochschule
Nordwestschweiz


PAUL SCHERRER INSTITUT
PSI


D-BSSE
Department of Biosystems
Science and Engineering


csem


Universitätsspital
Basel


Swiss TPH
Swiss Tropical and Public Health Institute
Schweizerisches Tropen- und Public Health-Institut
Institut Tropical et de Santé Publique Suisse

Educating
Talents
since 1460.

University of Basel
Petersplatz 1
P.O. Box 2148
4001 Basel
Switzerland

www.unibas.ch